

PACIFIC EARTHQUAKE ENGINEERING RESEARCH CENTER

Development of Simplified Analysis Procedure for Piles in Laterally Spreading Layered Soils

Christopher R. McGann

Pedro Arduino

Peter Mackenzie-Helnwein

Department of Civil and Environmental Engineering
University of Washington

Disclaimer

The opinions, findings, and conclusions or recommendations expressed in this publication are those of the author(s) and do not necessarily reflect the views of the study sponsor(s) or the Pacific Earthquake Engineering Research Center.

Development of Simplified Analysis Procedure for Piles in Laterally Spreading Layered Soils

**Christopher R. McGann
Pedro Arduino
Peter Mackenzie-Helnwein**

Department of Civil and Environmental Engineering
University of Washington

PEER Report 2012/05
Pacific Earthquake Engineering Research Center
Headquarters, University of California, Berkeley
December 2012

ABSTRACT

This work presents the development of a simplified procedure for the analysis of liquefaction-induced lateral spreading using a beam on nonlinear Winkler foundation approach. A three-dimensional finite element model, considering a single pile in a soil continuum, is used to simulate lateral spreading and two alternative lateral load cases. Sets of $p-y$ curves representative of the soil response in the 3D model are computed for various soil-pile systems. The affects of pile kinematics on these curves are evaluated and a computational procedure for $p-y$ curves is proposed. The computed curves are compared to $p-y$ curves defined by existing methods commonly used in practice to evaluate the applicability of these methods to lateral spreading analysis.

Comparison of the $p-y$ curves resulting from homogenous and layered soil profiles, in which a liquefied layer is located between two unliquefied layers, is used to identify reductions in the ultimate lateral resistance and initial stiffness of the $p-y$ curves representing the unliquefied soil due to the presence of the liquefied layer. These reductions are characterized in terms an exponential decay model. A simple procedure utilizing dimensionless parameters is proposed as a means of implementing appropriate reductions for an arbitrary soil profile and pile diameter. Beam on nonlinear Winkler foundation analyses of lateral spreading are conducted to validate and demonstrate the use of the proposed reduction procedure.

ACKNOWLEDGMENTS

This work was supported by the State of California through the Transportation Systems Research Program of the Pacific Earthquake Engineering Research (PEER) Center. Any opinions, findings, conclusions, or recommendations expressed in this material are those of the authors and do not necessarily reflect those of the funding agency.

CONTENTS

ABSTRACT	iii
ACKNOWLEDGMENTS	v
TABLE OF CONTENTS	vii
LIST OF FIGURES	xiii
LIST OF TABLES	xix
1 INTRODUCTION	1
1.1 Background	2
1.2 Scope of Work	4
2 THREE-DIMENSIONAL FINITE ELEMENT MODEL	7
2.1 Introduction	7
2.2 Model Overview	7
2.2.1 Selective Mesh Refinement	8
2.3 Boundary and Loading Conditions	9
2.3.1 Loading Conditions	9
2.4 Modeling the Soil-Pile Interface	10
2.4.1 Beam-Solid Contact Elements	10
2.5 Surface Load Elements	11
2.5.1 Formulation of Surface Load Elements	12
2.5.2 Validation of Surface Elements	14
3 MODELING THE PILES	17
3.1 Introduction	17
3.2 Template Pile Designs	17
3.3 Pile Elements	18
3.3.1 Fiber Section Models	19
3.4 Linear Elastic Pile Constitutive Behavior	20
3.5 Elastoplastic Pile Constitutive Behavior	20
3.5.1 Steel in Tension and Compression	22

3.5.2	Concrete in Compression	22
3.5.3	Concrete in Tension	23
3.5.4	One-Dimensional Fracture Mechanics of Concrete in Tension	24
3.5.5	Implementation of Tension Parameters	26
3.6	Validation of Pile Models	30
3.6.1	Moment-Curvature Response	30
3.6.2	Validation of Tension Parameters	36
4	MODELING THE SOIL	41
4.1	Introduction	41
4.2	Soil Elements	41
4.3	Linear Elastic Soil Constitutive Modeling	42
4.4	Elastoplastic Soil Constitutive Modeling	42
4.4.1	Drucker-Prager Constitutive Model	43
4.4.2	Determination of Material Parameters	46
4.5	Validation of Soil Models	47
4.5.1	Confined Compression Test	48
4.5.2	Conventional Triaxial Compression Test	50
4.5.3	Simple Shear Test	54
4.5.4	Hydrostatic Extension Test	57
4.5.5	Multi-Element Plane Strain Test	59
5	THREE-DIMENSIONAL FINITE ELEMENT ANALYSIS	61
5.1	Introduction	61
5.2	Summary of Considered Cases	62
5.2.1	Series 1: Elastic Piles with Elastic Soil	62
5.2.2	Series 2: Elastoplastic Piles with Elastic Soil	63
5.2.3	Series 3: Elastic Piles with Elastoplastic Soil	63
5.2.4	Series 4: Elastoplastic Piles in Elastoplastic Soil	63
5.3	General Behavior of Piles in Laterally Spreading Soil	64
5.4	Summary of Results from Three-Dimensional Lateral Spreading Simulations	68
5.4.1	The Effects of Pile Stiffness on the Soil-Pile System	70

5.4.2	The Effects of Pile Head Fixity	72
5.5	The Effects of Plasticity on the Laterally Spreading System	75
5.5.1	The Effects of Pile Plasticity	75
5.5.2	The Effects of Soil Plasticity on the Pile	75
5.6	Verification Models for Pile Behavior in Elastoplastic Soil	76
5.6.1	The First Simple Model	78
5.6.2	The Second Simple Model	81
5.6.3	Observations	83
5.7	Summary	85
6	COMPUTATION OF REPRESENTATIVE $p-y$ CURVES FROM THE THREE-DIMENSIONAL MODEL	87
6.1	Introduction	87
6.2	Computation of Force and Displacement Histories	87
6.3	Considered Kinematic Cases	89
6.4	Curve-fitting Strategies	89
6.4.1	Hyperbolic Tangent Function	90
6.4.2	Polynomial Function	91
6.5	Effects of Pile Kinematics on Computed $p-y$ Curves	93
6.5.1	Betti-Rayleigh Theorem of Reciprocal Work	98
6.5.2	Application of the Betti-Rayleigh Theorem	98
6.5.3	Proposed Solution to the Problem of Pile Kinematics	99
6.6	Effects of Selective Mesh Refinement on Computed $p-y$ Curves	100
6.7	Boundary Effects on Soil Response	102
6.8	Summary	107
7	APPLICABILITY OF CONVENTIONAL AND COMPUTED $p-y$ CURVES TO LATERAL SPREADING ANALYSIS	109
7.1	Introduction	109
7.2	A Brief Summary of the Considered Predictive Methods	109
7.2.1	Ultimate Lateral Resistance	110
7.2.2	Initial Stiffness	113
7.3	Comparison of Computed and Predicted $p-y$ Curves	115

7.3.1	Comparison of Ultimate Lateral Resistance	115
7.3.2	Comparison of Initial Stiffness	118
7.3.3	Comparison of $p-y$ Curves	121
7.4	Near-Surface Models	121
7.4.1	Initial Stiffness Distributions in Near-Surface Models	124
7.4.2	Ultimate Lateral Resistance Distributions in Near-Surface Models	124
7.5	Plane Strain Models	125
7.6	Summary	127
8	INFLUENCE OF LIQUEFIED LAYER ON THE SOIL RESPONSE	129
8.1	Introduction	129
8.2	Initial Observations	129
8.3	Updated Finite Element Model	134
8.3.1	Considered Soil Profiles	134
8.4	Characterizing the Influence of the Liquefied Layer	135
8.4.1	Reduction in Ultimate Lateral Resistance	135
8.4.2	Reduction in Initial Stiffness	135
8.5	Reduction Model	139
8.5.1	Parameter Identification	139
8.6	Reduction Procedure	140
8.7	Summary	142
9	BEAM ON NONLINEAR WINKLER FOUNDATION ANALYSIS	145
9.1	Introduction	145
9.2	Evaluation of Computed and Predicted $p-y$ Curves	146
9.2.1	Beam on Nonlinear Winkler Foundation Model	146
9.2.2	Modeling the $p-y$ Curves	147
9.2.3	Considered $p-y$ Curves	147
9.2.4	Results	148
9.3	Validation and Application of Proposed Curve Reduction Procedure	153
9.3.1	Test Profiles	153
9.3.2	Investigated Test Cases	154

9.3.3	Results	156
9.4	Effects of Soil Shear Modulus on Initial Stiffness of $p-y$ Curves	158
9.5	Summary	160
10	SUMMARY, CONCLUSIONS, AND RECOMMENDATIONS FOR FUTURE WORK	163
10.1	Summary and Conclusions	163
10.2	Recommendations for Future Work	168
	REFERENCES	171

LIST OF FIGURES

1.1	Schematic depicting the layered lateral spreading soil-pile system.	2
2.1	Typical finite element mesh for soil-pile system in deformed configuration.	8
2.2	A depiction of the imposed displacement profile for the lateral spreading model. . .	10
2.3	A top view of the finite element mesh for the soil mass. The pile is the dot in the center of the lower edge.	11
2.4	Details of the deformation in the soil elements around the pile using beam-solid contact elements.	11
2.5	Irregularly-shaped mesh used for surface load element validation.	14
2.6	Distribution of vertical stress in the surface load element validation model.	15
3.1	Template pile designs (to scale). (a) 0.61-m-diameter; (b) 1.37-m-diameter; (c) 2.5-m-diameter.	17
3.2	Dimensions and details of the three template piles. (a) 0.61-m-diameter; (b) 1.37-m-diameter; (c) 2.5-m-diameter.	18
3.3	Typical fiber discretization for a circular fiber section model.	19
3.4	Uniaxial constitutive relations used in fiber section models. (a) <i>Concrete02</i> model. (b) <i>Steel01</i> model.	21
3.5	Detail of tensile behavior in uniaxial concrete constitutive model.	23
3.6	Simplified fracture model for concrete in uniaxial tension.	24
3.7	Relationship between elongation, crack width, and element length for a single pile element.	25
3.8	Moment-curvature behavior for 0.61-m-diameter model illustrating softening behavior resulting from a large characteristic length, ℓ_c	28
3.9	Moment-curvature behavior for 2.5-m-diameter model with two values of characteristic length, ℓ_c	28
3.10	Moment-curvature behavior for 0.61-m-diameter model with various values of ℓ_c . Largest element length is 0.649 m. Smallest element length is 0.102 m.	29
3.11	Moment-curvature behavior for 1.37-m-diameter model with various values of ℓ_c . Largest element length is 1.79 m. Smallest element length is 0.231 m.	29
3.12	Distributions of stress and strain determined for 0.61-m-diameter cross section. . .	32

3.13	Comparison of moment-curvature responses for 0.61-m-diameter full (circular) pile model.	33
3.14	Comparison of moment-curvature responses for 0.61-m-diameter half-pile (semi-circular) model.	33
3.15	Comparison of moment-curvature responses for 1.37-m-diameter full (circular) pile model.	34
3.16	Comparison of moment-curvature responses for 1.37-m-diameter half-pile (semi-circular) model.	34
3.17	Comparison of moment-curvature responses for 2.5-m-diameter full (circular) pile model.	35
3.18	Comparison of moment-curvature responses for 2.5-m-diameter half-pile (semi-circular) model.	35
3.19	Cantilever beam analysis. The horizontal load, P , is increased linearly until the pile tip deflects a distance of one pile radius.	36
3.20	Moment-curvature response of cantilever model compared to zero-length element and independently calculated section responses for 0.61-m-diameter section. The cantilever model fails at this level of curvature.	37
3.21	Moment-curvature response of cantilever model compared to zero-length element and independently calculated section responses for 2.5-m-diameter section.	37
3.22	Force-displacement behavior for 0.61-m-pile section model as implemented in a cantilever beam model with various values of ℓ_c	38
3.23	Force-displacement behavior for 1.37-m-pile section model as implemented in a cantilever beam model with various values of ℓ_c	39
4.1	Drucker-Prager failure surface plotted in principal stress space.	43
4.2	Schematic depiction of the simulated CC test. (a) Hydrostatic compression phase; (b) Confined compression phase.	48
4.3	Stress paths for CC test.	49
4.4	Stress-strain responses of Drucker-Prager soil element subjected to CC test stress path.	49
4.5	Schematic depiction of the CTC test as performed in OpenSees. (a) Hydrostatic compression phase; (b) Application of deviator stress.	50
4.6	Comparison of simulated and theoretical CTC test stress paths.	51
4.7	Stress paths for CTC test in the perfectly plastic case (no strain hardening).	52
4.8	Stress paths for CTC test the linear isotropic strain hardening case.	52

4.9	Stress-strain responses of Drucker-Prager soil element subjected to a CTC stress path for the perfectly plastic case (no strain hardening).	53
4.10	Stress-strain responses of Drucker-Prager soil element subjected to a CTC stress path for the linear isotropic strain hardening case.	53
4.11	Schematic depiction of the SS test as performed in OpenSees. (a) Hydrostatic compression phase; (b) Simple shear phase.	54
4.12	Stress paths for SS test in the perfectly plastic case (no strain hardening).	55
4.13	Stress-strain responses of Drucker-Prager soil element subjected to a SS test stress path for the perfectly plastic case (no strain hardening).	55
4.14	Stress paths for SS test in the linear isotropic strain hardening case.	56
4.15	Stress-strain responses of Drucker-Prager soil element subjected to a SS test stress path for the linear isotropic strain hardening case.	56
4.16	Schematic depiction of the HE test as performed in OpenSees.	57
4.17	Stress paths for HE test, on the meridian plane for three values of the tension softening parameter, δ	58
4.18	Stress-strain response of Drucker-Prager soil element subjected to a HE test stress path for three values of tension softening parameter, δ	58
4.19	A representation of the load case modeled by the multi-element plane strain test for the Drucker-Prager material model.	59
4.20	The deformed mesh for the plane strain test with the distribution of vertical stress in the soil elements (magnification factor = 10).	60
4.21	Stress paths for a selection of Gauss points along the top row of the plane strain model.	60
5.1	Deformed shape and distribution of lateral stress for the Series 1 free-head case with a 0.61-m-diameter pile. Stresses are given in kPa.	64
5.2	Pile summary plots for a 0.61-m-diameter pile. Series 1, free-head case. The liquefied layer is the shaded region.	66
5.3	The effective length, L_{eff} , is the distance between the extreme moments in each solid soil layer, as shown in this moment diagram.	67
5.4	Soil deformation pattern in the vicinity the pile for the Series 4 case highlighting the unliquefied soil elements pushing into the liquefied layer.	68
5.5	Load distributions resulting from the lateral spreading ground motion for the free-head Series 1 cases for 0.61-m and 2.5-m-diameter piles.	70
5.6	Deflected shapes of free-head piles for various cases. (a) Series 1, 0.61-m-diameter; (b) Series 1, 2.5-m-diameter; (c) Series 2, 0.61-m-diameter; (d) Series 2, 2.5-m-diameter.	71

5.7	Upward heave of soil elements at the ground surface for the Series 4 case with a 2.5-m-diameter pile (magnification factor = 1).	73
5.8	Moment distributions and deflected shapes for the fixed-head Series 1 cases with 2.5-m and 1.37-m-diameter piles.	74
5.9	Pile summary plots for a 0.61-m-diameter pile. Series 3, free-head case. The liquefied layer is the shaded region.	77
5.10	The two simple beam models used for verification of results. (a) The first simple model. (b) The second simple model.	78
5.11	Displaced shape, shear diagram, and moment diagram for the first simple model.	80
5.12	Displaced shape, shear diagram, and moment diagram for the second simple model.	83
5.13	Normalized relationships between $L_{eff, \max} M$, and p for the two simple models.	84
6.1	Computation of $p-y$ curves from the 3D FE model.	88
6.2	Determination of displacements suitable for use in $p-y$ curves for the lateral spreading case.	88
6.3	Pile kinematic cases. (a) Lateral Spreading; (b) Top pushover; (c) Rigid pile.	89
6.4	Example of computed $p-y$ data with fitted initial tangent stiffness and hyperbolic tangent curve for a 1.37 m diameter pile.	92
6.5	The lateral resistance ratio, LRR, is the ratio of the soil resistance values computed in two reference $p-y$ curves at a prescribed value of displacement.	93
6.6	Comparison of the lateral spreading kinematic case to the rigid pile case for a 1.37-m-diameter pile. Both analyses use a three-layer liquefied soil system.	95
6.7	Comparison of the top pushover kinematic case to the rigid pile case for a 1.37-m-diameter pile. Both analyses use homogenous soil profiles.	95
6.8	Computed $p-y$ curves from the top pushover and rigid pile cases in homogenous soil for a 0.61-m-diameter pile. The fitted initial tangents are shown for each case.	96
6.9	Computed $p-y$ curves from the lateral spreading and rigid pile cases in non-homogenous soil for a 0.61-m-diameter pile. The fitted initial tangents are shown for each case.	97
6.10	Two separate load cases, P and Q , with respective displacements, u and v , applied to the same points on a general elastic body.	98
6.11	Distributions of k_T and p_u for 1.37-m-diameter pile in homogenous soil profile.	101
6.12	Examples of smoothing process on curve parameters for 1.37-m-diameter pile. (a) Distribution of p_u from rigid pile in liquefied soil profile; (b) Distribution of k_T from rigid pile in liquefied soil profile; (c) Distribution of k_T from top pushover in homogenous soil profile.	101

6.13	Laterally-extended mesh for 0.61-m-pile design.	103
6.14	Comparison of $p-y$ curve parameter distributions for extended and standard meshes for a 0.61-m-diameter pile.	104
6.15	Plan view showing the distribution of vertical displacement (i.e., soil heave) in the soil elements. The areas near the pile indicate the greatest magnitude of displacement, while the constantly shaded areas near the boundaries have zero displacement.	104
6.16	Contour plot of vertical soil displacements in the extended mesh. Only upward displacements are considered.	105
6.17	Contour plot of vertical soil displacements for the rigid pile case in the standard mesh. Only upward displacements are considered.	105
6.18	Distribution of the first invariant of stress, I_1 , in the standard mesh for a 0.61-m-diameter pile.	106
6.19	Distribution of the first invariant of stress, I_1 , in the extended mesh for a 0.61-m-diameter pile.	106
7.1	Distributions of ultimate lateral resistance for a 0.5-m-diameter pile as specified by four predictive methods.	110
7.2	Recommended coefficient of subgrade reaction after API (1987). The conversion from units of lb/in^3 is obtained through multiplication with a factor of 271.45 to obtain units of kN/m^3	114
7.3	Distributions of ultimate lateral resistance and initial stiffness for each of the three template pile designs as compared to commonly referenced distributions.	116
7.4	Comparison of computed $p-y$ data with fitted hyperbolic tangent curves for a 2.5-m-diameter pile.	117
7.5	Distribution of stress in the direction of loading at full lateral displacement of a 0.61-m-diameter pile in the rigid pile kinematic case.	118
7.6	Norm of the deviatoric plastic strain, $\ e^p\ $, for a 0.61-m-diameter pile.	119
7.7	Linear elastic and elastoplastic k_T distributions computed from 3D FE analysis.	120
7.8	Computed and API recommended $p-y$ curves for a 1.37-m-diameter pile.	121
7.9	Near-surface mesh for a 1.37-m-diameter pile.	122
7.10	Comparison p_u and k_T distributions for default and near-surface meshes over the first 10 m below the ground surface.	123
7.11	Distributions of initial stiffness computed from the near-surface models using both elastoplastic and elastic soil elements.	124
7.12	Computed p_u distributions for near-surface models.	125
7.13	Comparison parameter distributions for default and plane strain FE models.	126

7.14	Comparison of estimated p_u distributions with corresponding results from plane strain model for a 2.5-m-diameter pile.	127
8.1	Distributions of p_u and k_T for homogenous and liquefied soil profiles for a 1.37-m-diameter pile.	130
8.2	Computed p_u ratios for a series of overburden pressures, p_{vo} . The five cases are compared at lower right.	132
8.3	Computed k_T ratios for a series of overburden pressures, p_{vo} . The five cases are compared at lower right.	133
8.4	Updated layered soil 3D FE mesh.	134
8.5	Comparison of p_u and k_T in homogenous and liquefied soil profiles for a 0.61-m-diameter pile.	136
8.6	Computed p_u ratios above the liquefied layer for a 0.61-m-diameter pile.	137
8.7	Computed p_u ratios below the liquefied layer for a 0.61-m-diameter pile.	137
8.8	Computed k_T ratios above the liquefied layer for a 1.37-m-diameter pile.	138
8.9	Computed k_T ratios below the liquefied layer for a 1.37-m-diameter pile.	138
8.10	Dimensionless relations for p_u above and below the liquefied layer.	140
8.11	Dimensionless relations for k_T above and below the liquefied layer.	141
9.1	Schematic representation of the BNWF model.	146
9.2	Deflected shape, shear force, and moment diagrams for BNWF and 3D FE analyses of lateral spreading for a 1.37-m-diameter pile with linear elastic behavior.	152
9.3	Evolution of extreme moment demands in top and bottom layers with increasing displacement of upper soil layer during BNWF and 3D FE lateral spreading analyses for a 1.37-m-diameter pile.	153
9.4	Distributions of p_u used in BNWF models.	155
9.5	Distributions of k_T used in BNWF models.	155
9.6	Comparison of maximum pile shear and moment demands.	156
9.7	Deformed shapes of pile in the VC2 and PC3 BNWF analyses.	158
9.8	Comparison of initial stiffness distributions for various values of soil shear modulus, G	159
9.9	Comparison of maximum pile shear and moment demands for higher shear modulus cases.	160

LIST OF TABLES

3.1	Material and section property values in linear elastic pile models.	20
3.2	Steel material property input values in fiber section models.	21
3.3	Concrete material property input values in fiber section models.	21
3.4	Concrete fracture energies and crack propagation slopes.	25
3.5	Characteristic length and tension softening modulus in pile models.	27
4.1	Material parameters in isotropic linear elastic soil constitutive model.	42
4.2	Material input parameters used in Drucker-Prager soil constitutive model.	47
5.1	Overview of the four considered test Series.	62
5.2	Summary of 3D lateral spreading analyses for the 2.5-m-diameter pile.	69
5.3	Summary of 3D lateral spreading analyses for the 1.37-m-diameter pile.	69
5.4	Summary of 3D lateral spreading analyses for the 0.61-m-diameter pile.	69
6.1	Overview of the four considered kinematic comparison cases.	94
7.1	Approximate coefficients of subgrade reaction for initial portion computed k_T distributions.	119
8.1	Considered soil profiles for each pile diameter.	136
8.2	Reduction coefficients for ultimate lateral resistance, p_u	142
8.3	Reduction coefficients for initial stiffness, k_T	142
8.4	Summary of proposed $p-y$ curve reduction procedure.	143
9.1	Overview of the considered BNWF analysis cases for each pile.	148
9.2	Pile bending response summary for BNWF analysis with a 2.5-m-diameter pile. . .	149
9.3	Pile bending response summary for BNWF analysis with a 1.37-m-diameter pile. .	149
9.4	Pile bending response summary for BNWF analysis with a 0.61-m-diameter pile. .	150
9.5	Relative error between BNWF and 3D FE results for 2.5-m-diameter pile.	151
9.6	Relative error between BNWF and 3D FE results for 1.37-m-diameter pile.	151

9.7	Relative error between BNWF and 3D FE results for 0.61-m-diameter pile.	151
9.8	Maximum pile bending demands in BNWF lateral spreading simulations.	156
9.9	Maximum pile bending demands in BNWF lateral spreading simulations for higher shear modulus cases.	160

1 Introduction

Pile foundations are used extensively to provide support for bridges and wharf facilities, very often in seismically active regions where there is potential for liquefaction-induced lateral spreading. The kinematic demands placed upon a pile during such an event are complex. Due to the challenges presented by this problem, it is difficult to obtain reasonable estimates of the bending moment and shear force demands placed upon a pile. Design procedures for piles subject to this load case must therefore rely on simplified, and often over-conservative, analytic methods. A simplified method of analysis that captures essential elements of the liquefaction-induced lateral spreading load case would be ideal for use as a design procedure.

The purpose of this study is to investigate the pile and soil responses to lateral spreading, and to evaluate the applicability of conventional analysis methods to this load case, in order to develop a simplified design procedure for the lateral spreading load case. This evaluation is conducted with respect to one of the current state-of-the-practice design paradigms for the analysis of laterally-loaded piles, the $p-y$ method (McClelland and Focht, 1958; Matlock and Reese, 1960; Reese and Van Impe, 2001), as well as with respect to other conventional analysis tools. These goals will be accomplished through investigation of the response of a single pile to a simulated lateral spreading event using the OpenSees (<http://opensees.berkeley.edu>) finite element (FE) analysis platform developed at the Pacific Earthquake Engineering Research (PEER) Center. The investigation will involve several sizes of piles embedded in soil systems consisting of varying soil profiles and properties, and will utilize both one- and three-dimensional finite element (FE) models. This work is an extension of past research conducted by Lam et al. (2009), who used linear elastic 3D FE models to develop a simplified method for predicting the magnitude and location of the maximum bending moment and shear force demands for a pile subject to lateral spreading.

It is hypothesized that 1D soil response curves reflecting the kinematic loading, the effects of depth, and the interaction between the soil layers occurring during a lateral spreading event can be computed using 3D FE models. The resulting force density-displacement ($p-y$) curves can then be used to evaluate the applicability of conventionally-defined curves to lateral spreading analysis, as well as to further investigate the behavior of the pile-soil system during this type of event. This report describes the development of all of the necessary models and discusses the findings made. A simplified design procedure for piles subject to lateral spreading is proposed, validated, and demonstrated.

1.1 BACKGROUND

The problem of liquefaction-induced lateral spreading is very important in the design of deep foundation systems in certain situations. Common scenarios for which this phenomenon must be considered include bridge piers and foundations for port facilities that lie in seismically active regions. Often, in the areas in that these structures are constructed, layered soil systems will be encountered in which a potentially liquefiable layer is present between two layers which have a lower liquefaction potential. The system presented in Figure 1.1 is an example of one such situation. In this soil system, a relatively loose sand layer separates two denser layers of sand. The potential for liquefaction is much greater in the loose sand layer than it is in the surrounding material.

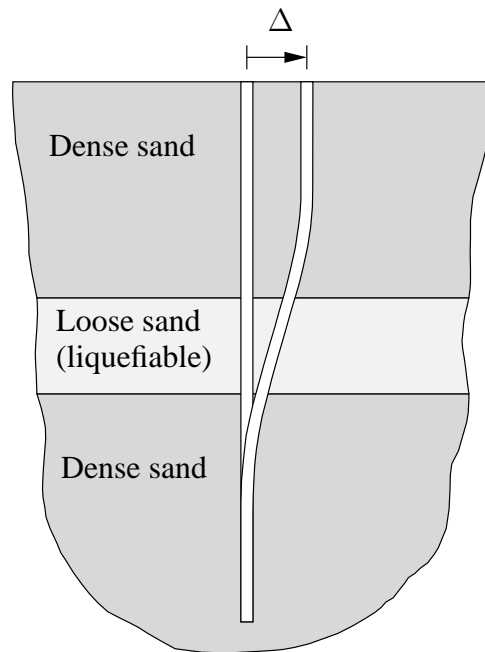


Figure 1.1 Schematic depicting the layered lateral spreading soil-pile system.

During or slightly after a seismic event, a liquefied condition can develop in the loose liquefiable layer with the potential for lateral displacement of the upper non-liquefiable layer relative to the bottom soil layer. Under these circumstances, a pile embedded in such a soil profile is subject to kinematic demand, causing it to deform in a manner similar to that shown in Figure 1.1. If the pile is embedded to a sufficient depth, the base of the pile will remain essentially fixed in the lower soil layer while the upper portion of the pile is displaced laterally, resulting in large bending moment and shear force demands within the pile.

There are many challenges that arise when modeling the response of a pile to lateral loads. Due to these challenges, the most common method employed during numerical analysis of piles is the $p-y$ method (McClelland and Focht, 1958; Matlock and Reese, 1960; Reese and Van Impe, 2001). There are other simplified approaches that may be employed in designing piles to resist lateral loads, but with the advent of easily-implemented computer programs based on the $p-y$ method, it has become the most prevalent.

In this analytic method, the 3D laterally-loaded pile problem is emulated using a beam on nonlinear Winkler foundation (BNWF) approach in which uncoupled nonlinear force density-displacement ($p-y$)¹ curves are used to describe the lateral soil-pile interaction. For cohesionless soils, the majority of the $p-y$ curves currently used in practice are based on the lateral load tests and associated semi-empirical analysis of Reese et al. (1974). In the type of loading used, the pile deforms in such a manner that the soil response near the surface is captured well, however, there is a lack of information at depth.

The $p-y$ curves recommended by Reese et al. have been used in many lateral pile design applications, often with great success. However, application of these curves to analyses outside the original scope of the work, such as large diameter piles, drilled shafts, or a different load case, can prove difficult due to problems inherent to the analysis approach and to the $p-y$ curves developed by Reese et al. (1974). These problems include:

1. The tendency for the $p-y$ curves to be too stiff with depth.
2. The reliance upon the single pile kinematic represented by the empirical results.
3. The uncoupled behavior of the individual $p-y$ curves with depth.

Most of the effects of these problems can be circumvented through careful modeling decisions. For example, Finn and Fujita (2002) compared the results of dynamic BNWF analyses with centrifuge and 3D FE analysis data, and found good agreement at low acceleration levels and with certain curve parameters. Despite known shortcomings inherent to the method, the $p-y$ analysis approach can be used successfully in lateral pile analysis.

For the case of liquefaction-induced lateral spreading, several considerations must be made in order to obtain sensible results from a BNWF analysis. Large pile deformations may occur below the near surface zone, and depending upon the depth of the liquefied layer, the pile kinematics may be completely different than those of a top-loaded lateral pile test. Additionally, the liquefied zone of soil within the soil profile must be properly accounted for in the soil response represented by the $p-y$ curves.

Modifications to the $p-y$ curves can circumvent problems associated with a lack of information at depth in the original experiments of Reese et al. (1974) – Brandenburg et al. (2007) showed that $p-y$ curves with modified initial stiffness produce results which are reasonably similar to centrifuge test data for the lateral spreading case – however, a detailed examination of the effect of pile kinematics on the measured soil response has not been conducted. With respect to the liquefied layer of soil, recommendations have been made as to modifications to the $p-y$ response to account for the liquefaction itself (Brandenburg et al., 2007), however, no recommendations exist to account for the strength differential between the liquefied and unliquefied material. Using 3D FE analysis, Yang and Jeremic (2005) and Petek (2006) have demonstrated that in a soil profile

¹In the usually employed nomenclature, which appears to date from the 1950s, the symbol p is used to denote the pressure acting on the pile in units of FL^{-2} , although in the final curves it usually represents the reaction force per unit length of the pile, FL^{-1} , and the pile deflection is given by the symbol y . To be consistent with solid mechanics convention, the displacement should be taken as u , y is a coordinate direction, however, the original symbols p and y will be used to remain consistent with practical usage (Scott, 1981).

in which a single weaker layer of soil is located between two stronger soil layers, the presence of the weaker layer effectively reduces the available lateral response of the surrounding material. The potential for a liquefied zone of soil to act in a similar manner and the corresponding effect this may manifest in $p-y$ curves has not yet been explored.

1.2 SCOPE OF WORK

This report details the work related to the development of a set of 3D FE models for the lateral spreading case and the evaluation of the results obtained. The work encompasses the development and validation of all of the necessary FE models, lateral spreading analysis using the 3D FE model, computation of representative $p-y$ curves from the 3D model for several types of pile kinematics, the evaluation of the applicability of a BNWF analysis using $p-y$ curves to the lateral spreading load case, and the proposal of a simplified analysis procedure for piles affected by liquefaction-induced lateral spreading using a BNWF approach.

This study does not intend to include the simulation of the liquefaction process. In all cases, it is assumed that the liquefiable soil has lost most of its strength and only the residual strength is considered. This simplification allows the use of quasi-static simulations to represent the post-liquefaction effects of lateral spreading.

Finite Element Model Development

Chapters 2, 3, and 4

- A template 3D soil-pile interaction model is created. This model employs beam-column elements to model the piles, solid brick elements for the soil, and beam-solid contact elements to define the soil-pile interaction.
- Fiber section models are developed for a series of template reinforced concrete piles. The nonlinearity of the piles is captured through these fiber sections, which define the behavior of the piles at a cross-sectional level.
- A Drucker-Prager elastoplastic constitutive model is explored for the soil elements.
- It is important to ensure that computer models exhibit verifiably-correct behavior when applied to simple load cases. Validating simulations are performed to ensure that all components of the models display predictable responses.
- From the template model, specialized cases with various element types, input parameters, and loading conditions are generated for use in this study.

3D Lateral Spreading Analysis

Chapter 5

- The bending response of piles subject to a lateral spreading event is evaluated through a parametric study conducted using the developed 3D FE models.
- Several parameters are considered such as the diameter of the pile, the constitutive models for both the pile and the soil, and the support conditions of the pile head.
- The observed trends in pile and soil behavior are discussed and analyzed.

Computation of Representative $p-y$ Curves

Chapter 6

- Using the developed 3D FE model $p-y$ curves are computed considering elastic pile elements and an elastoplastic soil constitutive model.
- The computational process is discussed and various factors, such as pile kinematics, that can influence the computed $p-y$ curves are identified and discussed.

Evaluation of Computed and Conventional $p-y$ Curves

Chapter 7

- Several conventional means for estimating the lateral response of a given soil profile are identified and compared to each other, and to the $p-y$ curves computed from 3D FE analysis.
- Several additional FE models are developed to further explore the individual merits of the conventional and computed sets of $p-y$ curves.

Influence of a Weak Liquefied Layer on Response of Soil System

Chapter 8

- The influence of the weaker liquefied soil layer on the stronger surrounding unliquefied material is characterized.
- A series of new 3D FE models are developed that consider a variety of liquefied layer depths and thicknesses.
- A parameter study is conducted using the new FE models to obtain a mathematical model for the observed reductions in the response of the unliquefied material.
- A procedure to reduce $p-y$ curves to account for the presence of a liquefied layer is proposed.

Beam on Nonlinear Winkler Foundation Analysis of Lateral Spreading

Chapter 9

- The $p-y$ curves obtained from the 3D models are extended for use in a BNWF model, which is analyzed for the lateral spreading load case. A set of conventionally derived $p-y$ curves are also utilized in this model.
- Using the BNWF model, a parameter study investigating the relative responses obtained using the two sets of $p-y$ curves is conducted. The parameter study considers both elastic and elastoplastic pile elements.
- The pile bending demands obtained from the BNWF analyses are compared to equivalent results obtained in the 3D modeling effort.
- The proposed procedure for reducing $p-y$ curves to account for the presence of a liquefied layer of soil is validated and demonstrated for computed and conventionally defined $p-y$ curves. Recommendations are made for the analysis of piles affected by liquefaction-induced lateral spreading using a BNWF approach.

2 Three-Dimensional Finite Element Model

2.1 INTRODUCTION

The response of a single pile embedded in a laterally spreading layered soil profile is investigated using a 3D FE model. During liquefaction-induced lateral spreading, complex events occur, especially at the soil-pile interface and the layer boundaries. Due to this complexity, it is difficult to accurately represent this problem using 1D or 2D models. For the purposes of this research, it was important to account for the fundamentally three-dimensional nature of the problem; leading to the creation of a 3D FE model of the soil-pile system.

The open-source FE framework OpenSees (<http://opensees.berkeley.edu>), developed through the Pacific Earthquake Engineering Research (PEER) Center, is used for all numerical simulations. The commercial program GiD (CIMNE, 2008) is used as a graphical pre- and post-processor for OpenSees.

2.2 MODEL OVERVIEW

A typical FE mesh used in this study is shown in its deformed configuration in Figure 2.1. The model includes three distinct layers of soil. These soil layers consist of two thick layers of unliquefiable soil between which a relatively thin layer of liquefiable soil is located. The elements of the embedded pile are located in the middle of the soil system. As shown, this model takes advantage of the inherent symmetry of the problem.

There are three pile designs considered in this research. The size and layout of the layers in the lateral spreading model are dependent upon the diameter of the embedded pile, leading to the creation of three separate base models differing only in their dimensions. In these models, the thickness of the upper and lower soil layers are set arbitrarily equal to ten pile diameters. This thickness is adequate to essentially hold the base of the pile fixed in place relative to the top of the pile. The thickness of the liquefiable layer is arbitrarily set as one pile diameter in this study.

It is critical to define a sensible horizontal extent for the soil in the model to ensure that boundary effects do not affect the results. Past work with laterally loaded piles found in the literature (Brown and Shie, 1990; Yang and Jeremic, 2005) used thirteen and eleven pile diameters on either side of the pile, respectively. Using this information and past modeling experience, the models include a horizontal extent of ten pile diameters from the pile centerline. The ten-diameter lateral distance

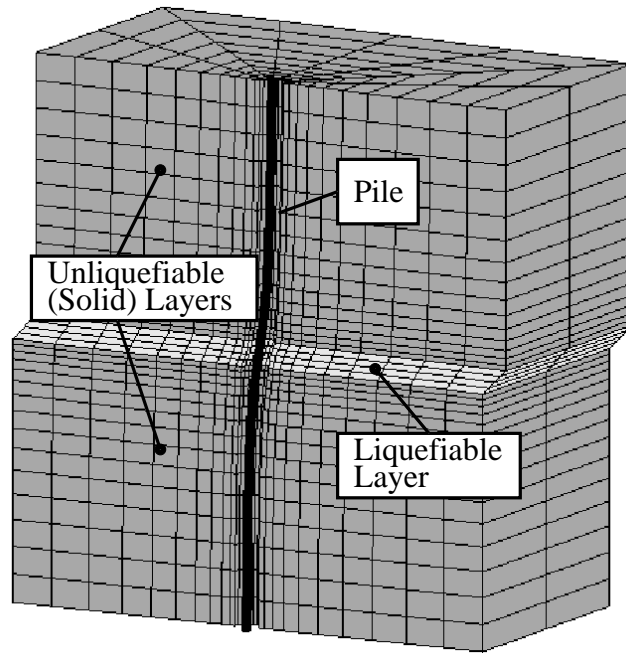


Figure 2.1 Typical finite element mesh for soil-pile system in deformed configuration.

is considered to be wide enough to allow for the effective reduction of the free-field kinematic demand imposed upon the soil system in the areas surrounding the pile. Additionally, this distance is deemed sufficiently wide so as to remove the pile from any effects imposed by the applied boundary conditions at the extents of the model.

Chapters 3 and 4 discuss the pile and soil models incorporated into the three-dimensional lateral spreading model as well as the motivations behind their selections. All further information pertaining to these components of the model can be found there.

2.2.1 Selective Mesh Refinement

When a pile is pushed through a soil profile with a liquefied layer, it is important to capture the interaction between the pile and the soil near the solid-to-liquefied layer interface with a relatively high degree of resolution. For this case, the regions near the top and bottom of the pile are comparatively less important. The models are built to take advantage of the relative levels of importance assigned to the various sections along the length of the pile through the use of selective refinement. The vertical size of the soil and pile elements is somewhat large at the top and bottom of the mesh. These large elements gradually transition into smaller elements from either side of the liquefied layer, with the smallest elements existing in the middle of that layer. Similarly, the horizontal size of the soil elements is large at the boundaries of the mesh and becomes smaller as the radial distance to the center of the pile decreases. This pattern of selective refinement is illustrated in Figure 2.1. Effectively, the models have been developed such that the mesh is refined in the areas of importance and left unrefined in the other areas.

2.3 BOUNDARY AND LOADING CONDITIONS

In order for a FE model to be effective in modeling a specific case, appropriate boundary conditions must be defined. The lateral spreading model requires boundary conditions that offer support to the elements as well as those that restrict unnecessary motions. As shown in Figure 2.1, symmetry is employed in the model, and only the soil on one side of the pile is considered. This use of symmetry introduces additional boundary conditions into the model.

The boundary conditions on the soil nodes are relatively simple. These nodes are created with only three translational degrees of freedom. To support the model against gravity loading, the soil nodes on the base of the model are held fixed against displacements in the vertical direction (the direction parallel to the axis of the pile). To enforce the symmetry condition, all of the nodes on the symmetry plane are held fixed against translation normal to this plane. Additionally, all of the soil nodes lying on the outer surfaces of the model are held fixed against horizontal in-plane translations and translations normal to their surface to enhance the stability of the model.

The base node of the pile is held fixed against translation in the vertical direction (parallel to the pile axis), a required stability condition. The pile is allowed to rotate in the plane of loading at each node with the exception of cases where a fixed support condition is imposed at the head of the pile. The pile requires fixing of the torsional rotation and out-of-plane rotations (rotation axis in-plane) to enforce the symmetry of the model.

2.3.1 Loading Conditions

The first step in the analysis of the lateral spreading model is to apply gravity loads. All of the soil elements are assigned a unit weight of $\gamma = 17 \text{ kN/m}^3$. During the self-weight analysis, gravity is switched on and the soil elements generate a linearly increasing stress profile with depth. This procedure creates an appropriate distribution of confining pressures in the model, critical to determining the effective strength of the soil elements and to obtaining sensible results. Only after the self-weight analysis has successfully converged does the model move on to the lateral analysis. The self-weight of the pile is neglected.

During a simulated lateral spreading event, the lower unliquefied layer is assumed to remain stationary while the upper unliquefied layer and the liquefied middle layer experience lateral translations relative to the lower layer. This kinematic loading is achieved in the model by gradually imposing a set displacement profile to the soil nodes on all outer surfaces of the model excluding the symmetry face. This displacement profile represents the far-field kinematic demands on the soil system, with the upper layer translating relative to the lower layer. The presence of the pile alters the behavior of the soil, creating a near-field kinematic demand to which the pile will be subjected. The imposed profile is only applied to the boundary nodes in order to allow ample distance over which the far-field kinematic demand can be reduced to the more manageable near-field demand.

The horizontal displacement is imposed as constant upon the entire height of the upper unliquefied layer and as linearly increasing over the height of the liquefied layer. No displacements are imposed upon the lower unliquefied layer. The imposed displacement profile is shown in Figure 2.2.

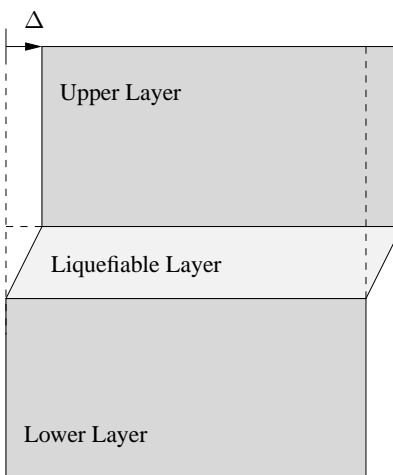


Figure 2.2 A depiction of the imposed displacement profile for the lateral spreading model.

Excepting those restrictions, all other soil nodes are free to move in any direction. The magnitude of the constant horizontal displacement in the upper layer is taken to be one pile radius.

2.4 MODELING THE SOIL-PILE INTERFACE

It is important to recognize that the behavior of a laterally loaded pile embedded in a soil system is governed, in part, by the complex interaction between the soil and the pile. Before the pile begins to move, the stresses applied by the soil should be uniform (for a given depth) and normal to the pile surface. After the pile has deflected laterally, the stresses on the leading side of the pile increase, while the stresses on the following side of the pile decrease. Additionally, these stresses may now have both normal and shear components, depending upon the particular loading conditions (Reese and Van Impe, 2001). The amount of resistance provided by the soil depends upon the amount of pile deflection that has occurred, which in turn depends upon the amount of resistance provided by the soil (among other factors). This interactive relationship between the soil and the pile is crucial to the lateral spreading problem and must be accounted for in the FE model.

One suitable means to account for the interaction between soil elements and any embedded structural components is the use of contact elements. In this study, the interaction between the soil and the embedded pile is defined through beam-solid contact elements developed and implemented in OpenSees by Petek (2006).

2.4.1 Beam-Solid Contact Elements

As shown in Figure 2.3, the soil elements form a semi-circle of blank space around the pile elements. Because standard beam-column elements have no physical size, this blank space is included to represent the extents of the pile. Existing between the single row of pile elements and the adjacent perimeter of soil elements are contact elements that define both the physical size of the pile and the ways in which the pile and soil elements interact.

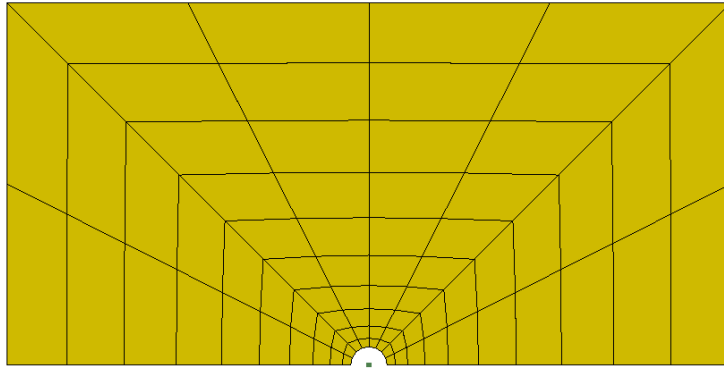


Figure 2.3 A top view of the finite element mesh for the soil mass. The pile is the dot in the center of the lower edge.

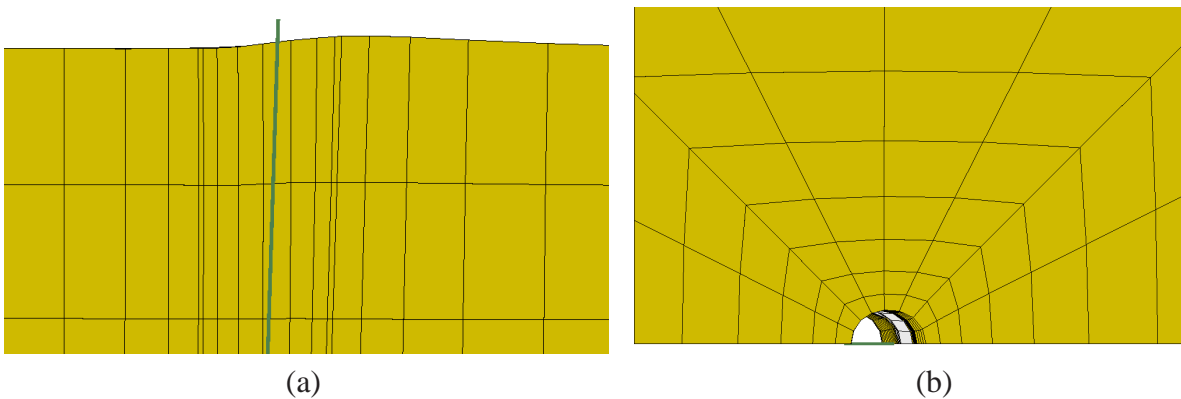


Figure 2.4 Details of the deformation in the soil elements around the pile using beam-solid contact elements.

The contact element developed by Petek (2006) is formulated to create a link between the pile, modeled using beam-column elements, and the solid brick elements of the surrounding soil. The ability to use beam-column elements is highly advantageous from a modeling standpoint. The contact element creates a frictional interface allowing for sticking, slip, and separation that is capable of modeling the coupling between vertical and horizontal displacements. Figure 2.4 provides an example of how these elements function within the lateral spreading model, showing the way in which the soil elements deform around the pile as it moves laterally. The ability of these elements to create a gap between the trailing edge of the pile and the surrounding soil elements is visible at the top of Figure 2.4(a). Further information into the development and formulation of these beam-to-solid contact elements is available in Petek (2006).

2.5 SURFACE LOAD ELEMENTS

In order to achieve the goals of this research, it is necessary to have models in which the liquefied layer is located at varying depths within the soil system. Due to the computational limitations

induced by working with 3D FE models, the mesh is selectively refined in the area of the liquefied layer as opposed to a uniform refinement. This strategy, while sensible for computational optimization, necessitates the creation of customized meshes and input files for each case. In lieu of laboriously creating a series of models for each pile for liquefied layers at various depths, a uniform overburden pressure is applied to the ground (free) surface of the soil elements in the model. This overburden pressure, applied as a surface load, creates stress conditions in the soil that are equivalent to moving the liquefied layer to a deeper location.

In OpenSees, there is no built-in surface loading capability, forces can only be applied at a nodal level. Due to the irregular shape of elements in the lateral spreading model, as shown in Figure 2.3, determination of the equivalent nodal forces for a uniform surface load is a tedious task. One that would need to be performed for every increment of overburden pressure in every model. Instead of pursuing that strategy for the application of overburden pressure in the FE model, a new element is developed in OpenSees which is able to determine the appropriate nodal forces for a given magnitude of uniform pressure in a quadrilateral element. No additional stiffness is provided by these surface load elements, and the increase in computational cost is minimal, as only the assembly phase is affected. This new element eases the implementation of surface loads for the purpose of this research, while also increasing the capabilities of the OpenSees platform.

2.5.1 Formulation of Surface Load Elements

The developed surface load element is based upon a relatively simple strategy. The internal force vector for each element is replaced by the external force vector that would result from the application of a uniform surface loading. By creating a force imbalance in the elements, for equilibrium to be satisfied there must exist an equal-but-opposite set of external forces applied to each of the elements on the surface. This set of external forces is manifested in the application of energetically conjugate nodal forces representing the uniform surface loading.

The formulation of the surface load elements begins with the weak form of the principle of virtual displacements

$$-\int_V \boldsymbol{\sigma} : \nabla^s \boldsymbol{\eta} dV + \int_V \mathbf{b} \cdot \boldsymbol{\eta} dV + \int_{\partial V_\sigma} \bar{\mathbf{t}} \cdot \boldsymbol{\eta} dS = 0 \quad (2.1)$$

where $\boldsymbol{\sigma}$ is the stress tensor, ∇^s is the symmetric vector operator, $\boldsymbol{\eta}$ is an arbitrary displacement function, V is the volume of the body, \mathbf{b} is the body force acting on the body, $\bar{\mathbf{t}}$ is the surface traction vector, ∂V_σ is the portion of the surface of the body with prescribed stresses, and S is the surface of the body.

Equation (2.1) expresses equilibrium for the system in terms of an arbitrary displacement function $\boldsymbol{\eta}$. The vector of external forces, which follows from the third term of Equation (2.1), can be determined by, first, expressing the arbitrary displacement as

$$\boldsymbol{\eta} = \sum_I N_I(\boldsymbol{\xi}, \boldsymbol{\eta}) \cdot \boldsymbol{\eta}_I \quad (2.2)$$

where N_I are the (linear) shape functions, the subscript I refers to each of the four nodes for the element, and $\boldsymbol{\eta}_I$ are arbitrary nodal displacements. The shape functions, N_I , can be expressed for

these quadrilateral elements as

$$N_I = \frac{1}{4}(1 + \bar{\xi}_I \xi)(1 + \bar{\eta}_I \eta) \quad (2.3)$$

by mapping a bi-unit square onto the quadrilateral surface patch. The normalized coordinates $\bar{\xi}_I$ and $\bar{\eta}_I$ represent the nodal coordinates on the bi-unit square.

Applying Equation (2.2) to the external force term of Equation (2.1) results in

$$\sum_I \left(\int \bar{\mathbf{t}} \cdot N_I(\xi, \eta) J d\xi d\eta \right) \cdot \boldsymbol{\eta}_I =: \sum_I \mathbf{f}_I^{ext} \cdot \boldsymbol{\eta}_I \quad (2.4)$$

which must hold for any arbitrary nodal displacement $\boldsymbol{\eta}_I$, thus uniquely defining the nodal force

$$\mathbf{f}_I^{ext} = \int \bar{\mathbf{t}} \cdot N_I(\xi, \eta) J d\xi d\eta \quad (2.5)$$

where J is the Jacobian determinant necessary for the coordinate transformation to ξ and η , and the integration is performed over the bi-unit square to which the element has been mapped.

For a uniform surface pressure applied perpendicular to a given surface, the traction vector, $\bar{\mathbf{t}}$, is

$$\bar{\mathbf{t}} = -p \mathbf{n}(\xi, \eta) \quad (2.6)$$

in which p is the scalar magnitude of the pressure, and \mathbf{n} is the unit vector defining the outward normal of the surface. To establish the outward normal for the surface elements, general base vectors are defined for each element. There are two general base vectors, one in the ξ direction, \mathbf{g}_ξ , and the other in the η direction on the element, \mathbf{g}_η . This general base can be found from the nodal position vector as

$$\mathbf{x}(\xi, \eta) = \sum_I N_I(\xi, \eta) \cdot \mathbf{x}_I \quad (2.7)$$

where \mathbf{x}_I are the nodal position vectors. The base vectors follow as

$$\mathbf{g}_\xi = \frac{\partial \mathbf{x}}{\partial \xi} = \sum_I \frac{\partial N_I}{\partial \xi} \cdot \mathbf{x}_I = \sum_I \frac{\bar{\xi}_I}{4} (1 + \bar{\eta}_I \eta) \cdot \mathbf{x}_I \quad (2.8)$$

and

$$\mathbf{g}_\eta = \frac{\partial \mathbf{x}}{\partial \eta} = \sum_I \frac{\partial N_I}{\partial \eta} \cdot \mathbf{x}_I = \sum_I \frac{\bar{\eta}_I}{4} (1 + \bar{\xi}_I \xi) \cdot \mathbf{x}_I \quad (2.9)$$

A local normal vector, $\hat{\mathbf{n}}$, for each element is defined by the cross product of the two base vectors as

$$\hat{\mathbf{n}} = \mathbf{g}_\xi \times \mathbf{g}_\eta \quad (2.10)$$

This vector contains information about both the area and the direction of the outward normal for its respective element. It can be shown that the norm of $\hat{\mathbf{n}}$ is equal to the surface Jacobian determinant, J . Thus, the relationship between $\hat{\mathbf{n}}$ and \mathbf{n} can be expressed as

$$\mathbf{n} = \frac{1}{J} \hat{\mathbf{n}} \quad (2.11)$$

This relation is used to express the surface traction of Equation (2.6) in terms of the local normal vector as

$$\bar{\mathbf{t}} = -\frac{p}{J}\hat{\mathbf{n}} \quad (2.12)$$

where p is the magnitude of the surface pressure and J is the Jacobian determinant.

Applying Equation (2.12) to Equation (2.5), the external force acting at node I is obtained as

$$\mathbf{f}_I^{ext} = -p \int \hat{\mathbf{n}}(\xi, \eta) N_I(\xi, \eta) d\xi d\eta \quad (2.13)$$

The integral of Equation (2.13) is evaluated using four-point Gaussian integration of the form

$$\mathbf{f}_I^{ext} = \sum_{\alpha=1}^2 \sum_{\beta=1}^2 -p \hat{\mathbf{n}}(\xi_{\alpha}, \eta_{\beta}) N_I(\xi_{\alpha}, \eta_{\beta}) w_{\alpha} w_{\beta} \quad (2.14)$$

in which the Gaussian quadrature and weights are $(\xi_{\alpha}, w_{\alpha}) = (\eta_{\beta}, w_{\beta}) = (\pm \frac{1}{\sqrt{3}}, 1)$.

In each surface element, the internal force vector is set equal to the vector of forces resulting from a uniform surface traction as determined by Equation (2.14). To satisfy equilibrium, the elements must be subject to a set of nodal forces in opposition to the prescribed external force.

2.5.2 Validation of Surface Elements

A simple model is created in order to validate the successful implementation of the surface load elements in OpenSees. The model is meshed using irregularly-shaped elements as depicted in Figure 2.5. The newly created surface load elements are applied to the upper surface of this model over four layers of linear-elastic isotropic brick elements. The irregular shape of the mesh allows the elements to be tested for generality, as they should create energetically consistent nodal loads across the surface regardless of the shape of the quadrilateral elements, and thus create a constant stress in the solid.

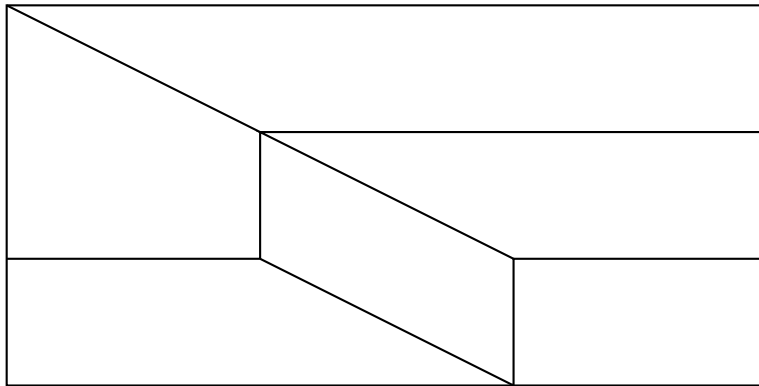


Figure 2.5 Irregularly-shaped mesh used for surface load element validation.

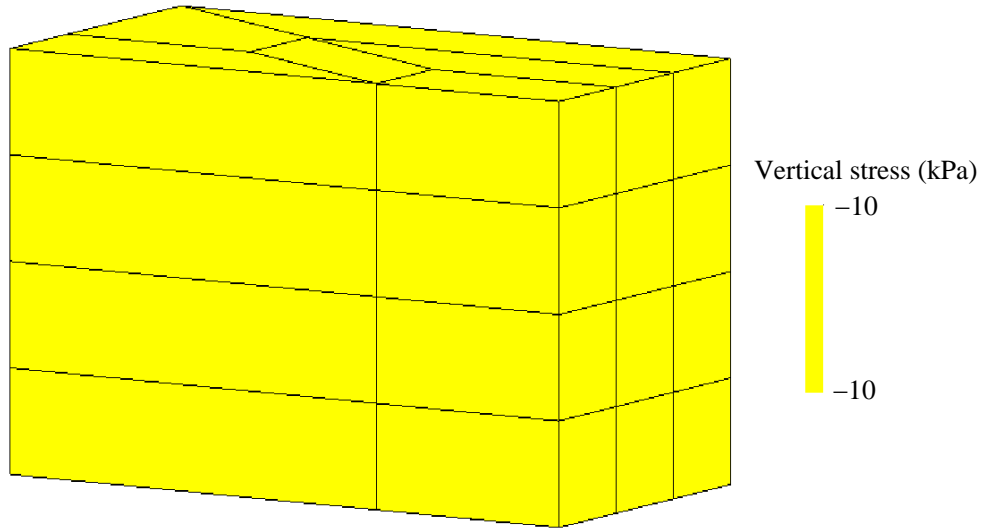


Figure 2.6 Distribution of vertical stress in the surface load element validation model.

The validation test used for the surface load elements, consists of the application a uniform loading of 10 kPa to the upper surface of the model. The base of the model is held fixed against translation in the direction of the loading. As shown in Figure 2.6, which shows a 3D view of the validation model, the surface load elements are able to create nodal forces that create an equivalent loading to the assumed uniform load, resulting in a constant vertical stress distribution of -10 kPa. This result validates that the surface load elements created for use in OpenSees perform as intended.

3 Modeling the Piles

3.1 INTRODUCTION

This study includes three deep foundation models that vary in diameter and bending stiffness. For simplicity, the term pile will be used to refer to all foundation elements discussed in the remainder of this report. Each pile model is based upon a template reinforced concrete pile known to have been used in practice. All three pile designs are modeled with circular cross sections. The three piles are selected such that they represent a reasonable variation in size and stiffness; thus providing data that is relevant to the range of size and stiffness where most practical pile designs fall. The study includes a small pile, a mid-sized pile, and a large pile with respective diameters of 0.61 m, 1.37 m, and 2.5 m. Both linear elastic and nonlinear elastoplastic constitutive models are created for each pile diameter.

3.2 TEMPLATE PILE DESIGNS

Figure 3.1 shows scale section views of the three template piles to emphasize their relative sizes. The majority of piles that are commonly used in practice have cross-sectional areas falling somewhere in the range defined by these three piles. Defining a reasonable range of pile sizes encourages interpolation of computed results as opposed to extrapolation.

The selected 0.61-m-diameter pile is a design common to the Port of Los Angeles, where piles of this type are employed in wharf foundations. This pile is representative of one of the smallest pile

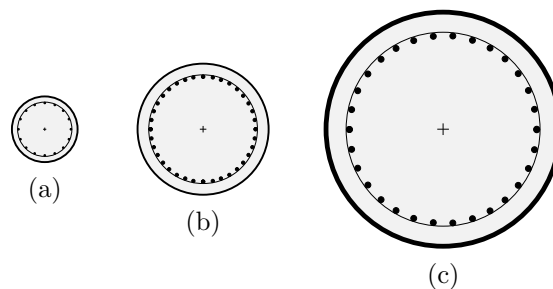


Figure 3.1 Template pile designs (to scale). (a) 0.61-m-diameter; (b) 1.37-m-diameter; (c) 2.5-m-diameter.

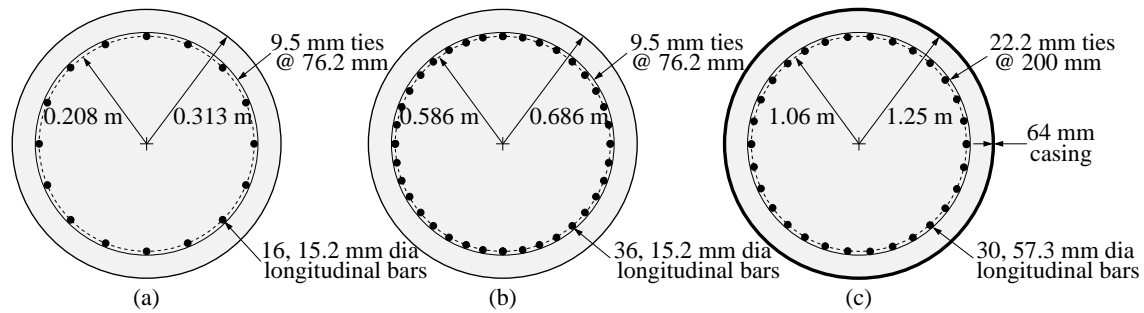


Figure 3.2 Dimensions and details of the three template piles. (a) 0.61-m-diameter; (b) 1.37-m-diameter; (c) 2.5-m-diameter.

designs that would commonly be encountered in applications where potentially liquefiable soils are present. The actual pile design has a 0.61-m-wide octagonal cross section, however, to ease implementation in the numerical model, a circular cross section is created having an equivalent area. The amount and location of the longitudinal and spiral reinforcement found in the actual octagonal pile is left unchanged in the equivalent circular model.

A 2.5-m-diameter pile used on the Bay Bridge in the San Francisco Bay is selected to be representative of one of the larger pile designs that would be encountered in practice, thus establishing the higher end of the range of practical piles. The template 2.5-m-pile is a drilled-shaft, with a steel casing surrounding an inner core of concrete and reinforcing steel. This casing greatly increases the bending stiffness of the 2.5-m-diameter pile as compared to the other selected designs, even more so than the increased size.

The third template pile is included to establish an intermediate case. The selected 1.37-m-diameter pile was used on the Dumbarton Bridge (Menlo Park to Fremont, California) replacement project. The actual pile design called for a precast concrete ring, which was to be filled in with a core of concrete and reinforcing steel after being driven into place. For ease of modeling, it is assumed that once the infill has cured, the pile acts as a solid cross section.

A summary of the relevant dimensions and details for each of the three template pile designs is provided in Figure 3.2. The reinforcing steel layouts shown are incorporated into fiber section models which simulate the composite behavior of these reinforced concrete piles.

3.3 PILE ELEMENTS

The piles are modeled using beam-column elements with a displacement-based formulation. The OpenSees designation for the beam-column elements used in the model is *dispBeamColumn*. These elements are able to include distributed plasticity, and integration within the elements is based on the Gauss-Legendre quadrature rule. These beam-column elements are used in conjunction with elastic and elastoplastic constitutive formulations incorporated by means of fiber section models. No geometric nonlinearity is considered. The pile nodes have six degrees of freedom (3 translational, 3 rotational).

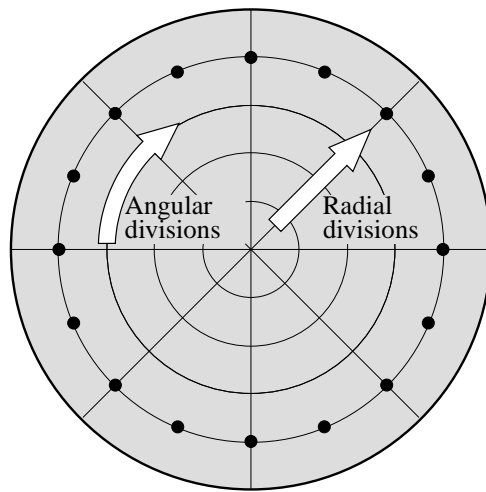


Figure 3.3 Typical fiber discretization for a circular fiber section model.

3.3.1 Fiber Section Models

The three pile designs display differing responses to bending loads based upon the strength, distribution, and size of the concrete and steel available in their cross section. In order to incorporate the unique behavior of each pile into a FE model, fiber section models are created for each pile design. These fiber section models incorporate all of the relevant aspects of the template pile designs, and define the behavior of each pile model at a cross-sectional level. Due to symmetry considerations, only one-half of each pile is modeled, resulting in semi-circular fiber section models.

Fiber section models are effective when modeling composite materials such as reinforced concrete piles. Fiber sections have a geometry defined in two levels; an overall geometry, in this case semi-circular, within which exists many smaller subregions of regular shape. A circular shape, or any sector thereof, lends itself well to the discretization framework shown in Figure 3.3 with a set of divisions set at even intervals along the radius of the circle, as well as divisions that are set at equal angular increments. Reinforcement steel is included as individual fiber regions with appropriate areas and locations. This type of fiber discretization is employed in all of the fiber models created for this research.

Each subregion of the fiber model is assigned its own unique uniaxial constitutive model. In the case of reinforced concrete, it follows that the subregions representing the reinforcement are given the uniaxial behavior of steel, and the surrounding subregions representing the concrete portion of the cross section are assigned uniaxial constitutive behavior based upon that of concrete. Through defining the fiber model in this manner, a composite constitutive behavior is achieved which approximates the 3D behavior of an actual pile while still enabling the use of standard beam elements.

Table 3.1 Material and section property values in linear elastic pile models.

Pile Diameter	A (m ²)	E (GPa)	G (GPa)	I (m ⁴)
0.61-m-	0.154	31.3	12.52	0.0038
1.37-m-	0.739	28.7	11.48	0.0869
2.50 m	2.454	102.4	40.96	0.9587

3.4 LINEAR ELASTIC PILE CONSTITUTIVE BEHAVIOR

Linear elastic constitutive behavior is assigned to the beam-column elements using elastic cross-sectional models. The elastic sections are based upon the template pile designs, however, no composite action is considered. For each pile diameter, the cross-sectional area, A , and the second moment of the area, I , are determined based on half-pile cross sections. An appropriate elastic modulus, E , is selected for each pile such that the linear elastic bending stiffness, EI_y , is equal to the initial bending stiffness of the corresponding elastoplastic pile model. Poisson's ratio, ν , is assumed to be 0.25, allowing a shear modulus, G , to be defined. The linear elastic constitutive and section properties are summarized in Table 3.1

3.5 ELASTOPLASTIC PILE CONSTITUTIVE BEHAVIOR

Fiber section models are used to incorporate elastoplastic pile constitutive behavior into the FE model. Two uniaxial constitutive models are defined for each fiber section model, one each for the concrete and steel portions of the cross section, respectively. The resulting behavior will consider the composite action of the reinforced concrete piles on a cross-sectional level.

OpenSees provides a series of predefined uniaxial constitutive models that can be effectively incorporated into fiber section models. From this index of provided constitutive models, the *Concrete02* and *Steel01* models are chosen to model the concrete and steel portions of the pile cross sections, respectively. Figure 3.4 shows the general forms of these constitutive models, slightly exaggerated for clarity, along with the input parameters required to properly define the behavior. The corresponding input values for each pile diameter are provided in Tables 3.2 and 3.3.

The selected uniaxial concrete model has the ability to account for the effects of confinement on the compressive behavior and the ability to link the tensile behavior to the development of cracks in the pile. The uniaxial steel model has elastoplastic behavior and a relatively simple set of input parameters. When these individual materials are combined via the fiber models, the resulting constitutive behavior of the pile model is suitably representative of that expected for a reinforced concrete pile.

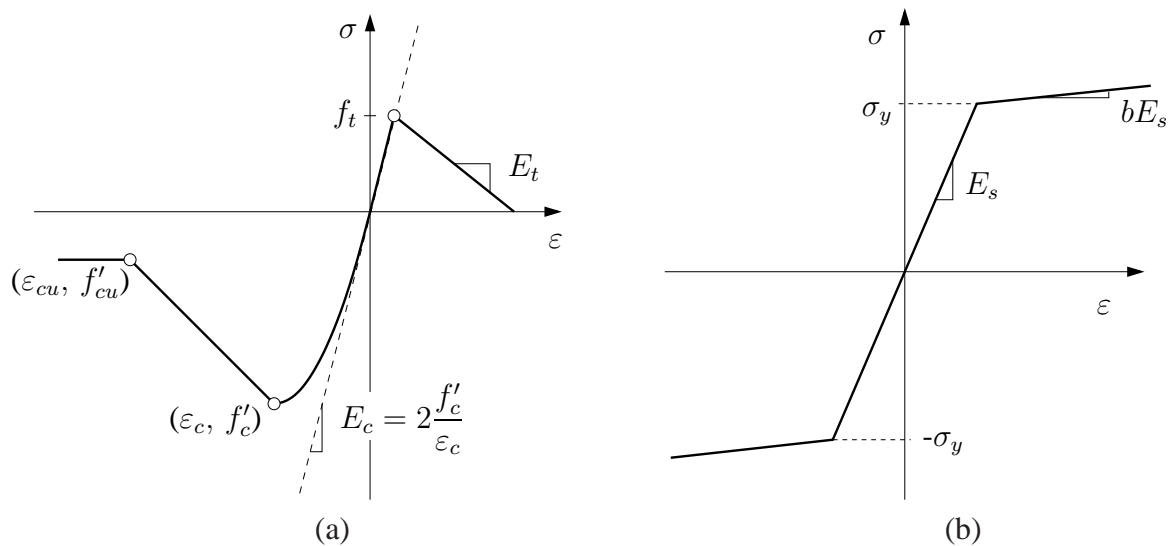


Figure 3.4 Uniaxial constitutive relations used in fiber section models. (a) *Concrete02* model. (b) *Steel01* model.

Table 3.2 Steel material property input values in fiber section models.

Pile Diameter	σ_y (MPa)	E_s (GPa)	b
0.61-m-	1860	200	0.001
1.37-m-	1860	200	0.001
2.50 m	520	200	0.001

Table 3.3 Concrete material property input values in fiber section models.

Pile Diameter	f'_c (kPa)	ϵ_c	f'_{cu} (kPa)	ϵ_{cu}	f_t (kPa)	E_t (MPa)
0.61-m-	44816	0.003	8960	0.015	4170	-2080
1.37-m-	43170	0.003	8270	0.011	4000	-1400
2.50 m	20684	0.003	4140	0.013	2830	-13800

3.5.1 Steel in Tension and Compression

The chosen uniaxial steel material model, while not intended solely for use in reinforcement modeling, has many of the salient features that are desirable in a steel constitutive model. As shown in Figure 3.4(b), the *Steel01* model is a bilinear plasticity model that incorporates isotropic strain hardening in the post-yield behavior. The initial portion of the model is linear elastic, with a slope defined by the modulus of elasticity, E . The hardening slope of the curve is defined as the product of the elastic modulus and a specified hardening ratio, b , which was taken as a somewhat arbitrary value of 0.001. Although this constitutive model is relatively simple, the bilinear model creates a situation in which there is a constant tangent in the plastic region, thus, simplifying the computations without significantly affecting the results. The longitudinal reinforcement fibers in all three pile models, as well as the steel tube in the 2.5-m-pile model, are defined using this uniaxial constitutive model.

3.5.2 Concrete in Compression

In compression, the selected uniaxial concrete constitutive model is based upon the work of Kent and Park (1971), who derived the model from tests conducted with confined concrete beam-columns. This model has three distinct regions of behavior that define the initial, crushing, and post-crushing relationships between the axial stress and strain in each subregion of the fiber elements. Whenever possible, the material parameters used as input values in the constitutive models are based on the corresponding properties in the template pile designs.

In the initial loading region, from the origin up to the maximum compressive stress and strain, the behavior is parabolic. The maximum strength in compression, f'_c , for each model was taken directly from the template pile designs (see Table 3.3 for values). Per American Concrete Institute (ACI) recommendations, all three piles are assumed to have a peak strain of $\varepsilon_c = 0.003$ when their maximum compressive stress has been reached (ACI, 2005). The initial tangent of this region of the model is equal to the modulus of elasticity, E , which is defined as

$$E = 2 \frac{f'_c}{\varepsilon_c} \quad (3.1)$$

Once the strain in the model exceeds the set value of ε_c , the concrete begins to soften due to the onset of crushing. This is represented by the descending linear region of the material behavior shown in Figure 3.4(a). The speed at which this softening occurs is based upon the amount of confinement provided by the longitudinal bars and spiral ties included in the cross section. With greater levels of confinement, larger axial strains can be achieved in the concrete core before the contribution of that concrete to the strength of the pile becomes minimal. To account for the influence of the amount of confinement in each pile model, the post-crushing behavior for the respective concrete constitutive models are defined in accordance with a procedure detailed in Park and Paulay (1975). Using this procedure, ε_{cu} , the strain at which the concrete is considered entirely crushed, can be defined based upon the known geometry of the core and the amount of steel by which it is confined. The crushed strains for each model are provided in Table 3.3.

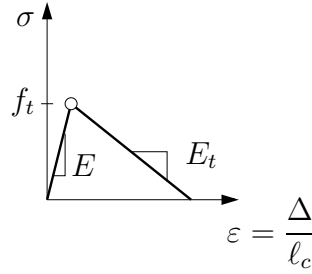


Figure 3.5 Detail of tensile behavior in uniaxial concrete constitutive model.

After the strain in a particular subregion of the fiber model has reached ε_{cu} , the concrete is considered to be completely crushed, however, confined concrete has the documented ability to sustain small levels of stress at very large strains. To account for this, a residual strength is defined for each pile model, as shown in Table 3.3. In all cases, the residual concrete strength is set as $f_{cu} = 0.2f'_c$ per Park and Paulay (1975).

3.5.3 Concrete in Tension

When the concrete subregions of the fiber models are subjected to tensile strains, it is desirable for there to be a limited amount of tensile strength followed by a region of tension softening due to the onset of cracking in the material. The selected uniaxial constitutive model includes both of these features. An enlargement of the tensile portion of the uniaxial concrete constitutive behavior is provided in Figure 3.5. As shown, the tensile behavior for this model can be fully described through three variables: the tensile strength, f_t , the elastic modulus, E , and the tension softening stiffness, E_t .

The tensile strength of the concrete in each pile model is defined based on the ACI recommended modulus of rupture for concrete in bending

$$f_r = 0.62\sqrt{f'_c} \quad (3.2)$$

with f_r and f'_c in units of MPa (ACI, 2005). The modulus of rupture is slightly greater than the strength of concrete in uniaxial tension, however, tensile stresses will be generated in the models due to the application of bending loads, not uniaxial tensile loads. Therefore, defining the tensile strength to be the modulus of rupture may yield more realistic results.

The tension softening stiffness, E_t , which is the slope of the linear softening portion of the tensile stress-strain curve shown in Figure 3.5, defines the rate at which the stress degrades with increasing tensile strains. In this region of the model there is a linear constitutive relation between the stress and the strain is assumed to be

$$d\sigma = -E_t d\varepsilon \quad (3.3)$$

Sensible values for E_t are determined for each pile based upon the principles of fracture mechanics as they apply to plain concrete. A discussion of this process is provided in Section 3.5.4.

Eventually, when the tensile strain becomes large enough, the concrete will have cracked sufficiently such that it can no longer provide any resistance to increasing tensile strains. This is

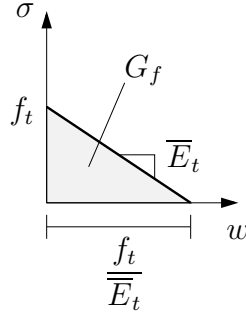


Figure 3.6 Simplified fracture model for concrete in uniaxial tension.

represented in Figure 3.5 by the point at which the softening curve crosses the strain axis. This limiting value of strain varies for each model based upon their respective tensile strengths and softening moduli.

3.5.4 One-Dimensional Fracture Mechanics of Concrete in Tension

When concrete approaches its tensile capacity, defined in this model by the modulus of rupture, cracks will begin to form. Though the cracks may propagate relatively rapidly, the surrounding concrete does not lose all tensile strength instantaneously. Instead, the tensile stress in the region of the crack is assumed to degrade over time as a function of the width of the crack opening, w . The rate at which this occurs varies depending upon the material in question.

Models of varying levels of complexity have been developed to describe the relationship between the tensile stress and the rate at which cracks will open in a material, (e.g. Kaplan, 1961; Bazant and Becq-Giraudon, 2002; Xu and Zhang, 2008). For the purposes of this research, a simplified crack propagation model has been adopted. This model is shown in Figure 3.6, where the tensile stress is plotted as a linear function of the crack opening. This assumed relationship between incremental stresses and crack widths is defined by the crack propagation slope, \bar{E}_t , and can be written as

$$d\sigma = -\bar{E}_t dw \quad (3.4)$$

an expression that is helpful in relating \bar{E}_t to the desired input value of E_t .

As shown in Figure 3.6, there is a certain amount of energy that must be expended before the concrete in the area of the crack loses its tensile strength entirely. This energy is called the fracture energy, or fracture toughness, and is commonly denoted as G_f . Fracture energy is a fundamental material property that can be determined via laboratory tests or from empirical formulas present in the literature. The fracture energy for each pile model is defined as shown in Table 3.4; values determined using the empirical procedure developed by Bazant and Becq-Giraudon (2002).

In a general sense, the value of the fracture energy for a given material is dependent upon the specific relationship between the tensile stress and the crack opening width, defined by the function $\sigma(w)$. The fracture energy is equal to the following integral

$$G_f = \int_0^{+\infty} \sigma(w) dw \quad (3.5)$$

Table 3.4 Concrete fracture energies and crack propagation slopes.

Pile Diameter	G_f (kJ/m ²)	\overline{E}_t (MN/m ³)
0.61-m-	0.155	55450
1.37-m-	0.150	53100
2.50 m	0.109	36520

which essentially states that G_f is equal to the area under the curve defined by $\sigma(w)$. Applying this to the simplified model shown in Figure 3.6, the fracture energy can be related to the tensile stress at the onset of cracking, f_t , and the crack propagation rate, \overline{E}_t , as

$$\begin{aligned} G_f &= \frac{1}{2} f_t w \\ &= \frac{f_t^2}{2\overline{E}_t} \end{aligned} \quad (3.6)$$

Solving Equation (3.6) for the unknown crack propagation slope results in

$$\overline{E}_t = \frac{f_t^2}{2G_f} \quad (3.7)$$

which defines \overline{E}_t in terms of the known values for concrete fracture energy and tensile strength. The values of \overline{E}_t calculated for each pile diameter are summarized in Table 3.4.

A consideration of what is happening in a single pile element during cracking is beneficial when attempting to relate the stress degradation slope, \overline{E}_t , to the tension softening slope, E_t . Figure 3.7 shows such an element both before ($w = 0$) and after ($w > 0$) the onset of cracking. For simplicity it is common to assume that there is a single crack in each element that occurs at the midpoint of its length. This assumption defines the characteristic length, ℓ_c , which is the distance between cracks, to be equal to the element length.

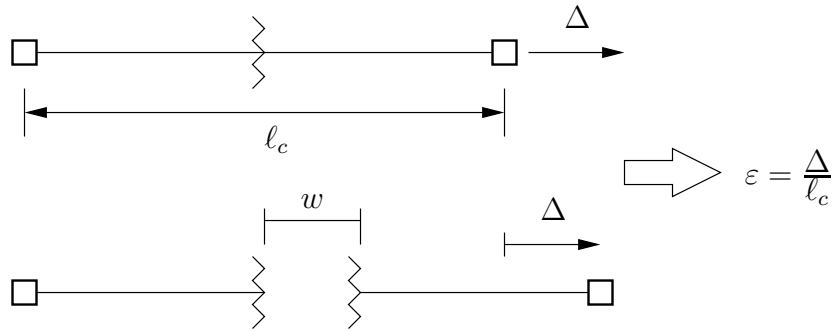


Figure 3.7 Relationship between elongation, crack width, and element length for a single pile element.

The change in length of the element, $d\Delta$, can be related to the change in strain within the element, $d\varepsilon$ by the simple kinematic relation

$$d\Delta = \ell_c d\varepsilon \quad (3.8)$$

As implied by Figure 3.7, the addition of a crack with increasing width into the element modifies Equation (3.8) into the form

$$d\Delta = \ell_c d\varepsilon^e + dw \quad (3.9)$$

where $d\varepsilon^e$ is the change in elastic strain and dw is the change in crack opening width. Assuming linear elastic behavior in the uncracked zone, Equation (3.9) can be written in terms of stress as

$$d\Delta = \frac{\ell_c}{E} d\sigma + dw \quad (3.10)$$

in which E is the elastic modulus. Expanding Equation (3.10) using Equations (3.4) and (3.8) yields

$$\left(1 - \frac{\ell_c \bar{E}_t}{E}\right) dw = \ell_c d\varepsilon \quad (3.11)$$

which can be solved for the incremental change in crack width, yielding

$$dw = \frac{\ell_c}{\left(1 - \frac{\bar{E}_t \ell_c}{E}\right)} d\varepsilon \quad (3.12)$$

The constitutive relation defining the behavior of the tension-softening portion of the concrete model follows from Equations (3.4) and (3.12) as

$$d\sigma = -\frac{\bar{E}_t \ell_c}{\left(1 - \frac{\bar{E}_t \ell_c}{E}\right)} d\varepsilon \quad (3.13)$$

which when compared with Equation (3.3) defines the tension softening modulus to be

$$E_t = \frac{\bar{E}_t \ell_c}{\left(1 - \frac{\bar{E}_t \ell_c}{E}\right)} \quad (3.14)$$

This result, combined with Equation (3.7), enables the calculation of the tension softening modulus for any finite element discretization using known material parameters and element sizes.

3.5.5 Implementation of Tension Parameters

The resultant tension softening modulus from Equation (3.14) is largely dependent upon the chosen characteristic length, ℓ_c . The other terms are material-dependent parameters, but the characteristic length is somewhat arbitrary. As was discussed previously, ℓ_c is initially taken to be equal to the element length, thus implying that a single crack develops in each element. As the length of an element increases, this assumption becomes less valid. Assuming that there is an adequate

Table 3.5 Characteristic length and tension softening modulus in pile models.

Pile Diameter	ℓ_c (m)	E_t (kPa)
0.61-m-	0.07	-2.08e6
1.37-m-	0.05	-1.40e6
2.50 m	0.42	-1.38e7

amount of longitudinal and shear reinforcement provided in a pile, it could be expected for cracks to develop at spacings in the range of 5-10 cm. Specifying ℓ_c to be equal to the expected crack spacing can reduce E_t considerably. Reducing the tension softening modulus can result in models that exhibit fewer convergence issues without altering the results in a significant manner.

Preliminary sensitivity studies performed with the three pile models have shown that the 0.61-m and 1.37-m-diameter models are very sensitive to the specified input value for E_t . In these models, there is a significant reduction in stiffness when the concrete cracks in tension. If E_t is set at too large a value, the resulting softening behavior is too steep and the elements are unable to converge. An example of this severe softening behavior can be seen inside the circled region of the moment-curvature response shown in Figure 3.8. The convergence issues encountered for these two pile models identified the need for a more careful selection of the characteristic length values.

Because the 2.5-m-diameter model is encased in a steel tube, it does not display a similar loss of strength at the onset of tension cracking. This is illustrated by Figure 3.9, which shows the moment-curvature behavior for the 2.5-m-diameter cross section for two extreme values of ℓ_c . There is no discernable difference, thus the characteristic length and the corresponding tension softening stiffness can be set at any sensible value.

Characteristic lengths of $\ell_c = 7$ cm and $\ell_c = 5$ cm are selected for the 0.61-m and 1.37-m-diameter models, respectively. For the 2.5-m-diameter model, ℓ_c is set as the length of the smallest pile element. Table 3.5 summarizes the characteristic length and softening stiffness values.

As shown in Figures 3.10 and 3.11, reducing the tension softening modulus for the 0.61-m and 1.37-m-diameter models results in a smoother transition between the initial and ultimate behavior of the cross section, and the convergence issues associated with a large tension softening stiffness disappear. The validation work performed in order to support the reduction in these parameters is discussed in Section 3.6.2.

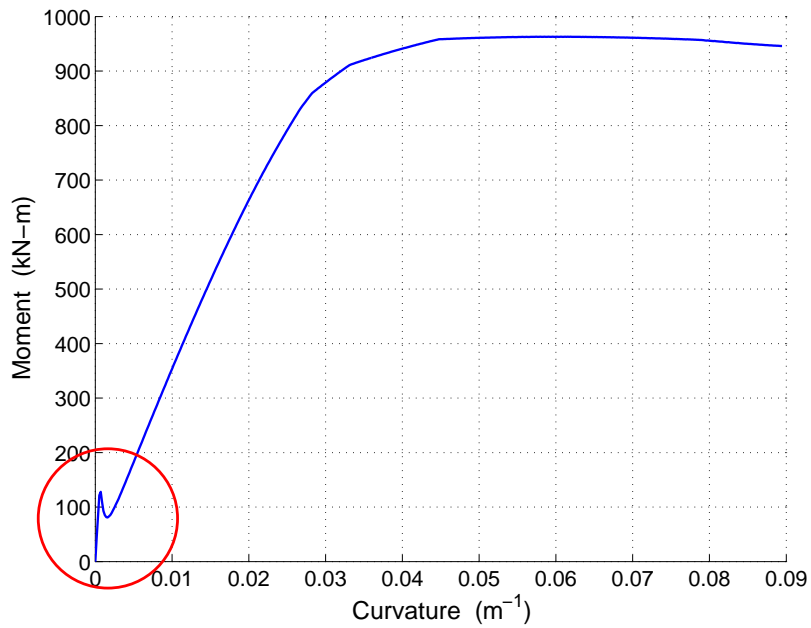


Figure 3.8 Moment-curvature behavior for 0.61-m-diameter model illustrating softening behavior resulting from a large characteristic length, ℓ_c .

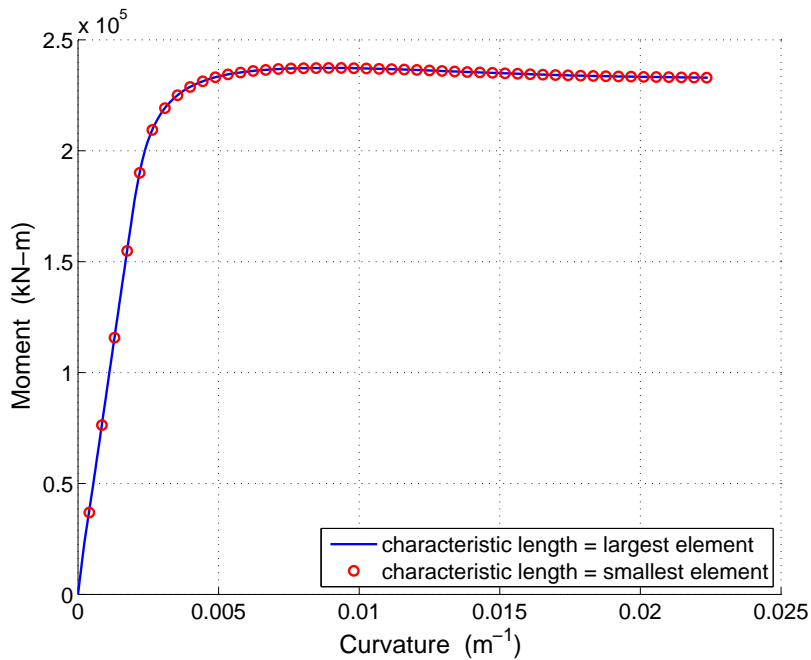


Figure 3.9 Moment-curvature behavior for 2.5-m-diameter model with two values of characteristic length, ℓ_c .

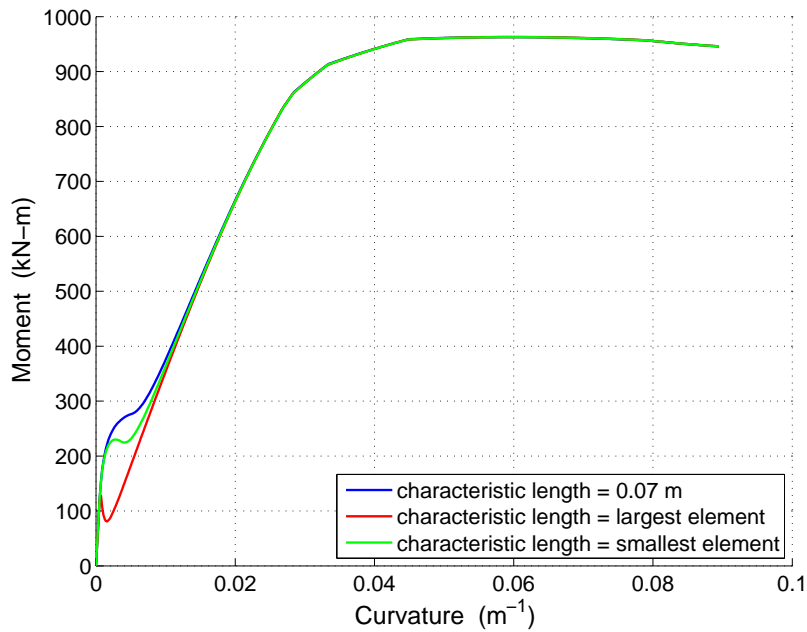


Figure 3.10 Moment-curvature behavior for 0.61-m-diameter model with various values of ℓ_c . Largest element length is 0.649 m. Smallest element length is 0.102 m.

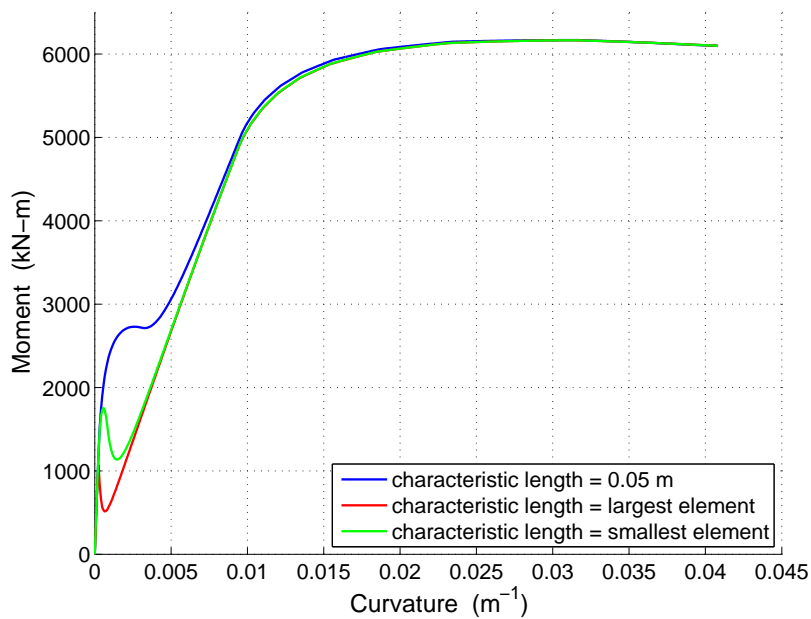


Figure 3.11 Moment-curvature behavior for 1.37-m-diameter model with various values of ℓ_c . Largest element length is 1.79 m. Smallest element length is 0.231 m.

3.6 VALIDATION OF PILE MODELS

In all computer simulations, it is important to ensure that user-created models exhibit reasonable behavior in response to easily verifiable loading conditions. Each step in the creation of the pile models, from the behavior of the cross section to the overall behavior model, must first be validated before implementation into the lateral spreading model.

To ensure that the fiber section models for each pile are created and implemented correctly, the behavior of each is evaluated and verified through a series of simple analyses. The first step is to verify the moment-curvature relation for each fiber model, thus providing reassurance that the models are created properly. Once this has been established, a cantilever beam model is implemented to test the global behavior of the pile models. Unless otherwise noted, all of the fiber section validation work is performed using the half-pile fiber section models created for use in the lateral spreading model.

3.6.1 Moment-Curvature Response

Using OpenSees, zero-length element models are created with the previously defined semi-circular fiber section models. One node is held fixed, and the other is left free with respect to rotation. The element is then subjected to, first, a constant axial load to represent the self weight of the pile, and second, a linearly-increasing applied moment. The force and deformation responses of the section are recorded during this process, from which a moment-curvature diagram can be created. This procedure is a relatively simple way to establish the moment-curvature behavior for a fiber section model in OpenSees.

Computer aided hand-calculations are performed to verify that the correct initial tangents and the true moment-curvature behaviors of the cross section have been captured in the OpenSees analysis. These calculations are implemented in MATLAB and utilize a numeric integration algorithm in combination with a Newton-Raphson iterative procedure. Computing the moment-curvature response of a cross section requires iteratively solving the following equation

$$\mathbf{R} = \begin{Bmatrix} N - \int_A \sigma dA \\ M - \int_A y \sigma dA \end{Bmatrix} = \mathbf{0} \quad (3.15)$$

where \mathbf{R} is the residual, N is the applied normal force, M is the applied moment, σ is the axial stress, A is the area of the cross section, and y is distance from the neutral axis. Incremental changes in the residual are computed using the following equation

$$d\mathbf{R} = \begin{bmatrix} -\int \partial\sigma/\partial\varepsilon & -\int \partial\sigma/\partial\phi \\ -\int y\partial\sigma/\partial\varepsilon & -\int y\partial\sigma/\partial\phi \end{bmatrix} \quad (3.16)$$

in which ε is the axial strain and ϕ is the curvature. The curvature is increased incrementally in constant steps towards a pre-defined ultimate value. For each curvature step, the axial strain distribution in the cross section can be computed as

$$\varepsilon(y) = \varepsilon_{\text{current}} + \phi y \quad (3.17)$$

where $\varepsilon(y)$ is the axial strain as a function of position y , ϕ is the curvature at the current step, and $\varepsilon_{\text{current}}$ is the mean axial strain at the beginning of each iteration. The distributions of stress resulting from this computed strain distribution are calculated using the appropriate constitutive models for the concrete and steel portions of the cross section.

The cross section is divided into subregions. Rectangular and circular subregions are used for the concrete and steel portions of the cross section, respectively. Each subregion has a particular center position, y_i , and area, A_i . Using these subregions, the internal normal force and moment acting on the cross section can be approximated using the following sums

$$\int_A \sigma dA \approx \sum \sigma_i A_i \quad (3.18)$$

$$\int_A y \sigma dA \approx \sum y_i \sigma_i A_i \quad (3.19)$$

where σ_i is the stress acting at the center of each of i subregions. Additionally, the terms of Equation (3.16) are computed as

$$\int \frac{\partial \sigma}{\partial \varepsilon} \approx \sum E_c A_{ci} + E_s A_{si} \quad (3.20)$$

$$\int \frac{\partial \sigma}{\partial \phi} \approx \sum E_c y_{ci} A_{ci} + E_s y_{si} A_{si} \quad (3.21)$$

$$\int y \frac{\partial \sigma}{\partial \varepsilon} \approx \sum E_c y_{ci} A_{ci} + E_s y_{si} A_{si} \quad (3.22)$$

$$\int y \frac{\partial \sigma}{\partial \phi} \approx \sum E_c I_{ci} + E_s I_{si} \quad (3.23)$$

in which E_c , y_{ci} , and A_{ci} are the concrete elastic modulus and the center location and area for each concrete subregion, respectively, and E_s , y_{si} , and A_{si} are the corresponding terms for the steel portion of the cross section.

The internal normal force and moment obtained from Equations (3.18) and (3.19) are used to compute the residual using Equation (3.15). If the residual is not a zero vector, an updated strain distribution is computed using the newly computed residual and the incremental change in the residual determined in Equations (3.20)–(3.23). The process then repeats, iterating until Equation (3.15) is satisfied for the current curvature step before moving on to the next. The moment-curvature response of the cross section is determined by recording the converged values of the moment for each curvature step.

The converged final stress and strain distributions acting over the cross section are recorded and shown in Figure 3.12 for the 0.61-m-diameter section. The similarity to the specified uniaxial steel and concrete constitutive models shown in Figure 3.4 verifies that the constitutive models are correctly implemented in the independent calculation procedure.

The moment-curvature response of each pile model obtained from OpenSees is compared to the corresponding response computed using the developed MATLAB scheme in Figures 3.13 to 3.18.

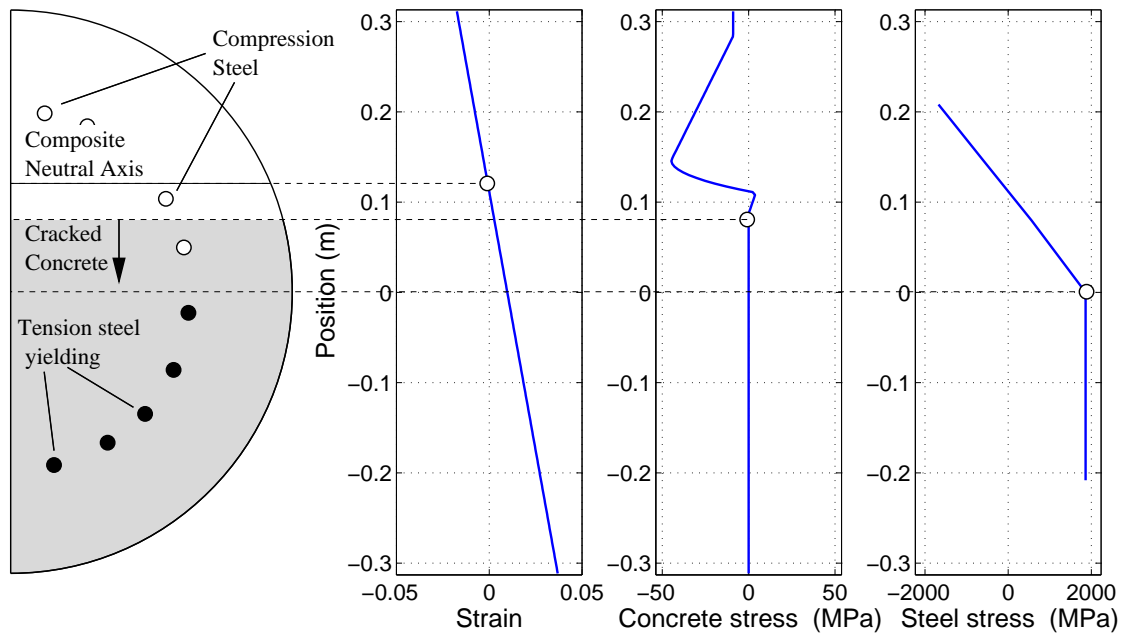


Figure 3.12 Distributions of stress and strain determined for 0.61-m-diameter cross section.

Calculations are conducted for full, circular fiber models in addition to the semi-circular section models developed for use in the 3D lateral spreading model. As shown, there is considerable agreement between the independently calculated and OpenSees curves for each model; the general shapes are nearly identical and the calculated initial tangents match the OpenSees results. Any differences can be attributed to the differing degrees of accuracy in the discretization of the cross sections. These analyses provide verification that the fiber models are displaying predictable and intended responses as implemented in OpenSees.

The circular cross sections are analyzed in order to verify that the semi-circular fiber section models have been correctly implemented. The resulting pile moments and forces in the lateral spreading model should be half as large as would be expected for the full cross sections due to symmetry considerations. The semi-circular models (Figures 3.14, 3.16, and 3.18) display moments which are exactly one-half of those returned by the circular models for a given curvature value. This verifies the correct implementation of the semi-circular fiber section models.

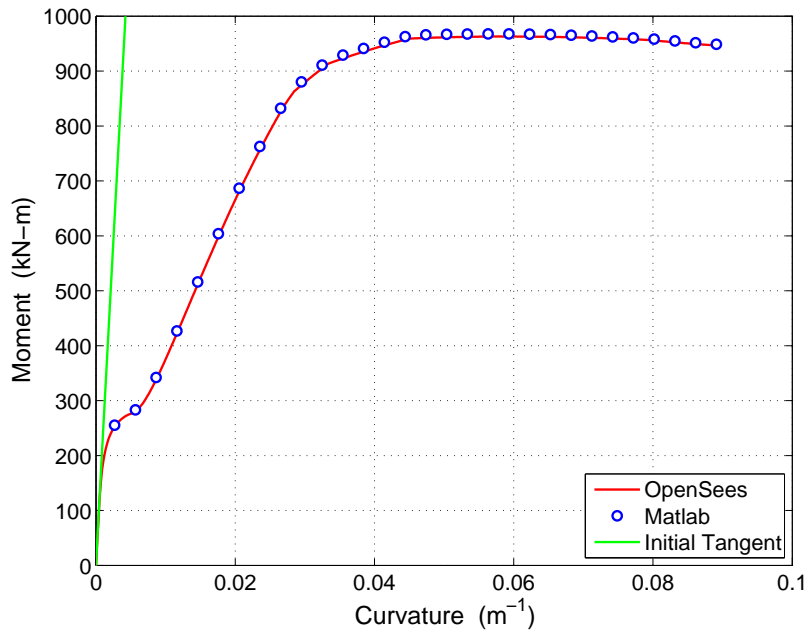


Figure 3.13 Comparison of moment-curvature responses for 0.61-m-diameter full (circular) pile model.

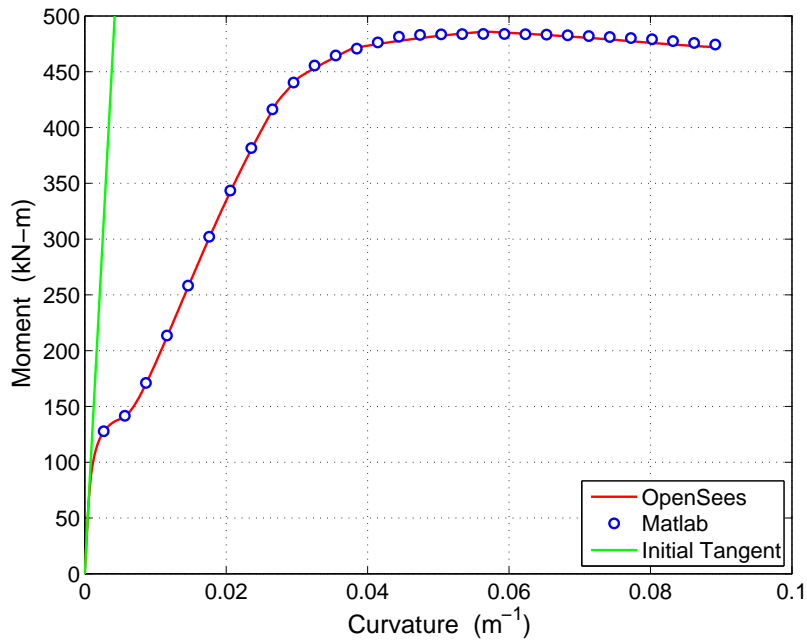


Figure 3.14 Comparison of moment-curvature responses for 0.61-m-diameter half-pile (semi-circular) model.

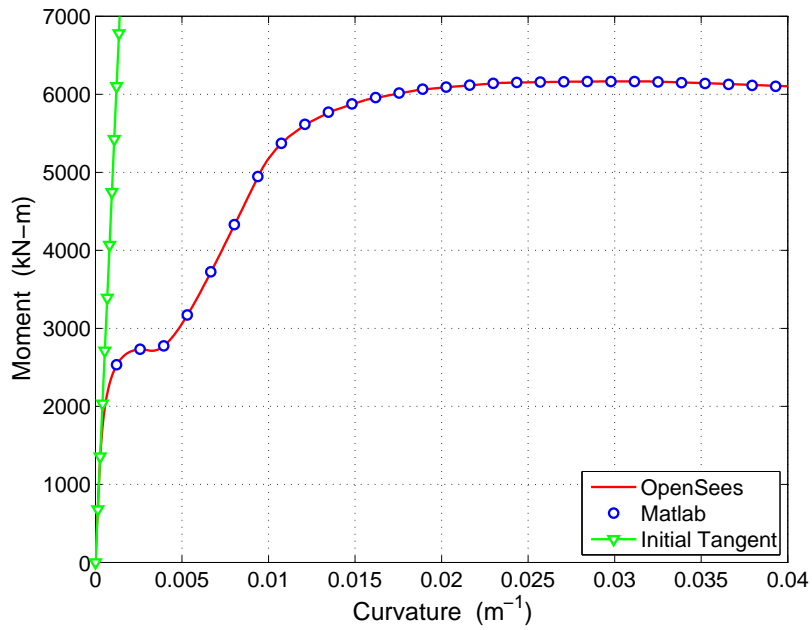


Figure 3.15 Comparison of moment-curvature responses for 1.37-m-diameter full (circular) pile model.

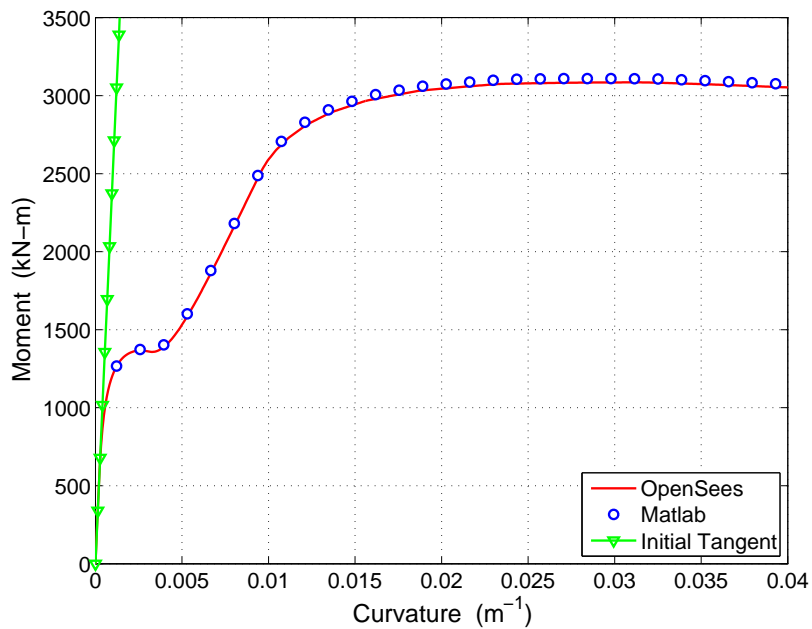


Figure 3.16 Comparison of moment-curvature responses for 1.37-m-diameter half-pile (semi-circular) model.

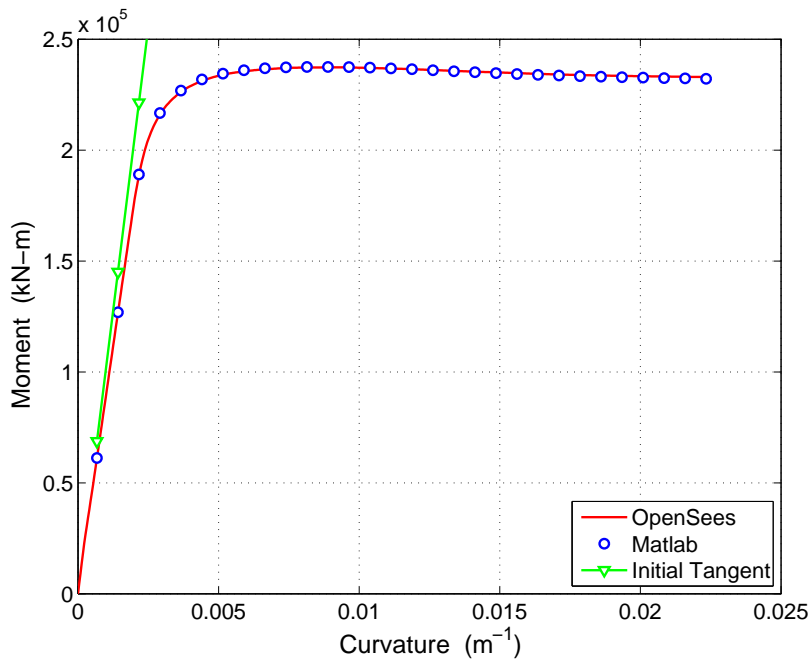


Figure 3.17 Comparison of moment-curvature responses for 2.5-m-diameter full (circular) pile model.

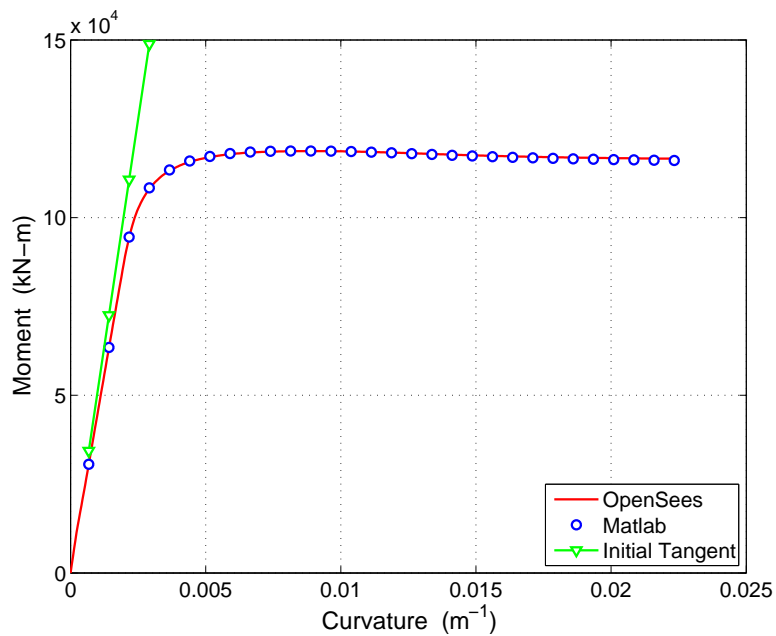


Figure 3.18 Comparison of moment-curvature responses for 2.5-m-diameter half-pile (semi-circular) model.

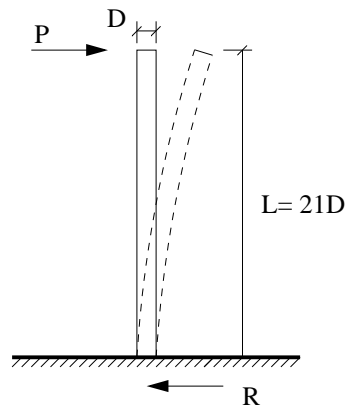


Figure 3.19 Cantilever beam analysis. The horizontal load, P , is increased linearly until the pile tip deflects a distance of one pile radius.

Cantilever Beam Implementation

In order to ensure that the behavior of the section models is consistent regardless of the loading configuration, a simple cantilever beam model is used. A schematic of this model is provided in Figure 3.19. The cantilever beams utilize the fiber section models for each pile. The moment-curvature responses for the 0.61-m and 2.5-m-diameter piles in the element adjacent to the fixed base are compared to previous results in Figures 3.20 and 3.21. The similarity shown provides verification that the cross-sectional model can be successfully implemented into a 3D simulation.

3.6.2 Validation of Tension Parameters

As discussed in Section 3.5.5, the 0.61-m- and 1.37-m-diameter models exhibit convergence problems when assigned large values of the tension softening modulus, E_t . While it is important to select input parameters that allow for convergence, it is equally important to validate that any changes in the parameters are sensible and do not significantly alter the resulting behavior of the pile models. To show that a suitable compromise between accuracy/detail resolution and numerical stability in the tension softening parameter does not significantly affect the results, the behavior of the pile models for several values of E_t is compared via two validation studies.

In the first validation study, the moment-curvature behavior of the pile models is compared for three separate values of E_t . This behavior is generated for each model using the zero-length element approach discussed in Section 3.6.1. Two of the three tension softening stiffness values are based upon characteristic lengths set equal to the sizes of the largest and smallest elements, respectively, in each pile model. These characteristic lengths derive from the assumption that a single crack develops in each element. The third value of E_t is determined by setting the characteristic length to be the assumed crack spacings listed in Table 3.5.

For the lateral spreading model, it is important that the behavior of the pile elements at large curvature and displacement demands remains unaffected by changes in the tension softening modulus. Part of the goal of this research is to evaluate the maximum moments, shear forces, and curvatures

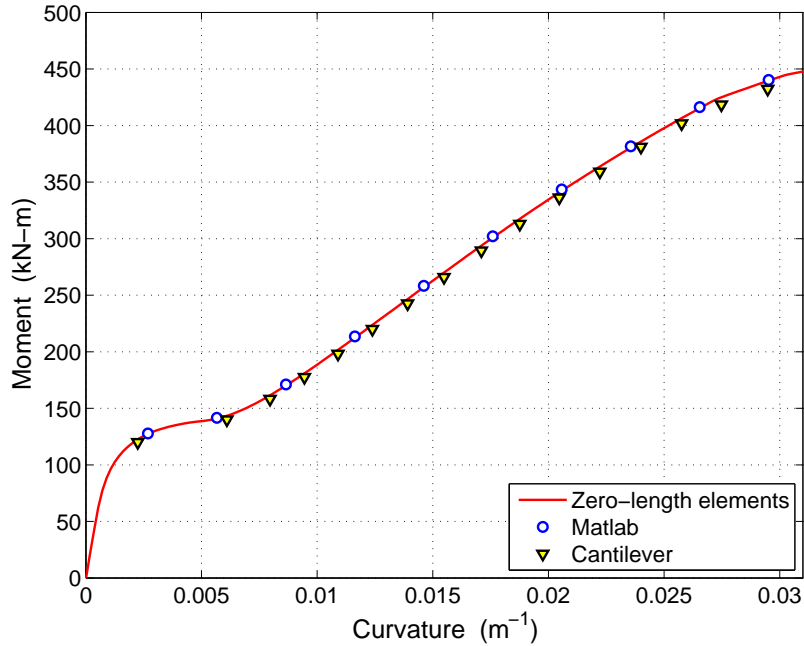


Figure 3.20 Moment-curvature response of cantilever model compared to zero-length element and independently calculated section responses for 0.61-m-diameter section. The cantilever model fails at this level of curvature.

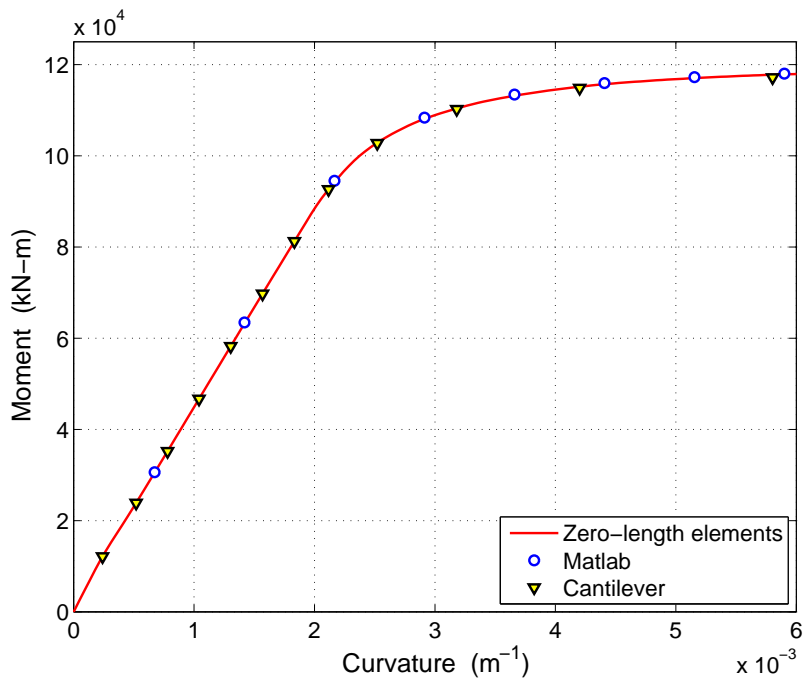


Figure 3.21 Moment-curvature response of cantilever model compared to zero-length element and independently calculated section responses for 2.5-m-diameter section.

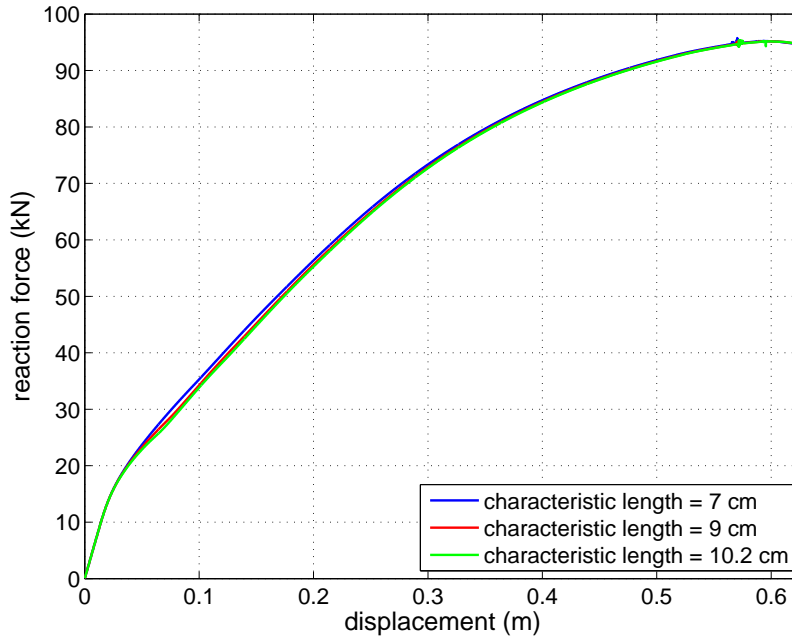


Figure 3.22 Force-displacement behavior for 0.61-m-pile section model as implemented in a cantilever beam model with various values of ℓ_c .

that develop in a pile embedded in a laterally spreading soil system. For this reason, the behavior at middling curvature and displacement demands is relatively unimportant. Also, since the stiffness of the pile is crucial in determining how the free-field curvature demand on the soil will affect the embedded pile, it is desirable that changes in E_t leave the initial tangent stiffness of the models similarly unaffected.

As shown in Figures 3.10 and 3.11, the initial tangent stiffness of the pile model is not affected by the selected characteristic lengths, validating that altering ℓ_c to improve numerical stability does not alter the initial stiffness of the pile models. These figures also show that at larger curvature demands, above about 0.015 m^{-1} in the 0.61-m-diameter model and about 0.007 m^{-1} in the 1.37-m-diameter model, the moment-curvature behavior is unaltered by the magnitude of the tension softening modulus. Thus, validating that the respective selections of ℓ_c are sensible with respect to the resulting moment-curvature response of the pile models in the range of curvatures that is important to this research.

Further validation of the selected tension softening moduli is made through a second validation study. This second study is an examination of the force-displacement behavior of cantilever beams modeled with the 0.61-m- and 1.317 m diameter sections. A schematic of this model is presented in Figure 3.19, and the results of this validation exercise are shown in Figures 3.22 and 3.23. Each model is assigned a tension softening modulus resulting from characteristic lengths of decreasing magnitude, starting from setting ℓ_c as the smallest element length in the respective models. The cantilever beam models for each pile section model mimic the mesh and geometry of the piles as used in the lateral spreading models exactly.

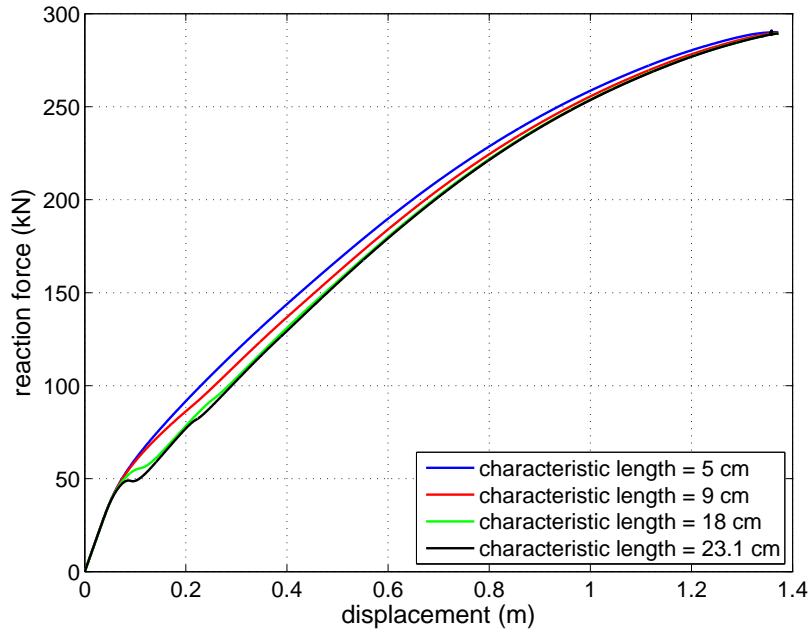


Figure 3.23 Force-displacement behavior for 1.37-m-pile section model as implemented in a cantilever beam model with various values of ℓ_c .

The effects of the changes in magnitude of the tension softening parameter are more apparent in the cantilever model, where the elements have lengths, as compared to the zero-length element approach used to generate the moment-curvature behavior of the models. This is demonstrated by the observation that the cantilever models for both pile models are unable to converge past a few time steps when the characteristic length is set as the largest element length. Once the tensile stress in the cross section reaches that which signals the onset of cracking, no converged solution can be found. The models display convergence issues even when ℓ_c is set as the smallest element length, though, unlike the case where the characteristic length is equal to the largest element length, the models will converge, albeit with a large number of small load steps. As in the moment-curvature study, the initial behavior is the same regardless of parameter selection, and all of the cases reach essentially the same reaction force at the final displacement.

The selections of ℓ_c summarized in Table 3.5, and the resulting tension softening moduli are made with consideration towards a realistic crack spacing as well as with respect to the convergence behavior of the pile models. The cantilever verification study validates that the selected characteristic length parameter will allow the pile models to reach convergence when implemented in a model with actual geometry, validation that the zero-length elements cannot provide. Additionally, the cantilever study demonstrates that the magnitude of the tension softening modulus only affects the middle range of the models' behavior; the initial and final ranges are unaffected.

4 Modeling the Soil

4.1 INTRODUCTION

The behavior of the soil surrounding the piles is important to the problem of a pile embedded in laterally spreading soils as it is both the source of and the medium through which the kinematic demands of the moving soil mass are transmitted to the embedded pile foundations. In the layered soil system considered in this study, the thickness of the liquefied layer and the various material properties of the surrounding soil layers are integral to defining how a pile experiences a lateral spreading event. Seemingly minor changes in the material properties or the configuration of the layers can significantly alter the resultant behavior of an embedded pile. In order for the results of this study to be valid for most piles in different soils, it is critical to select appropriate values for the soil parameters.

The typical considered soil system consists of three individual soil layers modeled as a 3D continuum surrounding the pile. A global view of the complete FE model is shown in Figure 2.1, in which the various soil layers and the general layout of the soil elements are clearly visible. Soil modeling decisions are made based upon the assumption that all three layers are made up entirely of homogenous (within each layer) cohesionless soil.

Two separate soil constitutive models are considered. One of these models considers the soil to be linear elastic while the other soil model considers elastoplastic behavior using a Drucker-Prager constitutive model developed and implemented for use in OpenSees (Petek, 2006).

4.2 SOIL ELEMENTS

The soil continuum is modeled using eight-node brick elements. The soil nodes defining these elements are created with three translational degrees of freedom. The number of soil elements ranges from 2720 to 3360 depending upon pile diameter considered in each particular case. The degree of mesh refinement is increased in the middle of the model as compared to the regions near the top and bottom of the model. This meshing scheme allows the areas of importance, i.e. the areas near the liquefied interface, to have a relatively fine mesh, while leaving the outlying regions with a coarser level of refinement.

Unless otherwise noted, the elements of all three soil layers are assigned a unit weight, $\gamma = 17 \text{ kN/m}^3$, which is typical for most soil conditions. The first step in the lateral spreading analysis

is to apply the self-weight of the soil elements, thus creating an appropriate distribution of vertical stress in the model. This is critical to determining the soil shear strength and soil-pile contact resistance with depth. Using this approach, both the soil and the embedded pile will behave in a manner consistent with a real soil-pile system when subjected to the simulated lateral spreading event.

4.3 LINEAR ELASTIC SOIL CONSTITUTIVE MODELING

For certain aspects of this research, the elements of soil surrounding the piles are assumed to display isotropic linear elastic behavior. This simplification allows for a means of comparison between elastoplastic pile and elastic soil lateral spreading models with simpler, entirely elastic models, as well as a basic case with which to test the elastoplastic pile models in the global lateral spreading model. The isotropic linear elastic material parameters in each soil layer are provided in Table 4.1. The elastic modulus, E , of the unliquefied layers explicitly considers a modulus reduction, per the guidelines of Kulhawy and Mayne (1990), appropriate for the levels of shear strain expected in the lateral spreading analysis. The shear modulus, G , and bulk modulus, κ , values are included for comparison with the elastoplastic soil constitutive model.

Table 4.1 Material parameters in isotropic linear elastic soil constitutive model.

Soil Layer	E (kPa)	ν	G (kPa)	κ (kPa)
Unliquefied	25000	0.350	9260	27777.8
Liquefied	2500	0.485	842	27777.8

During liquefaction of the middle layer, the pore water pressure in the layer increases, thus reducing the effective stress in the layer. As the magnitude of the pore water pressure becomes closer to the total mean stress in the layer, the shear strength becomes significantly smaller. The compressibility of the layer, however, should not change quite as drastically. For this reason, the soil material parameters are selected based upon an assumption that the bulk modulus, κ , remains consistent throughout the soil mass. In a fully liquefied state, the middle soil layer should have a Poisson's ratio close to 0.5, matching that of an incompressible fluid. Using a value of $\nu = 0.5$ would create an infinite bulk modulus, and cause a multitude of numerical issues. To avoid this result, a value of $\nu = 0.485$ is selected for the liquefied middle layer. Using this parameter and the consistent bulk modulus of $\kappa = 27777.8$ kPa, appropriate values for the elastic and shear moduli are computed. These values are summarized in Table 4.1.

4.4 ELASTOPLASTIC SOIL CONSTITUTIVE MODELING

The material nonlinearity considered in this research is introduced in the soil models through a Drucker-Prager constitutive model. The Drucker-Prager model is the simplest constitutive model that is appropriate for use with cohesionless soils. Other, more sophisticated constitutive models have been developed, however, the Drucker-Prager model is deemed sufficient to meet the goals of

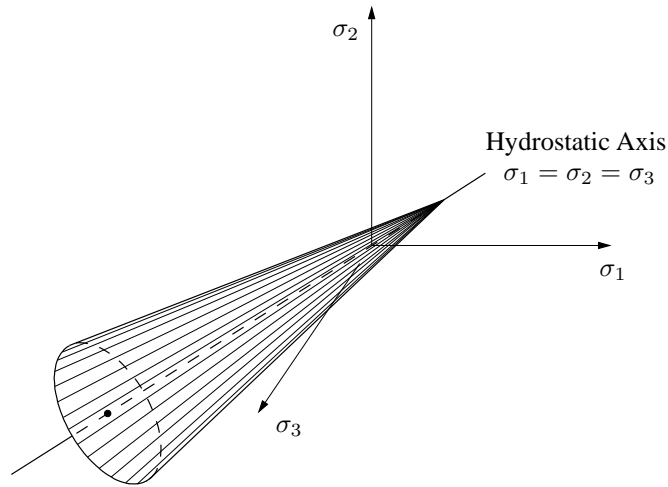


Figure 4.1 Drucker-Prager failure surface plotted in principal stress space.

this research. The particular model employed is one that was implemented in OpenSees by Petek (2006). The following section includes a basic discussion of the various components defining the Drucker-Prager model, as implemented in OpenSees. Section 4.4.2 includes a discussion on the particular material parameters used in the models and the impetus behind their use.

4.4.1 Drucker-Prager Constitutive Model

The Drucker-Prager constitutive model is one of the earliest soil plasticity models, developed as an extension of the von Mises yield criterion from one to two material parameters by Drucker and Prager (1952). Whereas the von Mises criterion is useful for metals, where independence from hydrostatic pressure is observed, the Drucker-Prager criterion was developed to account for the effects of hydrostatic pressure on the behavior of soil materials. As with the von Mises criterion, isotropic and kinematic strain hardening laws can be incorporated into the Drucker-Prager model, though it is not a required feature.

In a 3D principal stress space, the Drucker-Prager yield surface is a circular cone centered around the hydrostatic stress axis, where $\sigma_1 = \sigma_2 = \sigma_3$. This surface is shown in Figure 4.1 using a standard continuum mechanics sign convention (i.e., tension positive). The conical shape is the direct visual result of the effects of hydrostatic pressure on the behavior of a Drucker-Prager material. As compressive hydrostatic pressure increases, an increasing amount of deviatoric stress must be applied in order to bring the material to yield.

The material model can be fully defined by the free energy function, ψ , state equations, the Drucker-Prager yield condition, $f(\boldsymbol{\sigma}) \leq 0$, and evolution laws (flow rule and hardening law); all of which follow from classical rate-independent plasticity theory. For a 3D formulation, including linear isotropic and kinematic strain hardening, the free energy function can be written as a function of the state variables, which include: the strain, $\boldsymbol{\varepsilon}$, the plastic strain, $\boldsymbol{\varepsilon}^p$, the and the

respective isotropic and kinematic hardening parameters, α^{iso} and α^{kin} , as

$$\psi(\boldsymbol{\varepsilon}, \boldsymbol{\varepsilon}^p, \alpha^{iso}, \alpha^{kin}) = \frac{1}{2}(\boldsymbol{\varepsilon} - \boldsymbol{\varepsilon}^p) : \mathbb{C} : (\boldsymbol{\varepsilon} - \boldsymbol{\varepsilon}^p) + \frac{1}{2}K(\alpha^{iso})^2 + \frac{1}{2}\alpha^{kin} : \mathbb{H} : \alpha^{kin} \quad (4.1)$$

where

$$\mathbb{C} = 3k\mathbb{I}^{vol} + 2G\mathbb{I}^{dev} \quad (4.2)$$

is the elastic tensor, expressed in terms of the bulk and shear moduli (k and G), and the fourth-order volumetric and deviatoric operators, \mathbb{I}^{vol} and \mathbb{I}^{dev} . The fourth-order tensor \mathbb{H} , characterizing a shift of the yield surface in the deviatoric plane, can be defined in terms of the scalar kinematic hardening variable, H , as

$$\mathbb{H} = \frac{2}{3}H\mathbb{I}^{dev} \quad (4.3)$$

and K is a constant (scalar) isotropic hardening parameter. From the free-energy function of Equation (4.1), the three state equations can be written relating the state variables to the stress

$$\boldsymbol{\sigma} = \frac{\partial \psi}{\partial \boldsymbol{\varepsilon}} = \mathbb{C} : (\boldsymbol{\varepsilon} - \boldsymbol{\varepsilon}^p), \quad (4.4)$$

the isotropic hardening stress

$$q^{iso} = -\frac{\partial \psi}{\partial \alpha^{iso}} = -K\alpha^{iso}, \quad (4.5)$$

and the kinematic hardening stress (or back-stress)

$$\mathbf{q}^{kin} = -\frac{\partial \psi}{\partial \alpha^{kin}} = -\mathbb{H} : \alpha^{kin}. \quad (4.6)$$

When implementing this model in an algorithm using compressed matrix representations for the involved second- and fourth-order tensors, it is important to note the difference between stress-type (contravariant) second-order tensors, such as $\boldsymbol{\sigma}$ and \mathbf{q}^{kin} , and strain-type (covariant) second-order tensors such as $\boldsymbol{\varepsilon}$ and α^{kin} (Helnwein, 2001). Due to these differences, it is often beneficial to express the yield condition entirely in terms of one type of variable. Written in terms of stress-type variables, the yield condition for the Drucker-Prager model can be expressed as

$$f(\boldsymbol{\sigma}, q^{iso}, \mathbf{q}^{kin}) = \|\mathbf{s} + \mathbf{q}^{kin}\| + \rho I_1 + \sqrt{\frac{2}{3}}q^{iso} - \sqrt{\frac{2}{3}}\sigma_Y \leq 0 \quad (4.7)$$

in which

$$\mathbf{s} = dev(\boldsymbol{\sigma}) = \boldsymbol{\sigma} - \frac{1}{3}I_1\mathbf{1} \quad (4.8)$$

is the deviatoric stress tensor,

$$I_1 = tr(\boldsymbol{\sigma}) \quad (4.9)$$

is the first invariant of the stress tensor, and the two parameters ρ and σ_Y are positive material constants. It is common to define an additional variable $\boldsymbol{\eta}$ such that

$$\boldsymbol{\eta} = \mathbf{s} + \mathbf{q}^{kin} \quad (4.10)$$

The adoption of this additional variable allows for the expression of Equation (4.7) in the form

$$f = \|\boldsymbol{\eta}\| + \rho I_1 - \sqrt{\frac{2}{3}} (\sigma_Y - q^{iso}) \leq 0 \quad (4.11)$$

which is useful for its relative simplicity in notation.

The final set of equations characterizing the Drucker-Prager model are the three evolution laws that describe how the state variables $\boldsymbol{\varepsilon}^p$, α^{iso} , and α^{kin} change over time. These laws are defined in terms of various derivatives of the loading function

$$g(\boldsymbol{\eta}, I_1, q^{iso}) := \|\boldsymbol{\eta}\| + \bar{\rho} I_1 - \sqrt{\frac{2}{3}} (\sigma_Y - q^{iso}) \quad (4.12)$$

in which $\bar{\rho}$ is a non-associative parameter ranging from $0 \leq \bar{\rho} \leq \rho$, and a nonnegative scalar consistency parameter, γ . The evolution law for plastic strains, known commonly as the flow rule, can be written as

$$\dot{\boldsymbol{\varepsilon}}^p = \gamma \frac{\partial g}{\partial \boldsymbol{\sigma}} = \gamma \left(\frac{\boldsymbol{\eta}}{\|\boldsymbol{\eta}\|} + \bar{\rho} \mathbf{1} \right) \quad (4.13)$$

The parameter $\bar{\rho}$ controls the evolution of plastic volume change. When $\bar{\rho} = \rho$, the plastic flow is said to be fully associative and $g = f$. The evolution laws for the hardening variables, commonly referred to as hardening laws, are expressed as

$$\dot{\alpha}^{iso} = \gamma \frac{\partial g}{\partial q^{iso}} = \gamma \sqrt{\frac{2}{3}} \quad (4.14)$$

and

$$\dot{\alpha}^{kin} = \gamma \frac{\partial g}{\partial \mathbf{q}^{kin}} = \gamma \left(\frac{\boldsymbol{\eta}}{\|\boldsymbol{\eta}\|} \right) \quad (4.15)$$

The Drucker-Prager model implemented in OpenSees by Petek (2006) includes a tension-cutoff surface in addition to the standard Drucker-Prager yield surface. This tension-cutoff better captures the limited tensile capacity of a cohesionless soil. Additionally, the condition of $\|\mathbf{s}\| \geq 0$, which follows from a basic property of norms, requires a second surface.

The tension cutoff surface can be defined by the yield condition

$$f_2(\boldsymbol{\sigma}, q^{ten}) = I_1 + q^{ten} \leq 0 \quad (4.16)$$

where q^{ten} is a stress-type variable associated with the softening variable, α^{ten} , by the state equation

$$q^{ten} = -T_o \exp(-\delta \alpha^{ten}) \quad (4.17)$$

in which δ is a softening coefficient and T_o is a constant related to the Drucker-Prager yield surface as

$$T_o = \sqrt{\frac{2}{3}} \frac{\sigma_Y}{\rho} \quad (4.18)$$

The flow rule of Equation (4.13) is extended for the tension cutoff surface as

$$\dot{\boldsymbol{\epsilon}}^p = \gamma_1 \frac{\partial g_1}{\partial \boldsymbol{\sigma}} + \gamma_2 \frac{\partial f_2}{\partial \boldsymbol{\sigma}} = \gamma_1 \left(\frac{\boldsymbol{\eta}}{\|\boldsymbol{\eta}\|} + \bar{\rho} \mathbf{1} \right) + \gamma_2 \mathbf{1} \quad (4.19)$$

and the softening law is formulated as

$$\dot{\alpha}^{ten} = \gamma_2 \frac{\partial f_2}{\partial Q^{ten}} = \gamma_2 \quad (4.20)$$

4.4.2 Determination of Material Parameters

The material constants defining the Drucker-Prager constitutive model are selected such that there is consistency with the elastic soil elements, as well as a degree of realism in the magnitudes used for each soil layer. To this end, the elastic constants of bulk and shear moduli defined for the linear elastic soil models are used in the elastoplastic models. To create a more realistic pressure-dependent elastic stiffness in the elastoplastic model, the elastic parameters are modified to include the ability to update the bulk modulus according to the relation

$$\kappa = \kappa_0 \sqrt{1 + \frac{|\sigma_m|}{|\sigma_{ref}|}} \quad (4.21)$$

in which κ_0 is the reference bulk modulus listed in Table 4.2, $\sigma_m = I_1/3$ is the mean stress in each element, and σ_{ref} is a reference pressure taken to be equal to atmospheric pressure (101 kPa). A similar relation is used to update the shear modulus in the model, in which G_0 is the reference shear modulus listed in Table 4.2.

In order to obtain sensible values for the Drucker-Prager material constants ρ and σ_Y , the following correlations have been made with the somewhat more common, and measurable, Mohr-Coulomb material constants of cohesion, c , and friction angle, ϕ , after the discussion detailed in Chen and Saleeb (1994) as follows:

$$\rho = \frac{2\sqrt{2} \sin \phi}{\sqrt{3} (3 - \sin \phi)} \quad (4.22)$$

$$\sigma_Y = \frac{6c \cos \phi}{\sqrt{2} (3 - \sin \phi)} \quad (4.23)$$

Assuming a small amount of cohesion for numerical stability, $c = 3.56$ kPa, and internal friction angles of $\phi = 36^\circ$ in the unliquefied layers and $\phi = 0^\circ$ in the liquefied layer, the Drucker-Prager material constants are computed for each layer using Equations (4.22) and (4.23). These values are summarized in Table 4.2. With respect to associative and non-associative plastic flow, several combinations are explored. Models are run with the non-associative parameter $\bar{\rho}$ set equal to both ρ , creating fully associative flow, and zero, creating isochoric non-associative flow. Additionally, based on the assumptions of drained conditions and a medium initial density for the unliquefied layers, an intermediate case where $\bar{\rho} = 0.150$ is used. This is done so that there will be some dilation of the soil, but not quite as much as would occur for the case with $\bar{\rho} = \rho$.

Table 4.2 Material input parameters used in Drucker-Prager soil constitutive model.

Soil Layer	κ_0 (kPa)	G_0 (kPa)	ϕ ($^\circ$)	σ_Y (kPa)	ρ	γ (kN/m ³)
Unliquefied	27777.8	9260	36	5.00	0.398	17
Liquefied	27777.8	842	0	4.97	0.000	17

It is interesting to note that when setting $\phi = 0^\circ$, resulting in $\rho = 0$, the Drucker-Prager yield condition of Equation (4.7) reduces to the von Mises yield criterion. In effect, the elastoplastic lateral spreading model is constructed by considering the unliquefied layers to be Drucker-Prager materials and the liquefied middle layer as a low shear stiffness von Mises material. To provide a degree of simplicity in the model, the linear isotropic hardening and tension softening parameters are set to zero in the lateral spreading simulations.

4.5 VALIDATION OF SOIL MODELS

As with all of the other aspects of this research, it is important to validate the elastoplastic soil models through simple tests before installing them into a larger model. The Drucker-Prager soil model is evaluated through a series simulated geotechnical tests with a single element of elastoplastic soil. The chosen tests are all commonly performed to evaluate the mechanical characteristics of soil samples, and allow for validation that the OpenSees implementation of the Drucker-Prager model is performing as expected. The selected geotechnical tests are:

1. Confined compression (CC) test
2. Conventional triaxial compression (CTC) test
3. Simple shear (SS) test
4. Hydrostatic extension (HE) test.

With the exception of the hydrostatic extension test, all of the simple, single element, tests start from an initial hydrostatic stress state, $\sigma_1 = \sigma_2 = \sigma_3 = -p_o$, where p_o is an initial confining pressure. Each test is conducted for various initial confining pressures both with and without the inclusion of linear isotropic hardening. Unless otherwise indicated, the material parameters used in each test are those listed in Table 4.2.

When dealing with 3D stress states, plots of the various invariants of the stress and strain tensors are often the most effective means for visualizing the behavior of a particular material. If chosen carefully, such plots can display data in a more meaningful manner than traditional stress-strain plots. For each material test, four plots are chosen with the intent of fully characterizing the stress-strain response of the Drucker-Prager soil element. The chosen invariant axes include the norm of the deviatoric stress tensor, $\|\mathbf{s}\|$, the first invariant of the stress tensor, $I_1 = \text{tr}\boldsymbol{\sigma}$, the norm of the deviatoric strain tensor, $\|\mathbf{e}\|$, the trace of the strain tensor, $\text{tr}(\boldsymbol{\varepsilon})$, and the mean stress, $I_1/3$.

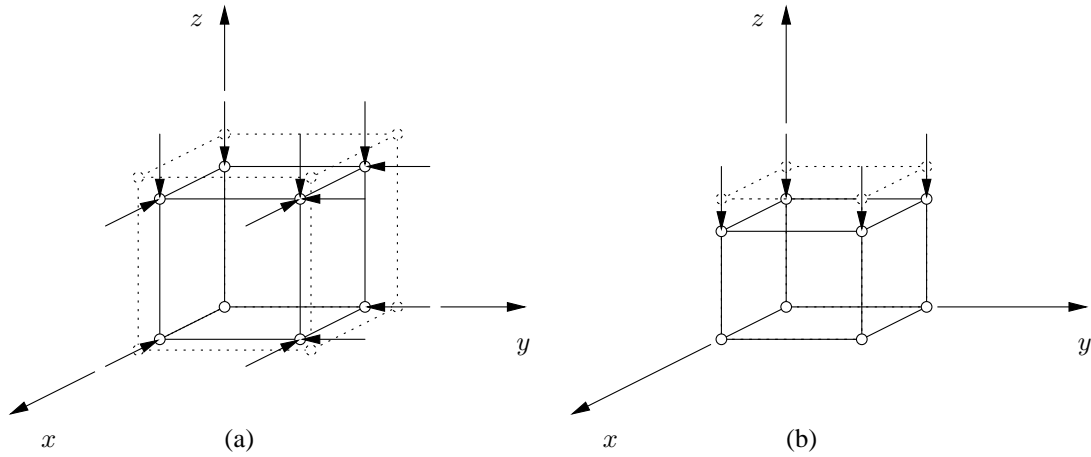


Figure 4.2 Schematic depiction of the simulated CC test. (a) Hydrostatic compression phase; (b) Confined compression phase.

4.5.1 Confined Compression Test

In a CC test the soil element is first brought to an initial state of hydrostatic stress. While holding the displacements fixed in the first and second principal stress directions, the displacement in the third principal direction is increased, creating an increase in the compressive stress in that direction. To achieve this in the context of the single element model, an entirely strain-controlled approach is adopted. The approach used to model this test is depicted schematically in Figure 4.2.

As with the models in all of the soil tests, this model considers the soil element to be a unit cube. The nodes in the $x - y$, $y - z$, and $z - x$ planes are held fixed with respect to displacements normal to their faces. The nodes on the element faces opposite the fixed faces are moved inwards by equal increments to create the hydrostatic stress state. After the desired hydrostatic stress state has been reached, the nodes on the positive x - and y -faces are held fixed against x - and y -direction displacements, respectively, while the nodes on the positive z -face of the element are moved downwards, see Figure 4.2(b). The stresses acting in the x - and y -directions do not stay constant, instead, the strains in those directions are held constant.

The stress path for the CC test is shown on the meridian plane ($I_1 - \|s\|$ axes) in Figure 4.3 for three values of initial confining pressure ($p_0 = 10$, $p_0 = 20$, and $p_0 = 40$ kPa). As expected, the normal stress increases along the I_1 axis during the hydrostatic loading phase, and then deviatoric stresses begin to develop during the confined compression phase. For the particular loading ratio used in the CC test, the soil element remains in the elastic range, never reaching the yield state, an event that would be evident by the stress path intersecting the line of the failure surface. Because the element remains entirely elastic during this test, no strain hardening cases are considered.

The material-response summary presented Figure 4.4 shows the stress-strain behavior of the soil element during the CC test on a series of four axes. Since the material remains entirely elastic during this test, the slopes of the curves in all four plots remain constant. This verifies both the initial expectations for this test as well as the stress path shown in Figure 4.3.

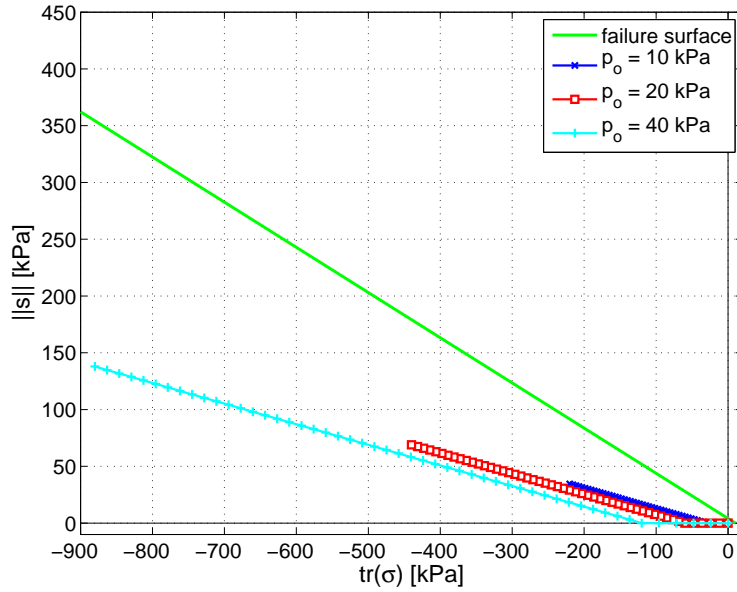


Figure 4.3 Stress paths for CC test.

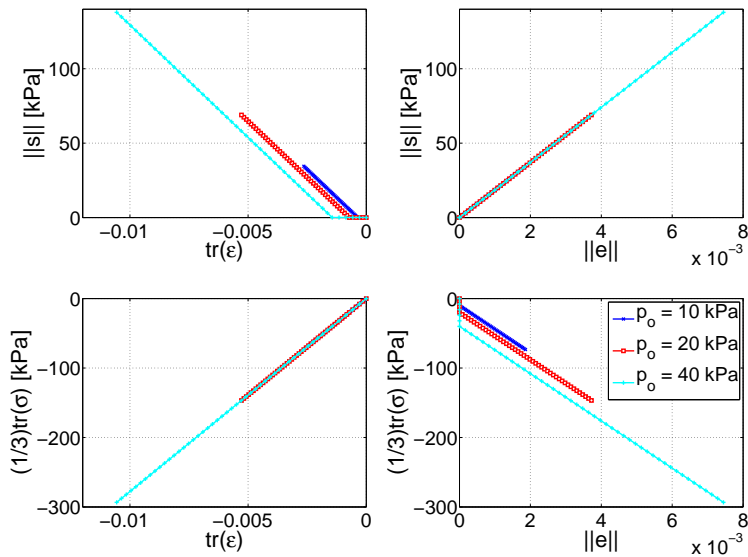


Figure 4.4 Stress-strain responses of Drucker-Prager soil element subjected to CC test stress path.

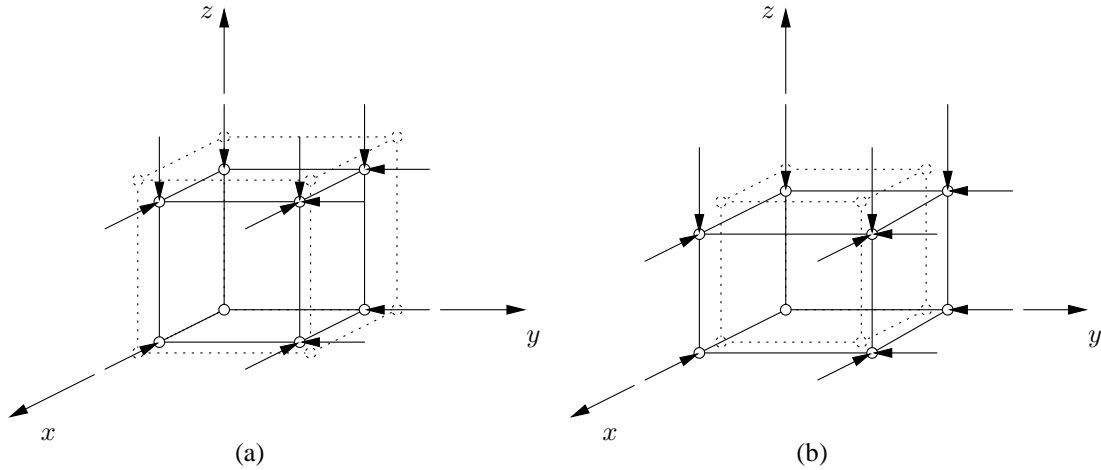


Figure 4.5 Schematic depiction of the CTC test as performed in OpenSees. (a) Hydrostatic compression phase; (b) Application of deviator stress.

4.5.2 Conventional Triaxial Compression Test

The CTC test is one of the most widely used test in soil mechanics. In this test, after the initial hydrostatic loading phase, two of the principal stresses are kept constant (i.e., $\sigma_1 = \sigma_2 = -p_o$), while the third principal stress, σ_3 is increased. This test differs from the confined compression test in that the first and second principal stresses do not change from their initial value at the the end of the hydrostatic phase, whereas the first and second principal stresses in the CC test increase in proportion to the applied stress increase in the third principal direction.

The CTC test is achieved in a single element model as depicted in Figure 4.5. This test uses mixed stress and strain control as opposed to the pure strain control of the CC test, however, the geometric boundary conditions are the same as those in the CC test model. The hydrostatic stresses are applied under stress control, by applying compressive loads on the free degrees of freedom. Once the desired hydrostatic state is achieved, the loads on the positive x - and y -faces are held fixed for the duration of the test, ensuring that the principal stresses in two directions remain constant, while the nodes on the positive z -face of the element are moved downwards under strain control to create the increase in the third principal stress. The nodes on the non-fixed faces of the element are left free to displace outward during this process.

Verification that the material model behaves in a predictable manner during this test can be obtained through a comparison of the predicted slope of the stress path resulting from the CTC test with the data returned from OpenSees. It can be shown that the slope of the CTC test stress path on a meridian ($I_1 - \|s\|$) plane, is equal to $\sqrt{2/3}$. A line with this slope is plotted against the stress path returned from OpenSees for the $p_0 = 10$ kPa case. As shown in Figure 4.6, the single element test slope is identical to the theoretical slope, thus providing further validation that the Drucker-Prager material model has been successfully implemented into OpenSees.

The simulated CTC stress paths for a soil element with no strain hardening are shown in Figure 4.7 for three values of initial confining pressure, p_0 . A corresponding plot is shown in Figure 4.8 for a soil element including linear isotropic strain hardening. For the strain hardening cases, the

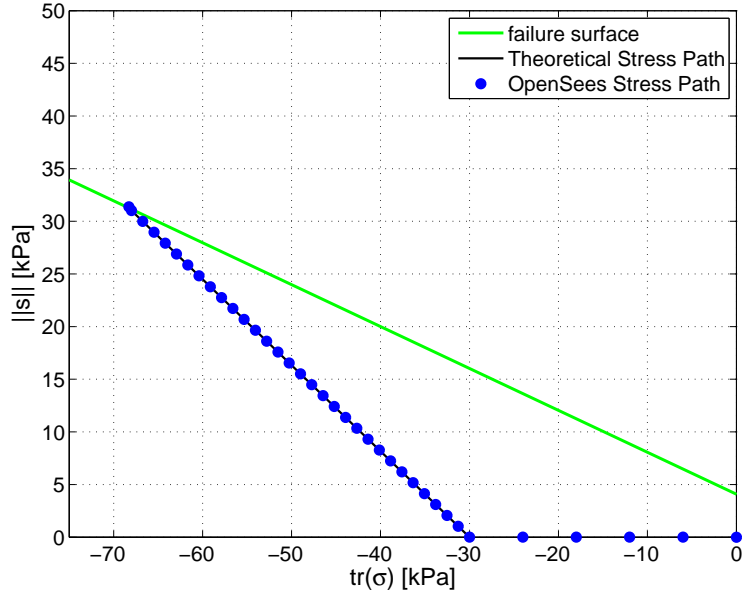


Figure 4.6 Comparison of simulated and theoretical CTC test stress paths.

hardening parameter K is set to 100,000 kPa to enhance visualization. The CTC test brings the element to failure for all cases. For the three cases without strain hardening, once the deviatoric stress has increased to the point where the stress path intersects the failure surface, the material yields and the stresses no longer increase with increasing strain. This behavior is consistent with the expectations for a perfectly plastic material.

When linear isotropic hardening is included, the model exhibits behavior that is somewhat altered. Instead of displaying perfectly plastic behavior, the soil element hardens with increasing strain, allowing for the stresses to increase beyond the initial limiting values for the perfectly plastic cases. The inclusion of strain hardening effectively acts to expand the failure surface with increasing plastic strain. Again, the Drucker-Prager soil element behaves as expected, providing assurance that the OpenSees implementation is correct.

The stress and strain invariant plots of Figures 4.9 and 4.10 provide a more complete look at the plastic behavior of the soil element during the CTC test. The perfectly plastic behavior of the model for the cases without strain hardening is even more evident in Figure 4.9 than in Figure 4.7. After the elastic portion of the loading, the slopes of the curves all go to zero, indicating increases in shear and normal strain with no corresponding increases in shear or normal stress. For the cases with strain hardening, there is a change in slope at the end of the elastic range, however, here the slopes do not go to zero, instead they change according to the amount of strain hardening considered. The behavior displayed in these two figures validates that the OpenSees implementation of the Drucker-Prager model displays the intended post-yield behavior when the soil is brought to yield by an increase in normal stress.

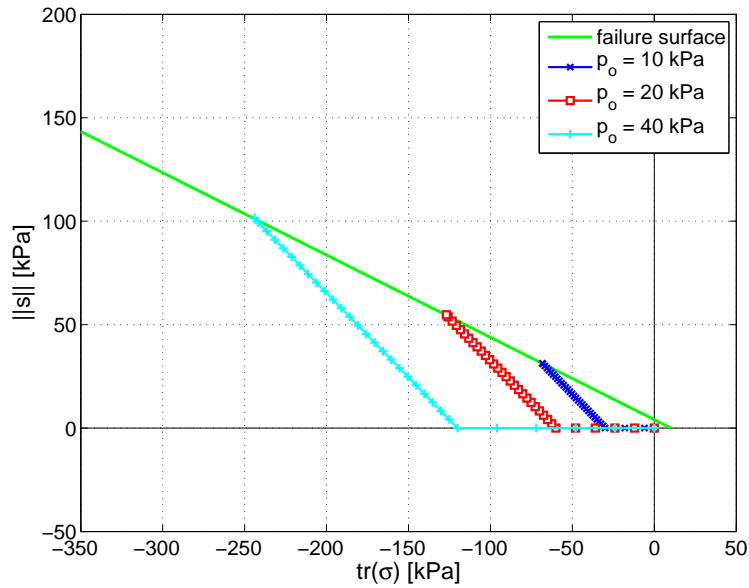


Figure 4.7 Stress paths for CTC test in the perfectly plastic case (no strain hardening).

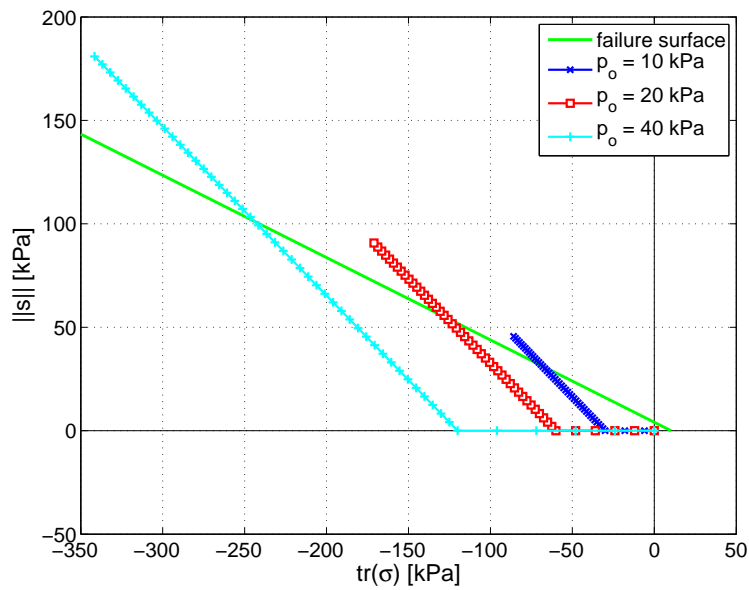


Figure 4.8 Stress paths for CTC test the linear isotropic strain hardening case.

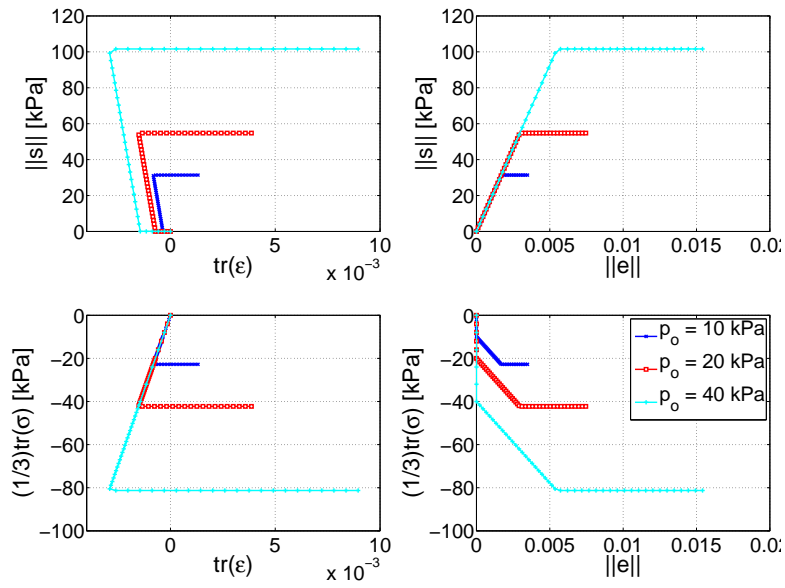


Figure 4.9 Stress-strain responses of Drucker-Prager soil element subjected to a CTC stress path for the perfectly plastic case (no strain hardening).

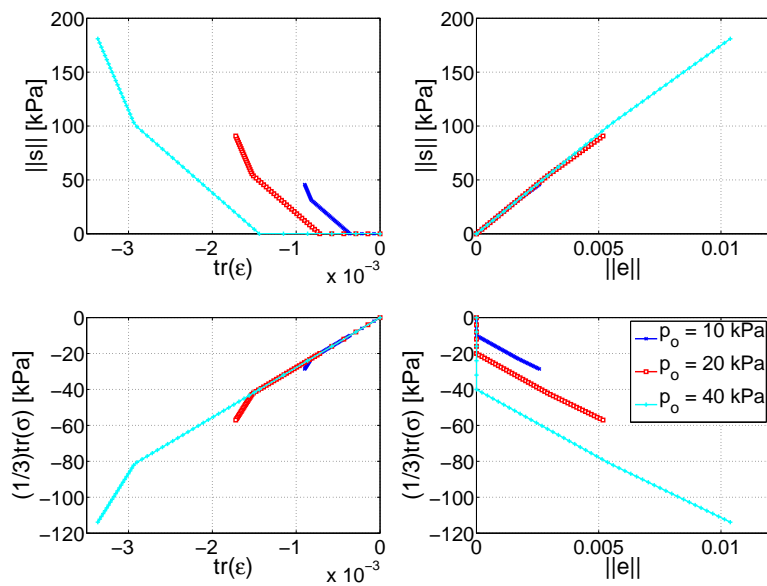


Figure 4.10 Stress-strain responses of Drucker-Prager soil element subjected to a CTC stress path for the linear isotropic strain hardening case.

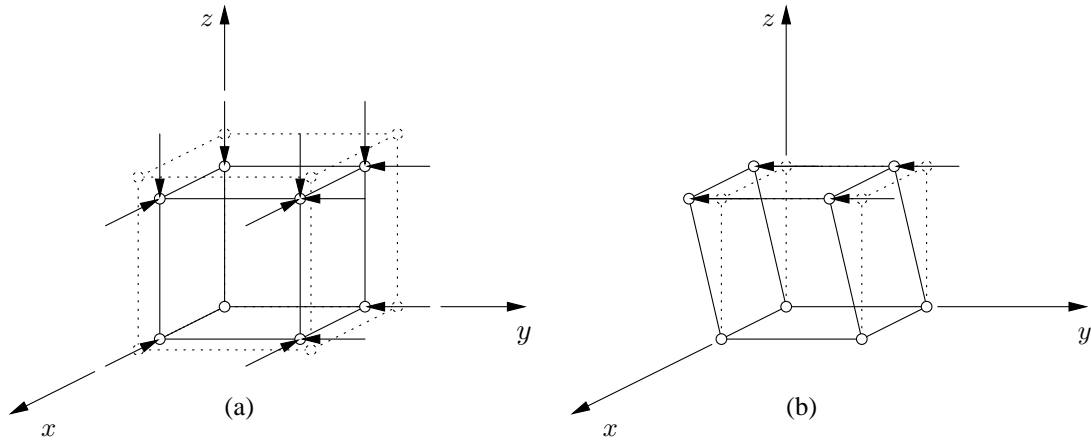


Figure 4.11 Schematic depiction of the SS test as performed in OpenSees. (a) Hydrostatic compression phase; (b) Simple shear phase.

4.5.3 Simple Shear Test

In the SS test, the soil element is brought to failure in pure shear, i.e., $\Delta I_1 = 0$. The OpenSees implementation of the SS stress path is conducted entirely under strain control. Figure 4.11 provides a visual representation of the single element SS test as analyzed in OpenSees. The initial hydrostatic state is induced in an identical manner to the previously described CC test. From this initial hydrostatic state, the nodes at the base of the element are held fixed while the upper nodes are displaced in the negative y -direction by equal increments. During this test, the upper nodes are not displaced in the x - or z -directions, resulting in an isochoric deformation. This type of deformation results in the desired state of pure shear stress (small strain only).

The SS test is run for three values of initial confining pressure, both with and without the inclusion of linear isotropic strain hardening. Figure 4.12 shows the stress paths for the three confining pressures on the meridian plane for the perfectly plastic cases; and Figure 4.13 shows the stress-strain behavior during this test. In the elastic range, the element only experiences an increase in deviatoric stress, the expected behavior. Once the soil element yields, the mean normal stress decreases (increased compression), and the deviatoric stress continues to increase with increasing deviatoric strain. However, there is no change in the total volumetric strain. The initial drop in volumetric strain, $\text{tr } \epsilon$, indicated in Figure 4.13 corresponds to the hydrostatic loading phase.

Figures 4.14 and 4.15 show the stress paths and the stress-strain behavior, respectively, for a soil element with linear isotropic strain hardening. A hardening coefficient of $K = 100,000$ kPa is selected for for enhanced visualization. For these cases, the elastic behavior is unchanged; the stress path lies in the deviatoric plane from the initial hydrostatic state up until the initial yield point. Subsequent yielding under the inclusion of strain hardening allows for greater increases in deviatoric stress during the continued application of increasing deviatoric strains.

The results of the single element simple shear tests provide further validation that the Drucker-Prager material model reproduces the expected behaviors when subject to known stress/strain paths. When implemented in an element subject to pure shear, the material model is able to produce consistent results for all of the investigated cases.

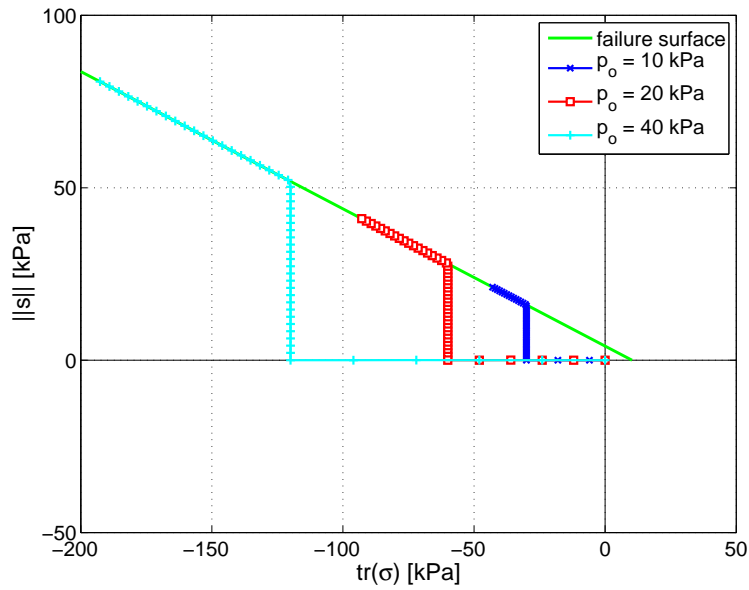


Figure 4.12 Stress paths for SS test in the perfectly plastic case (no strain hardening).

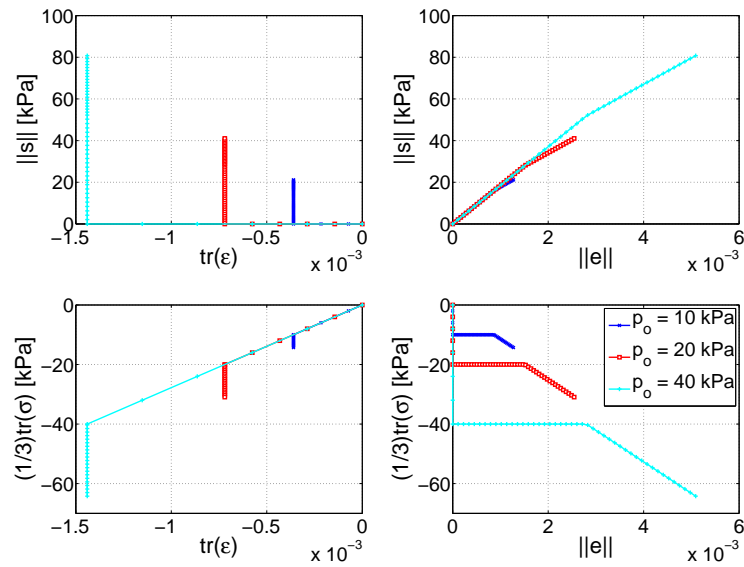


Figure 4.13 Stress-strain responses of Drucker-Prager soil element subjected to a SS test stress path for the perfectly plastic case (no strain hardening).

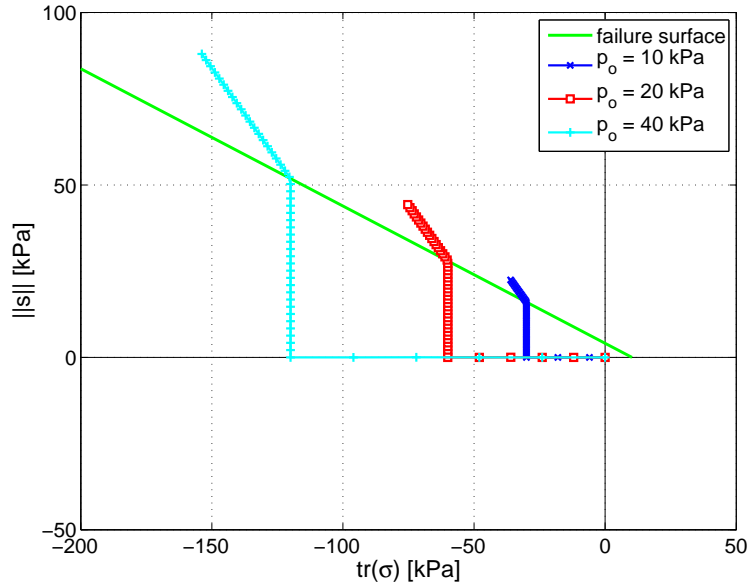


Figure 4.14 Stress paths for SS test in the linear isotropic strain hardening case.

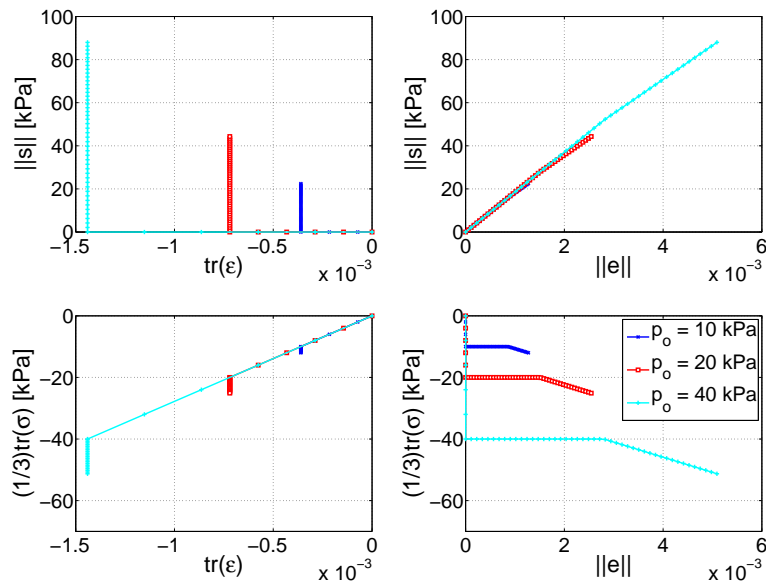


Figure 4.15 Stress-strain responses of Drucker-Prager soil element subjected to a SS test stress path for the linear isotropic strain hardening case.

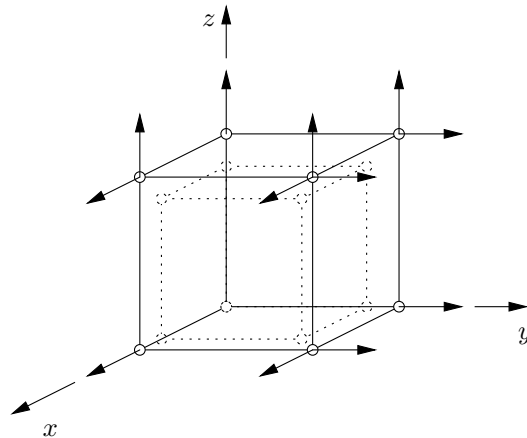


Figure 4.16 Schematic depiction of the HE test as performed in OpenSees.

4.5.4 Hydrostatic Extension Test

The final single element test performed in pursuit of validating the OpenSees implementation of the Drucker-Prager material model is a hydrostatic extension (HE) test. In this test, the soil element is subject to equally increasing principal stresses until failure is achieved. The resulting stress path follows the hydrostatic axis in the tensile direction, eventually reaching the tip of the cone depicted in Figure 4.1.

To achieve the HE test in a single element model, the procedure is essentially the opposite of the hydrostatic compression phases of the prior tests. From the same base model and boundary conditions, the free nodes are displaced outward in equal increments as represented schematically in Figure 4.16. The HE test is performed both to test the tensile behavior of the model and to evaluate the effectiveness of the tension-cutoff implementation.

Due to the nature of this test, multiple confining pressures were not included in the results. However, the HE test is conducted for three values of the tension softening coefficient, δ . As shown in Figure 4.17, the intended stress path is returned by the model. Providing assurance that the Drucker-Prager material model can handle tensile stresses as well as compressive stresses. The stress and strain invariant plots of Figure 4.18 verify that the element develops no deviatoric strains nor stresses during the single element HE test. As is expected, only normal stresses and strains are experienced by the soil element.

The effect of changes in the the magnitude of δ is evident in the lower left plot of Figure 4.18. When $\delta = 0$, the element displays perfectly plastic behavior after the tensile limit is reached, indicating that no softening occurs. The degree of softening increases with increasing values of δ , just as intended by the inclusion of the tension softening surface in the material model. All of the behavior displayed by the Drucker-Prager soil element in the HE test is consistent with expectations, thus providing further verification as to the correct implementation of the material model in OpenSees.

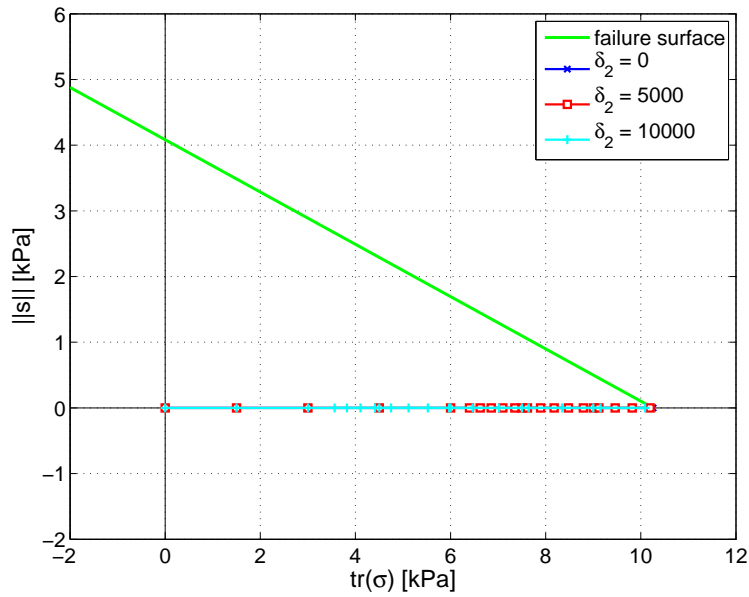


Figure 4.17 Stress paths for HE test, on the meridian plane for three values of the tension softening parameter, δ .

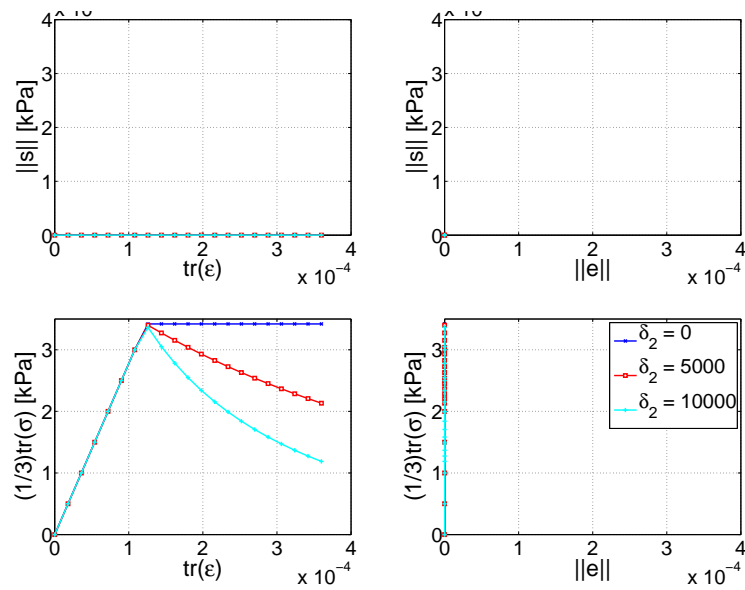


Figure 4.18 Stress-strain response of Drucker-Prager soil element subjected to a HE test stress path for three values of tension softening parameter, δ .

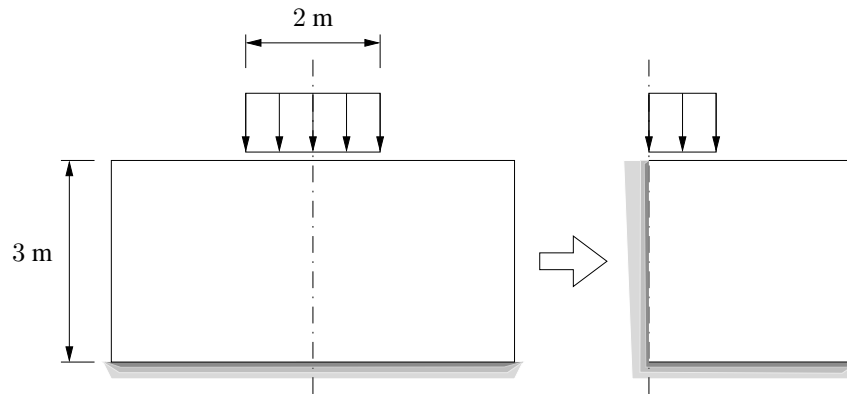


Figure 4.19 A representation of the load case modeled by the multi-element plane strain test for the Drucker-Prager material model.

4.5.5 Multi-Element Plane Strain Test

In the mechanical behavior tests described in Sections 4.5.1 through 4.5.4, the OpenSees implementation of the Drucker-Prager material model is tested with the use of a single element. To assess the model in a somewhat broader context, a multi-element plane strain test is conducted. A schematic of this test is shown in Figure 4.19. In this test, a distributed load is applied to a portion of the upper surface of a wall of soil material. The base of the model is held fixed against vertical displacements, and the large planar surfaces of the model are held fixed against out-of-plane displacements to create plane strain conditions. The symmetry shown in Figure 4.19 is applied by fixing displacements in the horizontal direction. The purpose of this plane strain test is to evaluate the behavior of the Drucker-Prager material model in the context of a multi-element model.

The mesh for the plane strain test is 3 m wide, 3 m tall, and 1 m thick. The soil elements are defined with the unliquefied layer material parameters summarized in Table 4.2. A distributed load is applied over a 1 m square. This load is increased linearly until the two nodes in the symmetry plane have undergone a 5 mm downward displacement. The deformed shape of the mesh, magnified by a factor of ten, is shown in Figure 4.20 along with the distribution of the vertical stress component, σ_{yy} . As shown, the model is reacting in a manner consistent with initial expectations. Compressive stresses develop in the left hand portion of the model (the area beneath the load), while tensile stresses are generated in the right hand portion as those soil elements expand. Though the presented results are only for a twenty-four element square mesh, this same test was conducted with differing numbers of elements. In all cases the model displays predictable behavior as well as a quadratic rate of asymptotic convergence, further validating the OpenSees implementation of the Drucker-Prager material model.

To further illustrate and verify the abilities of the Drucker-Prager material model, the stress paths for several Gauss points along the top row of the mesh are plotted on the meridian plane in Figure 4.21. As shown, several elements are brought to yield in both tension and compression, while others remain in the elastic range during the test. Figure 4.21 provides further validation that the Drucker-Prager soil elements can be successfully implemented in a multi-element model, one which causes the elements to undergo a variety of stress paths.

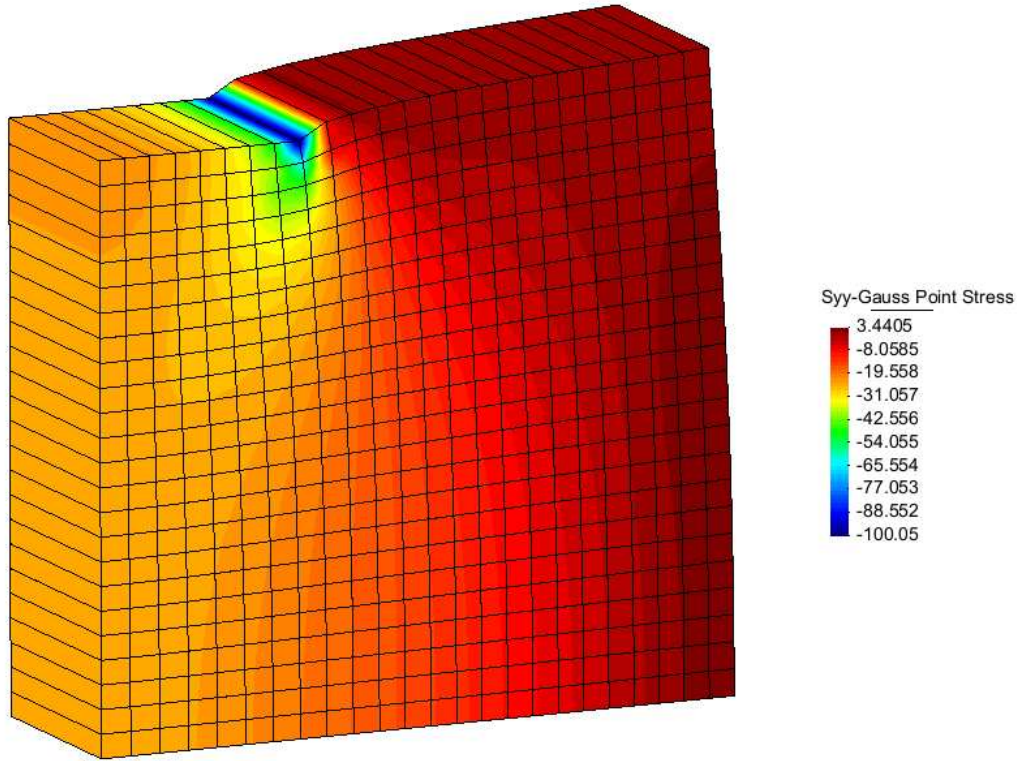


Figure 4.20 The deformed mesh for the plane strain test with the distribution of vertical stress in the soil elements (magnification factor = 10).

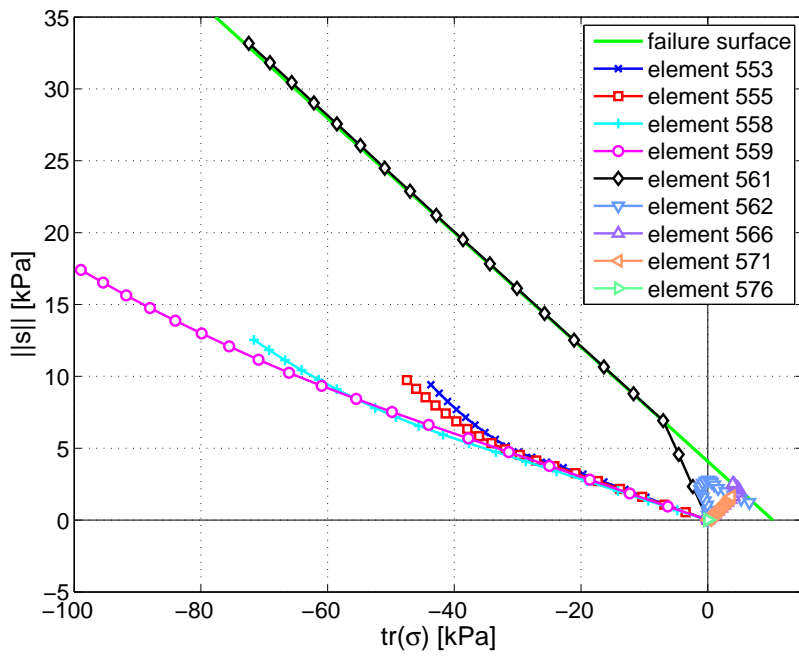


Figure 4.21 Stress paths for a selection of Gauss points along the top row of the plane strain model.

5 Three-Dimensional Finite Element Analysis

5.1 INTRODUCTION

Piles embedded in laterally spreading cohesionless soils must be able to withstand large bending demands. The magnitude and location of the largest shear and moment demands are dependent upon many factors. Among these factors are the size and stiffness of the pile, the strength of the surrounding soil, the boundary and support conditions of the pile, the amount of lateral displacement that occurs, and the depth of the liquefied layer.

Single piles in laterally spreading soil systems are analyzed by means of a 3D FE model (see Chapter 2). This model includes beam elements for the piles, brick elements for the soil, and beam-solid contact elements to define the interaction between the pile and the surrounding soil. Two separate pile head support conditions are considered in these simulations: (1) a fixed-head condition and, (2) a free-head condition. The fixed-head condition restricts the rotation of the pile head and is the most representative of an actual pile application, while the free-head cases allow the pile head to rotate freely and provide a means of comparison.

In all of the considered cases, the piles are subject to the imposed displacement profile discussed in Section 2.3 having a magnitude of one pile radius in the upper soil layer. This distance is sufficient to cause inelastic behavior in the elastoplastic pile and soil models, while remaining small enough to facilitate relatively short run-times in OpenSees. Run-time per case ranges from approximately four hours in linear elastic cases to 26 hours in elastoplastic cases, and varies for the three pile models. For all cases the thickness of the liquefied layer is set at one pile diameter. The dimensional scheme discussed in Section 2.2 is utilized, with a liquefied layer located ten pile diameters below the ground surface.

The behavior of a single pile in a laterally spreading soil system is evaluated through comparisons between the data returned from each of 24 cases run with various combinations of piles, soil, and pile support conditions. The models are evaluated via the bending behavior of the piles, the stresses that develop in the soil, and the soil-pile interface forces developing in the contact elements, among other factors. The individual results of each modeling approach are examined and compared in order to provide further insight into the lateral spreading problem.

5.2 SUMMARY OF CONSIDERED CASES

Various combinations of pile and soil constitutive models are considered. With respect to the piles, these combinations create two general sets of lateral spreading cases; those with elastic pile models and those with elastoplastic pile models. The pile models used in each set are discussed in detail in Chapter 3. Two soil constitutive models are used in combination with each set of pile models, an elastic soil model, and an elastoplastic soil model which employs a Drucker-Prager constitutive model. The details of each of these soil models are discussed in Sections 4.3 and 4.4, respectively. When combined with the variation in the pile head fixity, this set of parameter combinations yields a set of cases that are divided into four main categories, designated as Series 1-4. The four test Series each consider the following six pile cases:

1. Free-head 2.5-m-diameter pile.
2. Free-head 1.37-m-diameter pile.
3. Free-head 0.61-m-diameter pile.
4. Fixed-head 2.5-m-diameter pile.
5. Fixed-head 1.37-m-diameter pile.
6. Fixed-head 0.61-m-diameter pile.

This creates a total of 24 distinct analysis cases. Each test Series is differentiated by means of the type of pile and soil constitutive models that are employed in its respective set of six cases. The highlights of each Series are presented in the following discussion. A brief summary of the four test Series is presented in Table 5.1.

5.2.1 Series 1: Elastic Piles with Elastic Soil

Using linear elastic piles in the lateral spreading model allows for general behavioral mechanisms to be developed for the lateral spreading case. The elastic pile embedded in linear elastic soil models are the simplest cases that are evaluated using the 3D lateral spreading model. These cases are computationally cheap when compared to the other cases (run-time per case approximately four hours), however, the data returned by these models is not, in itself, indicative of the type of

Table 5.1 Overview of the four considered test Series.

	Series 1	Series 2	Series 3	Series 4
Elastic Pile	X		X	
Elastic Soil	X	X		
Elastoplastic Pile		X		X
Elastoplastic Soil			X	X

behavior that would occur in an actual lateral spreading event. Instead of offering direct insights into pile behavior, the fully elastic cases provide a benchmark for comparison and evaluation of more computationally intensive models.

5.2.2 Series 2: Elastoplastic Piles with Elastic Soil

The use of elastoplastic pile models allows for the examination of the interaction between the soil and the pile during a lateral spreading event in a more realistic fashion than that which is returned by elastic pile models. When using elastoplastic piles, the piles are able to yield and develop plastic hinges under the influence of the imposed displacement profile. This changes the way in which the soil and pile interact in the model, often in dramatic fashion. This Series is considered as an intermediate set of cases through which comparisons can be drawn between the entirely linear elastic cases (Series 1) and the entirely elastoplastic series of cases (Series 4). Additionally, this series allows for the effects of plastic behavior in the piles to be examined in an isolated fashion.

5.2.3 Series 3: Elastic Piles with Elastoplastic Soil

These six cases offer a direct means of evaluation for the effects of yielding in the soil on the behavior of the pile in the lateral spreading case. Leaving the pile elastic creates a situation in which the only differences between these cases and the entirely elastic cases must be due to the plastic behavior of the soil, allowing any mechanisms to be pinpointed. Additionally, the elastic pile in elastoplastic soil series allows for the extraction of $p-y$ curves at various depths within the soil system, providing a means of comparison for the results of the 3D lateral spreading model with other, more commonly used models for the lateral analysis of piles. The $p-y$ curves are determined from the resulting contact forces applied to each pile node and the displacement of the pile relative to the soil at each of these positions. Further discussion on this process can be found in Chapter 6.

5.2.4 Series 4: Elastoplastic Piles in Elastoplastic Soil

The fully elastoplastic cases offer the most realistic glimpse into the behavior of the lateral spreading problem, though at the highest computational cost (run-times approximately 24 to 26 hours). This set of cases enables observations to be made into the behaviors that develop when both the piles and the soil yield and display plastic behavior. Additionally, it is of interest to evaluate if the results found in the fully elastoplastic series can be successfully reproduced by using a BNWF analysis with elastoplastic pile models and the $p-y$ curves computed from the Series 3 model.

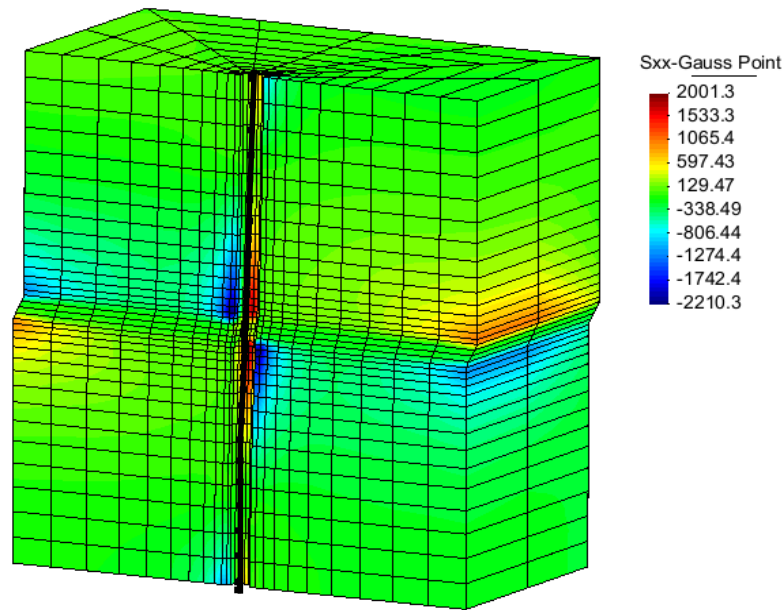


Figure 5.1 Deformed shape and distribution of lateral stress for the Series 1 free-head case with a 0.61-m-diameter pile. Stresses are given in kPa.

5.3 GENERAL BEHAVIOR OF PILES IN LATERALLY SPREADING SOIL

In all of the cases, the interaction between the soil and the pile, governed by their respective material properties, defines the resulting behavior of the system. General patterns of behavior are observed through consideration of several comparative measures. These results are deemed most indicative of the pile behavior as a whole, and include the magnitudes of the maximum moment and shear force demands in the pile, and the locations of these extreme values. Also of interest are the evolution of the extreme moments in the pile, and the way in which the lateral spreading soil deformation profile manifests itself as a load on the pile.

As the upper layer of soil begins to displace laterally with respect to the immobile lower layer, the entire pile provides resistance to this motion as the upper portion is pushed along with the flow of soil. This behavior is illustrated in Figure 5.1, which shows the the distribution of horizontal normal stress (in the direction of motion) in the soil elements, as well as the deformed shape of the system, for the Series 1 free-head case with a 0.61-m-diameter pile.

The entirely linear elastic case is selected for Figure 5.1 to illustrate the lateral stress distribution in the soil because it allows truly large stresses to develop. The locations of the largest tensile and compressive lateral stress in the elastic soil elements identify where initial yielding is likely to occur in both the elastoplastic soil models and in an actual soil system. If the elements are assigned elastoplastic behavior, the yielding that may occur would likely obscure the marked differences in stresses that are able to develop in the linear elastic case, making it difficult to differentiate between the stresses in adjacent locations.

From the lateral stresses developed in the vicinity of the pile, it can be clearly seen that the imposed displacement profile puts the pile in bending. In the lower solid layer, the distribution of compres-

sive stresses shows that the pile pushes back into the soil at its base while it is pushed into the soil at the interface with the liquefied soil layer. The opposite is observed in the upper soil layer, where the pile resists the ground motion at the interface with the liquefied layer and is pushed into the soil at the pile head. Additionally, at each location of large compressive stress on the leading and trailing faces of the pile, there is a corresponding zone of tensile stress in the soil. These tensile regions signify where the soil elements are being pulled apart by either the passive or active passage of the pile through the soil. While the results of Figure 5.1 are for a 0.61-m-diameter pile, this same pattern of lateral stress is present in all of the lateral spreading models.

In addition to the lateral stress near the pile, it is also of interest to observe the distribution of lateral stresses in the remainder of the soil system. The lateral stresses in the liquefied layer remain relatively small during the simulated lateral spreading event, however, the imposed ground motion causes large compressive and tensile stresses to develop in the solid soil layers at the boundaries of the model. These zones of increased stress are higher near the symmetry plane. Though these distributions are most certainly at least partially due to the boundary and loading conditions imposed upon the model, these results suggest that the pile is able to influence a far wider area than just its immediate vicinity during a lateral spreading event.

Figure 5.2 shows a series of plots that detail exactly how the lateral spreading ground motion affects the embedded pile. This figure presents results obtained from the same 0.61-m-pile case as the lateral stress distribution shown in Figure 5.1, the entirely linear elastic, free pile head case. This series of summary plots illustrates the general pattern of shear force and bending moment demands that develop in a pile during a lateral spreading event, as well as the deflected shape of the pile. All of the piles display distributions of bending demands that are similar in form to the general shapes presented here.

The maximum shear force demand occurs at the center of the liquefied layer, depicted as the shaded region in Figure 5.2, where the differential motions of the two solid layers are felt most strongly by the pile, and minimal resistance is provided by the liquefied soil. It can be expected that in any lateral spreading event, the largest shear force demand will occur at, or very near, this location. There are also extreme values of shear in each of the two solid layers, located approximately two-thirds of the total layer thickness away from the interface with the liquefied layer. The extreme shear demand in the lower layer is greater due to the increase in confining stress with depth.

The locations of minimum moment occur at the center of the liquefied layer, where there is zero moment, and due to the boundary condition of this model, at each end of the pile, where the moment is also zero. The extreme moments in the pile correspond to the locations of zero shear force, with one maximum in each of the unliquefied soil layers. The absolute maximum moment occurs in the lower solid layer. As with the extreme shear force demand in that layer, the extreme moment demand here is larger than the extreme value in the upper layer due to the increased overburden pressure with depth. The locations of the extreme moments in each layer tend to stay relatively constant in this entirely linear elastic model. The distance between these locations defines an effective length, L_{eff} , for the pile, as shown schematically in Figure 5.3. The effective length is a parameter signifying, in part, the influence of the liquefied layer on the pile. The effective length is a convenient parameter to use in simplified analyses of the lateral spreading problem, as well as a useful parameter for comparing the results for the various pile sizes.

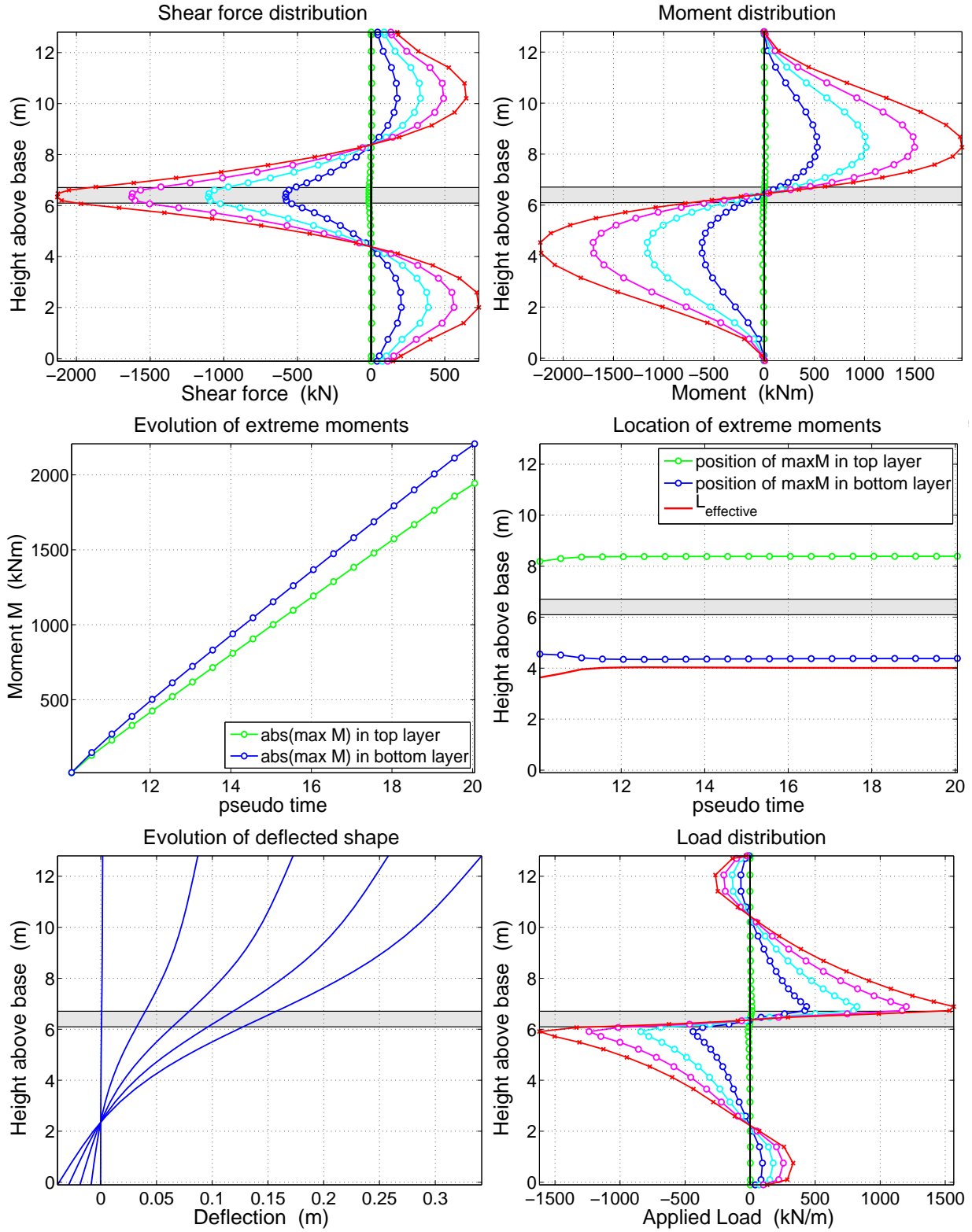


Figure 5.2 Pile summary plots for a 0.61-m-diameter pile. Series 1, free-head case. The liquefied layer is the shaded region.

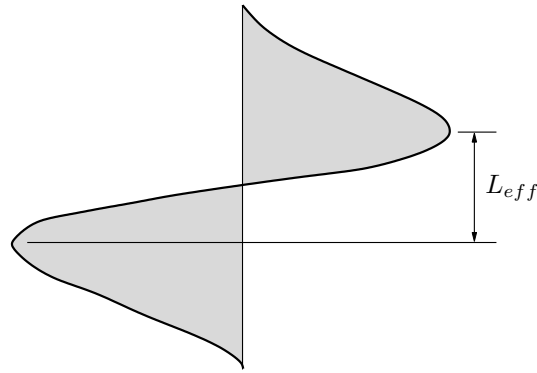


Figure 5.3 The effective length, L_{eff} , is the distance between the extreme moments in each solid soil layer, as shown in this moment diagram.

In addition to the plots related to the deformation and bending demands in the pile, Figure 5.2 also shows the distribution of load imposed upon the pile by the lateral flow of the upper soil layer. This plot of the load distribution on the pile is determined from the slope of the shear diagram using the familiar relation

$$\frac{dV}{dx} = -w(x) \quad (5.1)$$

in which $w(x)$ is the distributed load and V is the shear force. The plot of the load distribution provides a insight into how the displacement of the surrounding soil manifests as load acting upon the pile and corresponds well to the distribution of lateral stress in the soil, as shown in Figure 5.1. The magnitude and shape of this load profile varies from pile to pile and also shows a dependence on the constitutive models used to represent the pile and the soil, though the shape presented in Figure 5.2 is indicative of the general shape resulting from each case.

It is also observed that the liquefied layer of soil affects the behavior of the solid soil layers. The degree of this influence depends upon a few factors, including the stiffness of the pile and the constitutive model used for the soil. Additionally, the degree of influence of the liquefied layer on the soil near its boundaries is most significant in the vicinity of the pile, becoming less apparent as distance from the pile increases. The cases with elastoplastic soils exhibited an increased amount of interaction between the unliquefied and liquefied soil layers, with the unliquefied layers being pushed into the weaker liquefied layer. Figure 5.4 shows the pile pushing the unliquefied (dark) soil elements into the liquefied (light) layer for the Series 4 case for a 0.61-m-diameter pile. The motion of the upper layer is to the right. As shown, this behavior occurs on either side of the pile in the areas in which the pile is cutting into the soil. In addition to the push-out observed on the leading edges of the pile, there is significant gapping taking place on the trailing edges of the pile, leading to the evident mesh distortion.

The behavior displayed in Figure 5.4 during the lateral spreading motion lessens the amount of lateral resistance that can be provided by the soil in the area surrounding the liquefied layer. The unliquefied soil can be pushed into the adjacent weaker layer more easily than it can be pushed into the adjacent solid soil elements or flow around the pile, effectively reducing the strength and stiffness of the unliquefied soil near the liquefied layer. This reduction in resistance can significantly alter the behavior of the pile, causing increased curvature demands and increasing the potential for

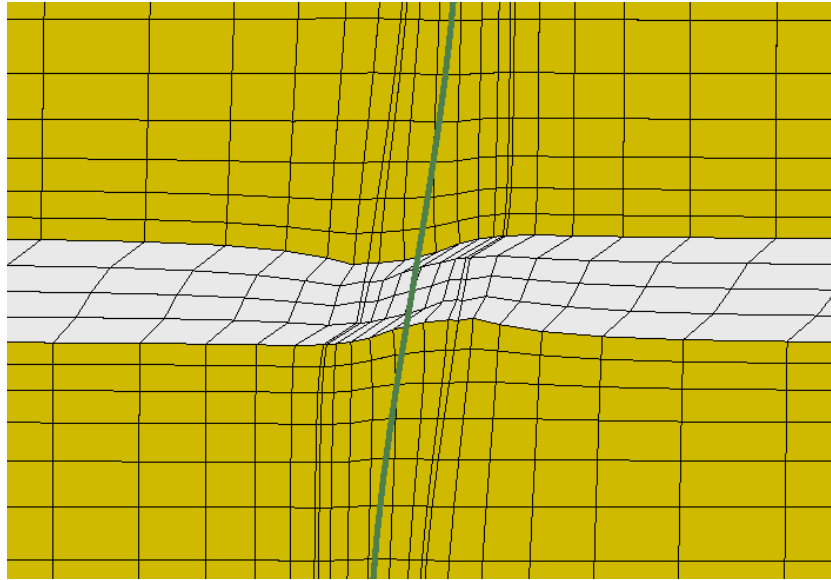


Figure 5.4 Soil deformation pattern in the vicinity the pile for the Series 4 case highlighting the unliquefied soil elements pushing into the liquefied layer.

the formation of plastic hinges. Additionally, this reduction in soil strength results in a smaller effective length for the pile, which results in an increased moment and curvature demand on the pile and a corresponding increase in the potential for pile failure due to the lateral spreading event.

5.4 SUMMARY OF RESULTS FROM THREE-DIMENSIONAL LATERAL SPREADING SIMULATIONS

A small parametric study consisting of 24 distinct cases is conducted using the 3D lateral spreading model. There are three pile designs included in the study, each with elastic and elastoplastic constitutive formulations. These piles are given two separate boundary conditions: a fixed pile head condition and a free pile head condition. There are two soil constitutive models incorporated into the study, one linear elastic and the other an elastoplastic Drucker-Prager model. In all of the simulations the liquefied layer is assigned a thickness of one pile diameter, this layer is centered between two 10 pile diameter thick unliquefied soil layers; and the lateral displacement of the upper unliquefied layer with respect to the lower layer is one pile radius.

The results of all 24 lateral spreading cases are summarized in Tables 5.2, 5.3, and 5.4 for the 2.5-m, 1.37-m, and 0.626-m piles, respectively. These tables list the maximum values of shear force, $\max V$, moment, $\max M$, curvature, $\max \phi$, and displacement, $\max U$, for the pile, as well as the effective length, L_{eff} . The data in these tables is separated based upon the particular parameters and constitutive models used in each of four Series, as well as by the fixity of the pile head in each simulation. The specifics of each of the four Series are summarized in Table 5.1.

From the results presented in Tables 5.2, 5.3, and 5.4, a few behavioral trends are observed. The stiffness of the pile, or more importantly the ratio of the pile stiffness to the lateral stiffness of the

Table 5.2 Summary of 3D lateral spreading analyses for the 2.5-m-diameter pile.

Pile-Soil Type	max V (kN)	max M (kNm)	max ϕ (m ⁻¹)	max U (m)	L_{eff} (m)
Series 1: Free	46100	235500	0.0012	1.47	17.62
Series 2: Free	40600	186600	0.0021	1.43	16.19
Series 3: Free	54000	300500	0.0015	1.57	16.14
Series 4: Free	48800	227200	0.0036	1.51	15.11
Series 1: Fixed	53500	389500	0.0020	1.27	35.51
Series 2: Fixed	42600	195500	0.0023	1.30	18.32
Series 3: Fixed	63200	393500	0.0020	1.30	18.77
Series 4: Fixed	50900	230100	0.0039	1.33	15.96

Table 5.3 Summary of 3D lateral spreading analyses for the 1.37-m-diameter pile.

Pile-Soil Type	max V (kN)	max M (kNm)	max ϕ (m ⁻¹)	max U (m)	L_{eff} (m)
Series 1: Free	10600	24300	0.0049	0.76	8.12
Series 2: Free	5070	6460	0.0191	0.73	5.17
Series 3: Free	12000	30600	0.0061	0.80	7.54
Series 4: Free	4970	6575	0.1046	0.69	4.74
Series 1: Fixed	10800	24900	0.0050	0.71	8.47
Series 2: Fixed	5076	6467	0.0190	0.71	5.16
Series 3: Fixed	12500	31000	0.0062	0.73	7.65
Series 4: Fixed	4969	6574	0.1045	0.69	4.74

Table 5.4 Summary of 3D lateral spreading analyses for the 0.61-m-diameter pile.

Pile-Soil Type	max V (kN)	max M (kNm)	max ϕ (m ⁻¹)	max U (m)	L_{eff} (m)
Series 1: Free	2130	2228	0.0095	0.34	3.63
Series 2: Free	1200	804	0.0248	0.32	2.66
Series 3: Free	2027	2569	0.0109	0.38	3.62
Series 4: Free	1258	981	0.0443	0.31	2.86
Series 1: Fixed	2196	2293	0.0097	0.32	3.83
Series 2: Fixed	1198	805	0.0249	0.31	2.65
Series 3: Fixed	2200	2592	0.0110	0.33	3.74
Series 4: Fixed	1258	981	0.0445	0.31	2.86

soil, plays a significant role in defining the interaction between the piles and the soil. This is manifested not only in the observation that increased pile capacity leads to increased bending demands, but also in the way in which the dependent variables from each Series relate to those from the other Series for each respective pile. The fixity of the pile head also affects the resultant behavior of the soil-pile system during the lateral spreading event, though certain trends are consistent in both the free-head and fixed-head cases.

The degree of plasticity incorporated into the models also plays a significant role in the resultant behavior of the soil-pile system. Comparison between the Series 1 and 2 cases gives a feeling for what happens when the piles yield. Similarly, comparison between the Series 1 and 3 data allows the effects of soil plasticity to be analyzed. The fully elastoplastic cases of Series 4 offer observations into the behavior of the soil-pile system when elements in each medium display plastic behavior. These observations are discussed in further detail in the subsequent sections.

5.4.1 The Effects of Pile Stiffness on the Soil-Pile System

As the size of the pile increases, so does the bending stiffness, EI , of the pile. The bending stiffness of the pile is an important factor in defining how a pile reacts to a lateral spreading event. More important, perhaps, is the ratio of the pile bending stiffness to the lateral stiffness provided by the soil. For large pile-to-soil stiffness ratios, the behavior of the soil-pile system during a lateral spreading event is governed primarily by the pile. Conversely, as this ratio becomes smaller, the influence of the soil becomes more apparent in the overall behavior of the system. The piles can no longer cut easily into the soil, instead the soil is able to resist the piles, increasing the curvature demand and altering the locations of the maximum moments.

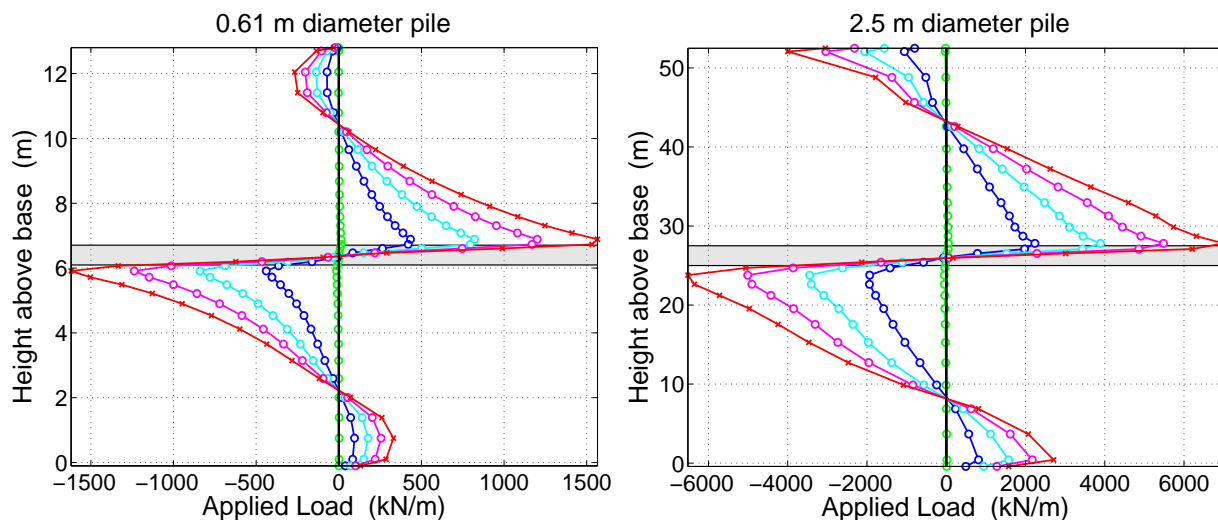


Figure 5.5 Load distributions resulting from the lateral spreading ground motion for the free-head Series 1 cases for 0.61-m and 2.5-m-diameter piles.

The load distribution plots of Figure 5.5, which show the loading applied to the pile by the imposed lateral spreading displacement for the Series 1 free pile head cases for 0.61-m and 2.5-m-diameter piles, typify the differences between small and large pile-to-soil stiffness ratios. It is important to note that the load distributions shown in Figure 5.5 are the loads that are felt by the piles over their respective lengths. These loads are the result of both the soil pushing against the pile in the upper layer and the pile pushing against the soil in the lower layer. If the pile-to-soil stiffness ratios for each model were set to be equal, the resulting load distributions would be identical despite the increased size of the larger pile.

For the 0.61-m-diameter pile, which has a relatively small stiffness ratio, the magnitude of the load applied by the surrounding soil is much smaller than it is for the 2.5-m-diameter pile.

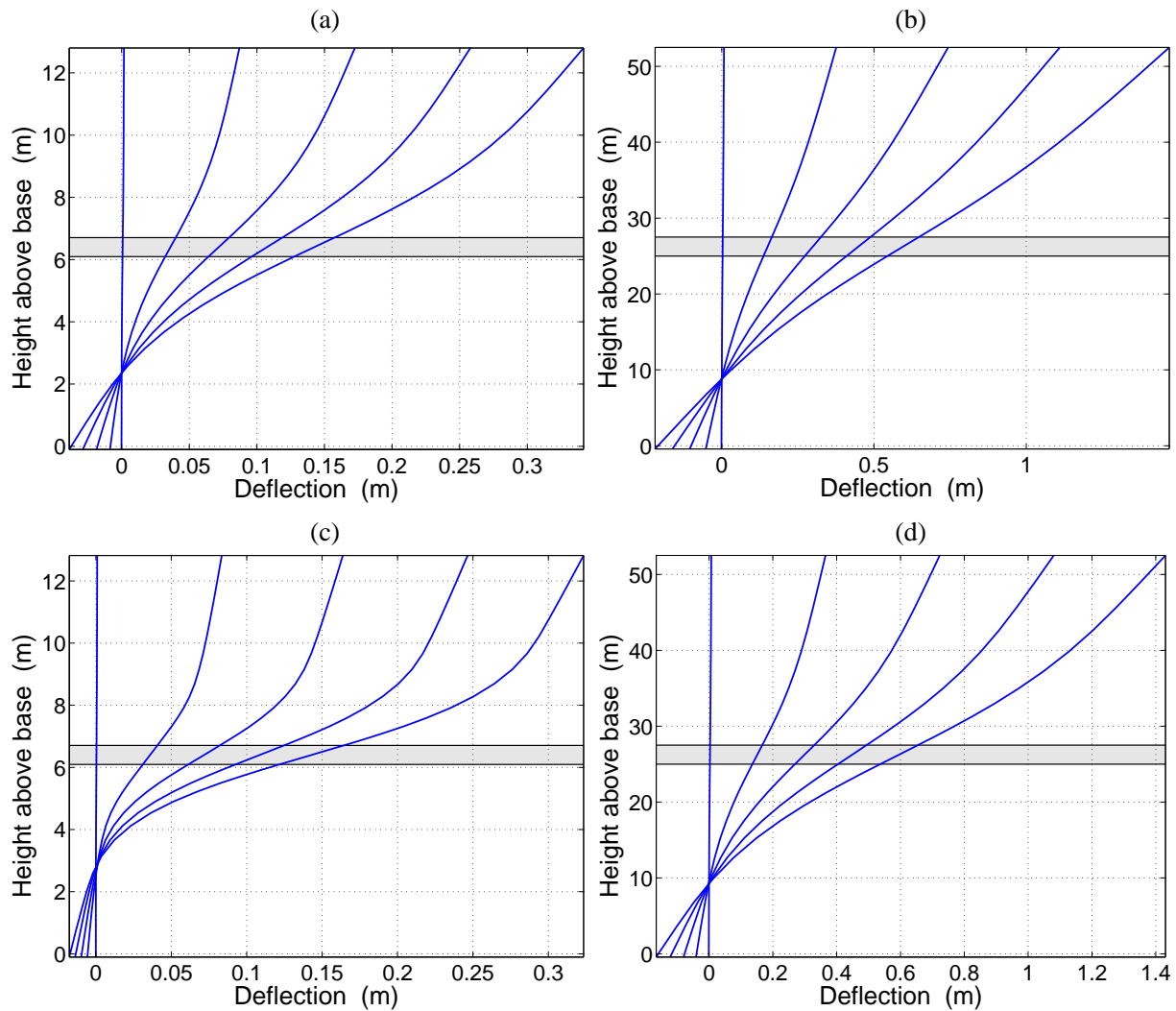


Figure 5.6 Deflected shapes of free-head piles for various cases. (a) Series 1, 0.61-m-diameter; (b) Series 1, 2.5-m-diameter; (c) Series 2, 0.61-m-diameter; (d) Series 2, 2.5-m-diameter.

This indicates that the stiffer 2.5-m-diameter pile is cutting further into the soil, activating more resistance from the surrounding soil elements. This is confirmed by the displaced shapes for these two piles shown in Figure 5.6. In the entirely linear elastic Series 1 case shown in Figure 5.6(b), the 2.5-m-diameter pile remains almost straight during the deformation due to its high stiffness ratio. The corresponding case for the 0.61-m-diameter pile shown in Figure 5.6(a) displays visible curvature, indicating that the soil imposes larger curvature and bending demands on the pile with the smaller pile-to-soil stiffness ratio.

The elastoplastic pile in elastic soil Series 2 cases of Figures 5.6(c) and (d) accentuate this observation. Even with elastoplastic pile elements creating the potential for plastic hinge formation, the displaced shape of the stiffer pile remains essentially straight and is much further from the imposed displacement profile than the softer pile, providing verification that this trend is not isolated to the entirely elastic cases.

The effects of the pile-to-soil stiffness ratio can also be seen in the locations of the maximum moments for each of the piles. As depicted in Figure 5.2 for a 0.61-m-diameter pile, the maximum moments occur somewhat beyond the extents of the liquefied layer. The ratio of the effective length of the pile, which is the distance between the maximum moments, to pile diameter decreases as the stiffness ratio decreases. This normalized comparison indicates that the maximum moments become closer together as the pile-to-soil stiffness ratio decreases, thus creating a larger curvature demand and a proportionally larger moment and shear demand in the pile.

The larger the ratio of a pile's bending stiffness to the lateral stiffness of the soil in which it is embedded, the more the pile controls the overall behavior of the laterally spreading soil-pile system. Larger, stiffer, piles are better able to cut into the soil during the lateral spreading event. As the pile pushes further into the soil, this leads to an increased potential for yielding in the soil. Additionally, the larger the stiffness ratio becomes, the larger the potential for push-out of the solid soils into weaker adjacent layers becomes.

A larger pile-to-soil stiffness ratio also sees increased interaction between the unliquefied and liquefied layers. For a given soil stiffness, more unliquefied material is pushed into the liquefied layer for a stiffer pile. The free surface at the top of the model sees similar behavior. As shown in Figure 5.7, the soil is pushed out above the ground surface by the pile. The magnitude of this soil heave increases with increasing stiffness ratio. As more unliquefied material is pushed into both the free surface at ground level and the liquefied interface, the soil becomes less able to resist the motion of the pile in those areas, increasing the pile deflections and the potential for failure of the pile head connection during a lateral spreading event.

5.4.2 The Effects of Pile Head Fixity

The fixed pile head condition simulates a rigid pile cap or other structure affixed to the top of the pile, preventing the pile head from rotating. The free-head cases represent the opposite end of the spectrum, piles which are not subject to significant rotational resistance at the pile head connection. In actual applications, the support or connection at the pile head will likely fall somewhere between these two extremes, although the condition is often closer to the fixed-head piles than not.

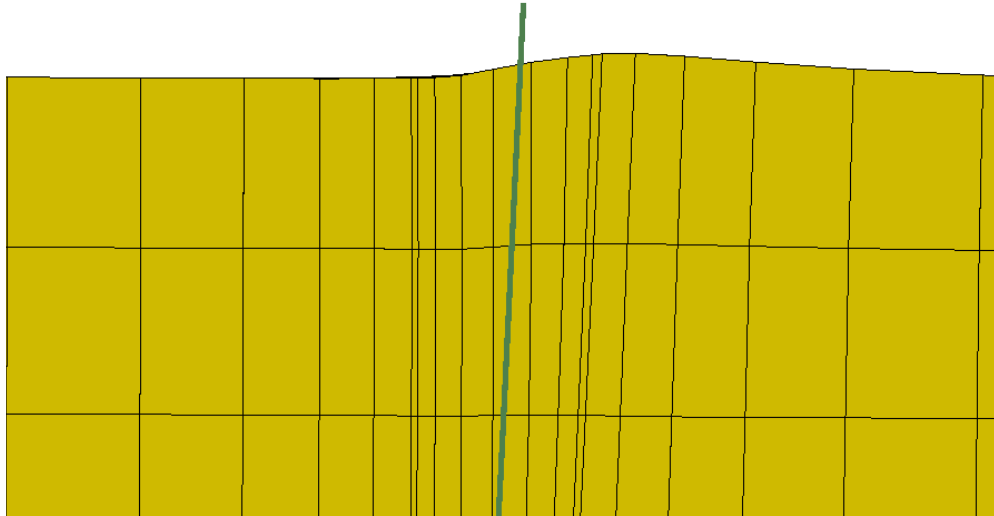


Figure 5.7 Upward heave of soil elements at the ground surface for the Series 4 case with a 2.5-m-diameter pile (magnification factor = 1).

For all three pile diameters, the inclusion of a fixed pile head into the lateral spreading model results in maximum moment and shear force demands that are greater than, or approximately equal to, the demands resulting from the corresponding free-head cases. The magnitude of the difference between these extreme values is related to the pile-to-soil stiffness ratio. For the 2.5-m-diameter pile, which has a large stiffness ratio, the relative difference between the maximum demands for the fixed-head and free-head piles are significantly larger for all analysis Series. For the other two piles, which have relatively smaller pile-to-soil stiffness ratios, the differences are less significant.

The addition of in-plane rotational fixity at the pile head increases the amount of curvature in the pile in this layer, thus increasing the magnitude of the resulting extreme moment. Additionally, for larger stiffness ratios, the inclusion of a fixed pile head not only increases the extreme moment in the upper solid layer of soil, it shifts the absolute maximum moment from below the liquefied layer, where it was located in the free-head cases, to above the liquefied layer. The moment diagrams of Figure 5.8 demonstrate this observation. For a 2.5-m-diameter pile, the largest curvature demand occurs at the fixed pile head and the absolute maximum moment occurs at this point. For a 1.37-m-diameter pile, which has a smaller pile-to-soil stiffness ratio, a large curvature demand occurs at the fixed head; however, the soil in the lower unliquefied layer imposes a larger demand, resulting in the absolute maximum moment demand remaining below the liquefied layer.

The deflected shapes of each pile shown in Figure 5.8 support this observation. The lower half of the 2.5-m-diameter pile remains almost perfectly straight throughout the lateral spreading deformation while there is visible curvature at the top of the pile due to the pile head fixity. For the softer 1.37-m-diameter pile, there is visible curvature occurring in both the upper and lower portions of the pile and the bending demand in the upper portion is due to a combination of the pile head condition and the imposed soil deformation. In design applications, it would be conservative to assume a fixed-type pile head condition if there is any indication that the pile may be less apt to rotate at that location. Considerations to this end become increasingly important for cases with large pile-to-soil stiffness ratios.

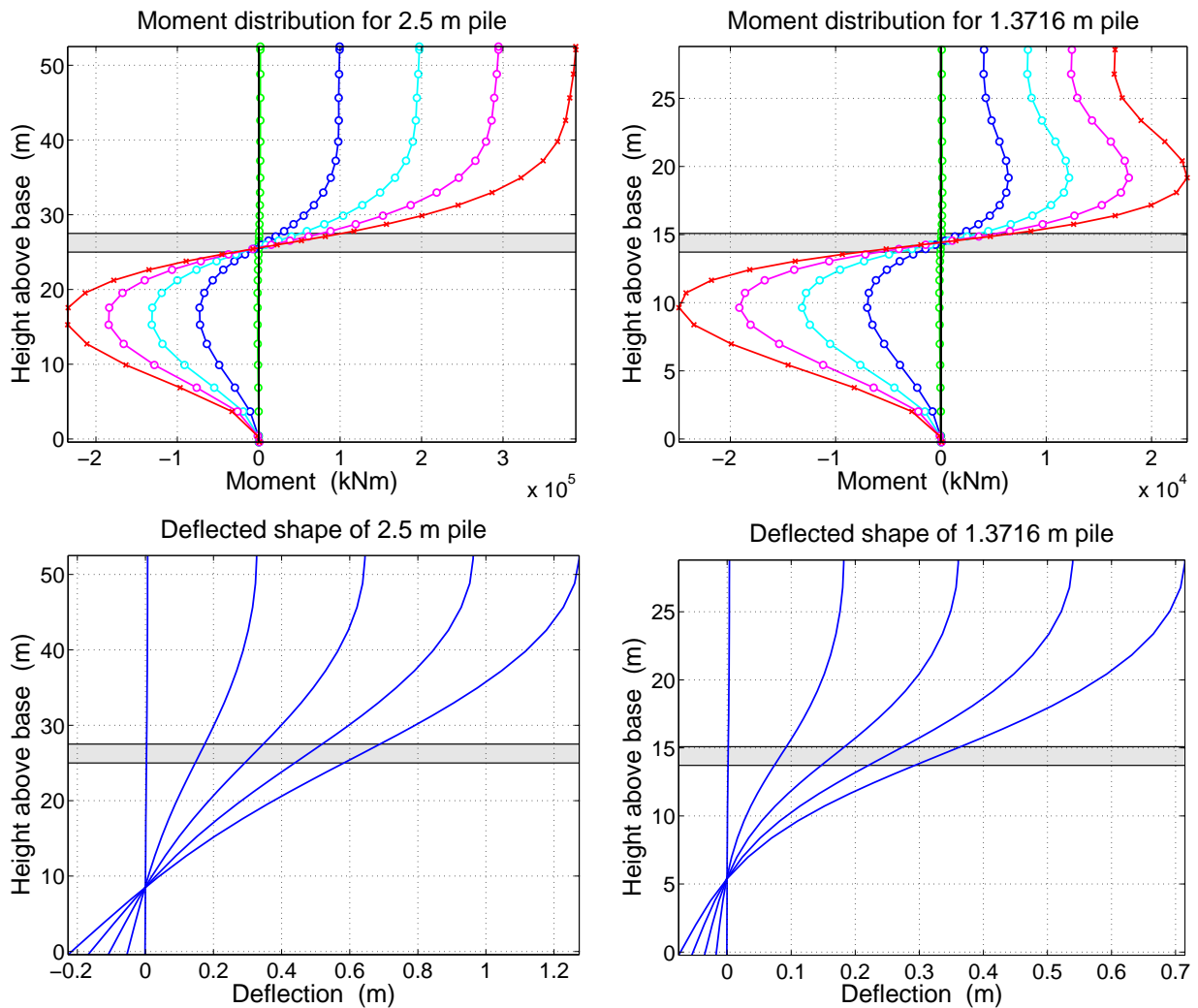


Figure 5.8 Moment distributions and deflected shapes for the fixed-head Series 1 cases with 2.5-m and 1.37-m-diameter piles.

Another interesting observation to be made with regards to the pile head fixity is the location of the extreme moments for the fixed-head cases. With the exception of the Series 1 case for the 2.5-m-diameter pile shown in Figure 5.8, the extreme moment in the upper soil layer is not located at the pile head. The magnitude of the moment at the pile head is not zero in these cases, but it is not the largest value in the upper layer. Instead, the extreme moment is located further down in the layer, near the boundary of the liquefied layer, in a similar location as found in the free-head cases. In the single case in which the extreme upper moment is located at the pile head, the combination of the large pile-to-soil stiffness ratio and fact that the elastic soil is able to continuously pick-up load results in the boundary condition, rather than the lateral layer motion, thereby imposing the largest curvature demand on the pile. In all of the other cases, the fixity at the pile head causes the extreme moment in the upper layer to move slightly upward, while affecting little or no change in the location in the extreme moment in the lower layer.

5.5 THE EFFECTS OF PLASTICITY ON THE LATERALLY SPREADING SYSTEM

Including plasticity in the constitutive models for either the piles or the soil creates a limit on the amount of stress that can build up in either component of the lateral spreading system. When the pile yields, plastic hinges develop, exacerbating the effects of the lateral spreading deformation on the pile. Similarly, when the soil surrounding the pile yields, no further resistance is offered against the passage of the pile, leading to increased bending demands.

5.5.1 The Effects of Pile Plasticity

When the pile models are assigned elastoplastic behavior, as in analysis Series 2 and 4, certain new trends develop in the behavior of the laterally spreading soil-pile system. In general, the cases run with elastoplastic pile models display smaller extreme moment and shear demands than their elastic-pile counterparts. Additionally, the locations of the extreme moments in each of the solid soil layers move closer to the boundary of the liquefied layer, leading to a significant reduction in the effective length of the pile. These general trends are present for all three piles and for both boundary conditions.

The decrease in the maximum moment and shear force magnitudes is attributed to the inelastic behavior in the piles. The bending stresses in the piles due to the lateral spreading ground motion are significant enough to cause the piles to leave their respective elastic ranges, leading to a reduced pile-to-soil stiffness over time. The reduction in this ratio indicates that more of the stress generated by the imposed displacement profile is carried by the soil elements. The lower stiffness ratio also indicates that the soil controls more of the behavior of the entire system, resulting in piles that experience far more deformation than in the elastic-pile cases.

In the elastoplastic pile cases, the piles not only experience more deformation than in the elastic pile cases, this deformation is concentrated over a smaller length of the pile. Essentially, the lateral spreading ground deformation causes two plastic hinges to develop in the pile. This is illustrated in Figures 5.6(a) and 5.6(c), which show the deflected shapes for the free-head 0.61-m-diameter pile cases for Series 1 and 2, respectively. Compared to the entirely linear elastic case, where the deformation is spread out over most of the pile, the deflected shape of the the Series 2 case shows that the curvature demand is focused in two areas, one in each solid soil layer. The tendency for the pile to become inelastic allows the soil to control the system, leading to a deformed shape that is closer to the imposed displacement profile.

5.5.2 The Effects of Soil Plasticity on the Pile

To evaluate the effects of considering plastic behavior in the soil on the behavior of the pile, the results of Series 1 and 3 are compared. Series 1 considers both the pile and soil to be elastic, while Series 3 considers the pile to be elastic and the soil to be elastoplastic. For each pile and boundary condition combination, any differences between the results of Series 1 and 3 can be assumed to be attributable to the plastic behavior of the soil elements.

To illustrate the differences between these two cases, a 0.61-m-diameter pile is used. This pile has the lowest pile-to-soil stiffness ratio of the three piles and therefore shows the effects of plastic soil in the most dramatic visual fashion, although the observations made for this pile are consistent across all three pile sizes. The results of the Series 3, free-head, analysis for the 0.61-m-diameter pile are shown in Figure 5.9. The plots shown are actually fairly similar to the corresponding plots for the Series 1 analysis shown in Figure 5.2, however there are some differences in certain behaviors. The general shape of the shear, moment, and load diagrams are unchanged across the two cases, although the results of the soil going plastic are evident in the more rounded shape of the load distribution. Additionally, the effects of yielding in the soil can be seen in the evolution of the extreme moments in each layer. In the Series 1 case, the moments grow in an almost linear fashion, while in the Series 3 case there is visible nonlinearity in the moment history.

The main difference between the two cases is the increase in maximum moment observed in the case with elastoplastic soil elements. The maximum moment in the entirely elastic case is 2228 kNm. In the elastic pile with elastoplastic soil case, the maximum moment increases to 2569.3 kNm. The locations of the extreme moments in each layer also differ between the Series 1 and 3 cases, with a larger effective length present for the elastic soil than that returned for the elastoplastic soil.

This increase in maximum moment for the elastoplastic soil is not limited to the free-head, 0.61-m-diameter pile cases. Similar increases in $\max M$ between the Series 1 and 3 results are also evident for both the 2.5-m and 1.37-m-diameter piles. Interestingly, as the pile-to-soil stiffness ratio becomes larger, the increase in maximum moment becomes more significant. For larger pile-to-soil stiffness ratios, the pile has an increased capacity for stress as compared to the soil, suggesting the presence of a stress transfer from the soil to the pile in the elastoplastic soil cases. The same type of increase in maximum moment occurs regardless of the pile head fixity, and is also evident between the Series 2 and 4 cases where the piles are elastoplastic, though the corresponding decrease in L_{eff} is not observed for the elastoplastic pile cases for the 0.61-m-diameter pile.

5.6 VERIFICATION MODELS FOR PILE BEHAVIOR IN ELASTOPLASTIC SOIL

In a traditional simplified analysis of a pile during a lateral spreading event, the pile is modeled as a fixed-fixed beam of length L_{eff} undergoing a set end displacement. In this model, the length of the beam is commonly estimated as the thickness of the liquefied layer combined with a prescribed embedment length on either side of the liquefied layer. Using this approach, which is sometimes favored by structural designers, the maximum moment occurring at either end of the pile is estimated as

$$\max M = \frac{6EI\Delta}{L_{eff}^2} \quad (5.2)$$

where EI is the bending stiffness of the pile, L_{eff} is the effective length of the pile, and Δ is the displacement at the end of the beam. If this model is correct, then it would be expected that an increase in L_{eff} would correspond to a decrease in the maximum moment, just as is observed in the 3D simulations. This approach is overly simplistic, however, and can lead to poor design solutions. The two simple beam models discussed in this section attempt to model the lateral

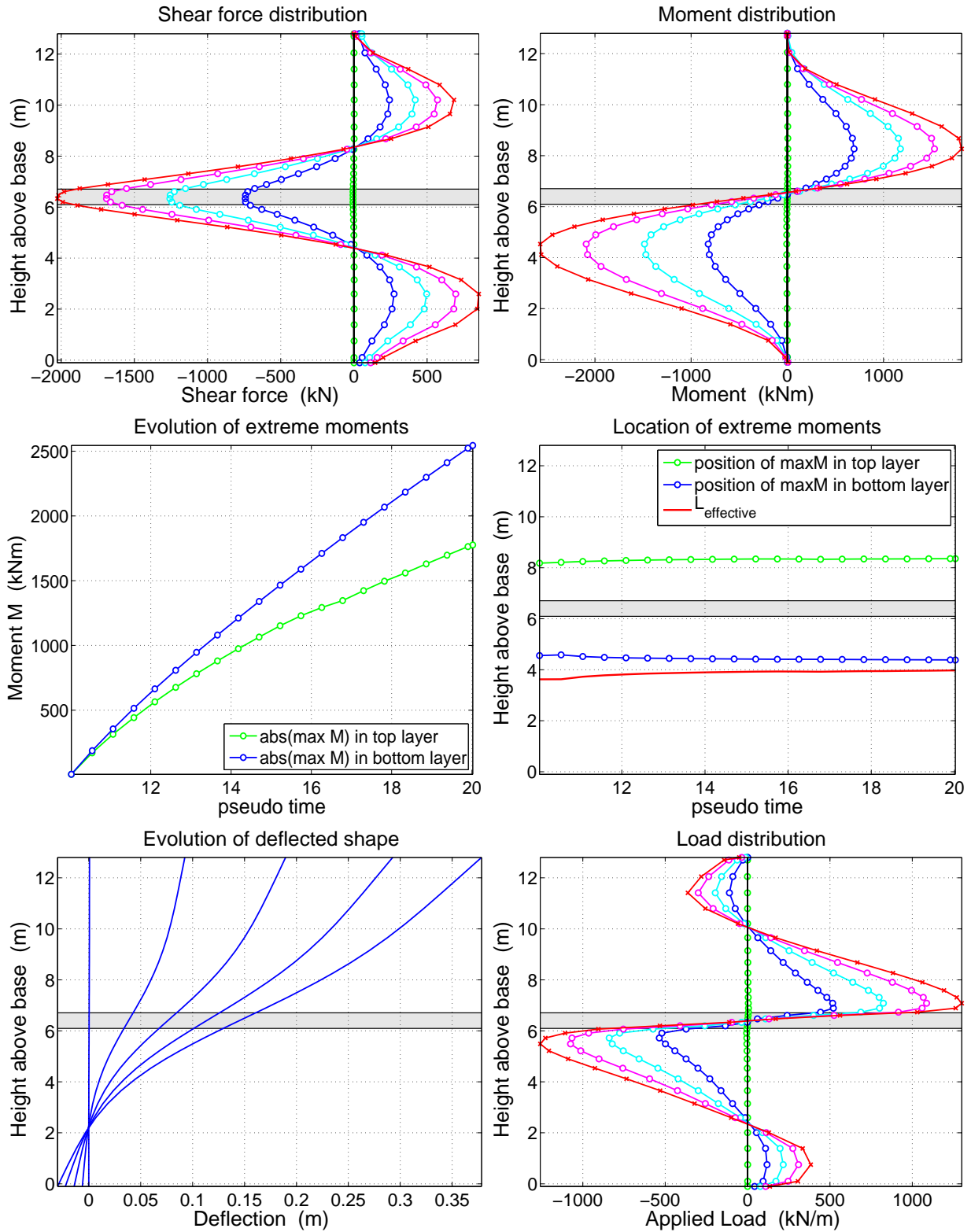


Figure 5.9 Pile summary plots for a 0.61-m-diameter pile. Series 3, free-head case. The liquefied layer is the shaded region.

spreading problem in a more accurate manner in order to verify observed behaviors and to gain a better understanding of the problem in general.

The two simple models are shown in schematic form in Figure 5.10. The beams are fixed at one end and have a slider capable of resisting rotations but not displacements at the opposite end. Each model is has a unique load distribution, $w(x)$, which approximates the lateral spreading load case with varying degrees of complexity. These models provide a more reasonable approximation of the type of loading that a pile embedded in laterally spreading soil would experience, while remaining simple enough to solve by hand. It is of interest to determine the relationship between the magnitude of the applied loading, represented by p in the models, and both the effective length of the beams and the maximum moment in the beams for a given constant end displacement.

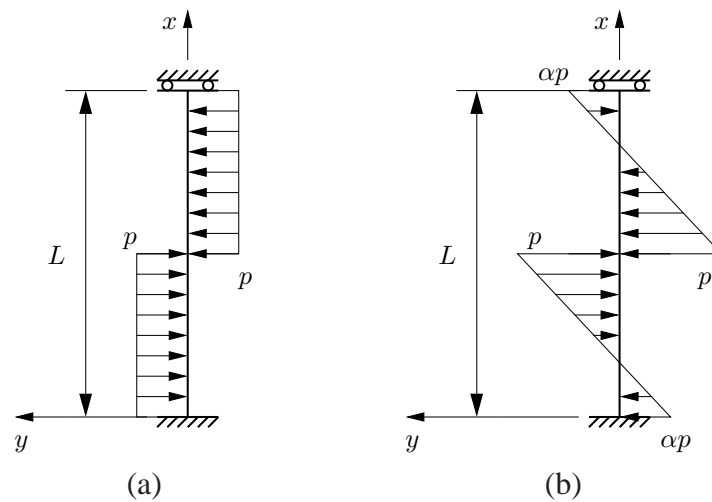


Figure 5.10 The two simple beam models used for verification of results. (a) The first simple model. (b) The second simple model.

5.6.1 The First Simple Model

The first simple beam model, depicted in Figure 5.10(a), is similar to the fixed-fixed model discussed previously in that it models a beam having a length equal to the effective length of the pile. This means that the maximum moments are located at the ends of the beam, while the shear force at those locations is zero. The shear force will have a maximum at mid-span, while the moment at the middle of the beam should be zero. This model essentially represents the region of the pile located between the maximum moments, and does not consider the regions of the pile that are outside of this central region.

The loading assigned to the first simple beam model is a constant distributed load that changes sign at mid-span. Due to the discontinuity in the loading, the applied load must be represented as two separate equations, one for each half of the beam, necessitating that the beam be solved in two

sections. For this model, the governing differential equation of bending can be written as

$$EI \frac{d^4 v}{dx^4} = \begin{cases} -w_1(x) = -p & \text{for } 0 < x < \frac{L}{2} \\ -w_2(x) = p & \text{for } \frac{L}{2} < x < L \end{cases} \quad (5.3)$$

These expressions can then be solved in order to obtain the displacement of the beam under the prescribed load case. The following expressions result from integrating Equation (5.3).

$$EI v_1(x) = -\frac{p}{24}x^4 + \frac{c_1}{6}x^3 + \frac{c_2}{2}x^2 + \frac{c_3}{2}x + c_4 \quad (5.4a)$$

$$EI v_2(x) = \frac{p}{24}x^4 + \frac{c_5}{6}x^3 + \frac{c_6}{2}x^2 + \frac{c_7}{2}x + c_8 \quad (5.4b)$$

In order to solve for the eight unknown constants, four boundary conditions and four compatibility conditions must be enforced. These boundary conditions are

$$v_1(x=0) = 0 \quad (5.5a)$$

$$\left. \frac{dv_1}{dx} \right|_{x=0} = 0 \quad (5.5b)$$

$$\left. \frac{dv_2}{dx} \right|_{x=L} = 0 \quad (5.5c)$$

$$V_L = EI \left. \frac{d^3 v_2}{dx^3} \right|_{x=L} = 0 \quad (5.5d)$$

The compatibility conditions, which describe the relationship between the two halves of the beam at the point where they meet, can be expressed as

$$v_1\left(x = \frac{L}{2}\right) = v_2\left(x = \frac{L}{2}\right) \quad (5.6a)$$

$$\left. \frac{dv_1}{dx} \right|_{x=\frac{L}{2}} = \left. \frac{dv_2}{dx} \right|_{x=\frac{L}{2}} \quad (5.6b)$$

$$M_{1,L/2} = EI \left. \frac{d^2 v_1}{dx^2} \right|_{x=\frac{L}{2}} = EI \left. \frac{d^2 v_2}{dx^2} \right|_{x=\frac{L}{2}} = M_{2,L/2} \quad (5.6c)$$

$$V_{1,L/2} = EI \left. \frac{d^3 v_1}{dx^3} \right|_{x=\frac{L}{2}} = EI \left. \frac{d^3 v_2}{dx^3} \right|_{x=\frac{L}{2}} = V_{2,L/2} \quad (5.6d)$$

Applying the boundary and compatibility conditions of Equations (5.5) and (5.6), the unknown constants in Equation (5.4) can be determined. This results in the following expression for the

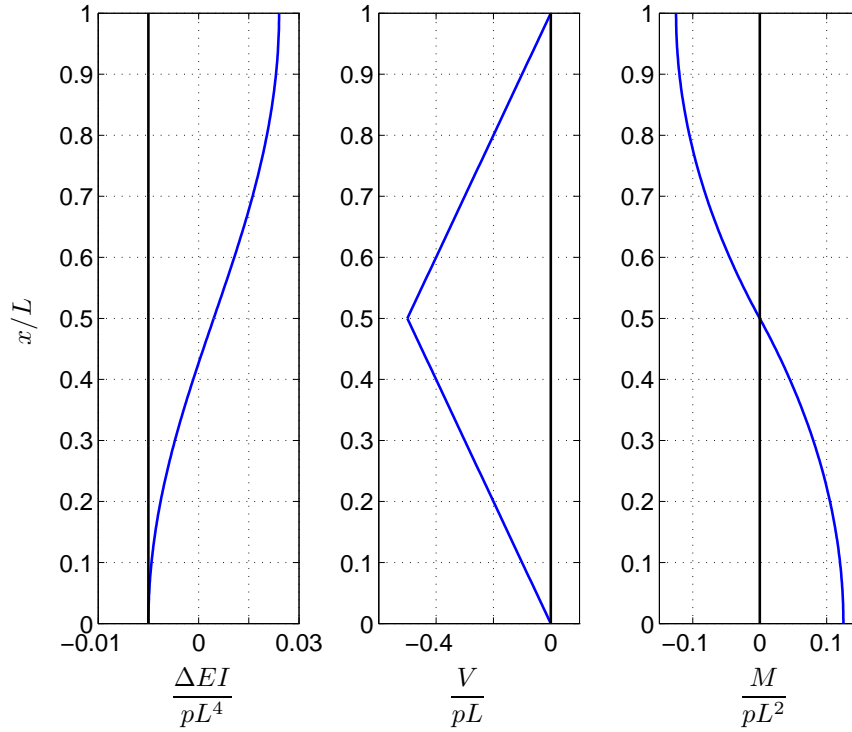


Figure 5.11 Displaced shape, shear diagram, and moment diagram for the first simple model.

displacement in the beam for the first simple model

$$v_1(x) = \frac{pL^4}{48EI} \left[3 \left(\frac{x}{L} \right)^2 - 2 \left(\frac{x}{L} \right)^4 \right] \quad (5.7a)$$

$$v_2(x) = \frac{pL^4}{192EI} \left[8 \left(\frac{x}{L} \right)^4 - 32 \left(\frac{x}{L} \right)^3 + 36 \left(\frac{x}{L} \right)^2 - 8 \left(\frac{x}{L} \right) + 1 \right] \quad (5.7b)$$

The displaced shape for the first simple model described by Equation (5.7), along with the corresponding expressions for the moment and shear in the beam, are plotted in Figure 5.11 using the shown dimensionless parameters. As shown, the maximum moments in the beam occur at the boundaries of the model and the maximum shear force occurs in the middle. This coincides with the intention of the first simple model to represent only the effective length, L_{eff} , of the pile subjected to the lateral spreading load case.

The maximum displacement, as shown in Figure 5.11, occurs at the position $x = L$. Substituting this into Equation (5.7b) defines the end displacement, Δ , as

$$\Delta = v_2(L) = \frac{5pL^4}{192EI} \quad (5.8)$$

where p is the magnitude of the applied load, EI is the beam stiffness, and L is the beam length. Recalling that for this simple model, the length of the beam is equal to the effective length, L_{eff} ,

for the lateral spreading load case, Equation (5.8) can be rearranged in order to obtain an expression for the effective length of the beam in terms of Δ , p , and EI .

$$L_{eff} = \left(\frac{192EI\Delta}{5p} \right)^{0.25} \quad (5.9)$$

The maximum moment in the beam can be determined in a similar manner. Evaluating the moment equation at $x = L$ gives an expression for the absolute value of the maximum moment in the beam of the form

$$\max M = \frac{pL^2}{8} \quad (5.10)$$

The expressions developed in Equations (5.9) and (5.10) can be used to explore the relationships between the effective length and maximum moment of the beam with the magnitude of the applied load.

5.6.2 The Second Simple Model

The second simple model expands the relatively basic concept behind the first model to include a beam that represents the entire length of the pile in the lateral spreading model and a distributed loading that varies in magnitude with position. The second simple beam model is schematically depicted in Figure 5.10(b). In a way, this model is a rough approximation of the load distribution resulting from the imposed displacement profile of the 3D lateral spreading model in the cases where the piles are entirely elastic. Notice the similarity of this assumed distribution to that returned from the 2.5-m-diameter pile in elastic soil shown in Figure 5.5.

As with the first model, the base of the beam is fixed while the opposing end of the beam is assigned a slider. In the second simple beam model, the maximum moment will not occur at the ends of the beam, instead, the moment should be zero at the ends. The maximum moment will occur at some location between the mid-span and end of the beam, with the exact location depending upon the assigned beam and load parameters. The shear force in the beam should still be zero at the ends and have a maximum at the center of the beam.

The distributed load acting upon the beam varies linearly with position, increasing in the lower section of the beam from a somewhat arbitrary value of $-\alpha p$ at the base to a value of p at mid-span. This loading pattern is then mirrored in the second half of the beam, with the load increasing linearly from a value of $-p$ at the center to αp at the top. To increase the generality of this model, the coefficient α is used to represent a constant loading factor such that $0 < \alpha < 1$. For most of the post-processing associated with this model, $\alpha = 0.5$.

As with the first simple model, there is a discontinuity in the loading at mid-span. For this reason, the beam must be represented by two sets of equations, each existing only over its respective half of the beam. For the second simple model the governing differential equation of bending can be written as

$$EI \frac{d^4 v}{dx^4} = \begin{cases} -w_1(x) = -2p(1 + \alpha) \frac{x}{L} + \alpha x & \text{for } 0 < x < \frac{L}{2} \\ -w_2(x) = -2p(1 + \alpha) \frac{x}{L} + p(2 + \alpha) & \text{for } \frac{L}{2} < x < L \end{cases} \quad (5.11)$$

Integrating these expressions to obtain the displacement of the beam results in

$$EIv_1(x) = -\frac{p}{60L}(1 + \alpha)x^5 + \frac{p}{24}\alpha x^4 + \frac{c_1}{6}x^3 + \frac{c_2}{2}x^2 + \frac{c_3}{2}x + c_4 \quad (5.12a)$$

$$EIv_2(x) = -\frac{p}{60L}(1 + \alpha)x^5 + \frac{p}{24}(2 + \alpha)x^4 + \frac{c_5}{6}x^3 + \frac{c_6}{2}x^2 + \frac{c_7}{2}x + c_8 \quad (5.12b)$$

For the second simple model, the boundary and compatibility conditions are unchanged from the first simple model, a fact that can be verified through examination of Figure 5.10. Therefore, Equations (5.5) and (5.6) are applied to determine the unknown constants of Equation (5.12), resulting in the following expressions for the displaced shape of the beam

$$v_1(x) = \frac{pL^4}{240EI} \left[-4(1 + \alpha) \left(\frac{x}{L}\right)^5 + 10\alpha \left(\frac{x}{L}\right)^4 + 5(1 - 2\alpha) \left(\frac{x}{L}\right)^2 \right] \quad (5.13a)$$

$$v_2(x) = \frac{pL^4}{960EI} \left[-16(1 + \alpha) \left(\frac{x}{L}\right)^5 + 40(2 + \alpha) \left(\frac{x}{L}\right)^4 - 160 \left(\frac{x}{L}\right)^3 + 20(7 - 2\alpha) \left(\frac{x}{L}\right)^2 - 40 \left(\frac{x}{L}\right) + 5 \right] \quad (5.13b)$$

The displaced shape and distributions of shear force and bending moment in the second model are shown in Figure 5.12 using the shown dimensionless parameters. The coefficient α is assigned a value of one-half. These plots verify that the second simple model accomplishes its goal of approximating the loading applied to a pile in the lateral spreading model. The shear force is zero at each end with a maximum in the center of the beam, and the moment has maximums where the shear is zero, occurring at a location between the center and the end of the beam. The distributions of both moment and shear for this model are fairly similar to those developed in the lateral spreading model. The results from the simple models are more uniform due to the prescribed load distribution, but they share the same general shape as their more complex counterparts.

An expression for the end displacement, Δ , occurring at the position $x = L$ (the top of the beam), is determined from Equation (5.13b) as

$$\Delta = \frac{(9 - 16\alpha)pL^4}{960EI} \quad (5.14)$$

To determine the effective length for the second simple model, the location of the maximum moment is computed in each segment of the beam. This is accomplished by determining the locations in which the shear force is zero. These locations are

$$\xi_1 = \frac{\alpha}{1 + \alpha} \quad \text{for } 0 < \xi_1 < \frac{1}{2} \quad (5.15a)$$

$$\xi_2 = \frac{1}{1 + \alpha} \quad \text{for } \frac{1}{2} < \xi_1 < 1 \quad (5.15b)$$

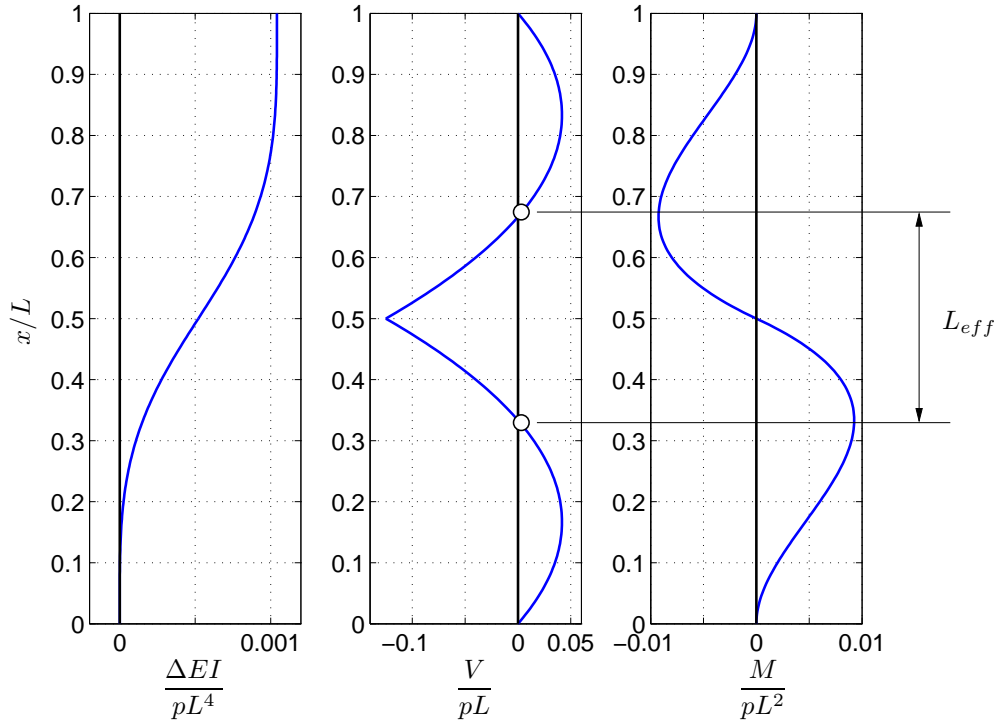


Figure 5.12 Displaced shape, shear diagram, and moment diagram for the second simple model.

The effective length of the beam is found as

$$\frac{L_{eff}}{L} = \min \left\{ 1, \min \left\{ \xi_2, \frac{1}{2} \right\} \right\} - \max \left\{ 0, \min \left\{ \xi_1, \frac{1}{2} \right\} \right\} \quad (5.16)$$

which defines the effective length for any value of the coefficient α . The maximum moment in the beam is determined by evaluating the moment equation at the previously obtained locations of maximum moment. For values of α which satisfy the conditions of Equation (5.15), the maximum moment in the beam can be expressed as

$$\max M = \frac{pL^2\alpha^3}{6(1+\alpha)^2} + \frac{pL^2}{24}(1-2\alpha) \quad (5.17)$$

5.6.3 Observations

When elastoplastic soil elements are used in the lateral spreading model, there is a limit to the amount of resistance the soil will provide. In the areas where yielding occurs, such as near the liquefied layer, the load on the pile increases as the contact zone between the soil and pile increases in length. In the simple models, this behavior could be represented as an increase in the magnitude of p . In order to gain insight from the two simple models, plots of p versus the effective length of the beam and p versus the maximum moment in the beam are made for each simple beam model for a constant end displacement, Δ .

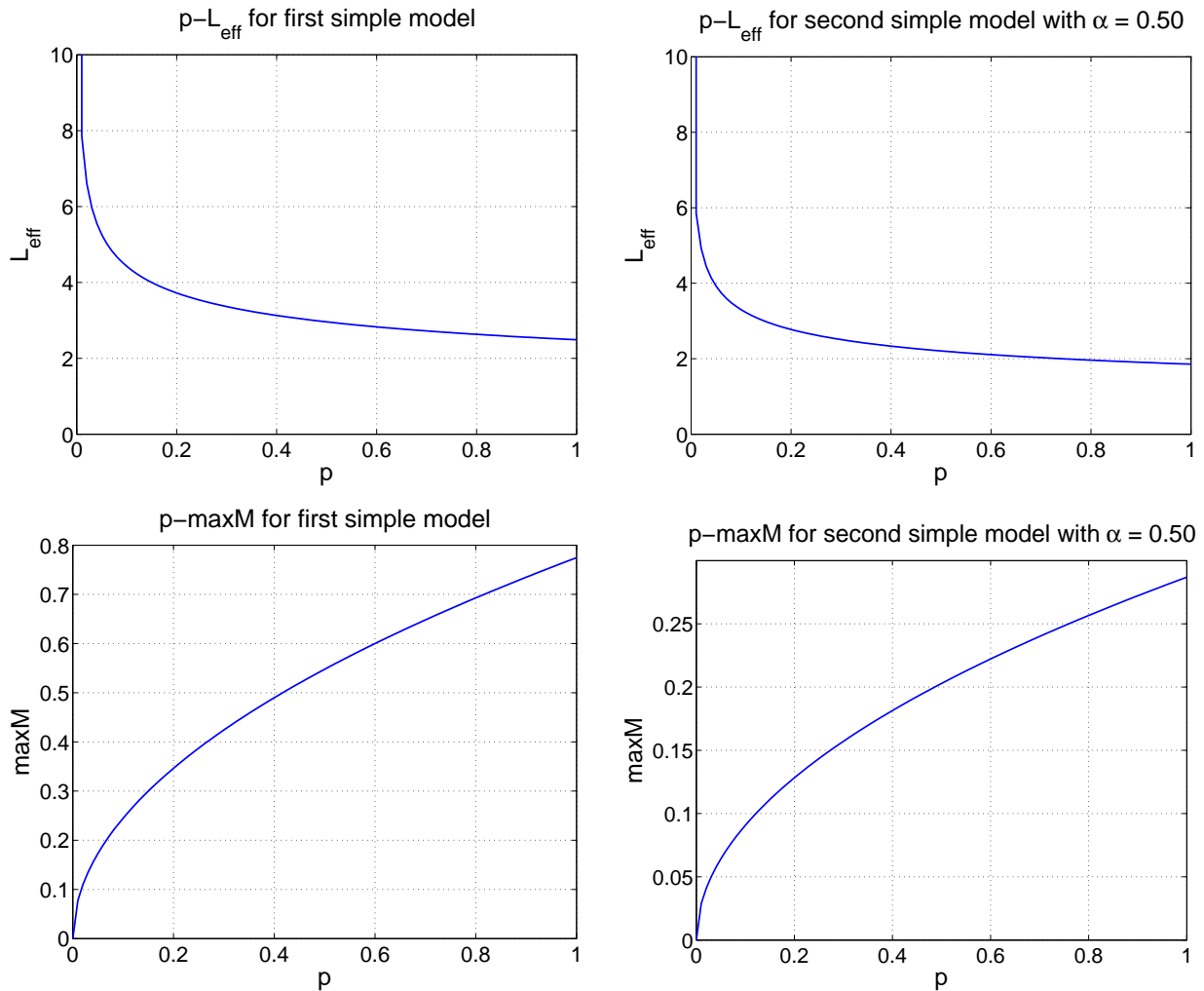


Figure 5.13 Normalized relationships between L_{eff} , $max M$, and p for the two simple models.

The plots of Figure 5.13 show the variation in the key bending parameters, effective length, L_{eff} , and maximum moment, $max M$, with the magnitude of the applied loading, p , for a constant end displacement of $\Delta = 1$. In all of the plots of Figure 5.13, dimensionless analysis is used to allow the curves to be shown in a normalized manner. For increasing values of p , the effective length of each model decreases while the maximum moment in the models increases. This is the same behavior observed for all three elastic pile models in the 3D lateral spreading simulations, attainable from models easily solved by hand.

It has been shown that the two simple beam models are able to approximate the behavior of the piles in the three-dimensional lateral spreading model. Both Figures 5.11 and 5.12 show moment and shear diagrams that are reasonably similar to the moment and shear diagrams resulting from the lateral spreading model. With this reassurance, it is concluded that the behavior of these models is representative of the behavior of the piles due to the imposed displacement profile. The observed tendency for increasing maximum moment and decreasing effective length for increasing magni-

tudes of the applied load distribution in the simple models verifies that the lateral spreading results are reasonable while also offering a mechanism for this behavior. These models may also be useful as a quick method to predict approximate demands for a pile subject to lateral spreading.

5.7 SUMMARY

During a lateral spreading event, an embedded pile foundation fundamentally alters the deformation of the soil system while simultaneously undergoing deformation of its own. Many factors contribute to the resultant behavior of the pile and the surrounding soil, among them the bending stiffness of the pile as compared to the lateral stiffness of the soil, the ultimate strength of both the pile and the soil, as well as the degree of fixity at the extents of the pile.

When the soil-pile system is modeled as entirely linear elastic, fundamental behavioral mechanisms can be observed in the system. As the lateral movement of the upper soil layer progresses, the pile embedded in the soil is pushed in the direction of flow. Depending upon the magnitude of the ratio of the pile's bending stiffness to the lateral stiffness of the soil, the pile also offers resistance to the lateral flow of soil, with greater resistance provided by those piles with the largest stiffness ratios. The bending demands which are generated in the piles follow consistent patterns for all pile sizes with the maximum shear force demand developing at the center of the liquefied layer due to the change in sign of the applied loading, and the maximum moment demands falling somewhat outside the boundaries of the liquefied layer, with one extreme value in each of the two solid soil layers. The distance between the maximum moments defines the effective length of the pile, L_{eff} , a parameter which provides an indication of the severity of the bending demand.

By altering the soil constitutive model to consider plastic behavior, the amount of load that the pile must carry increases, leading to increased bending demands when compared to the linear elastic models. This phenomenon has been verified through the use of simple beam models. In addition to changing the relationship between the pile and the soil, considering elastoplastic soil behavior allows for the observation of the ways in which the weaker liquefied layer affects the surrounding solid soil layers. As the pile is pushed into the soil, the solid soil near the boundary of the liquefied layer is able to be pushed into the adjacent liquefied layer, thus effectively reducing the lateral resistance of the soil in the regions near the liquefied layer. This final aspect of the behavior observed in the system is critical to the lateral spreading problem and is explored further in Chapter 8.

6 Computation of Representative $p-y$ Curves from the Three-Dimensional Model

6.1 INTRODUCTION

In current geotechnical engineering practice, it is common to analyze a pile foundation subject to lateral loads as a beam on a nonlinear Winkler foundation. It is therefore of interest to develop a lateral spreading analysis procedure that is compatible with this current design paradigm. Representative $p-y$ curves are computed from 3D FE analysis in order to evaluate the applicability of this approach to the lateral spreading problem. To this purpose, a reliable method for computing the $p-y$ curves must be established.

The computational process includes identifying the appropriate data recorded during the 3D simulations as well as evaluating the effects of various factors on the resulting $p-y$ curves. Investigations are made into the ways in which the pile deformation pattern (pile kinematics), the selective mesh refinement scheme employed in the models, and the location of the fixed boundaries affect the computed $p-y$ curves. It is determined that all three of these factors are influential and solutions to properly handle their respective effects are proposed.

6.2 COMPUTATION OF FORCE AND DISPLACEMENT HISTORIES

Computing a set of $p-y$ curves from the 3D FE model requires knowledge of the force and displacement histories for the pile nodes. The general computational process is shown in Figure 6.1. The forces exerted on the pile by the surrounding soil are determined directly from the beam-solid contact elements (Petek, 2006), which integrate the 3D interface tractions applied by the soil to the outer surface of the pile into a force vector at each pile node. By recording this vector, the resultant force components acting in the direction of loading are defined at each of the pile nodes.

Due to the symmetry condition present in the model, the magnitudes of these force components reflect only one-half of the full pile circumference. To obtain results consistent with the full diameter of the piles, these forces are doubled. In order to obtain mesh-independent values, each force must also be normalized by the tributary length of pile over which it acts. For each respective pile node, the tributary length is defined as half the distance to the adjacent pile nodes in either direction. For the end nodes, the tributary length is half the distance to the sole adjacent node.

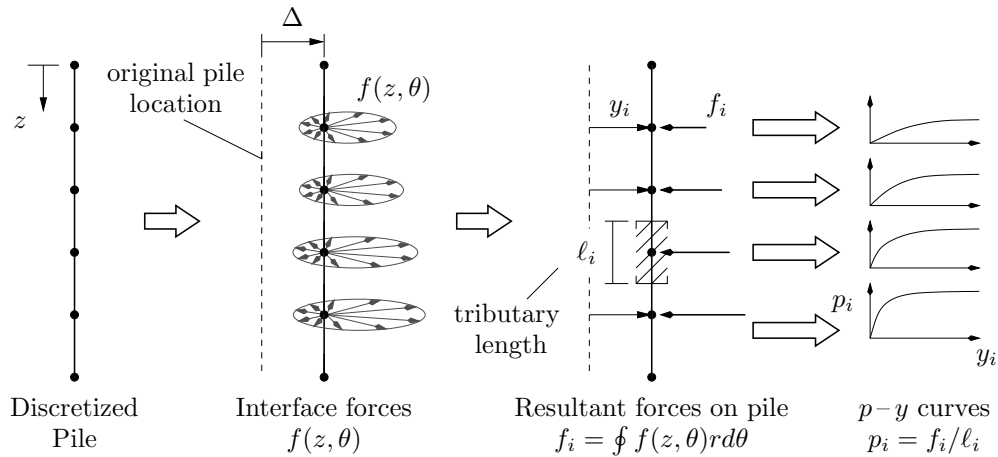


Figure 6.1 Computation of $p-y$ curves from the 3D FE model.

The desired displacement for generation of $p-y$ curves representative of the soil response is the differential displacement between the pile and the soil. In the case of the lateral spreading models, the displacement values recorded directly from the pile are not a measure of the distance that the pile is pushed into the surrounding soil, but a measure of the actual displacement experienced by the pile. To obtain the displacement of the pile relative to the surrounding soil for this case, the imposed far-field soil displacement profile is subtracted from the pile displacement profile recorded by the model, as schematically in Figure 6.2. For analyses in which all or part of the pile is directly pushed into the surrounding soil, this subtraction procedure is not required as the recorded pile displacements are the relative displacements between the pile and the surrounding soil.

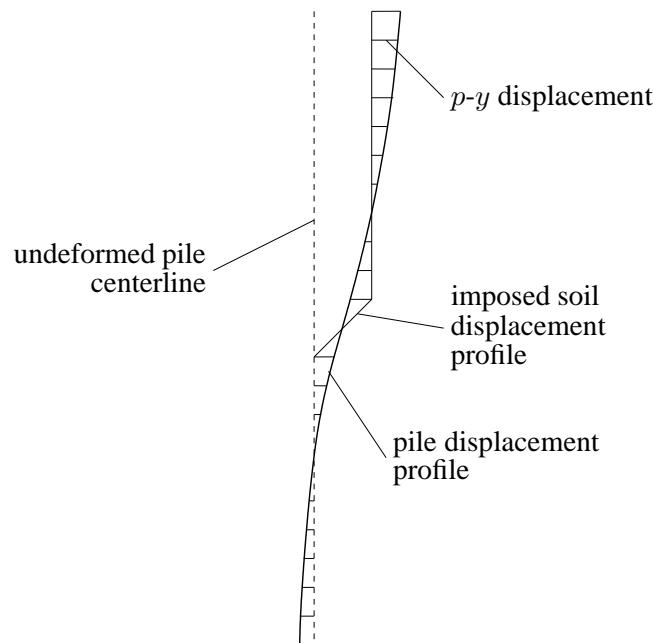


Figure 6.2 Determination of displacements suitable for use in $p-y$ curves for the lateral spreading case.

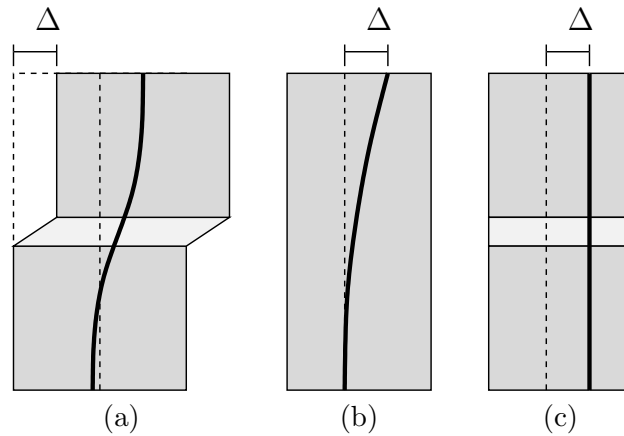


Figure 6.3 Pile kinematic cases. (a) Lateral Spreading; (b) Top pushover; (c) Rigid pile.

6.3 CONSIDERED KINEMATIC CASES

Three separate pile deformation patterns are considered in order to provide a means to evaluate the effects of varying pile kinematics on the $p-y$ curves resulting from the FE analysis. These cases include the following: (1) a lateral spreading case, Figure 6.3(a), which is the primary focus of this research; (2) a top pushover case, Figure 6.3(b), matching the type of test used to empirically derive $p-y$ curves; and (3) a rigid pile case, Figure 6.3(c), in which the pile is pushed a uniform lateral distance into the soil.

The top pushover case simulates a displacement controlled lateral load test. The top node of the pile is displaced laterally in the symmetry plane while all other pile nodes are free to translate and rotate in this plane. The pile head is left to rotate freely. This kinematic mode results in large deformations near the surface and small deformations at greater depths. For the rigid pile case, all pile nodes are translated laterally into the soil without rotation; the remaining boundary conditions on the soil are unchanged.

All three kinematic cases are modeled using the FE mesh used in the 3D lateral spreading simulations. The piles are modeled using the linear elastic formulation discussed in Section 3.4. Elastoplastic soil behavior is considered using the Drucker-Prager constitutive model discussed in Section 4.4. All three of the template pile designs are considered.

6.4 CURVE-FITTING STRATEGIES

The $p-y$ data returned from the simulations is a set of discrete points representing the force, normalized by element length, applied to the pile at specific values of displacement. In order to manipulate and analyze this data mathematically, curves must be fitted to the data points to obtain smooth and continuous functions that describe the $p-y$ curve at each node. To this end, a least squares curve-fitting strategy is employed for two separate functional forms, a polynomial function and a hyperbolic tangent function. The polynomial function is utilized to estimate the initial tangent for the $p-y$ curves, while the hyperbolic tangent function is used to describe the

shape of the $p-y$ curves and to define the ultimate resistance of each curve. Because the forces and displacements may be positive or negative, depending upon the specific deformation pattern in each case, the absolute values of the forces and displacements are used for curve-fitting purposes.

6.4.1 Hyperbolic Tangent Function

A hyperbolic tangent function is chosen to allow direct comparison to the API (1987) recommendations, which describe the shape of $p-y$ curves for cohesionless soils using this functional form. The fitted function has the form

$$p(y) = p_u \tanh\left(\frac{kz}{p_u} y\right) \quad (6.1)$$

in which z is the depth and the parameter k , with units of force/length³, affects the slope of the function. Equation (6.1) defines the two characteristic parameters used to compare and evaluate sets of $p-y$ curves: (1) the ultimate lateral resistance, p_u ; and (2) the initial tangent stiffness, $k_T = dp(y)/dy|_{y=0}$.

Least squares is used to determine the constants p_u and k for the $p-y$ data at each pile node. For Equation (6.1), the residual, r_j , at each pile node can be expressed as the difference between the value returned from the simulation and that estimated by the curve-fitting function.

$$r_j = p_j - p_u \tanh\left(\frac{kz}{p_u} y_j\right) \quad (6.2)$$

The best fit for the data is achieved when the error is at a minimum. For this problem, the error function is obtained as

$$\mathcal{E}(p_u, k) = \sum_j \frac{1}{2} r_j^2 = \sum_j \left[p_j - p_u \tanh\left(\frac{kz}{p_u} y_j\right) \right]^2 \quad (6.3)$$

The error is at a minimum when its gradient is zero. Because there are two parameters, it is expedient to perform the solution in vector form by defining the vector $\boldsymbol{\lambda}$ with two components $\lambda_1 = p_u$ and $\lambda_2 = k$. The gradient equations can thus be written in terms of this vector, $\boldsymbol{\lambda}$, as

$$\frac{\partial \mathcal{E}}{\partial \lambda_i} = \sum_j r_j \frac{\partial r_j}{\partial \lambda_i} = 0 \quad (6.4)$$

The necessary derivatives of the residual with respect to the two parameters λ_1 and λ_2 can be expressed as

$$\frac{\partial r_j}{\partial \lambda_1} = \frac{\partial r_j}{\partial p_u} = \frac{kz}{p_u} y_j \operatorname{sech}^2\left(\frac{kz}{p_u} y_j\right) - \tanh^2\left(\frac{kz}{p_u} y_j\right) = 0 \quad (6.5)$$

$$\frac{\partial r_j}{\partial \lambda_2} = \frac{\partial r_j}{\partial k} = -z y_j \operatorname{sech}^2\left(\frac{kz}{p_u} y_j\right) = 0 \quad (6.6)$$

Due to the nonlinear nature of Equations (6.5) and (6.6), an iterative procedure must be employed to obtain values for the unknown parameters, p_u and k . For a known value of $\boldsymbol{\lambda}^\ell$ in the current iteration, a Taylor series expansion is used to estimate the value of $p(y)$ in the next iteration as

$$p(y_j, \boldsymbol{\lambda}) \approx p(y_j, \boldsymbol{\lambda}^\ell) + \sum_i J_{ji} \Delta \lambda_i \quad (6.7)$$

in which $\boldsymbol{\lambda}^\ell$ contains the values of λ_1 and λ_2 in the current iteration, $\Delta \boldsymbol{\lambda} = (\Delta \lambda_1, \Delta \lambda_2)^T$ is the change in $\boldsymbol{\lambda}$ between iterations, and the Jacobian, \mathbf{J} , has components

$$J_{ij} = -\frac{\partial r_i}{\partial \lambda_j} \quad (6.8)$$

Plugging the result of Equation (6.7) into the residual gives

$$\begin{aligned} r_j &= y_j - p(y_j, \boldsymbol{\lambda}^\ell) - \mathbf{J} \cdot \Delta \boldsymbol{\lambda} \\ &= \Delta y_j - \mathbf{J} \cdot \Delta \boldsymbol{\lambda} \end{aligned} \quad (6.9)$$

Applying this result to the minimization problem Equation (6.4) leads to

$$\mathbf{J}^T \mathbf{J} \Delta \boldsymbol{\lambda} = \mathbf{J}^T \Delta \mathbf{y} \quad (6.10)$$

from which appropriate values for the components of $\boldsymbol{\lambda}$, the parameters p_u and k , can be determined by iterating with a Newton-Raphson procedure until the specified convergence criterion is met. For the presented results, the process continues to iterate until

$$\left| \frac{\Delta \lambda_j}{\lambda_j} \right| < 0.001 \quad (6.11)$$

An example of the $p-y$ curve data extracted from the 3D FE model and the associated fitted hyperbolic tangent curve is shown in Figure 6.4. As shown, the overall fit is good, however, the initial tangent indicated by the data is not represented well by the initial tangent of the hyperbolic tangent curve. Due to this observation, a polynomial function is fit to the initial data in order to better resolve the initial stiffness represented by the computed $p-y$ curves.

6.4.2 Polynomial Function

A cubic polynomial is fit to only the first several points of the $p-y$ curve data, ensuring that the initial tangent is accurately captured. The selected cubic polynomial has the form

$$p(y) = a_1 y + a_3 y^3 \quad (6.12)$$

in which coefficients a_1 and a_3 are constants determined by least squares. The coefficient a_1 is the initial slope of the curve. Taken in the context of a $p-y$ curve, this parameter provides a good representation of the initial stiffness, k_T .

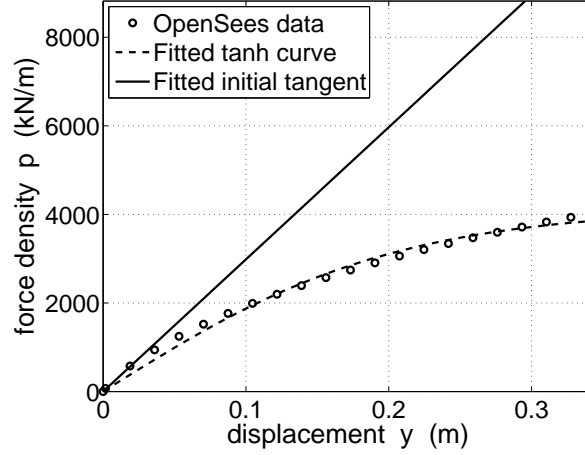


Figure 6.4 Example of computed $p-y$ data with fitted initial tangent stiffness and hyperbolic tangent curve for a 1.37 m diameter pile.

The least squares fit procedure seeks to minimize the error function, \mathcal{E} , defined as

$$\mathcal{E}(a_i) = \sum_j \frac{1}{2} [p_j - p(y_j)]^2 \quad (6.13)$$

where p_j and y_j are the values of force density and displacement, respectively, returned from the model at a given node for time step j , and $p(y_j)$ is the chosen curve-fitting function [i.e., Equation (6.12)] evaluated at each of the values of y_j . For a cubic polynomial, the error function can be expressed as

$$\mathcal{E} = \sum_j \frac{1}{2} [p_j - a_1 y_j - a_3 y_j^3]^2 \quad (6.14)$$

This error function is minimized by computing the derivatives with respect to both a_1 and a_3 , setting these to zero, and solving for the unknown constants. The resulting equations have the form

$$\begin{aligned} \frac{\partial \mathcal{E}}{\partial a_1} = 0 &= \sum_k (-p_k + a_1 y_k + a_3 y_k) y_k \\ \implies a_1 \sum_k y_k^2 + a_3 \sum_k y_k^4 &= \sum_k p_k y_k \end{aligned} \quad (6.15)$$

$$\begin{aligned} \frac{\partial \mathcal{E}}{\partial a_3} = 0 &= \sum_k (-p_k + a_1 y_k + a_3 y_k) y_k^3 \\ \implies a_1 \sum_k y_k^4 + a_3 \sum_k y_k^6 &= \sum_k p_k y_k^3 \end{aligned} \quad (6.16)$$

from which the unknown constants a_1 and a_3 can be determined using

$$\begin{Bmatrix} a_1 \\ a_3 \end{Bmatrix} = \begin{bmatrix} \sum y_k^2 & \sum y_k^4 \\ \sum y_k^4 & \sum y_k^6 \end{bmatrix}^{-1} \begin{Bmatrix} \sum p_k y_k \\ \sum p_k y_k^3 \end{Bmatrix} \quad (6.17)$$

An example of the fitted initial tangent stiffness provided by the cubic polynomial is shown in Figure 6.4. This stiffness is a much better representation of the initial tangent indicated by the data. For all subsequent discussion, it can be assumed that any reference made to the initial tangent stiffness, k_T , of the $p-y$ curves refers to that obtained using the cubic polynomial. All values of the ultimate lateral resistance, p_u , are determined from the fitted hyperbolic tangent functions.

6.5 EFFECTS OF PILE KINEMATICS ON COMPUTED $p-y$ CURVES

The rigid pile case, Figure 6.3(c), is used as a benchmark to evaluate the effects of pile kinematics on $p-y$ curves. This case eliminates the influence of pile deformation on the computed curves and activates the soil response consistently at all depths. The $p-y$ curves resulting from the lateral spreading, Figure 6.3(a), and top pushover, Figure 6.3(b), cases are generally comparable to those resulting from the rigid pile case, however, in certain locations the curves deviate from the benchmarks. This observation underscores a potential flaw in the assumption that representative $p-y$ curves can be extracted from the 3D finite element model without exception and identifies the need for a more careful approach to $p-y$ curve computation.

The lateral spreading, Figure 6.3(a), and top pushover, Figure 6.3(b), cases are compared to the benchmark case with respect to initial stiffness ratio (k_T ratio), and a lateral resistance ratio (LRR). The initial stiffness ratio is computed by dividing the initial tangent stiffness, k_T , in the variable kinematic cases, i.e., top pushover and lateral spreading, by the corresponding value of k_T in the rigid pile case. Because there are locations at which the displacements are very small and little soil resistance is mobilized, ultimate lateral resistances are not compared in this study.

The LRR compares the resistance provided at a specified level of lateral displacement for a given kinematic case to that provided at the same level of displacement for the benchmark case. This comparative means was used in a similar manner by Yang and Jeremic (2005) in their work with 3D FE analysis of layered soil profiles. An example of how the LRR works is illustrated in Figure 6.5. Four displacement increments are investigated in this study in an effort to gauge how the relationships between the curves may vary over time. The LRR is computed at displacements equal to 0.5%, 1%, 2%, and 4% of the pile diameter in each respective case.

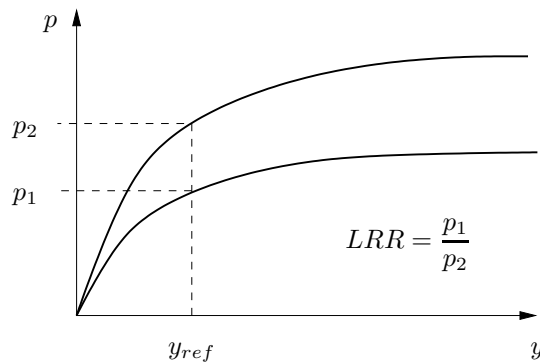


Figure 6.5 The lateral resistance ratio, LRR, is the ratio of the soil resistance values computed in two reference $p-y$ curves at a prescribed value of displacement.

Table 6.1 Overview of the four considered kinematic comparison cases.

	Rigid	Top Pushover	Lateral Spread
Homogenous Soil	X	X	
Layered (Liquefied) Soil	X		X

Table 6.1 provides a brief overview of the four kinematic comparison cases considered for each pile diameter. The top pushover case is run in an entirely homogeneous soil system, while the lateral spreading case is run in the three-layer liquefied soil model discussed previously. The results of these two variable kinematic cases are compared to a rigid pile analysis in a corresponding soil profile.

Computed k_T ratios and LRR's are presented in Figures 6.6 and 6.7 for the the lateral spreading and top pushover kinematic cases, respectively, for a 1.37-m- diameter pile. These results are typical of all considered piles. The evolution of the differential displacement between the pile and the soil is included to provide a context for the deformation pattern with depth. The depth and displacement scales are normalized by pile diameter.

If the resistance indicated by the $p-y$ curves depended only on relative soil-pile displacement, as assumed in the Winkler model, both the k_T ratio and LRR would be equal to 1.0. Figures 6.6 and 6.7 show that the k_T ratio and LRR deviate significantly from 1.0, hence, there are significant differences in the $p-y$ curves computed from the different pile kinematics.

Aside from the top few diameters of the top pushover comparisons, which are affected by interaction with the free surface, areas in which the displacement is large show good agreement between the respective $p-y$ curves. However, significant deviations occur in the areas in which the displacements are relatively small. At a particular depth, the $p-y$ curves for the lateral spreading and top pushover cases vary with respect to the rigid pile results based upon the magnitude of the pile displacement and how this displacement changes during the analysis.

Similar observations are made when looking at comparisons between the actual $p-y$ curves computed from the simulations. A selection of computed $p-y$ curves for a 0.61-m-diameter pile is shown in Figures 6.8 and 6.9. As shown, there are locations in which the curves match well and locations in which they do not. These plots also demonstrate the inadequacy of the top pushover and lateral spreading cases in the activation of the ultimate resistance of the soil, leading to the conclusion that a reasonable estimate of p_u is not possible for these cases.

Differing results for different kinematic cases are observed for all three pile diameters. The areas of greatest divergence do not occur at the same depth for different piles, therefore, depth or meshing effects can be ruled out as the causes of the difference. For all cases, the only difference between the compared analyses is the pile kinematics, thus, the observed differences must be attributable to this factor. An explanation for this observation is offered by way of the Betti-Rayleigh theorem of reciprocal work (Megson, 2005).

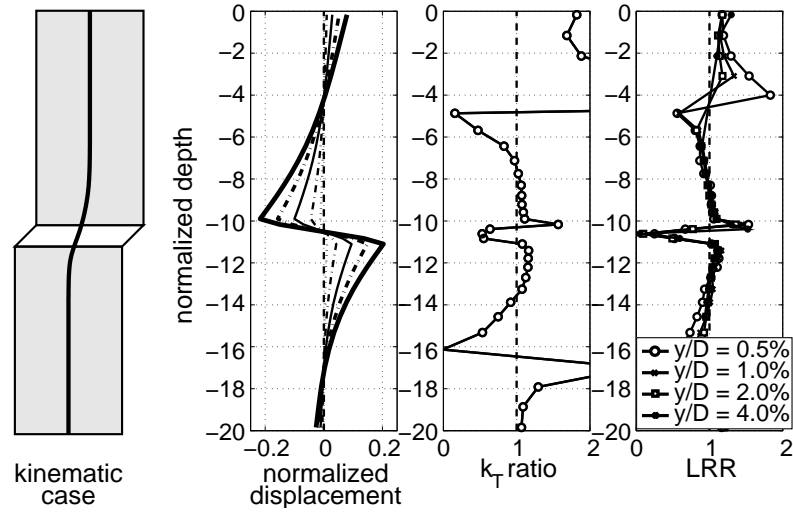


Figure 6.6 Comparison of the lateral spreading kinematic case to the rigid pile case for a 1.37-m-diameter pile. Both analyses use a three-layer liquefied soil system.

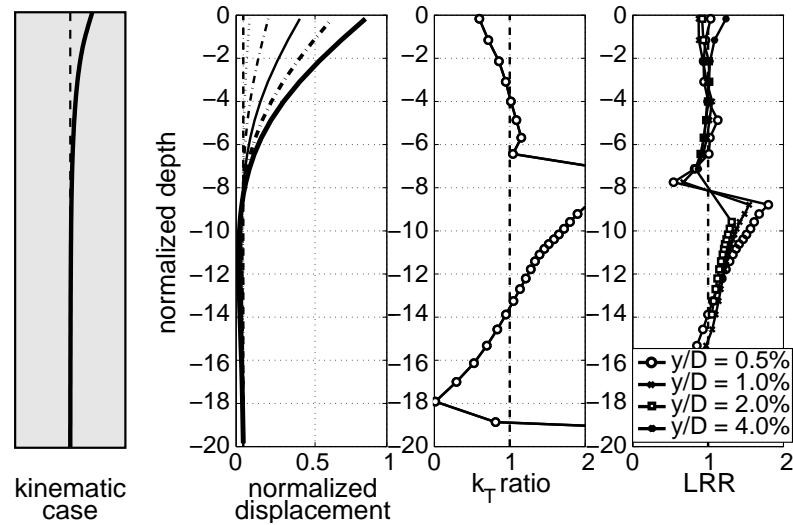


Figure 6.7 Comparison of the top pushover kinematic case to the rigid pile case for a 1.37-m-diameter pile. Both analyses use homogenous soil profiles.

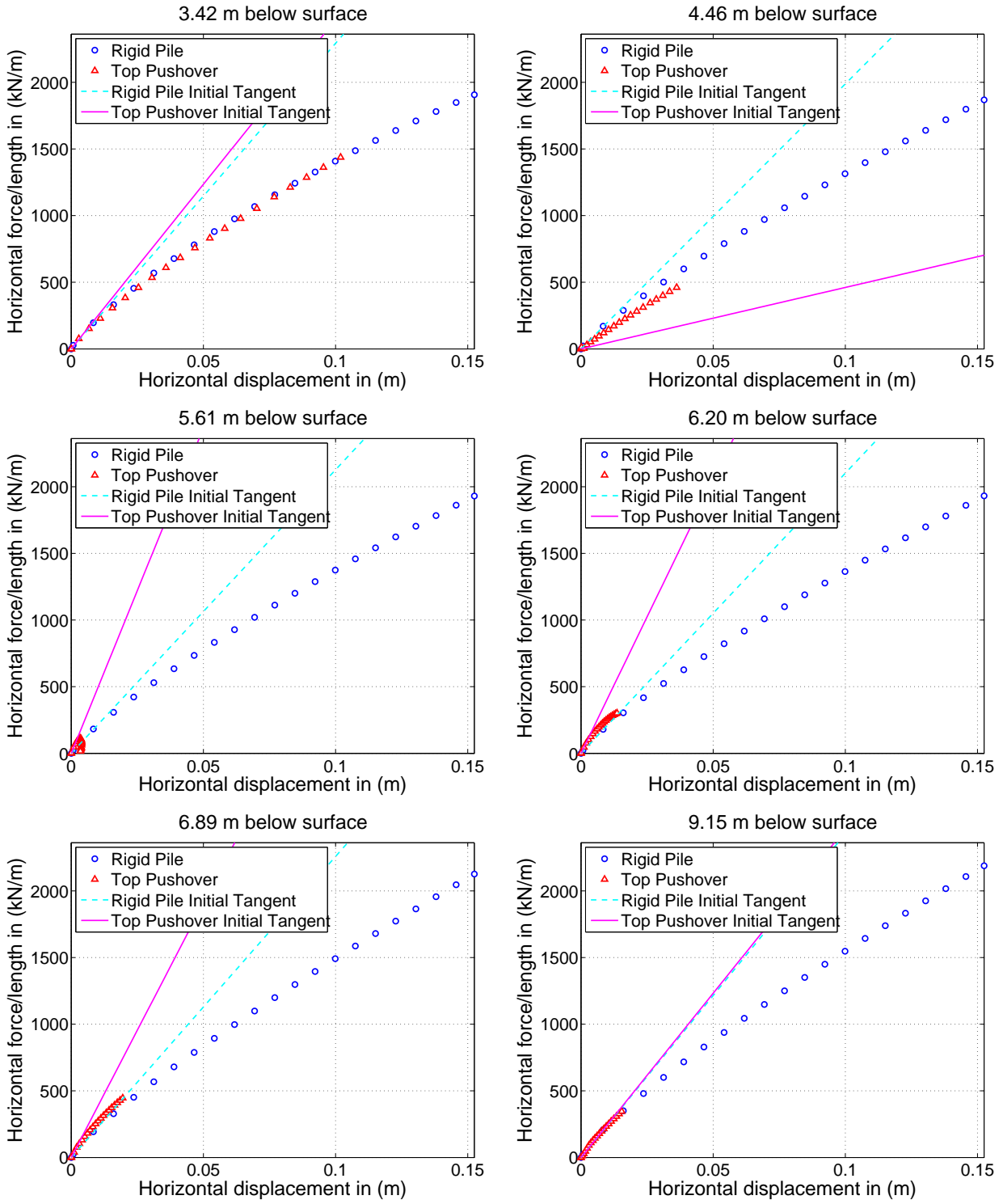


Figure 6.8 Computed $p-y$ curves from the top pushover and rigid pile cases in homogenous soil for a 0.61-m-diameter pile. The fitted initial tangents are shown for each case.

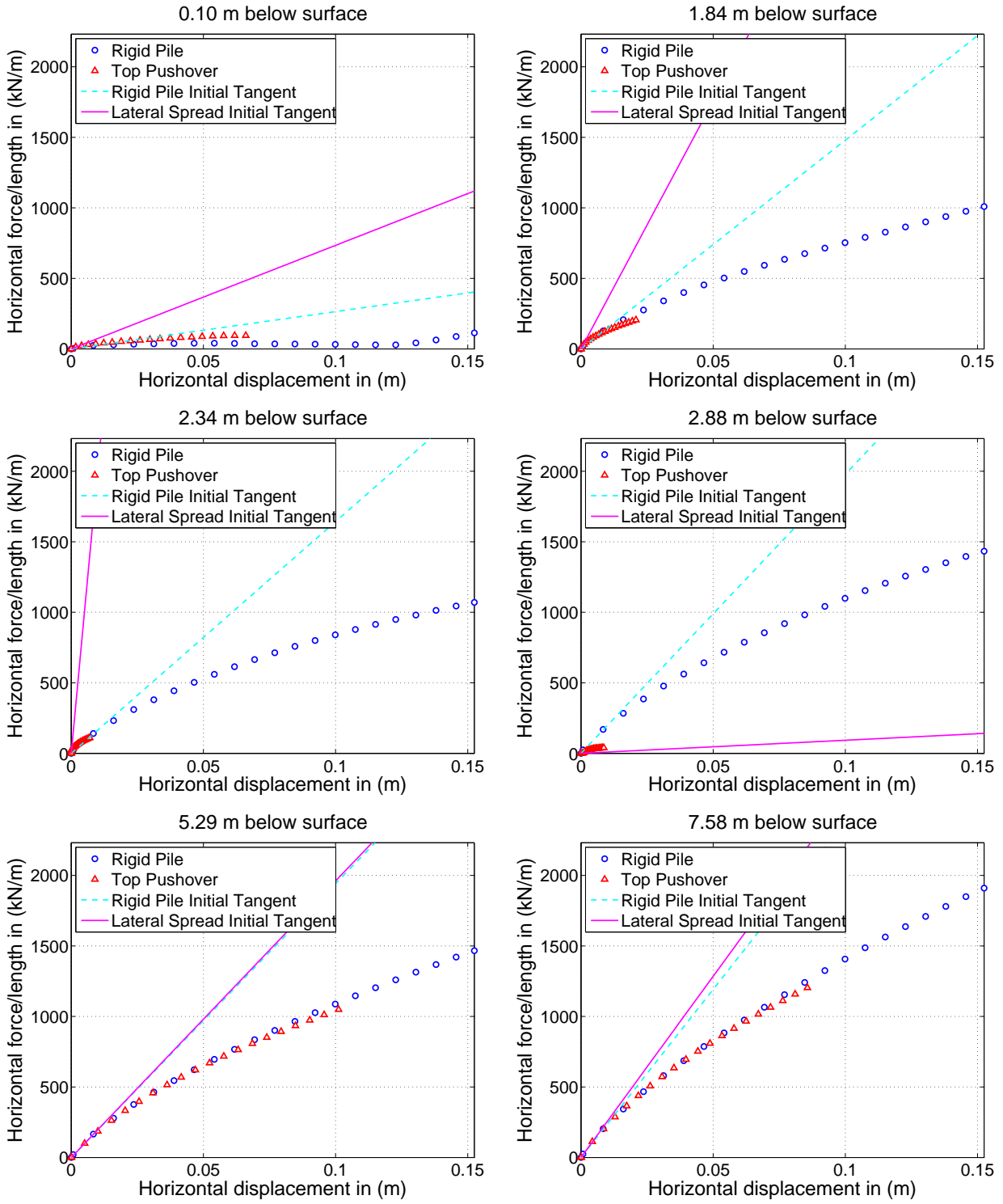


Figure 6.9 Computed $p-y$ curves from the lateral spreading and rigid pile cases in non-homogenous soil for a 0.61-m-diameter pile. The fitted initial tangents are shown for each case.

6.5.1 Betti-Rayleigh Theorem of Reciprocal Work

The Betti-Rayleigh theorem of reciprocal work is a principle which relates the work done by two separate load cases acting on a linear elastic body. Consider the elastic body of Figure 6.10 which depicts two separate load cases, **P** and **Q**, acting on the same points of the body, and their respective displacements, **u** and **v**.

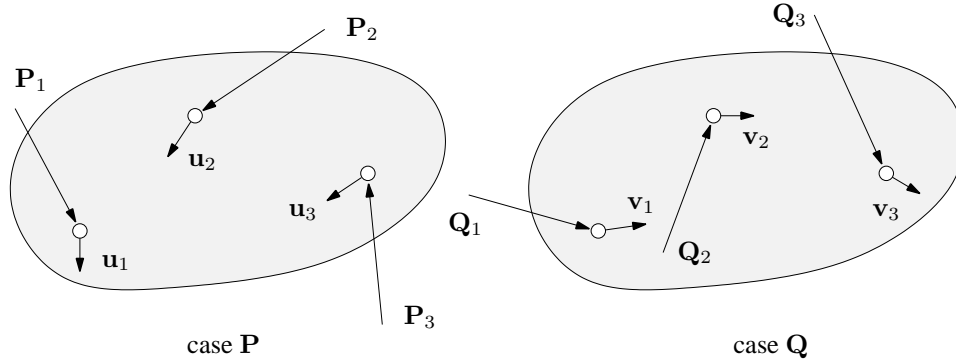


Figure 6.10 Two separate load cases, **P** and **Q**, with respective displacements, **u** and **v**, applied to the same points on a general elastic body.

The reciprocal theorem states that the work done by loads P_i when moving through the displacements produced by loads Q_j is equal to the work done by loads Q_j when moving through the displacements produced by loads P_i (Megson, 2005). The Betti-Rayleigh theorem can be expressed using the dot product as

$$\sum_i P_i \cdot v_i = \sum_j Q_j \cdot u_j \quad (6.18)$$

6.5.2 Application of the Betti-Rayleigh Theorem

To apply this theorem to the problem of a laterally loaded pile, it is convenient to designate load case **P** as the nodal forces applied to a pile having n nodes as its passage is resisted by the surrounding soil, indicating that **u** is the corresponding vector of nodal displacements. These are the terms that are related to each other to generate the $p-y$ curves at each pile node. If load case **Q** is a unit load applied at an arbitrary node, j , on the pile, then **v** represents the corresponding nodal displacements for this load and (6.18) can be written as

$$P_1 v_1 + P_2 v_2 + \dots + P_n v_n = u_j \quad (6.19)$$

from which a full set of equations can be written, in matrix form, as

$$[\mathbf{A}]\{\mathbf{P}\} = \{\mathbf{u}\} \quad (6.20)$$

in which **P** carries the lateral pile forces, **u** contains the lateral pile displacements, and the components A_{ij} are the displacements at each node i produced by a unit load at node j . Solving Equation (6.20) for the nodal forces results in

$$\{\mathbf{P}\} = [\mathbf{A}]^{-1}\{\mathbf{u}\} \quad (6.21)$$

which can be evaluated for the force, P_j acting at an arbitrary node j as

$$P_j = A_{j1}^{-1}u_1 + A_{j2}^{-1}u_2 + \dots A_{jn}^{-1}u_n \quad (6.22)$$

where A_{ji}^{-1} represents the components of $[\mathbf{A}]^{-1}$.

The effects of pile kinematics on the $p-y$ curve extraction procedure can be drawn from Equation (6.22) by considering what happens when the displacement at node j is varied in each kinematic case. In the top pushover and lateral spreading cases, if u_j is large, the force acting at node j is largely dependent upon u_j as the contribution by the term $A_{jj}^{-1}u_j$ in Equation (6.22) is dominant

$$P_j = A_{j1}^{-1}u_1 + A_{j2}^{-1}u_2 + \dots A_{jn}^{-1}u_n \approx A_{jj}^{-1}u_j \quad (6.23)$$

In this case, the assumption that there is a one-to-one relationship between the force and displacement at a node is relatively good, even though it is still an approximation. The regions of Figures 6.6 and 6.7 in which the k_T and lateral resistance ratios are nearly unity coincide with the areas in which the displacements are large, thereby supporting this explanation.

In contrast, great divergence between the $p-y$ curves returned by the rigid and top pushover cases is observed in the regions where the displacements of the pile are small. If u_j is small, then the contributions to the force acting at node j by the other terms in Equation (6.22) are no longer insignificant, meaning that at such a point, the assumption of a local force-displacement relationship is relatively poor. This effect is exacerbated when the displacement at a particular node is small compared to adjacent nodes at which the coefficients of $[\mathbf{A}]$ are relatively large. An example of this is most clearly made by looking at the middle sections of the lateral spreading cases. The nodes that are very near the center of the imposed displacement profile do not tend to move much during the entire process. The nodes just outside of this middle region undergo considerably larger displacements into the surrounding soil, thus affecting the results for the nodes in the middle region.

6.5.3 Proposed Solution to the Problem of Pile Kinematics

The findings discussed above suggest that the kinematics of the pile strongly influence the resulting $p-y$ curves for the variable pile kinematic cases and this must be considered when attempting to define a set of curves suitable for use in the analysis of a general pile deformation. The selected $p-y$ curves should reflect only the response of the soil, not a combination of the soil and pile responses. The pile response effect should be captured by the numerical model of choice.

In the rigid pile case the displacements at each node are identical. In the context of the Betti-Rayleigh theorem, this indicates that the coefficients of $[\mathbf{A}]$ are the determining factor in the force applied at a given node. This creates a situation whereby the assumption of a direct relationship between the forces and displacements at the individual nodes is relatively good, as $[\mathbf{A}]$ is diagonal dominant. This observation, and the fact that the pile does not deform, indicates that the rigid pile case produces $p-y$ curves that are not influenced by pile kinematics. Therefore, these curves reflect only the response of the soil. This is the benefit of the 3D FE analysis in comparison to full-scale field experiments. It will be shown that $p-y$ curves obtained from this pile kinematic produce reasonable results when applied to lateral spreading.

6.6 EFFECTS OF SELECTIVE MESH REFINEMENT ON COMPUTED $p-y$ CURVES

Examining the results for each of the kinematic cases, it is observed that there are fluctuations in the distributions of initial stiffness, k_T , and ultimate lateral resistance, p_u , with depth in the location of the liquefied layer. This behavior is present in all cases and for all piles, even those in which the soil profile is entirely homogenous. Figures 6.7 and 6.6 involve the ratios of two cases run using the same selectively refined mesh and therefore do not display similar fluctuations. While these ratios are valuable evaluation tools, the actual values of the curve parameters must also be verified as sensible, otherwise any conclusions drawn from the ratios are meaningless. In order to gain confidence in the computed $p-y$ curves, the cause of the fluctuations must be discerned.

It is hypothesized that the selective mesh refinement scheme is responsible for altering the results. The areas of inconstancy in the parameter distributions correspond not only to the location of the liquefied layer, but to the areas of differential mesh refinement. Because the failure of a cohesionless soil is governed by shear, it seems sensible to assume that the size of the elements will affect the perceived stiffness that the elements display towards this failure mechanism. For example, in the wedge-type soil failure mechanism that is common at shallower depths, all of the gauss points that are aligned with the failure surface must have reached yield in their associated constitutive models for the model to display the global behavior. Changing the vertical size of the elements changes the spacing of the gauss points and may alter the number of gauss points that must experience local failure in order for the global failure to occur, thus, altering the response of the soil as a whole, and, subsequently, the computed $p-y$ curves.

In order to test the hypothesis that the selective mesh refinement is responsible for the observed fluctuations in soil response, a uniform mesh is generated for each of the piles. This uniform mesh has the same outer dimensions and layout as the selectively refined meshes, however, the soil and pile elements are all uniformly sized in the vertical direction. Two rigid pile cases are run using this uniform model, one in a homogenous soil profile, and the other in a three-layer soil profile with a liquefied center layer. Figure 6.11 shows the distributions of k_T and p_u , respectively, over the length of a 1.37-m-diameter pile in homogenous soil using the uniform and selectively refined meshes. As shown, both the stiffness and resistance values fluctuate in the center of the pile for the selectively refined case. The uniform case does not display similar behavior. Instead, the distributions resulting from the uniform mesh are smooth over the entire length of the pile. These results support the hypothesis.

A solution is proposed to smooth the soil response in the selectively refined cases by using the results of the uniform mesh cases. This solution is proposed in lieu of running all previously analyzed cases a second time, using a uniform mesh, in order to obtain smooth soil response while simultaneously losing the valuable mesh resolution at the liquefied interface. Instead of that laborious pursuit, the selectively refined results are smoothed through multiplication with the ratio of the uniform and refined results obtained from a rigid pile in homogenous soil for each diameter. This proposed solution also allows for further verification of the hypothesis that the selectively refined mesh scheme is the cause of the fluctuations in soil response.

Figure 6.12 shows both the original and smooth distributions of initial stiffness and ultimate lateral resistance for several kinematic cases. For the ultimate resistance, only the rigid pile case is

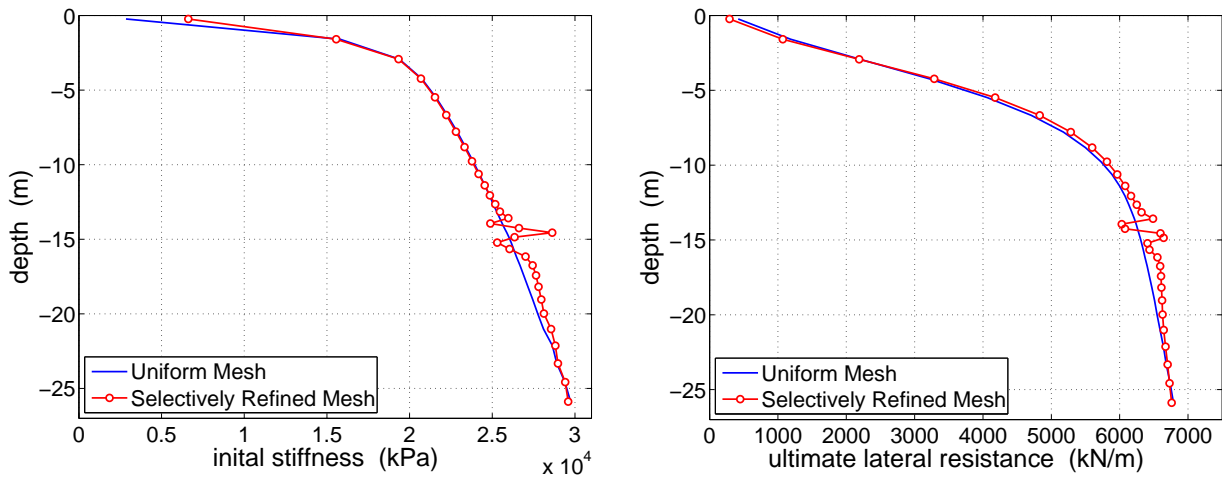


Figure 6.11 Distributions of k_T and p_u for 1.37-m-diameter pile in homogenous soil profile.

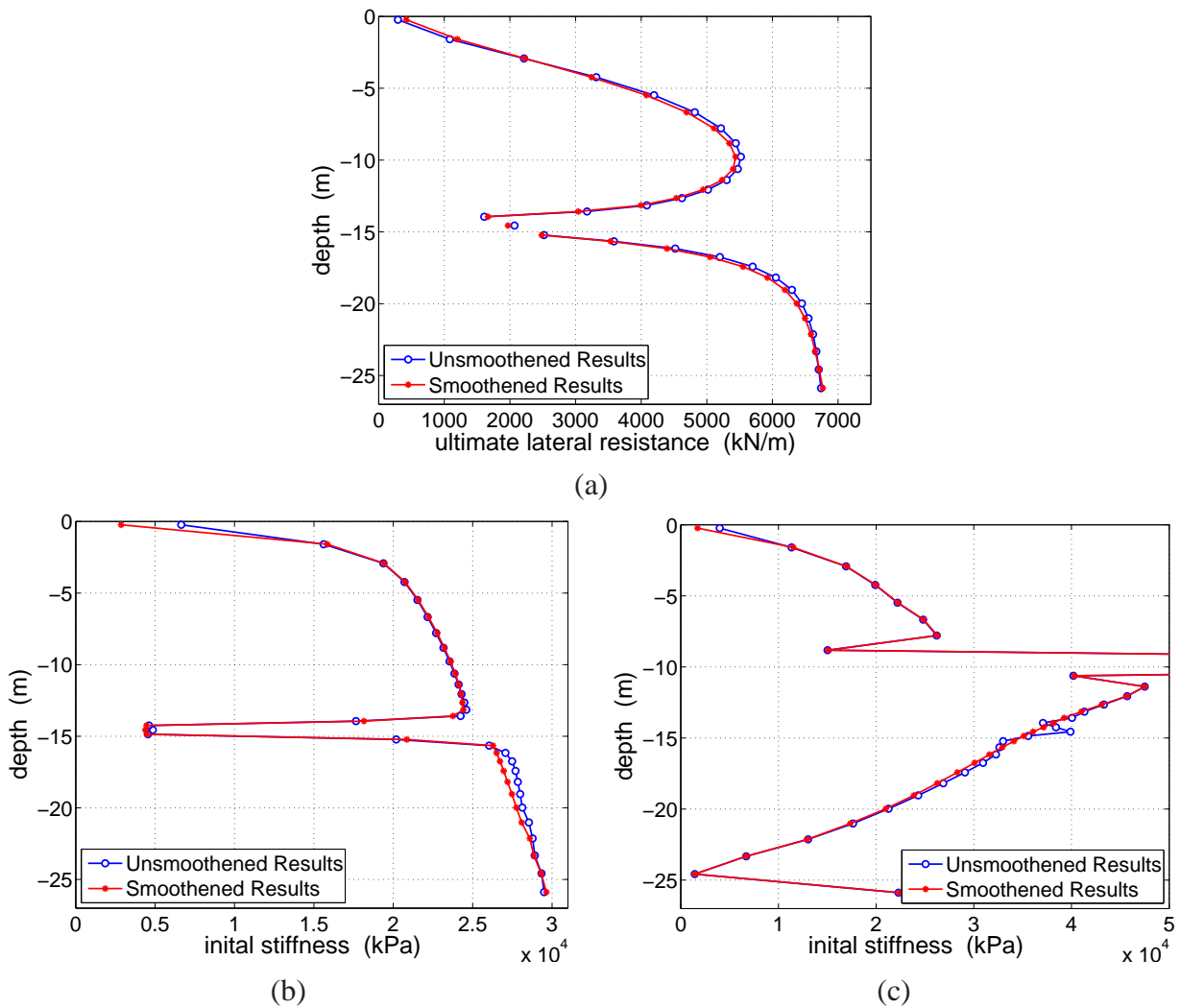


Figure 6.12 Examples of smoothing process on curve parameters for 1.37-m-diameter pile. (a) Distribution of p_u from rigid pile in liquefied soil profile; (b) Distribution of k_T from rigid pile in liquefied soil profile; (c) Distribution of k_T from top pushover in homogenous soil profile.

considered due to the inability of the alternate kinematic cases to fully activate the soil response at all depths. As shown, the smoothing process, involving the ratios obtained using the rigid pile cases in homogenous soil profiles, is able to remove the fluctuations in the parameter distributions for each of the alternative pile kinematic cases.

Though the stiffness distribution itself is suspect for reasons related to the pile kinematics, Figure 6.12(c) illustrates well the effect of the smoothing procedure. The presented case is a top pushover in an entirely homogenous soil profile. There are fluctuations in the data set in the area where the mesh is more refined (centered approximately at a depth of 14 m). Through multiplying the initial stiffness distribution from this top pushover case by the ratio of the uniform results to the selectively refined results for the rigid pile case, the inconsistencies in the results are removed, creating a smooth distribution through the depths encompassed by the increased mesh resolution.

The results of Figure 6.12 demonstrate the effectiveness of the smoothing procedure and verify the validity of the hypothesis with respect to the selective mesh refinement. The use of a selectively refined mesh can affect the results of a 3D FE simulation, but through careful diagnosis and recognition, these effects can be nullified in a relatively cheap and simple manner.

6.7 BOUNDARY EFFECTS ON SOIL RESPONSE

The FE models generated for the studies performed in this research are intended to include sufficient lateral extents such that the results are relatively unaffected by the fixed boundaries on the outside surfaces of the mesh. In order to gauge the significance of the fixed boundaries on the soil response recorded in the models, a new mesh is generated having increased lateral extents. This extended mesh is shown in Figure 6.13. The extended mesh shares a layout with the standard mesh used in the other aspects of this research, however, the soil elements are extended for an additional ten pile diameters in the direction of loading. By increasing the amount of soil between the pile and the fixed boundary, it is expected that the effects of the boundary on the lateral response of the soil profile can be discerned. All of the analyses discussed herein involve the rigid pile kinematic case.

The distributions of the characteristic $p-y$ curve parameters are plotted in Figure 6.14. As could be expected, the initial stiffness values returned from the two meshes are very similar. The proximity of the boundary should not significantly affect the response of the soil at such low levels of pile displacement. The differences between the two distributions are easily attributable to minor variations in the meshing around the pile between the two models. The ultimate lateral resistance, however, displays a reduction in magnitude for the extended mesh case as compared to the standard mesh case. This result confirms the suspicion that the fixed boundary is able to affect the results of the laterally-loaded pile models, at least with regards to the ultimate resistance provided by the soil elements.

The value of p_u returned by the models reflects the maximum load that the pile can exert on the soil before failure. This parameter is directly related to failure of the soil surrounding the pile. The Drucker-Prager plasticity model has a pressure-dependent yield surface, indicating that as the confining pressure on a particular element increases, there is a corresponding increase in the yield capacity for that element. This indicates that p_u should increase with either increasing depth or

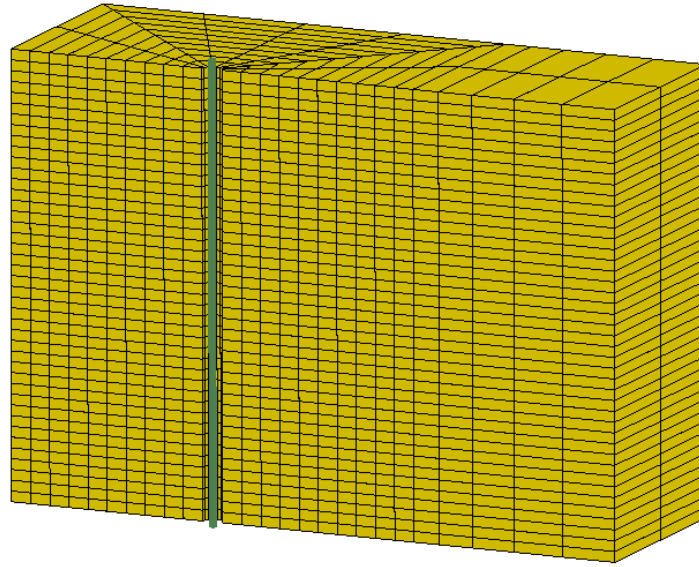


Figure 6.13 Laterally-extended mesh for 0.61-m-pile design.

with increasing confining stress. As the pile is pushed laterally, the soil elements must deform to accommodate its passage. At shallow depths, the overburden stress is relatively small, thus, the soil elements are pushed outwards and upwards by its passage. The distribution of this soil heave extends well in front of the pile, and to the side as well, as illustrated in Figure 6.15, which shows the distribution of vertical displacement in the soil in a plan view.

At increased depth, the overburden pressure in the soil elements becomes larger due to both the self weight of the soil and the active pressure provided by the overlying elements expanding upwards. The zone in which the soil elements are pushed upwards and outwards by the passage of the pile therefore reduces in areal extent with increasing depth, naturally forming a wedge-like shape of moving soil in front of the pile. This type of wedge failure can clearly be seen in Figure 6.16, which shows the distribution of positive vertical displacements in the extended mesh model. The formation of the wedge affects the deeper soil elements by actively increasing the confining pressure as it expands.

In the case of the standard mesh, shown in Figure 6.17, the proximity of the fixed boundary prevents the formation of a full wedge by limiting the forward movement of the soil elements. The boundary also allows for larger compressive lateral stresses to develop. The overburden pressure can be overcome more easily at deeper locations, leading to the increased magnitude in vertical displacements and the increased extents of this upwardly-moving zone displayed in Figure 6.17.

These increases in the volume of soil that is moved upwards and the magnitude of the vertical displacement leads to an increase in the confining pressure at lower depths, especially as compared to the results obtained from the laterally extended mesh. The stress increase can be observed in Figures 6.18 and 6.19, which show the distributions of the first invariant of stress, $I_1 = \sigma_1 + \sigma_2 + \sigma_3$, in the two models. As shown, the first stress invariant is significantly larger in compression in the standard mesh than in the extended mesh due to the proximity of the pile to the fixed boundary. The observed increase in the ultimate lateral resistance of the soil elements in the standard mesh

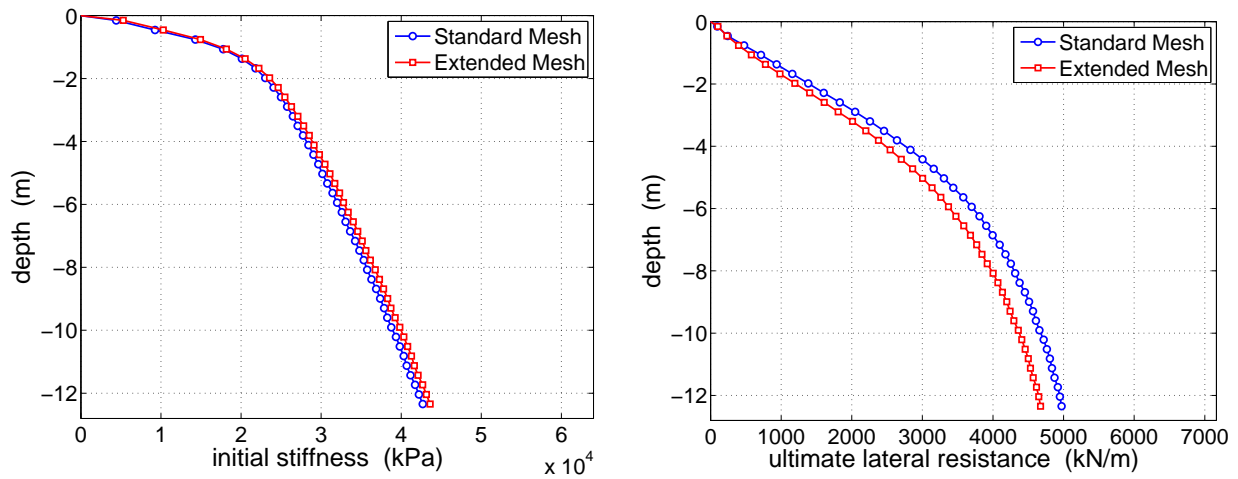


Figure 6.14 Comparison of $p-y$ curve parameter distributions for extended and standard meshes for a 0.61-m-diameter pile.

over that displayed by the extended mesh shown in Figure 6.14 is attributable to the increased confining stresses in that model.

The increase in the estimated values of p_u associated with the use of the standard mesh is apparent, but is not necessarily significant. In the current simulations, the pile is not pushed sufficiently far into the soil as to fully activate the ultimate resistance of the soil at depth. Due to this shortcoming, the obtained values of p_u in these locations are extrapolated by the curve-fitting procedure and may not represent the true capacity of the soil. This observation, along with alternative plasticity formulations that alleviate the boundary effects, is analyzed and discussed in Chapter 7.

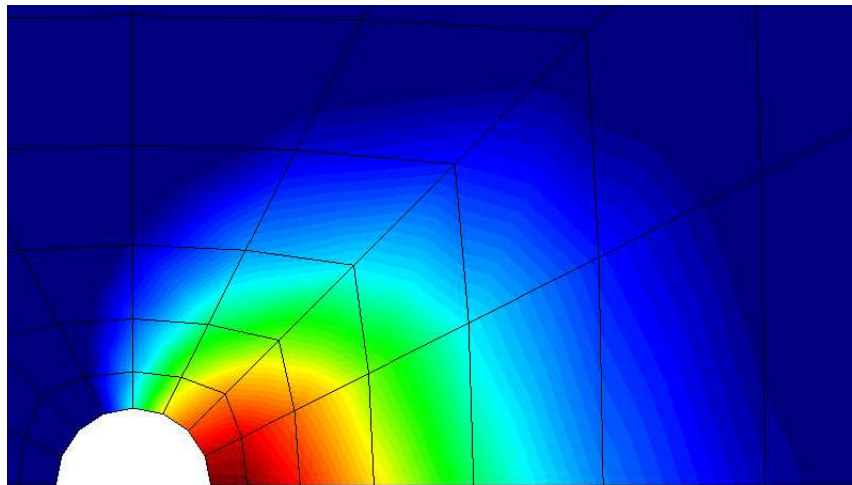


Figure 6.15 Plan view showing the distribution of vertical displacement (i.e., soil heave) in the soil elements. The areas near the pile indicate the greatest magnitude of displacement, while the constantly shaded areas near the boundaries have zero displacement.

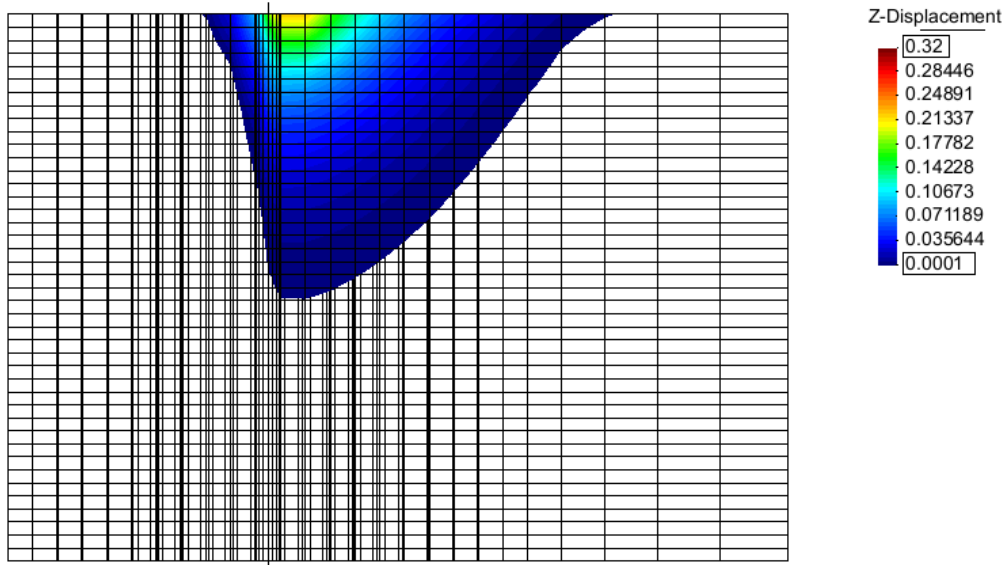


Figure 6.16 Contour plot of vertical soil displacements in the extended mesh. Only upward displacements are considered.

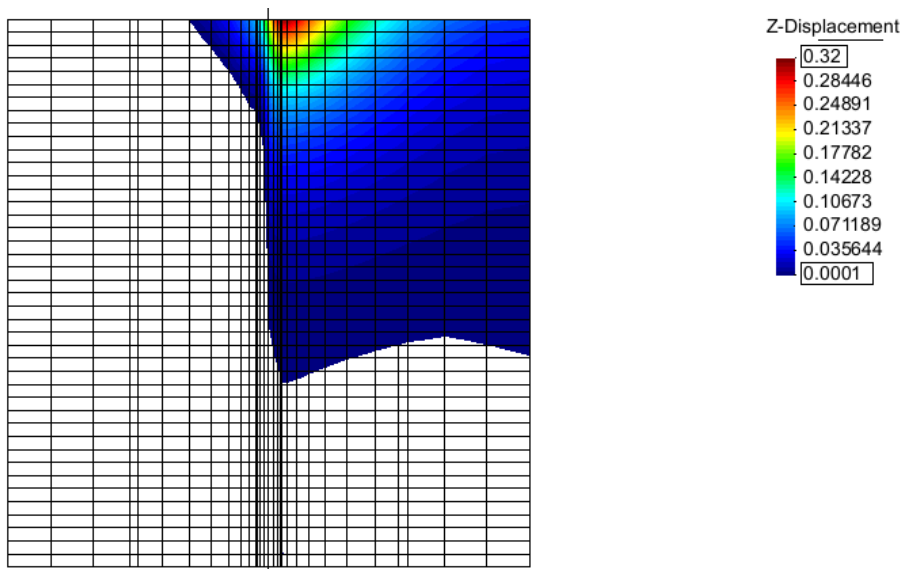


Figure 6.17 Contour plot of vertical soil displacements for the rigid pile case in the standard mesh. Only upward displacements are considered.

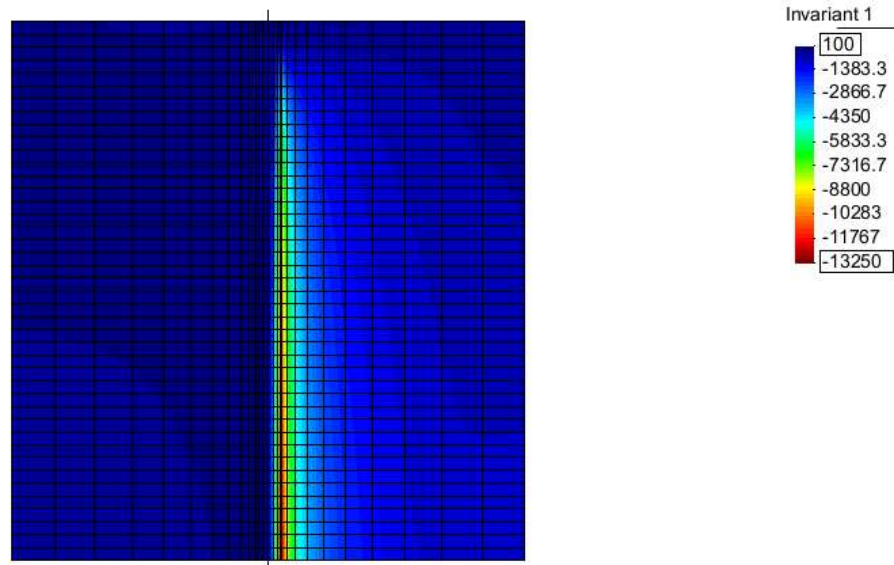


Figure 6.18 Distribution of the first invariant of stress, I_1 , in the standard mesh for a 0.61-m-diameter pile.

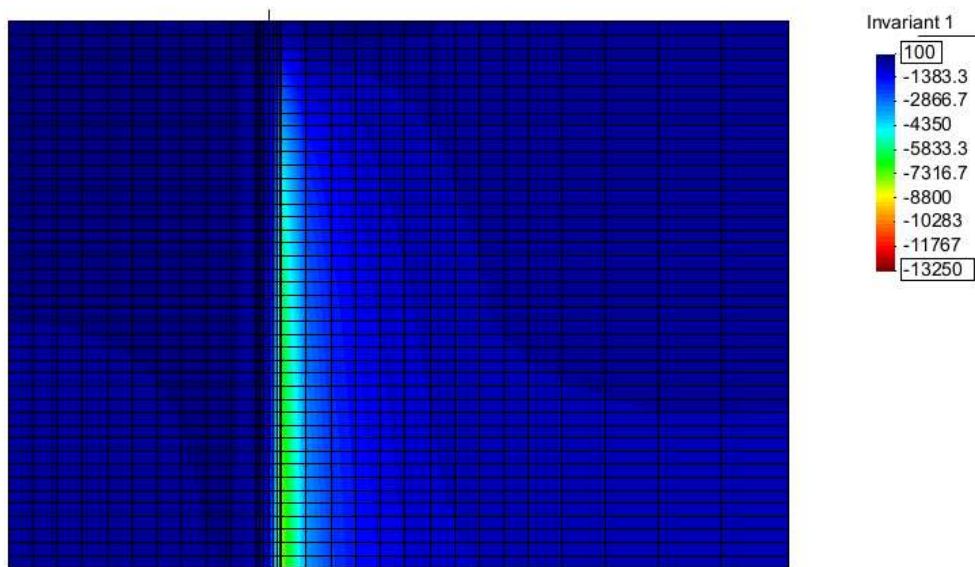


Figure 6.19 Distribution of the first invariant of stress, I_1 , in the extended mesh for a 0.61-m-diameter pile.

6.8 SUMMARY

It is of interest to evaluate the results obtained using 3D FE models of piles embedded in laterally spreading soils in the context of the commonly used $p-y$ method. In order to accomplish this goal, a method in which to extract reliable and sensible $p-y$ curves was developed. Least squares is used to fit functions to the computed data in order to describe the computed $p-y$ curves and to identify the key curve parameters of initial stiffness, k_T , and ultimate lateral resistance, p_u .

It is determined that the pile kinematics in these simulations play an important role in defining the success rate for $p-y$ curve extraction from the FE model. It is observed that in addition to the known effects of differential soil layer strength on the $p-y$ curves for a given case, there is also a tangible effect that can only be attributed to the kinematics of the piles. For lateral spreading and top pushover kinematics, the generated curves differ in quality and consistency based upon the magnitude of the displacement at their respective nodes and how these displacements evolve over the duration of the deformation. A rigid pile kinematic case is proposed as an appropriate means for computing $p-y$ curves from 3D FE analysis.

It is also observed that variations in the size of the mesh along the length of the pile cause the soil response to be inconsistently represented in the results. A uniformly-meshed model is generated, and the ratios of k_T and p_u in this new model to corresponding results obtained using a selectively refined mesh are used in order to smoothen the past results. When analyzing the ratios of two cases formed using the same mesh, these effects are unimportant; however, in order to view the parameter distributions with their actual values or to compare results from a dissimilar mesh, the smoothing process must be employed.

The effects of the fixed boundaries on the recorded soil response are also explored. It is determined that the initial stiffness of the curves is unaffected by the proximity of the boundary to the center of the pile; however, the ultimate lateral resistance of the curves is reduced by up to 10% when the lateral extents of the model are increased. This reduction is related to the ability of the extended soil mesh to allow a full soil failure wedge to develop as well as the increased capacity for the soil to compress before the pile begins to feel the boundary. This study indicates that the presence of the fixed boundary is able to affect the distribution of ultimate lateral resistance in the soil, though only to a certain degree.

7 Applicability of Conventional and Computed $p-y$ Curves to Lateral Spreading Analysis

7.1 INTRODUCTION

A simplified BNWF analysis of a pile subject to lateral spreading must utilize $p-y$ curves that appropriately represent the soil response and that are applicable to the pile kinematics involved. Many methods have been developed for the purpose of defining $p-y$ curves for various soil types. Ideally, one of these existing definitions, which are readily available to practicing engineers, can be used successfully for the lateral spreading load case; however, the applicability of these conventional $p-y$ curves to this type of analysis must be verified.

For cohesionless soils, the recommendations of the American Petroleum Institute (API, 1987) are commonly used to define distributions of initial stiffness and ultimate lateral resistance for $p-y$ curves. Other methods for defining these parameters exist, among them the methods of Broms (1964), Fleming et al. (1985), and Brinch Hansen (1961). To evaluate the applicability of these methods to the lateral spreading load case, comparisons are made between the previously identified characteristic curve parameters of initial stiffness, k_T , and ultimate lateral resistance, p_u , for these cited methods and the $p-y$ curves computed from 3D FE analysis.

Examination of the results from the 3D FE analysis indicate that increased mesh resolution is required to capture the appropriate soil response at near-surface depths. A solution is provided through the generation of a series of new meshes that only consider the soil and pile up to a depth of 10 m. The decrease in depth allows for increased mesh refinement over the standard models with no corresponding increase in computational demand. Evaluation of the existing 3D results indicates that the magnitudes of p_u returned from the 3D models at depth are significantly less than those predicted using cited methods. Plane strain models are generated and analyzed in order to investigate this observation. The results of the near-surface and plane strain 3D FE analysis are compared to existing methods for defining $p-y$ curves.

7.2 A BRIEF SUMMARY OF THE CONSIDERED PREDICTIVE METHODS

A laterally loaded pile is a difficult problem to analyze, as it is highly three-dimensional as well as nonlinear. This inherent complexity lends difficulty to the determination of suitable distributions of

ultimate lateral resistance and initial stiffness to represent the soil response along the length of the pile. Over the past fifty years, there have been multiple methods proposed for defining appropriate distributions of these parameters for cohesionless soils. These methods often utilize approximate analyses and semi-empirical strategies. Perhaps due to the inherent simplifications necessary to reach these proposed solutions, the results obtained from the various methods display significant variation.

7.2.1 Ultimate Lateral Resistance

Four methods for defining ultimate lateral resistance of cohesionless soils are considered. In general, each method defines p_u as functions of some soil shear strength parameter, such the angle of internal friction, the soil unit weight, the diameter of the pile, and the depth below the ground surface. These are all constant values for a particular problem, indicating that the resulting ultimate resistance values from the various methods should be similar, however, in practice, the various methods produce resistances that display significant variation for matching input parameters.

This tendency is demonstrated in Figure 7.1, which shows the distributions of p_u estimated by the four considered methods for a 0.5-m-diameter pile in soil having a unit weight, $\gamma = 20 \text{ kN/m}^3$, and a friction angle, $\phi = 35^\circ$. The four considered methods vary in complexity and, as shown, also vary greatly in their results, especially at depth. A summary of the essentials of each of the considered methods follows.

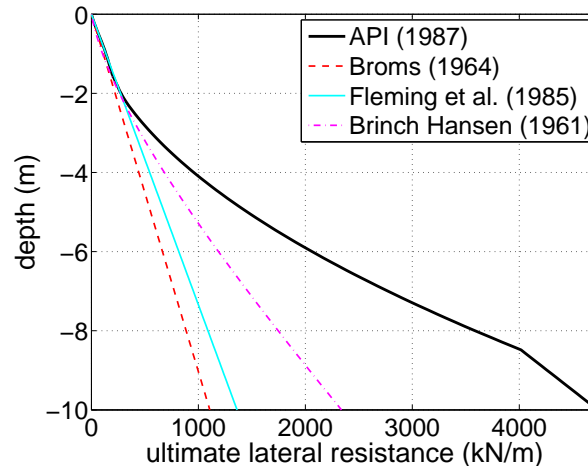


Figure 7.1 Distributions of ultimate lateral resistance for a 0.5-m-diameter pile as specified by four predictive methods.

Method of Broms

Broms (1964) proposed a method based upon the passive earth pressure coefficient, K_p , calculated using Rankine earth pressure theory as

$$K_p = \tan^2 \left(45^\circ + \frac{\phi}{2} \right) \quad (7.1)$$

Working under the assumptions that the active earth pressure acting on the back of the pile can be neglected and that the shape of the pile has little effect on the mobilized soil resistance, Broms proposed the following expression for the prediction of the ultimate lateral resistance, p_u , in units of force per unit length of pile

$$p_u = 3K_p\gamma zB \quad (7.2)$$

in which z is the depth, γ is the soil unit weight, and B is the pile diameter. Broms defined the distribution of passive pressure on the front of the pile to be equal to three times the Rankine earth pressure coefficient based upon correlations with limited empirical evidence, indicating that this tends to underestimate the magnitude of p_u which in turn leads to conservative results when applied to a pile. This method creates a distribution of lateral resistance that varies linearly with depth, making no distinctions for depth-appropriate failure mechanisms such as wedge failure at near-surface depths or flow-around failure at deeper depths. As shown in Figure 7.1, Broms' method estimates the lowest values of p_u with depth of all the considered procedures.

Method of Fleming et al.

Using a similar line of thought to that of Broms, Fleming et al. (1985) proposed a distribution of p_u that is proportional to the square of the Rankine passive earth pressure coefficient and is described by the expression

$$p_u = K_p^2\gamma zB \quad (7.3)$$

The method of Fleming et al. results in a linear distribution of p_u with depth with no consideration of depth-appropriate failures. Compared to the method of Broms, which tends to underestimate the magnitude of p_u , the values of p_u calculated using Equation (7.3) compare more favorably with empirical results. When the angle of internal friction $\phi = 30^\circ$, the results of Equations (7.2) and (7.3) are identical. For most sands encountered in the field, $\phi > 30^\circ$. Therefore, in the majority of cases, the method of Fleming et al. produces larger values of p_u with depth than the method proposed by Broms.

API Recommended Method

For cohesionless soils, the recommendations of the American Petroleum Institute API (1987) are commonly used to define $p-y$ curves for use in a BNWF analysis. The API recommendations adopt the work of Reese et al. (1974) with slight modifications, namely in the use of a hyperbolic tangent function to define the overall shape of the $p-y$ curves. The distributions of p_u and k_T proposed by Reese et al. match those recommended by the API exactly. The method recommended by the API returns the largest values of p_u with depth of any of the four considered methods.

The ultimate lateral resistance recommended by the API accounts for two distinct depth-specific

failure mechanisms, leading to two expressions

$$p_u = \bar{A}\gamma z \left[\frac{K_o z \tan \phi \sin \theta}{\tan(\beta - \phi) \cos \alpha} + \frac{\tan \beta}{\tan(\beta - \phi)} (B + z \tan \beta \tan \alpha) \right. \\ \left. + K_o z \tan \beta (\tan \phi \sin \beta - \tan \alpha) - K_a B \right] \quad (7.4)$$

$$p_u = \bar{A}\gamma z B [K_a (\tan^8 \beta - 1) + K_o \tan \phi \tan^4 \beta] \quad (7.5)$$

of which the lesser result is taken as p_u for a particular depth. The coefficient, \bar{A} is determined from the ratio of depth, z , to pile diameter, B . It is recommended to take $K_o = 0.4$ and define the other terms of Equations (7.4) and (7.5) as

$$\alpha = \frac{\phi}{2} \quad (7.6)$$

$$\beta = \frac{\pi}{4} + \alpha \quad (7.7)$$

$$K_a = \tan^2 \left(\frac{\pi}{4} - \alpha \right) \quad (7.8)$$

At near surface depths, Equation (7.4) accounts for a wedge-type failure of the soil. The wedge-type failure mechanism controls the ultimate lateral resistance resulting from this method from the ground surface until a certain depth at which the curves defined by Equations (7.4) and (7.5) intersect. At this intersection point, which generally occurs well below the ground surface, the failure mechanism changes from the wedge failure to a plane strain failure mode in which the soil must flow around the pile. The depth at which this transition occurs is dependent upon both the diameter of the pile and the friction angle of the soil. As the magnitudes of these values increase, the depth of the intersection between the wedge and plane strain failure curves also increases. In Figure 7.1, this intersection occurs at a depth of approximately 8.5 m.

Method of Brinch Hansen

The method of Brinch Hansen (1961) provides a means of estimating the ultimate lateral resistance for a general frictional soil with cohesion. Brinch Hansen proposed a distribution of ultimate lateral resistance of the form

$$p_u = (\gamma z K_q^D + c K_c^D) B \quad (7.9)$$

where c is the cohesive intercept, γ is the soil unit weight, z is the depth, and B is the pile diameter. The coefficients K_q^D and K_c^D are determined using a methodology developed by Brinch Hansen, who also approached the problem with consideration towards appropriate soil failure mechanisms with depth. This is accomplished by defining limiting values of p_u at the ground surface and at great depth. Using these limiting values, the ultimate lateral resistance at any arbitrary depth is determined through interpolation.

For a cohesionless soil, $c = 0$, and the second term of Equation (7.9) becomes zero. The coefficient K_q^D must be determined based upon two extreme cases. The limiting value of K_q^D existing at the surface ($z = 0$) is designated as K_q^0 and is defined as the difference between the passive and active coefficients corresponding to the lateral translation of a rough wall, resulting in the expression

$$K_q^0 = \exp \left[\left(\frac{\pi}{2} + \phi \right) \tan \phi \right] \cos \phi \tan \left(\frac{\pi}{4} + \frac{\phi}{2} \right) - \exp \left[- \left(\frac{\pi}{2} - \phi \right) \tan \phi \right] \cos \phi \tan \left(\frac{\pi}{4} - \frac{\phi}{2} \right) \quad (7.10)$$

The limiting value at great depth, K_q^∞ , is based upon the analysis of a deep strip foundation conducted using a plane strain soil failure mechanism. This analysis results in the following expression, which defines the largest possible value of K_q^D , occurring at depth $z = \infty$.

$$K_q^\infty = N_c d_c^\infty K_0 \tan \phi \quad (7.11)$$

The terms N_c , d_c^∞ , and K_0 in Equation (7.11) are defined as

$$N_c = \left[\exp(\pi \tan \phi) \tan^2 \left(\frac{\pi}{4} + \frac{\phi}{2} \right) - 1 \right] \cot \phi \quad (7.12)$$

$$d_c^\infty = 1.58 + 4.09 \tan^4 \phi \quad (7.13)$$

$$K_0 = 1 - \sin \phi \quad (7.14)$$

Using these limiting values, K_q^0 and K_q^∞ , Brinch Hansen proposed that the coefficient corresponding to any arbitrary depth be computed using

$$K_q^D = \frac{K_q^0 + K_q^\infty a_q \frac{z}{B}}{1 + a_q \frac{z}{B}} \quad (7.15)$$

in which the term a_q is determined as

$$a_q = \frac{K_q^0}{K_q^\infty - K_q^0} \cdot \frac{K_0 \sin \phi}{\sin \left(\frac{\pi}{4} - \frac{\phi}{2} \right)} \quad (7.16)$$

The method of Brinch Hansen estimates values for p_u that fall intermediately between the linear methods proposed by Broms and Fleming et al. and API recommended distribution.

7.2.2 Initial Stiffness

The API (1987) recommendations suggest the following hyperbolic tangent function to describe the shape of $p-y$ curves for cohesionless soils

$$p = Ap_u \tanh \left(\frac{kz}{Ap_u} y \right) \quad (7.17)$$

in which k is the coefficient of subgrade reaction, A is a coefficient based on empirical correlations to account for the type of loading (i.e., cyclic or static), and the other terms are as previously defined. Evaluating the derivative of Equation (7.17) with respect to y at the point $y = 0$ leads to a definition of the initial stiffness as $k_T = kz$.

The API recommends values of the coefficient of subgrade reaction, k , which are representative of sands both above and below the water table. Figure 7.2 shows the representative coefficient of subgrade reaction values for each case as functions of relative density and internal friction angle. As shown, the coefficient of subgrade reaction increases nonlinearly as the shear strength of the soil increases (as represented by increasing relative density or friction angle).

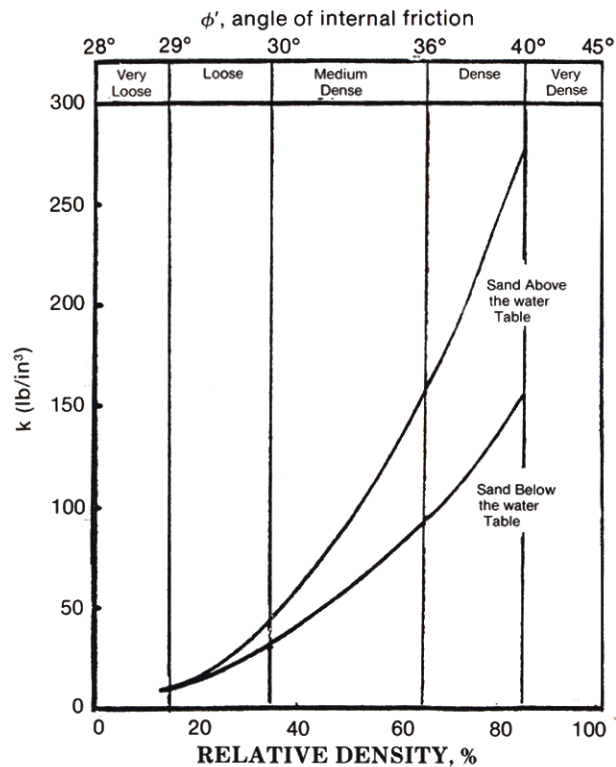


Figure 7.2 Recommended coefficient of subgrade reaction after API (1987). The conversion from units of lb/in^3 is obtained through multiplication with a factor of 271.45 to obtain units of kN/m^3 .

It is somewhat well known, and is shown in this report, that the linear distribution of initial stiffness recommended by the API does not represent the actual initial soil response well. These recommendations are based on lateral load tests, where the near-surface response is captured well. Extrapolation of this near-surface behavior to all depths leads to significant overestimation of the initial stiffness at increased depth. Recognizing that the elastic modulus of sand is roughly proportional to the square root of confining pressure, Boulanger et al. (2003) propose an approximate correction for the API subgrade reaction modulus. The corrected modulus, k^* , is computed as

$$k^* = c_\sigma k_{\text{API}} \quad (7.18)$$

where k_{API} is the API subgrade modulus from Figure 7.2, and the term c_σ accounts for variation in vertical effective stress, σ'_v , as

$$c_\sigma = \sqrt{\frac{\sigma'_{\text{ref}}}{\sigma'_v}} \quad (7.19)$$

in which σ'_{ref} is a reference stress taken to be 50 kPa. Using this correction procedure, the initial stiffness distribution, $k_T = k^*z$, is parabolic with depth.

7.3 COMPARISON OF COMPUTED AND PREDICTED $p-y$ CURVES

Soil response curves computed from 3D FE analyses are used to investigate the applicability of $p-y$ curves defined using the predictive methods cited above. The distributions of p_u and k_T along the length of the pile obtained from the 3D model are compared to those recommended by the predictive methods to evaluate the validity of each respective method. Because the considered predictive methods have no inherent ability for the inclusion of a liquefied layer, all of the comparisons made in this section are for a homogenous soil profile.

7.3.1 Comparison of Ultimate Lateral Resistance

Figure 7.3 shows computed p_u distributions for three pile diameters at left and computed k_T distributions at right. Plotted with the computed p_u distributions are corresponding distributions for the predictive methods discussed previously. These estimated distributions of p_u are determined using the appropriate pile diameter and depths for each case as well as a soil unit weight $\gamma = 17 \text{ kN/m}^3$ and friction angle $\phi = 36^\circ$, values that correspond to the soil constitutive model in the FE analyses.

All of the p_u distributions, both computed and estimated, show an increase in resistance with depth; however, the way in which p_u increases differs across the methods and the shape of the computed p_u distribution does not directly correlate to any of the considered predictive methods. At shallow depths, there is a fair amount of agreement for all methods. This similarity occurs from the surface to a depth of approximately two pile diameters. Beyond this depth, the distributions begin to diverge.

The computed and predicted p_u distributions display a diameter dependence. As pile diameter increases, the corresponding value of p_u also increases. A larger zone of soil is affected by a larger pile, and consequently, more resistance is provided prior to the yield of this zone. This effect becomes more pronounced with increasing depth. As depth and confining pressure increase, the shear strength of the soil also increases, leading to a larger ultimate lateral resistance.

In order to evaluate the applicability of the computed p_u distributions, it is important to consider how well the fitted curve parameters represent the recorded data. Figure 7.4 shows computed $p-y$ curves at five separate depths for a 2.5-m-diameter pile. Near the ground surface the ultimate resistance of the soil appears to have been activated and is appropriately reflected in the fitted parameters. As depth increases, it can no longer be assumed that the ultimate resistance has been

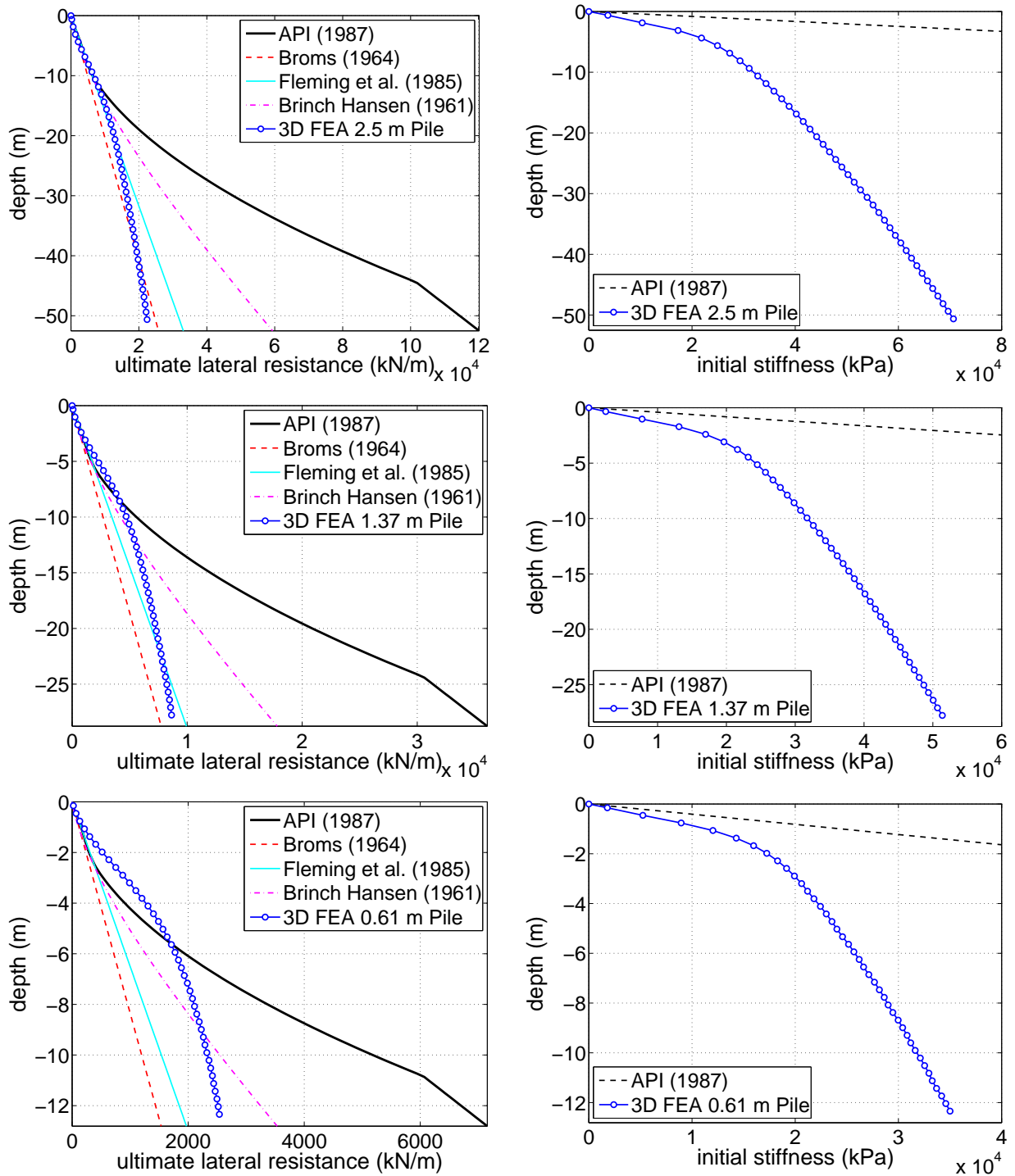


Figure 7.3 Distributions of ultimate lateral resistance and initial stiffness for each of the three template pile designs as compared to commonly referenced distributions.

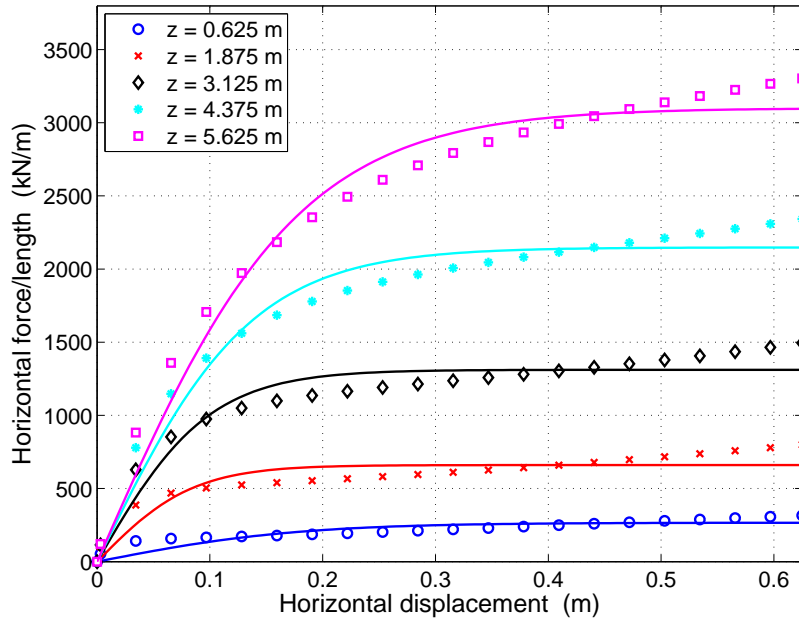


Figure 7.4 Comparison of computed $p-y$ data with fitted hyperbolic tangent curves for a 2.5-m-diameter pile.

achieved. The fitted curves appear to underestimate the ultimate resistance with increasing depth, and the degree to which p_u is underestimated tends to increase with depth.

Figure 7.5, which shows the distribution of stress in the direction of pile motion at the ultimate displacement of the pile, further supports this observation. As shown, the soil elements at shallower depths have reached a limiting value of stress during the deformation process, indicative of yielding in the soil, while the deep elements continue to gain stress, indicating that these elements have not yet experienced failure, nor activated an ultimate resistance.

The observation that the deeper curves do not display results indicating failure of the soil makes sense in the context of the Drucker-Prager soil model. The confining pressure increases with depth, and an increase in confining pressure leads to an increased yield strength in the soil model. The limitations of the current model are such that it is not possible to push the pile far enough to sufficiently activate the ultimate resistance at increased depths without suffering mesh distortion and failure of the simulation. Moreover, the small strain/deformation assumption already reaches its limits under the considered deformations. The region over which there is confidence in the ultimate lateral resistance distributions corresponds to the depths at which the FE analysis results are similar to the estimated p_u distributions. This observation identifies the need for further resolution in the finite element models at shallow depths. To accomplish this, near-surface models are generated and analyzed. The results are presented and discussed in the next section.

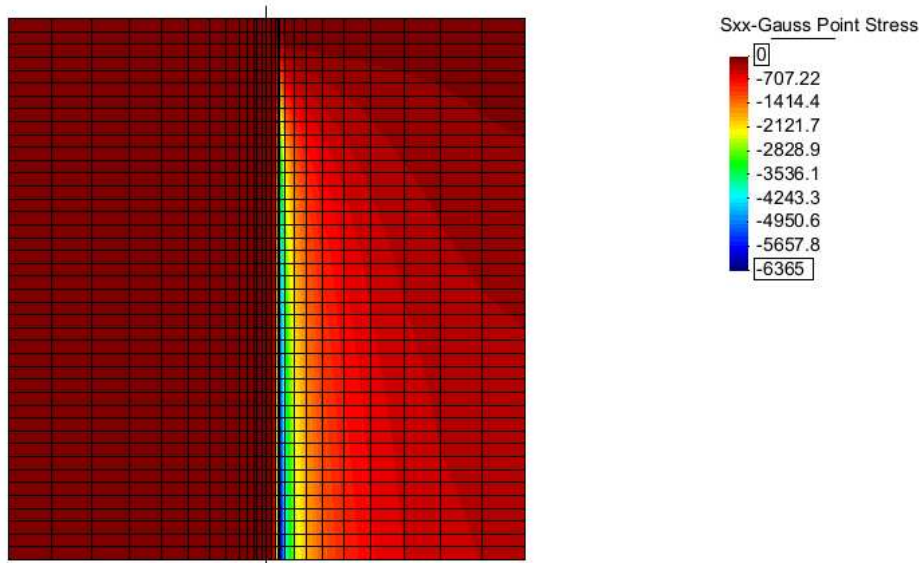


Figure 7.5 Distribution of stress in the direction of loading at full lateral displacement of a 0.61-m-diameter pile in the rigid pile kinematic case.

7.3.2 Comparison of Initial Stiffness

The k_T distributions obtained from 3D FE analysis vary significantly from the linear variation suggested by the API. In Figure 7.3, the linear stiffness shown is based on a subgrade modulus from Figure 7.2 for an internal friction angle $\phi = 36^\circ$. At any particular depth, the resulting linear k_T distribution is larger in magnitude than the computed distributions. This is especially true below the near-surface zone.

The computed initial stiffness distributions show an expected magnitude increase with increasing depth, however, the rate of increase is not constant over the length of the pile. As shown in Figure 7.3, the k_T distributions computed from 3D FE analysis display two distinct linearly-increasing zones. The stiffness at shallow depths is significantly less than those at depth, though the rate of increase in this near-surface zone is greater. As depth increases beyond this initial zone, the rate at which the stiffness increase begins to lessen, eventually reaching a constant level marked by the second zone of linear increase.

The two linear zones displayed by the computed k_T distributions do not correlate well with the API recommendations. There is a diameter dependence shown in the near-surface behavior that is not captured at all by the API k_T distribution. For further comparison, approximate values of subgrade modulus implied by the slope of the computed k_T distributions are used. In the near-surface zone, the approximate subgrade moduli for each pile are summarized in Table 7.1. Taken in the context of Figure 7.2, these values correspond to lower internal friction angles than that used in the 3D simulations. The subgrade modulus suggested at increased depths has a magnitude of approximately 1000 kN/m^3 , which is less than half of the lowest value of k recommended in Figure 7.2.

The two zones of differing response observed in the distributions of initial stiffness computed from

Table 7.1 Approximate coefficients of subgrade reaction for initial portion computed k_T distributions.

	Pile Diameter		
	0.61 m	1.37 m	2.5 m
k (kN/m ³)	11750	7650	5550

the 3D models are related to two separate soil constitutive responses. Near the ground surface, the absence of significant overburden pressure leads to the nearly immediate yield of the soil due to the shear stresses generated by the passage of the pile. Thus, the elastoplastic tangent, and not the purely elastic tangent, is reflected in the initial stiffness returned by the model. At deeper locations, the overburden pressure is large enough to increase the shear strength significantly, resulting in an increased elastic regime for those elements and initial stiffness values that are indicative of the elastic tangent.

The tendency for early yield at shallow depth is illustrated in Figure 7.6, which shows the distribution of the norm of the deviatoric plastic strain, $\|e^p\|$, a good indicator for yielding in the soil elements, for the FE mesh related to the 0.61-m-diameter pile. The distribution of $\|e^p\|$ shown represents the state of the soil in the early stages of loading (second increment in the total displacement of the pile). At this very low level of deformation, the near surface soil elements are already yielding. This zone of yielding is largest at the surface and shrinks with depth. These results suggest that the soil has yielded up to a depth of approximately 1.2 to 1.5 m below the ground surface, which corresponds well with the results shown in Figure 7.3 at which the initial stiffness rate changes for the 0.61-m-diameter pile.

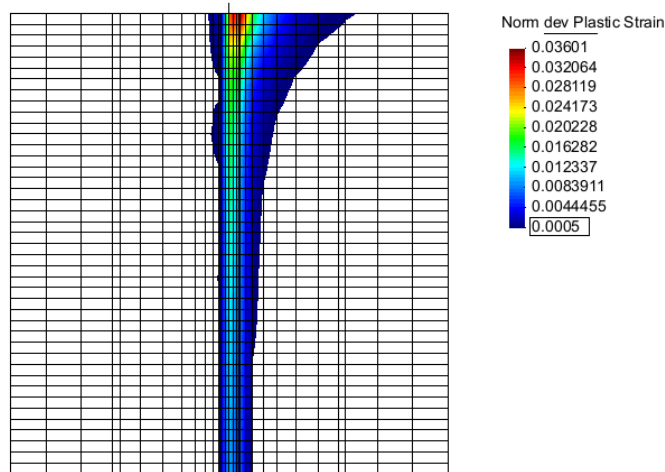


Figure 7.6 Norm of the deviatoric plastic strain, $\|e^p\|$, for a 0.61-m-diameter pile.

In order to explore this idea further, the existing models for each pile are run using linear elastic soil behavior for identical pile displacements. The results of these linear elastic simulations are plotted alongside the elastoplastic results for each pile in Figure 7.7. The elastic distributions increase linearly with depth, and do not start at zero. These elastic stiffness distributions represent

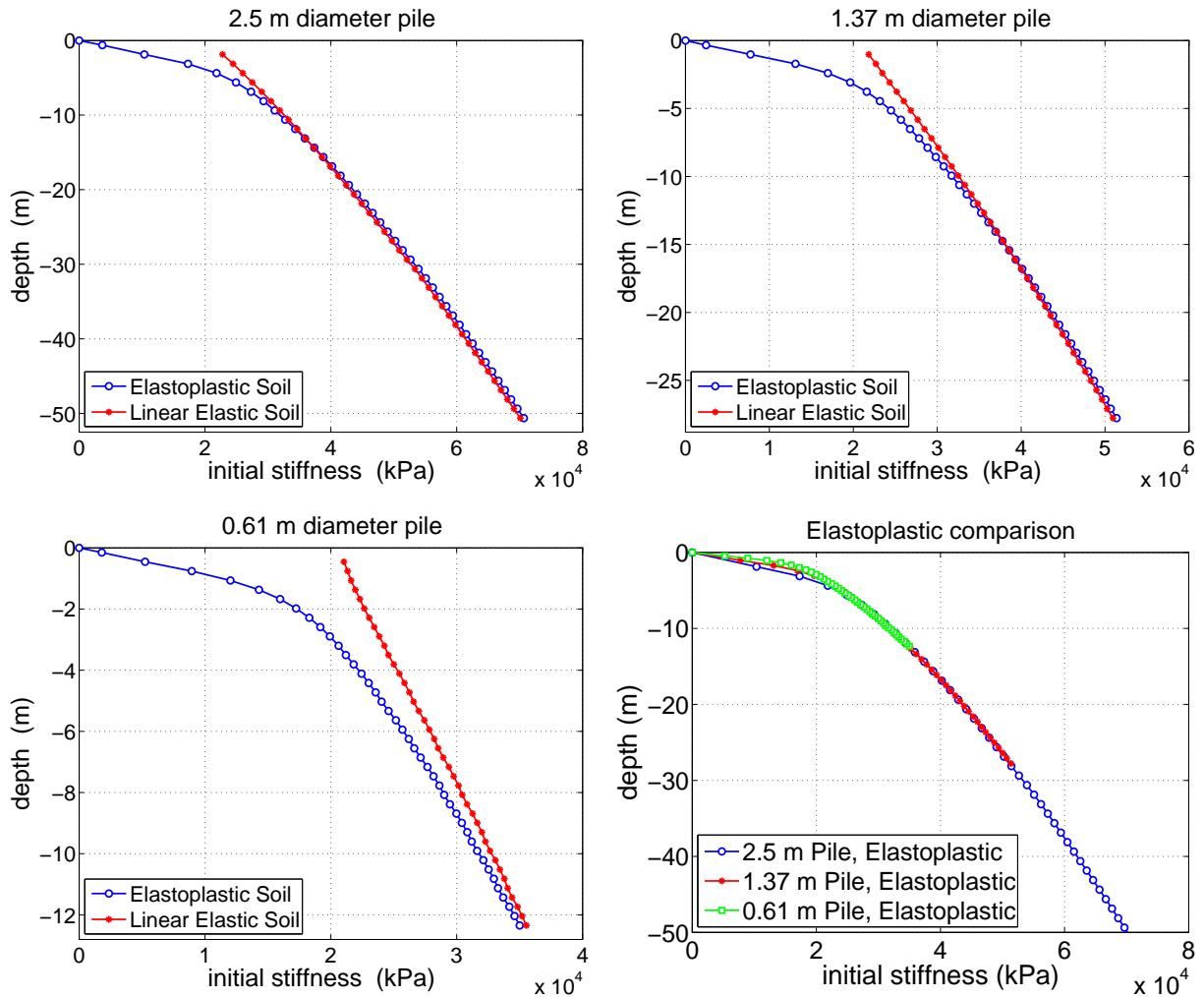


Figure 7.7 Linear elastic and elastoplastic k_T distributions computed from 3D FE analysis.

the largest possible values for the k_T resulting from the elastoplastic models. Once increasing overburden pressure has expanded the elastic regime sufficiently, the initial stiffness of the elastoplastic models should be entirely elastic. Above this point, the elastoplastic tangent is reflected in varying degrees in the elastoplastic initial stiffness distributions, with increasing effects of yielding towards the surface. The depth at which the elastoplastic stiffness becomes equal to the elastic stiffness should be similar for each pile, as the overburden pressure is the deciding factor. As shown in Figure 7.7, this depth is indeed similar for the three pile designs, occurring at approximately 10 m below the surface.

For circular piles, the elastic stiffness of the soil should not depend upon the diameter of the piles. This is confirmed in the lower-right plot of Figure 7.7, which compares the elastoplastic k_T distributions for each pile. As shown, the elastic regions for each distribution coincide. This similarity should not apply to the near-surface depths, where the initial stiffness reflects the yield of the soil. As pile diameter increases, the size of the zone of plasticity on the leading face of the pile should similarly increase. For the 2.5-m-diameter pile, more of the soil elements near

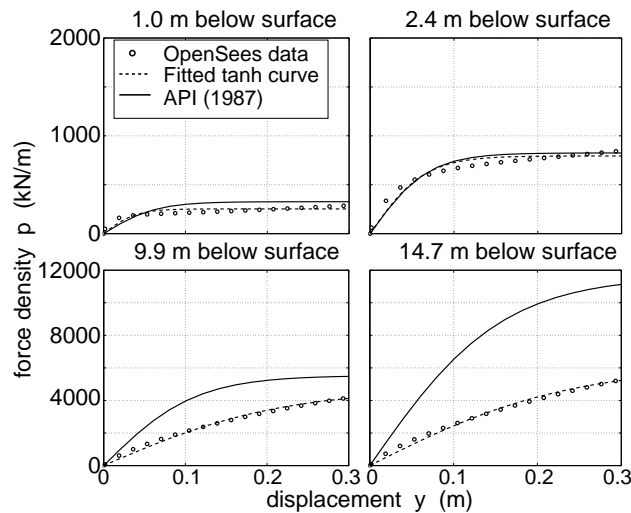


Figure 7.8 Computed and API recommended $p-y$ curves for a 1.37-m-diameter pile.

the surface are yielding than for the smaller piles, therefore, the initial stiffness returned for this larger pile is generally lower than those corresponding to the smaller piles near the surface. This is reflected in the extracted curves shown in Figure 7.7 and in the approximate near-surface subgrade modulus values summarized in Table 7.1. The stiffness at a given depth increases with decreasing pile diameter in this plastic zone.

The observation that the computed k_T distributions for the three pile diameters are similar at depth but differ near the ground surface leads to the desire to obtain a higher degree of resolution on the near-surface areas. A series of 10 m deep meshes are generated, one for each pile design, and analyzed using the same pile deformations. These results offer a means of validating observations made, as well as a closer look at the near-surface effects.

7.3.3 Comparison of $p-y$ Curves

Figure 7.8 shows representative computed $p-y$ data and fitted hyperbolic tangent curves obtained for a 1.37-m-diameter pile. The API 1987 recommended $p-y$ curves are shown for comparison. As is expected based upon the observed differences in k_T and p_u between the computed and API curves, the two sets of curves are comparable at shallow depths while differing substantially at greater depths. For analysis of top-loaded piles, these differences are relatively inconsequential; however, for analysis of a lateral spreading deformation, where large pile deformation can occur at depth, the problems created by these differences become apparent.

7.4 NEAR-SURFACE MODELS

In an effort to gain better insight in the results near the surface, a series of new meshes are generated that only consider the first 10 m below the surface. Modeling only the upper 10 m allows the analyses to focus on the zone of pronounced plasticity in the soil. Due to lessons learned about

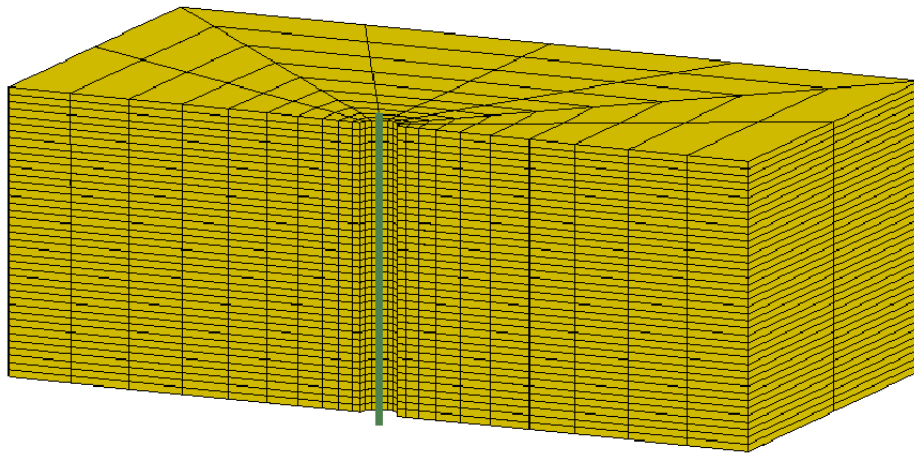


Figure 7.9 Near-surface mesh for a 1.37-m-diameter pile.

selective mesh refinement, the soil and pile elements in the near-surface models are uniformly sized in the vertical direction. Because these models have reduced volume as compared to the default full-sized models, an increase in vertical mesh refinement can be incorporated without increasing the number of degrees of freedom or the corresponding computational effort. These alternative models share the same 10-pile-diameter-by-20-pile-diameter footprint present in the full-sized models. This, along with the differential diameters of the piles, necessitates the creation of three such models, one for each pile design. The generated near-surface mesh for a 1.37-m-diameter pile is shown in Figure 7.9 as a reference.

Rigid pile cases are run using the near-surface models for both elastic and elastoplastic soil elements in order to establish representative $p-y$ curves. These simulations are similar to those previously discussed; however, in an effort to better capture the ultimate resistance, the piles are pushed further into the soil. This, along with the changes in the mesh, produces slightly different results than those obtained using the standard models. Figure 7.10 shows the p_u and k_T distributions resulting from both the default and near-surface meshes. As shown, there are differences between the two models, however, these differences are relatively minor. With respect to initial stiffness, only the results from the 2.5-m-diameter pile see significant change. This is likely due to the increase in mesh refinement present in the near-surface models.

The changes in meshing likely affect the ultimate resistance distributions to a degree as well. While the piles in the near-surface models are pushed further into the soil than in the standard models, this extra deformation only seems to benefit the results for the 0.61-m-diameter pile. The larger piles displace too much soil upwards in front of the piles at this higher level of lateral displacement. The contact elements modeling the pile-soil interface lose contact due to this upward movement of soil, and the results beyond this point become meaningless. For the 2.5-m and 1.37-m-diameter piles, the point at which contact is lost is approximately equal to the ultimate pile displacement specified in the previous models. In the 0.61-m-diameter model, the associated soil heave is much smaller in magnitude and contact is not lost. The resulting ultimate lateral resistances from the near-surface mesh for this pile are larger than in the standard mesh due to the increased soil deformation. In this case, more of the soil elements have reached an ultimate state and the extracted resistance distribution represents the true soil response in a better manner.

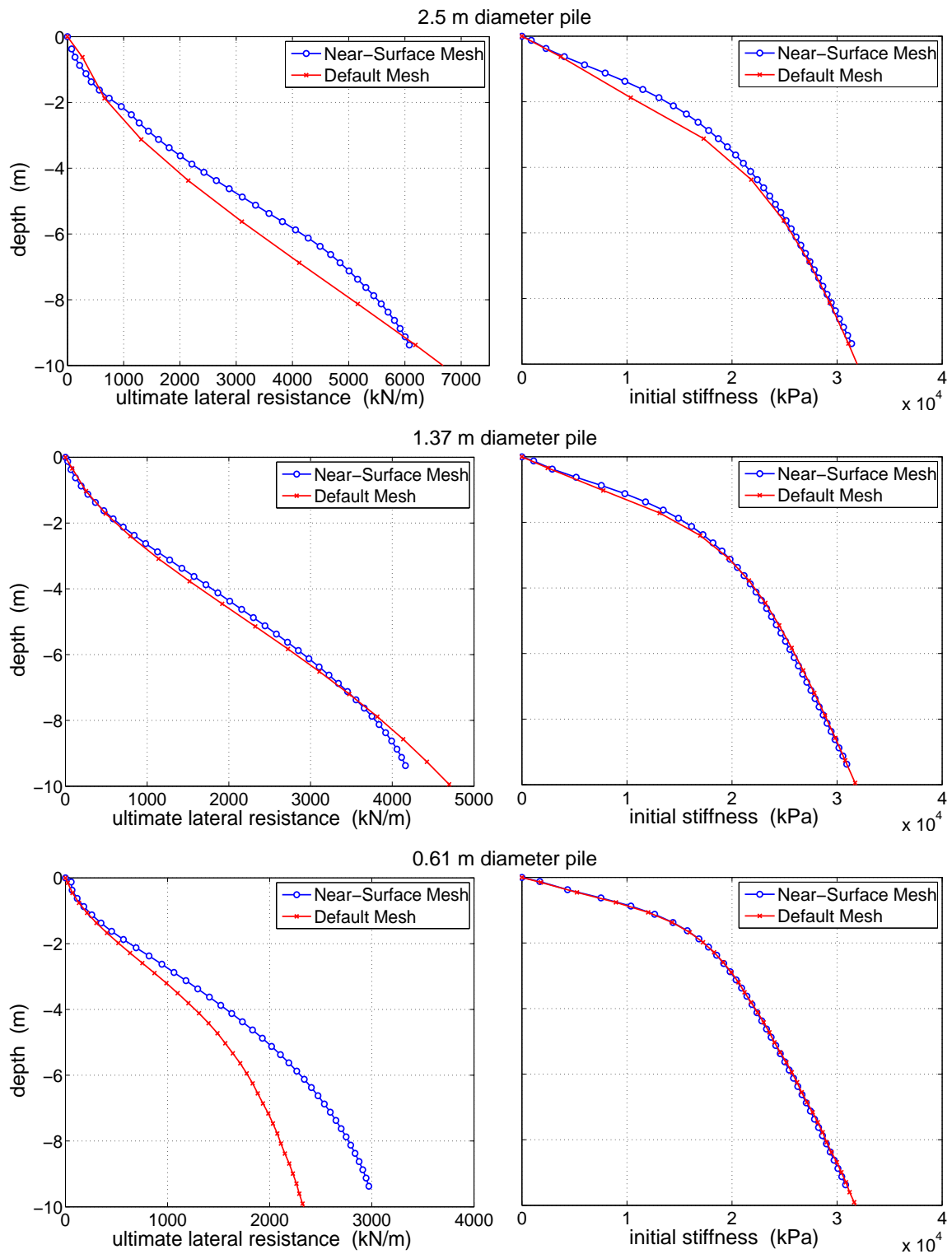


Figure 7.10 Comparison p_u and k_T distributions for default and near-surface meshes over the first 10 m below the ground surface.

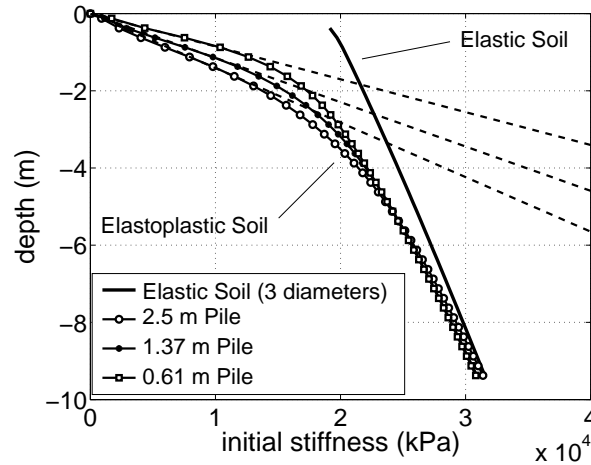


Figure 7.11 Distributions of initial stiffness computed from the near-surface models using both elastoplastic and elastic soil elements.

7.4.1 Initial Stiffness Distributions in Near-Surface Models

The initial stiffness distributions extracted from the near-surface models are only slightly different from those obtained from the standard models. The results from the 1.37-m and 2.5-m-diameter piles show slight increases in stiffness at shallow depths, likely due to the increased mesh refinement in these models. The benefit of the near-surface models with respect to initial stiffness can be seen in Figure 7.11, which shows the distributions resulting from the models for each of the piles. The differences between the initial stiffness in the plastic zone can clearly be seen. As the pile diameter increases, the amount of plasticity in the soil at shallow depth similarly increases. The computed k_T distributions demonstrate this mechanism, as the larger piles experience smaller initial soil stiffness than the smaller piles at corresponding depths. Also of note is the observation that all three of the models reach the elastic stiffness at the same depth. This expected behavior is due to the fact that the state of stress in the soil that defines the size of the elastic regime is independent of the size of the pile and merely dependent upon the weight of the overlaying soil.

7.4.2 Ultimate Lateral Resistance Distributions in Near-Surface Models

The distributions of ultimate lateral resistance in the near-surface models offer a better glimpse into the behavior of the soil at shallow depths. The near-surface models are created such that the pile nodes for each of the three pile diameters are located at the same series of depths, thus, direct comparisons can be made between the p_u distributions resulting from each pile model. Figure 7.12 shows the computed p_u distributions, illustrating the relative differences in magnitude due to changes in pile diameter. This figure clearly shows that as the pile diameter increases, the corresponding ultimate soil resistance to the passage of that pile also increases. As depth increases, this effect becomes more pronounced. This observation seems to be logical. It should take a much larger effort to push a larger pile through soil than it would take to push a smaller pile through the same soil. The ultimate resistance of that soil should increase with increasing pile diameter

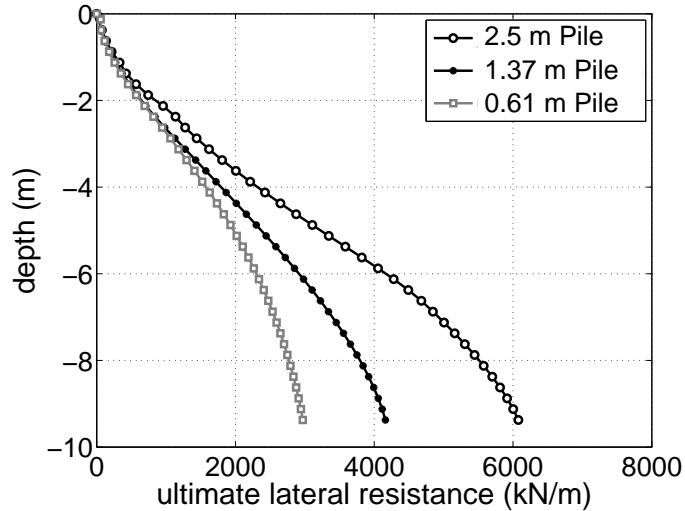


Figure 7.12 Computed p_u distributions for near-surface models.

and with increasing overburden pressure, exactly as observed from the results of the near-surface models.

The ultimate resistance of the soil does not become fully activated at advanced depths in the default mesh FE analysis. In an effort to gain a better estimate of this value with depth, the piles are pushed further into the soil in the near-surface models. As previously discussed, loss of contact between the larger piles and the soil due to a meshing issue renders this extra deformation meaningless for those models, however, the 0.61-m-diameter pile sees increased values of p_u over the results obtained from the standard model because of the extended lateral pile displacement. Though the results from the larger pile models do not see the benefits of the extra push, there is an increase in the number of adequately estimated points on the p_u distribution curves due to the decreased mesh size in the near-surface models as compared to the full-sized (default) counterparts.

7.5 PLANE STRAIN MODELS

With the current mesh and element formulations primarily used in this research, it seems unlikely that the models will be able to capture the true ultimate lateral resistance at all depths along the length of the pile. To establish the maximum attainable value of p_u at a given depth, a plane strain soil model is created. This model also allows a direct comparison to the estimated p_u distributions using the methods proposed by Brinch Hansen (1961) and API (1987). These two methods assumed a plane strain failure mechanism at depth, and the plane strain FE model allows insight into how close conditions in the default 3D model are to plane strain at increased depth.

As this is only a validation exercise, only a single plane strain model is created. This model considers the 2.5-m-diameter pile embedded in a soil continuum. The plane strain mesh shares a footprint with the corresponding standard mesh; however, the plane strain soil mesh is only one element thick in the vertical direction. The pile is reduced in length down to two elements with the middle pile node located at the center of the layer of soil elements. In order to compare the

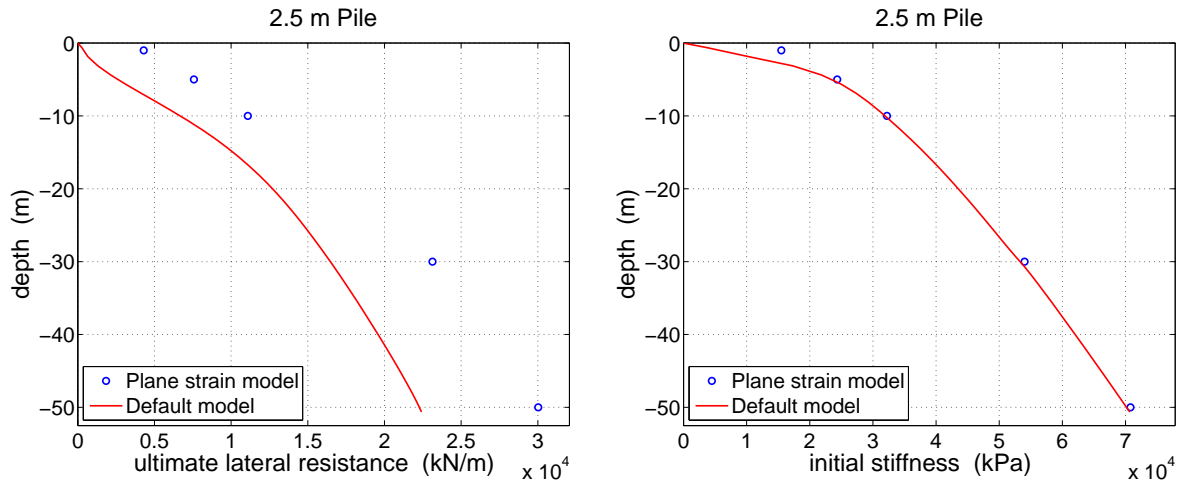


Figure 7.13 Comparison parameter distributions for default and plane strain FE models.

results of the plane strain model with other results, a method of simulating depth is devised that employs the surface load element developed for use in OpenSees during this research. A detailed discussion of these elements is provided in Section 2.5.

In order to obtain a distribution of results with depth at a minimum of modeling effort, a series of five depths is established. These depths are selected such that the resulting data provides a general sense of the $p-y$ curve parameter distributions over the full length of the pile. Appropriate overburden pressures corresponding to each of these depths are applied to the meshes via the surface load elements in order to determine the resulting displacements of the upper surface of the soil elements. When running the plane strain model, the upper nodes of the soil layer are slowly moved via displacement control through these recorded displacements, creating a depth-appropriate initial stress state in the soil elements, and then held fixed in the vertical direction as the pile is pushed into the soil layer. In this manner, the response of the soil for each of the selected depths is established for the plane strain condition.

In the plane strain model, there is no free surface. The early plasticity observed in the regular mesh at shallow depths should not occur. It is expected that the initial stiffness distribution obtained from the plane strain model should exceed that obtained from the standard mesh at shallow depths. At increased depths, the values of k_T obtained from either model should be approximately equal. Assuming the conditions in the default mesh at greater depths are nearly plane strain, the increase in elastic stiffness from the plane strain condition should not be significant.

The ultimate lateral resistances obtained from the plane strain model should be larger than those extracted from the standard model at corresponding depths, especially near the surface where the assumption of a plane strain failure mode is poor. The plane strain condition allows significantly larger confining pressures to develop in the soil elements, leading to a corresponding increase in strength. For this reason, the ultimate resistances from the plane strain model should represent the largest possible resistances that the soil can provide for the lateral displacement of a pile.

Figure 7.13 shows the distributions of p_u and k_T obtained from the plane strain model. As expected, near the surface, the k_T distribution is in excess of that obtained from the default model; at

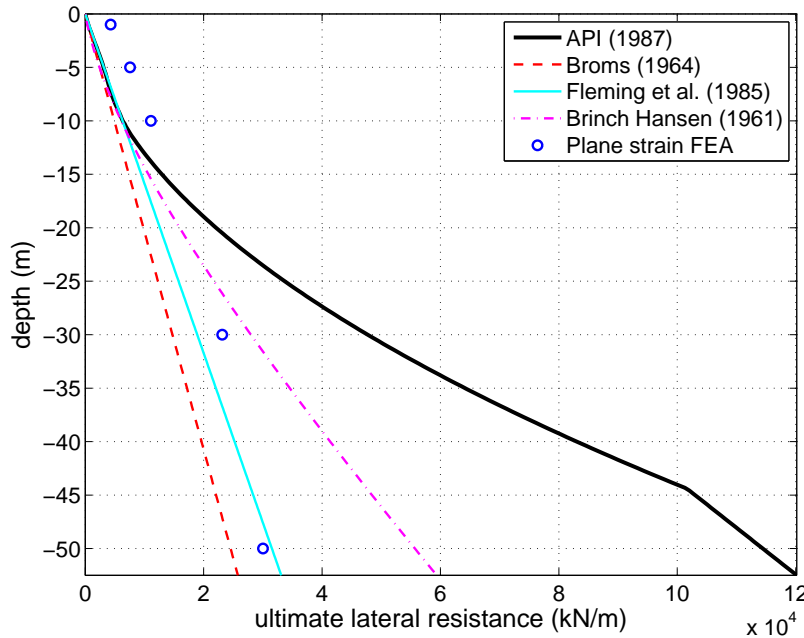


Figure 7.14 Comparison of estimated p_u distributions with corresponding results from plane strain model for a 2.5-m-diameter pile.

depth the distributions are nearly identical. The p_u distribution obtained from the plane strain case also displays the expected behavior. At each depth, the value of p_u resulting from the plane strain condition is greater in magnitude than the corresponding value from the default mesh case. The degree to which these values are exceeded decreases with depth. At a depth of 1 m, where the default models have shown that the plane strain assumption is not applicable, the ultimate resistance in the plane strain model is approximately ten times larger than the previous result, while at 50 m below the surface, the plane strain resistance is about 1.3 times larger.

Figure 7.14 shows estimated distributions for four predictive methods (Broms, 1964; Fleming et al., 1985; Brinch Hansen, 1961; API, 1987) alongside the distribution of p_u obtained from the plane strain FE analysis. As shown, the computed values of p_u at depth are significantly less than those predicted using the API method and are more similar to those predicted by the method of Fleming et al. (1985) or Brinch Hansen (1961).

7.6 SUMMARY

In current practice, the $p-y$ method, which models the soil-pile system as a beam on a nonlinear Winkler foundation, is commonly employed in the analysis of piles subject to lateral loads. Some conventional methods that may be employed in the definition of parameters appropriate for use in $p-y$ curves have been compared. It is observed that there are significant differences in the distributions of ultimate lateral resistance estimated by these methods at depths beyond the first few pile diameters below the surface. It is also observed that the distributions of p_u computed from the 3D FE models generally do not correlate well in their form with any of the predictive methods, though

the magnitudes of the resistances are relatively similar to the softer of the considered predictive methods. The prevalent distribution of initial stiffness recommended for use in $p-y$ curves is entirely linear and appears to be more appropriately applied to near-surface depths where the effects of early soil yield are observed. At increased depth, the full elastic stiffness of the soil is initially active. These values are significantly less than those suggested by conventional methods.

The method for obtaining ultimate resistances recommended by the API (1987) is one of the most commonly employed methods in the construction of $p-y$ curves for cohesionless soil. This method is based essentially upon a single series of field tests in which the piles are loaded at or above the ground surface. As discussed in Section 6.5, the pile kinematics greatly influence the recorded soil response, suggesting that results obtained from a top-pushover kinematic are not necessarily applicable to alternative load cases. Reese and Van Impe (2001) mention that there is more confidence in the form of the predicted results than in the magnitude, which appears to be a fairly valid conclusion as the plane strain FE analysis results provide further evidence that the predicted magnitudes may be excessive.

It is important to note that in the analysis of the top-pushover kinematic, an overestimation of the initial stiffness and ultimate lateral resistance at depth is relatively harmless. In places where the parameter distributions are excessively large, the piles are not undergoing deflections due to the kinematics of the loading. However, in the lateral spreading case, large pile deformations may occur in the areas where k_T and p_u are too large. In simplified analysis of piles subject to lateral spreading, careful selection of $p-y$ curve parameters is essential.

8 Influence of Liquefied Layer on the Soil Response

8.1 INTRODUCTION

In liquefaction-induced lateral spreading, after the onset of liquefaction, the shear strength of the affected soil is reduced significantly. The unliquefied soil near the layer interface is now able to squeeze into the softer layer near the pile during the application of a lateral load, effectively reducing the available lateral capacity and stiffness of the unliquefied soil near the liquefied layer.

Similar behavior occurs for laterally-loaded piles embedded in layered soil profiles in which a strength differential exists between two adjacent layers, e.g., a soft clay layer located between two layers of dense sand. Yang and Jeremic (2005) demonstrated this behavior using 3D FE analysis, and with respect to BNWF analysis of piles, Georgiadis (1983) developed a method to modify $p-y$ curves to account for differential layers. In a BNWF analysis of a pile subject to lateral spreading, the $p-y$ curves should be similarly modified to account for the presence of the liquefied soil layer.

The effect of a liquefied layer on the response of the adjacent unliquefied soil layers is evaluated through comparisons between the results of 3D FE analysis both with and without a liquefied layer. Through the use of overburden pressure applied to the surface of the models, the effect of varying levels of vertical stress at the liquefied interface is also investigated. These initial observations identify the need for a more comprehensive approach to the problem.

A series of new FE meshes are generated and used to compute representative $p-y$ curves for a series of soil profiles in which the vertical location and thickness of the liquefied layer are varied. It is determined that the reduction in the $p-y$ curve parameters of initial stiffness and ultimate lateral resistance is greatest at the layer interface and decays exponentially with increasing distance from the liquefied layer. A simplified procedure is developed to determine appropriate reductions in initial stiffness and ultimate lateral resistance for $p-y$ curves representing the unliquefied soil near the liquefied interface.

8.2 INITIAL OBSERVATIONS

The FE mesh discussed in Chapter 2 is used to evaluate the effect of a liquefied layer on the initial stiffness and ultimate lateral resistance of the unliquefied soil. In this model, the liquefied layer is

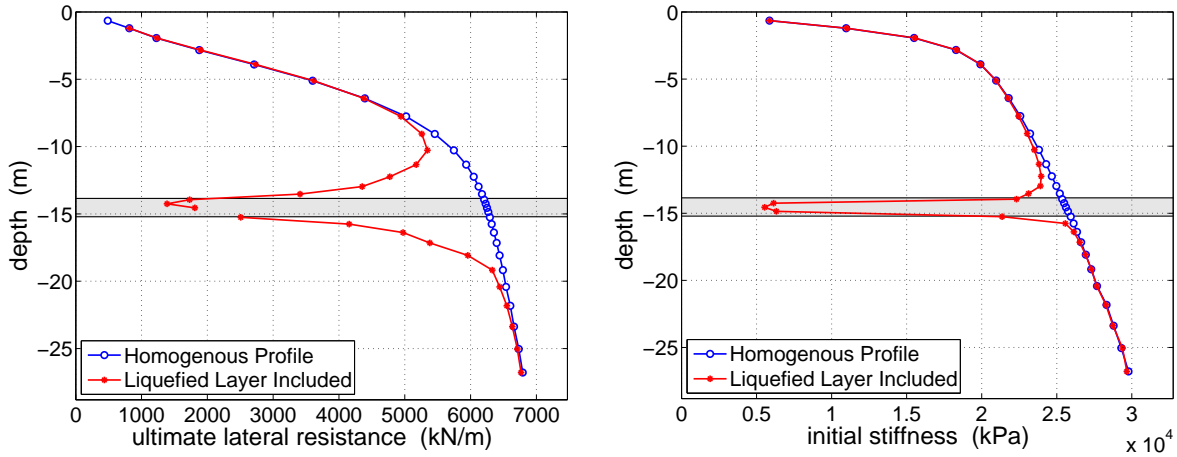


Figure 8.1 Distributions of p_u and k_T for homogenous and liquefied soil profiles for a 1.37-m-diameter pile.

located at a depth of 10 pile diameters below the ground surface and has a thickness of one pile diameter. This soil profile is not ideal for fully characterizing the influence of the liquefied layer for a general case; however, it is used in order to determine the important factors which affect this behavior. To this purpose, p – y curves are computed for homogenous soil profiles and profiles with a liquefied middle layer. The resulting curves are compared with respect to ultimate lateral resistance, p_u , and initial stiffness, k_T . Increasing depth to the liquefied layer is simulated through the application of overburden stresses to the ground surface of the model. This creates a stress state at the liquefied interface that corresponds to a deeper liquefied layer location.

Figure 8.1 presents a comparison of the p_u and k_T distributions resulting from homogenous and liquefied cases for a 1.37-m-diameter pile with no additional overburden pressure. These results are typical of all the considered cases, and have been smoothed to account for variations in mesh size using the procedure discussed in Section 6.6. As shown, the effects of the liquefied layer on the adjacent unliquefied layers are more evident in the distribution of p_u than that of k_T . The curve data obtained from within the liquefied layer is not always of a form that lends itself well to a hyperbolic tangent curve fit. For this reason, values of p_u cannot be computed at some of these nodes. The general trends are still apparent, however, and that is the more important consideration.

The portions of the p_u and k_T distributions in both the upper and lower solid layers are affected by the presence of the liquefied middle layer. The observed reductions in these parameters lessen in magnitude with increasing distance from the liquefied interface. Near the top and bottom of the soil profile, the homogenous and liquefied cases display nearly identical results. The observed reductions in ultimate resistance and initial stiffness are due to a similar behavior as that observed and discussed at shallow depths in Section 7.4. As the pile is pushed laterally into the soil profile, the soil from the solid layers is able to be pushed into the adjacent weaker layer more easily than it can be compressed laterally. This behavior is illustrated in Figure 5.4, which shows the deformed shape of the soil elements in the vicinity of the liquefied layer. When the soil is able to expand in this manner, it results in a decrease in the confining pressure in the areas adjacent to the liquefied layer and a subsequent decrease in the elastic regime for those elements. The soil in these locations

yielding sooner and thus cannot offer as much resistance to the passage of the pile before reaching its ultimate state.

It is of interest to evaluate the differences in effects of the liquefied layer on the two solid layers. The plots of Figure 8.1 provide a good visual comparison between the results obtained from each soil profile, however, it is difficult to gauge relative reductions. In order to provide a better measure of the relative differences between the homogenous and liquefied soil profiles, the ratios of the ultimate resistance and initial stiffness in the liquefied case are taken with respect to the homogenous case, e.g.,

$$p_u \text{ ratio} = \frac{p_u^{(\text{liquefied})}}{p_u^{(\text{homogenous})}} \quad (8.1)$$

These ratios are plotted for a 1.37-m-diameter pile in Figures 8.2 and 8.3 for five considered overburden pressures, representing five different locations of the liquefiable layer. The surcharge pressures are based on hypothetical soil fills with vertical thicknesses of 5, 10, 15, and 20 diameters of the 1.37-m-diameter pile. This results in surcharge pressures of 117, 233, 350, and 466 kPa, respectively, for a soil unit weight of $\gamma = 17 \text{ kN/m}^3$. In Figures 8.2 and 8.3 the location of the liquefied layer is indicated by the shaded region, and the presented results are typical of those obtained for all three piles.

The soil compacts under the applied overburden pressure and self-weight resulting in settlements. The diagrams are shown on the deformed soil body. As the applied overburden pressure increases, the zone of reduced ultimate resistance tends to decrease in thickness, meaning that a lesser extent of the solid layers are affected by the liquefied layer. This is illustrated well through comparison of the p_u ratios for all five overburden pressures at lower right in Figure 8.2. As overburden pressure increases, corresponding to a deeper location for the liquefied layer, the reduction in p_u decreases. At increased overburden pressures, there is increased shear strength in the upper and lower solid layers, which creates a smaller plastic zone. The two layers appear to be affected approximately equally at all five overburden pressures. This is a significant observation given the fact that methods commonly employed in BNWF analysis for accounting for the presence of a soft soil layer, such as that proposed by Georgiadis (1983), only consider the effects of a soft layer on the underlying solid layer. The observation that both surrounding layers are affected by a weaker middle layer confirms similar observations made by Yang and Jeremic (2005) and Petek (2006).

When the five initial stiffness ratios are shown together in the lower right plot of Figure 8.3, it is observed that there is little difference in the reductions in initial stiffness for increasing overburden pressures. The reduction in initial stiffness is also not nearly as widespread or as significant as the observed reduction in p_u . It appears that for a given liquefied layer thickness, the effects of this layer on the initial response of the surrounding solid layers is relatively consistent.

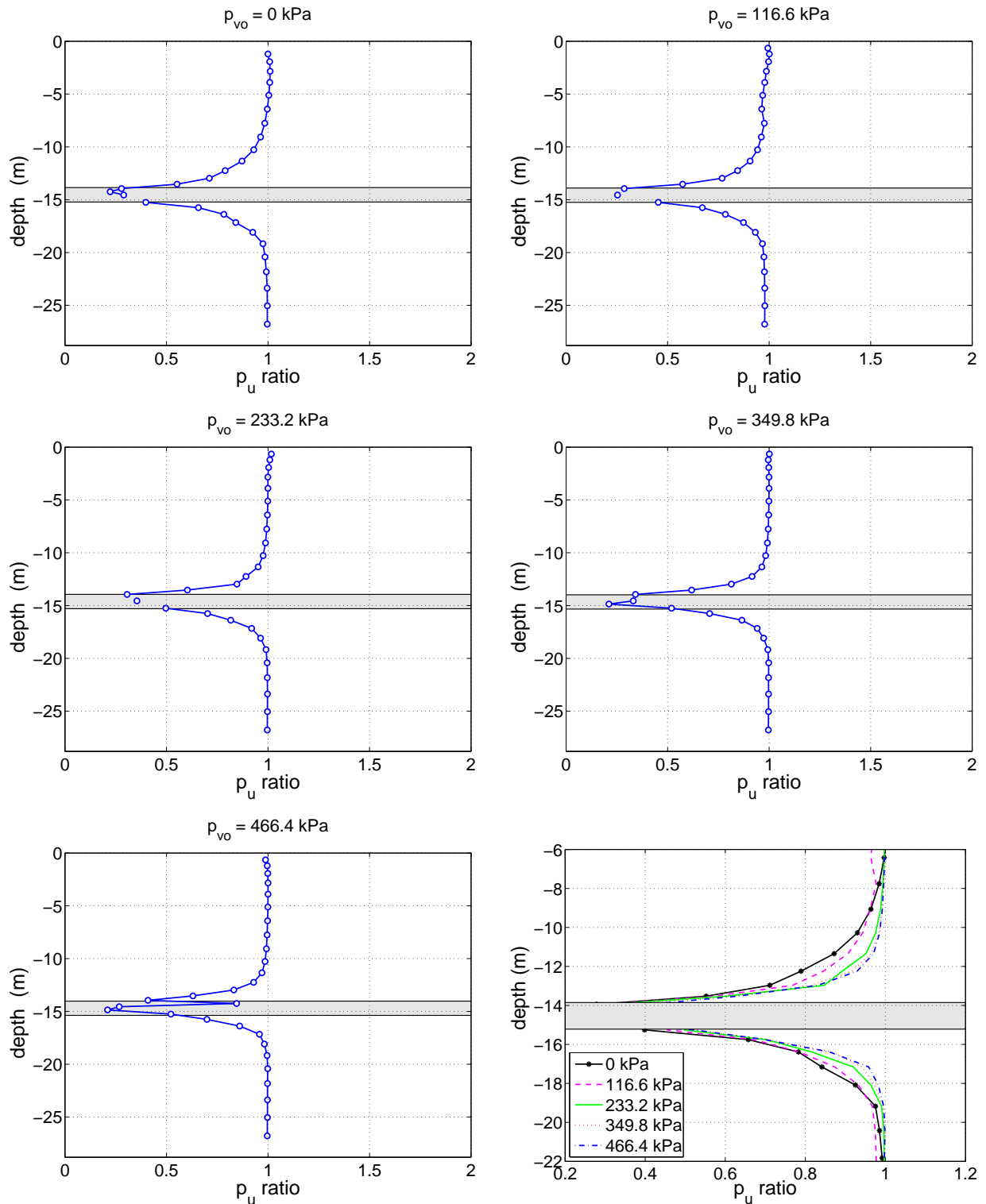


Figure 8.2 Computed p_u ratios for a series of overburden pressures, p_{vo} . The five cases are compared at lower right.

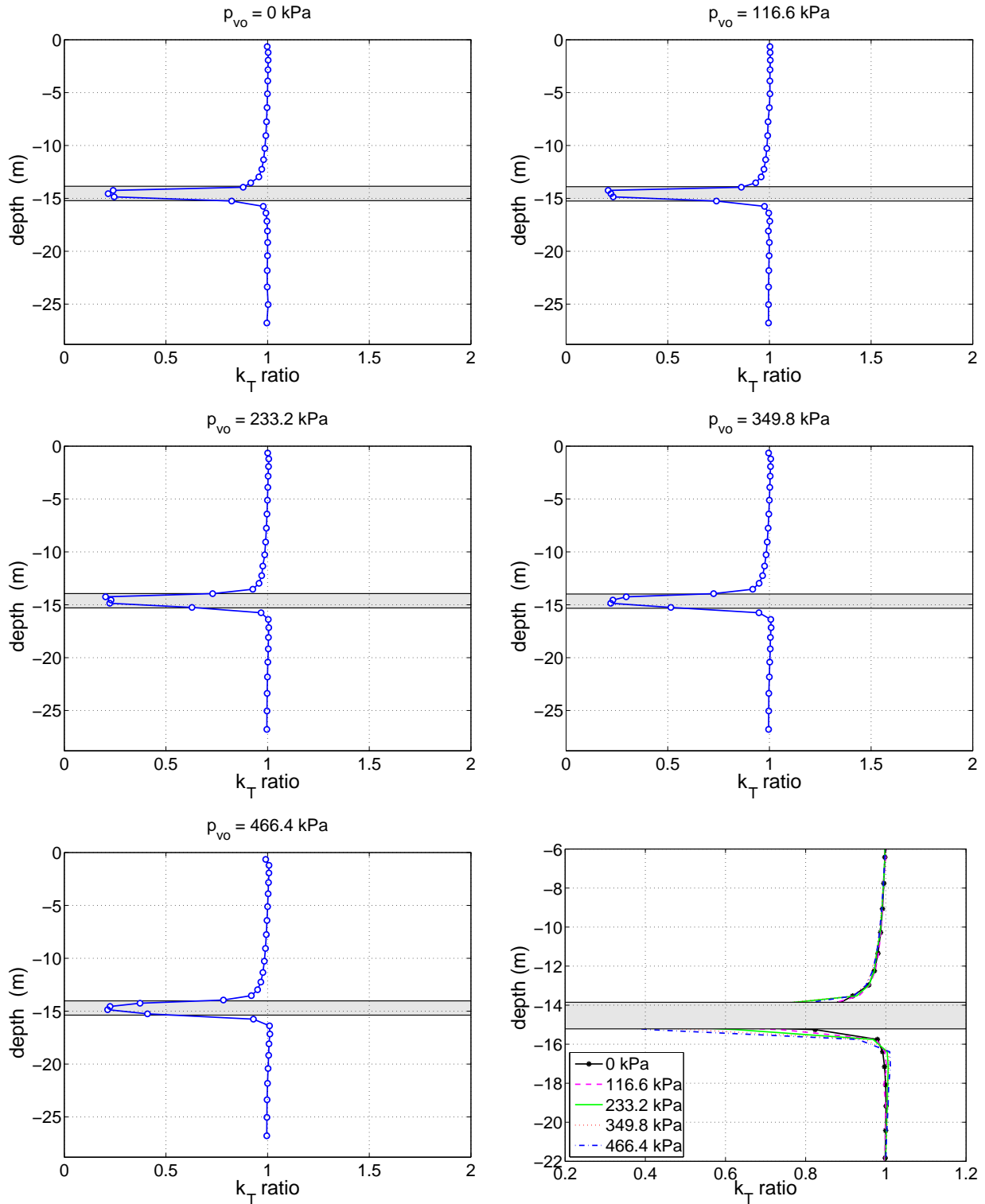


Figure 8.3 Computed k_T ratios for a series of overburden pressures, p_{vo} . The five cases are compared at lower right.

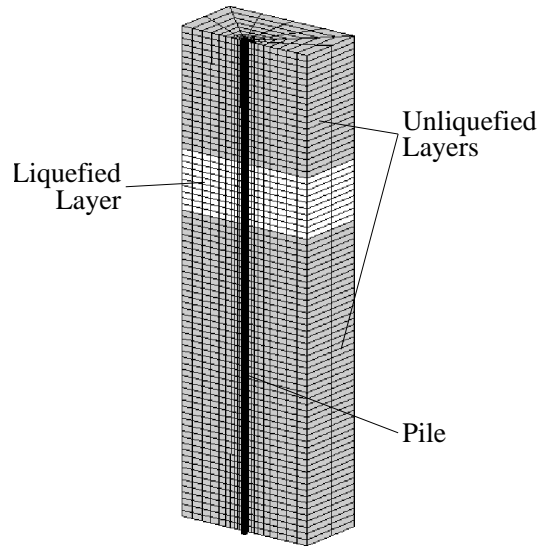


Figure 8.4 Updated layered soil 3D FE mesh.

8.3 UPDATED FINITE ELEMENT MODEL

The findings of these initial studies identify the need for a detailed examination of the effects of the liquefied middle layer on the surrounding unliquefied soil. For this purpose, a new FE model must be created in which the depth and thickness of the liquefied layer are not fixed. This model takes into account previous findings with respect to selective mesh refinement and eliminates the diameter-dependent depth scheme used in previously discussed models. With this new model, the vertical location and depth of the liquefied layer are varied to create a series of soil profiles.

The updated model has a height of 40 m and lateral extents of 10 pile diameters. Figure 8.4 shows the undeformed configuration of the updated FE mesh. The element formulations, boundary and loading conditions, and general scheme of the model match those discussed in previous chapters. The rigid pile kinematic is used to compute $p-y$ curves from this model.

8.3.1 Considered Soil Profiles

To obtain results representative of a variety of field conditions, a set of 21 soil profiles is considered for each of three pile diameters (0.61 m, 1.37 m, and 2.5 m). These profiles are differentiated by the thickness of the liquefied layer, T , and the depth to the bottom of the liquefied layer, H . The set of profiles includes four values of T and six values of H in order to capture the effects of these variables on the computed $p-y$ curves. Table 8.1 summarizes the considered soil profiles. The symbols corresponding to each depth are used to identify respective cases in Figures 8.10 and 8.11. Unmarked depth and thickness combinations are not considered.

8.4 CHARACTERIZING THE INFLUENCE OF THE LIQUEFIED LAYER

Figure 8.5 shows the distributions of p_u and k_T for $p-y$ curves resulting from 3D rigid pile FE analysis with a 0.61-m-diameter pile embedded in both a homogenous soil profile and a layered profile having a liquefied middle layer. For simplicity, the latter profile will be referred to as the liquefied profile. These results are similar to those found during the initial analyses and presented in Figure 8.1. The reductions in p_u and k_T are functions of the depth to the liquefied interface, characterized by the depth to the bottom of the liquefied layer, H , and the thickness of the liquefied layer, T . Similar results are obtained for 1.37-m and 2.5-m-diameter piles (not shown).

8.4.1 Reduction in Ultimate Lateral Resistance

Computed p_u ratios are shown in Figures 8.6 and 8.7 for the upper and lower unliquefied layers, respectively (the FE analysis data are represented as markers). As shown, for a constant liquefied layer depth the reduction in p_u tends to increase with increasing liquefied layer thickness, T , though there appears to be a limit to this effect, as the p_u ratios for $T = 5$ m and $T = 10$ m are essentially identical. For constant T , the reduction in p_u at a given distance from the liquefied layer, s , decreases for increasing liquefied layer depth. The ratios shown in Figures 8.6 and 8.7 are for a single pile diameter. As pile diameter increases, the p_u reduction at a given distance s increases for a particular soil profile.

8.4.2 Reduction in Initial Stiffness

Figures 8.8 and 8.9 show computed k_T ratios for the upper and lower unliquefied layers (the markers are the FE analysis data). The reductions in k_T have the same depth dependence observed in the p_u ratios, however, changes in liquefied layer thickness only affect minor changes in k_T . Significant reductions in k_T are more local to the liquefied interface, especially in the lower unliquefied layer. The extents of the affected zone increase with increasing pile diameter. The results for a 1.37-m-diameter pile are shown in Figures 8.8 and 8.9 to provide a better representation of the form of the computed k_T ratios.

Table 8.1 Considered soil profiles for each pile diameter.

	T (m)			
	1	2	5	10
5	△	△		
10	▽	▽	▽	
11	△			
12		△		
15	○	○	○	○
16	▽			
17		▽		
20	◇	◇	◇	◇
25	□	□	□	□

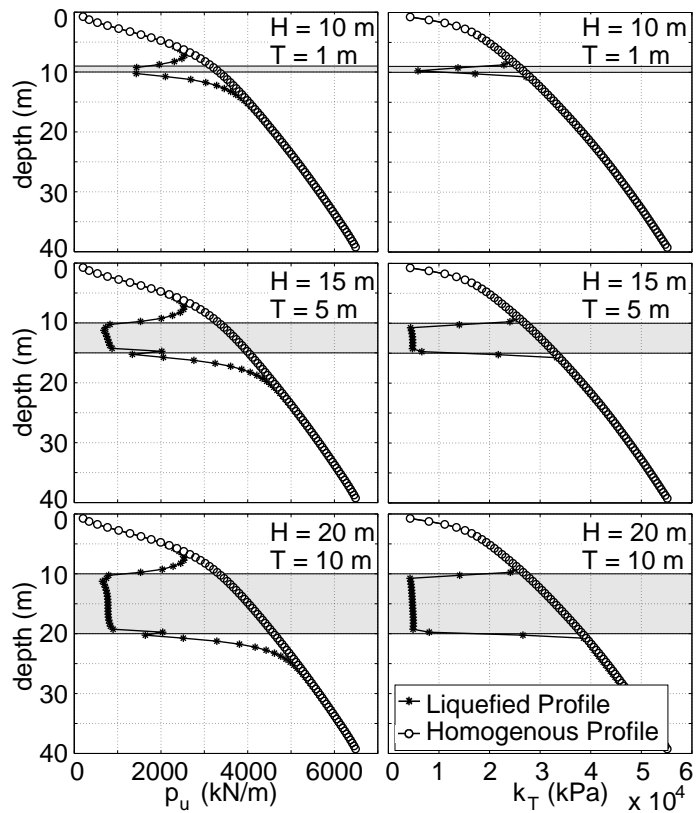


Figure 8.5 Comparison of p_u and k_T in homogenous and liquefied soil profiles for a 0.61-m-diameter pile.

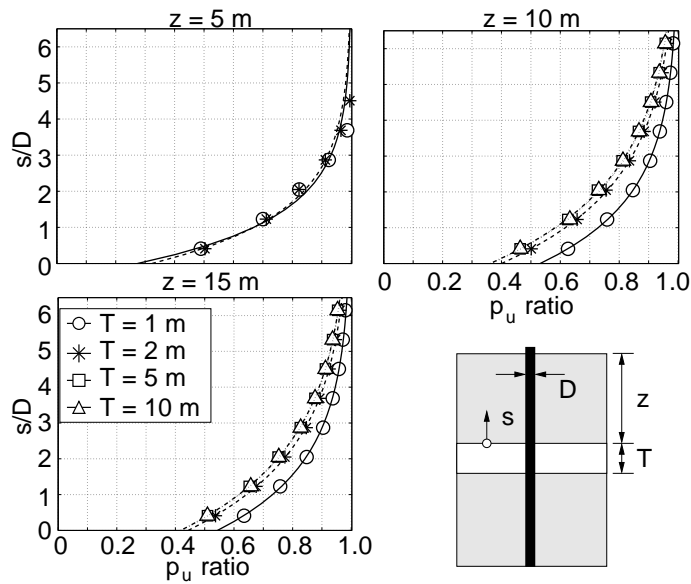


Figure 8.6 Computed p_u ratios above the liquefied layer for a 0.61-m-diameter pile.

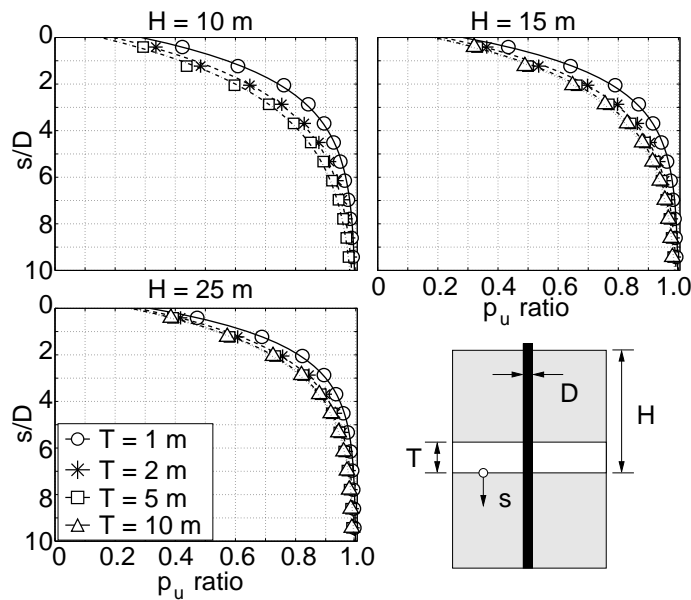


Figure 8.7 Computed p_u ratios below the liquefied layer for a 0.61-m-diameter pile.

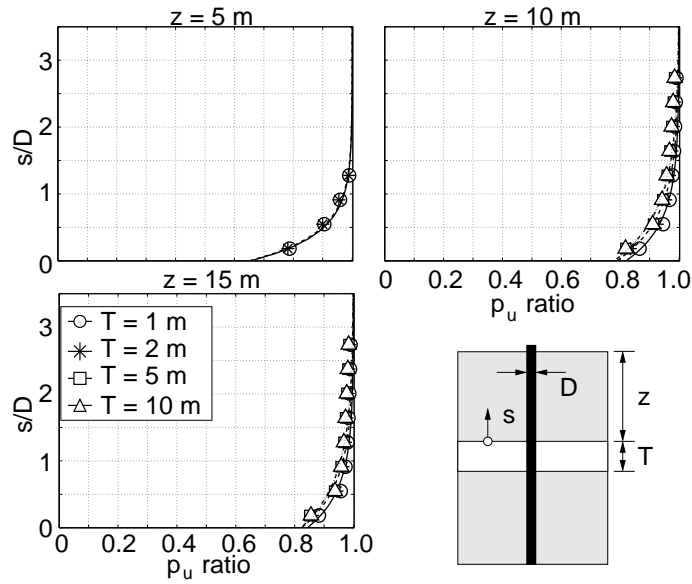


Figure 8.8 Computed k_T ratios above the liquefied layer for a 1.37-m-diameter pile.

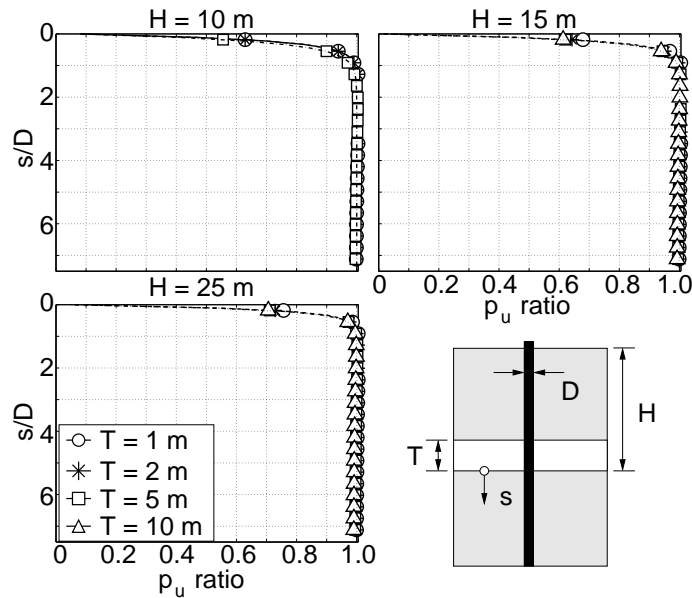


Figure 8.9 Computed k_T ratios below the liquefied layer for a 1.37-m-diameter pile.

8.5 REDUCTION MODEL

The reduction ratios shown in Figures 8.6 through 8.9 all share a similar functional form, suggesting an exponential decay model to characterize both $p-y$ curve parameters (McGann et al., 2010). The proposed exponential decay function

$$R^{(p,k)}(s) = 1 - R_0^{(p,k)} \exp\left(-\frac{s}{s_c^{(p,k)}}\right) \quad (8.2)$$

defines a reduction factor, R , as a function of distance from the liquefied interface, s , in terms of two independent parameters, R_0 and s_c . The interface reduction, R_0 , defines the magnitude of the reduction at the layer interface ($s = 0$), and the characteristic length, s_c , defines how quickly the reduction becomes negligible. The reduction factor of Equation (8.2) is applicable to both p_u and k_T distributions, and the superscripts are used to differentiate between the two, e.g.; $R^{(p)}$ corresponds to a reduction factor for p_u .

Using least squares, the exponential decay function in Equation (8.2) is fit with the p_u and k_T ratio data. Examples of fitted curves are shown in Figures 8.6 through 8.9 as solid or dashed lines (the markers represent points computed from individual 3D FE analysis). As shown, the chosen exponential decay function represents the data very well in both the top and bottom layers for both $p-y$ curve parameters.

8.5.1 Parameter Identification

In order to establish a means to predict appropriate reductions in p_u and k_T for a general combination of pile diameter, liquefied layer depth and thickness, and soil properties, a large parameter study is conducted. Using the rigid pile kinematic, sets of $p-y$ curves are computed for 126 distinct cases (3 pile diameters, 21 soil profiles, and 2 soil friction angles, $\phi = 30^\circ, 36^\circ$). The remaining soil properties are as listed in Table 4.2.

For each considered case, reduction ratios are obtained for p_u and k_T from the computed $p-y$ curve data. Exponential decay curves, Equation (8.2), are fit to each set of reduction data, defining a database of 126 R_0 and s_c parameters for p_u and k_T both above and below the liquefied layer. By plotting R_0 and s_c against various combinations of pile diameter, D , liquefied layer thickness, T , vertical effective stress at the base of the liquefied layer, σ'_v , soil unit weight, γ , and friction angle, ϕ , in a natural-log plot, dimensionless relations are established which relate the reduction parameters (R_0, s_c) to the problem parameters ($D, T, \sigma'_v, \gamma, \phi$).

The relations for which the data displayed the best correlation in the natural-log plots define three dimensionless parameters: the *dimensionless interface reduction*,

$$\eta = R_0 \frac{\sigma'_v \tan \phi}{\gamma D} \quad (8.3)$$

the *dimensionless characteristic length*,

$$\xi = s_c \frac{\sigma'_v \tan \phi}{\gamma D^2} \quad (8.4)$$

and the *dimensionless site parameter*,

$$\beta = \frac{(\sigma'_v \tan \phi)^3 T}{\gamma^3 D^4} \quad (8.5)$$

These dimensionless parameters are computed for all 126 sets of p_u and k_T both above and below the liquefied layer. Figures 8.10 and 8.11 show the relations between the dimensionless parameters for p_u and k_T , respectively. The particular cases can be identified by the markers used, which correspond to those identified in Table 8.1. The colors of the markers indicate the pile diameter: black for 2.5 m, gray for 1.37 m, and white for 0.61 m.

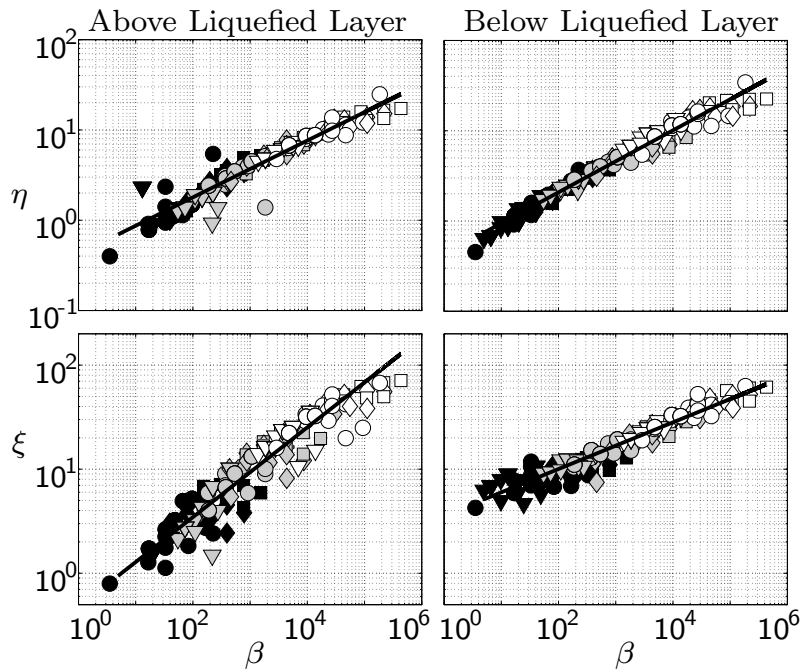


Figure 8.10 Dimensionless relations for p_u above and below the liquefied layer.

To test the applicability of these proposed dimensionless relations, selected soil profiles are analyzed for extreme values of friction angle ($\phi = 19^\circ$, $\phi = 54^\circ$) and soil unit weight ($\gamma = 9 \text{ kN/m}^3$, $\gamma = 25 \text{ kN/m}^3$), which envelope typical values. The dimensionless relations are found to be appropriate for even these extreme cases, indicating that the dimensionless relations are applicable for most reasonable cohesionless soils.

8.6 REDUCTION PROCEDURE

As shown in Figures 8.10 and 8.11, the data points display good correlation and a strong linear trend when plotted using the dimensionless parameters η , ξ , and β . There are a few outlying points, especially for k_T , however, the linear trend holds for the majority of the cases. Lines are fit to the data using least squares in order to identify mathematical expressions that describe the

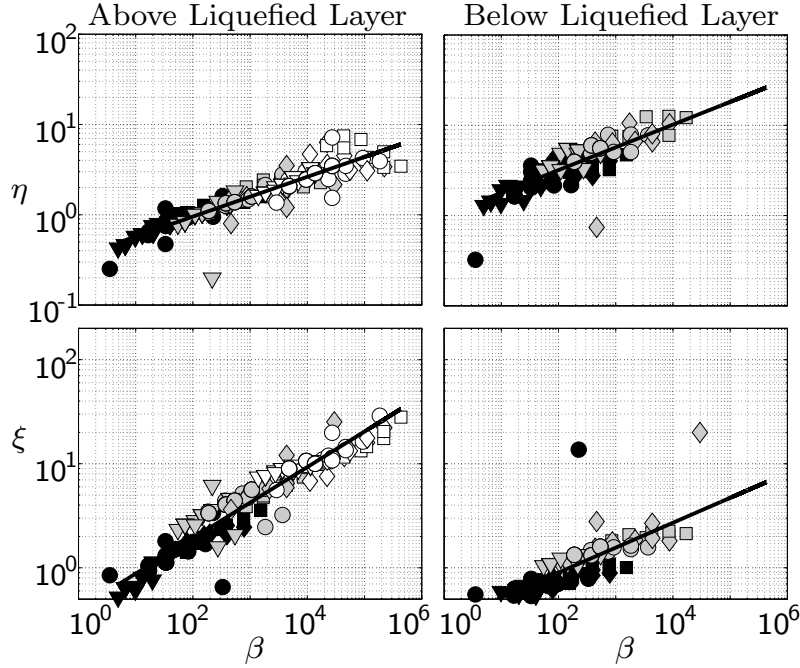


Figure 8.11 Dimensionless relations for k_T above and below the liquefied layer.

observed trends. Appropriate reductions in the p - y curve parameters can be determined from these expressions for a general problem.

A straight line in a natural-log plot represents

$$\ln \eta = b \ln \beta + \ln a \quad (8.6)$$

where the coefficients a and b are determined from the least squares procedure for p_u and k_T above and below the liquefied layer. Solving Equation (8.6) for η gives

$$\eta = a\beta^b \quad (8.7)$$

Similarly, ξ can be expressed in terms of β and two coefficients, c and d , as

$$\xi = c\beta^d \quad (8.8)$$

Combining Equations (8.7) and (8.8) with Equations (8.3) and (8.4) gives the following expressions for the interface reduction, R_0 , and the characteristic length, s_c , written entirely in terms of known quantities for any particular problem.

$$R_0^{(p,k)} = \frac{\gamma D}{\sigma'_v \tan \phi} a \beta^b \quad (8.9)$$

$$s_c^{(p,k)} = \frac{\gamma D^2}{\sigma'_v \tan \phi} c \beta^d \quad (8.10)$$

The reduction coefficients a , b , c , and d are defined in Tables 8.2 and 8.3 for p_u and k_T , respectively. These coefficients have been separated according to reductions above and below the liquefied layer.

Table 8.2 Reduction coefficients for ultimate lateral resistance, p_u .

	$R_0^{(p)}$		$s_c^{(p)}$	
	a	b	c	d
Above liquefied layer	0.421	0.315	0.474	0.432
Below liquefied layer	0.428	0.343	3.577	0.224

Table 8.3 Reduction coefficients for initial stiffness, k_T .

	$R_0^{(k)}$		$s_c^{(k)}$	
	a	b	c	d
Above liquefied layer	0.346	0.220	0.400	0.341
Below liquefied layer	1.000	0.252	0.299	0.239

For a particular problem, with known geometry and properties of the soil-pile system (i.e. D , γ , T , ϕ , σ'_v), any distributions of p_u and k_T with depth can be modified to account for the presence of a liquefied soil layer. The process involved is summarized in Table 8.4.

8.7 SUMMARY

3D FE analysis has been used to develop a simple procedure to modify $p-y$ curves to account for the presence of a liquefied layer of soil. It was observed that the reductions in the characteristic $p-y$ curve parameters of ultimate lateral resistance, p_u , and initial stiffness, k_T , are greatest at the liquefied interface and decay exponentially with increasing distance away from this point. Dimensionless analysis was used to identify characteristic dimensionless parameters and to determine appropriate reduction coefficients suitable for use with reasonable combinations of pile diameter, soil properties, and liquefied layer thickness and depth.

The benefits of this proposed reduction procedure will be demonstrated and verified via BNWF analyses of piles subject to liquefaction-induced lateral spreading in the following chapter. The results of these BNWF studies will be used to make recommendations for simplified analysis of this load case.

Table 8.4 Summary of proposed $p-y$ curve reduction procedure.

1. Select any $p-y$ curves for cohesionless soil profile without liquefied layer.
2. Define distributions of ultimate lateral resistance, $p_u^{(\text{unreduced})}(s)$, and initial stiffness, $k_T^{(\text{unreduced})}(s)$, as functions of distance from the liquefied layer, s , both above and below the liquefied layer.
3. Compute β according to Eq. (8.5).
4. Compute interface reduction, $R_0^{(k)}$, and characteristic length, $s_c^{(k)}$, for initial stiffness above and below the liquefied layer using Table 8.3 and Eqs. (8.9) and (8.10).
5. Compute reduction factor $R^{(k)}(s)$ above and below liquefied layer using Eq. (8.2).
6. Modify unreduced initial stiffness distribution above and below the liquefied layer, i.e.

$$k_T^{(\text{reduced})}(s) = R^{(k)}(s) \cdot k_T^{(\text{unreduced})}(s)$$

7. Compute interface reduction, $R_0^{(p)}$, and characteristic length, $s_c^{(p)}$, for ultimate lateral resistance above and below liquefied layer using Table 8.2 and Eqs. (8.9) and (8.10).
8. Compute reduction factor $R^{(p)}(s)$ above and below liquefied layer using Eq. (8.2).
9. Modify unreduced ultimate lateral resistance distribution above and below liquefied layer, i.e.

$$p_u^{(\text{reduced})}(s) = R^{(p)}(s) \cdot p_u^{(\text{unreduced})}(s)$$

9 Beam on Nonlinear Winkler Foundation Analysis

9.1 INTRODUCTION

Beam on nonlinear Winkler foundation models are used to determine a suitable approach to a simplified analysis of a pile subject to a lateral spreading event. It has been shown that common methods used to define $p-y$ curves for cohesionless soils estimate $p-y$ curves with distributions of ultimate lateral resistance, p_u , and initial stiffness, k_T , which are generally larger than corresponding distributions computed using 3D FE analysis. To assess how these increased parameter distributions affect the simulated pile response, the $p-y$ curves are used in lateral spreading analyses using a BNWF approach.

The BNWF model allows for direct comparison of the effects of using particular sets of $p-y$ curves in a lateral spreading analysis. There are several purposes for the BNWF analyses in this research:

1. Verification that the $p-y$ curves obtained from 3D FE analysis are representative of the 3D soil response and are applicable to alternative pile deformation patterns. The pile bending response obtained from BNWF analyses of lateral spreading using the computed $p-y$ curves are compared to corresponding results from 3D lateral spreading analysis.
2. Evaluation of the applicability of $p-y$ curves defined using predicted distributions of p_u and k_T to lateral spreading simulation using a BNWF approach. The simulated pile response obtained from BNWF analyses using these curves are compared to 3D FE analysis and the BNWF analyses using computed $p-y$ curves.
3. Verification of the effectiveness of the proposed reduction procedure to properly modify $p-y$ curves to account for the presence of a liquefied layer in a general soil profile. The reduction procedure is applied to $p-y$ curves computed from 3D models with homogenous soil profiles. The pile response obtained from a BNWF lateral spreading analysis using these reduced $p-y$ curves is compared to 3D results for a corresponding soil profile.
4. Identification of a simplified analysis procedure appropriate for the analysis of liquefaction-induced lateral spreading. Recommendations for the selection of predicted p_u and k_T distributions are made via comparison of the simulated pile bending response obtained using BNWF analysis with $p-y$ curves defined using various approaches to the 3D FE analysis results.

Each of these items are addressed via simulation of lateral spreading using a BNWF approach. To this purpose, a general BNWF model is developed in OpenSees. The results of these simulations are used to make recommendations for the simplified analysis of lateral spreading using a BNWF model.

9.2 EVALUATION OF COMPUTED AND PREDICTED $p-y$ CURVES

Evaluation of the computed and conventional $p-y$ curves in the context of the lateral spreading problem is conducted using a series of BNWF models. These models replace the soil continuum surrounding the pile with a series of nonlinear springs with behavior defined by $p-y$ curves. The results of the BNWF analyses are compared to each other and to the benchmark 3D results discussed in Chapter 5 with respect to the bending response of the pile.

9.2.1 Beam on Nonlinear Winkler Foundation Model

In the BNWF model, three sets of nodes exist in the same set of locations. There are the pile nodes, which are connected to each other via beam elements, and two sets of spring nodes. The nodes on the pile side of the springs are slave nodes to the pile nodes, sharing equal displacement (no rotation) with those nodes. The nodes on the soil side of the springs are held initially fixed. To simulate a lateral spreading event, an imposed displacement profile matching that used in the 3D lateral spreading models, is applied to the soil end of the nonlinear springs. This approach is similar to that used by Brandenberg et al. (2007). A schematic illustrating the BNWF model is provided in Figure 9.1. For the evaluation simulations, the soil stiffness is assumed to be negligible in the liquefied layer and thus is set to zero. The BNWF model utilizes the same beam elements as the 3D models, with both linear elastic and elastoplastic constitutive formulations.

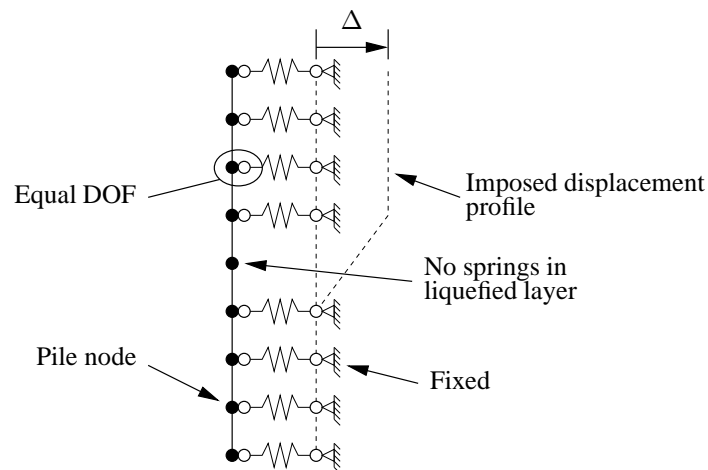


Figure 9.1 Schematic representation of the BNWF model.

9.2.2 Modeling the $p-y$ Curves

The $p-y$ curves are defined in OpenSees using zero-length elements and the provided *PySimple1* constitutive model, which allows for the definition of $p-y$ curves for both cohesive and cohesionless soils. The *PySimple1* constitutive model is based upon the work of Boulanger et al. (1999) in modeling seismic soil-pile-structure interaction. This constitutive model has an initially linear force density-displacement relationship and plastic force density-displacement behavior described by

$$p(y^p) = p_u - (p_u - p_0) \left[\frac{cy_{50}}{cy_{50} + |y^p - y_0^p|} \right]^n \quad (9.1)$$

in which p_u is the ultimate lateral resistance, y_{50} is the lateral displacement at which one-half of p_u has been mobilized during monotonic loading, and p_0 and y_0^p are the values of p and y^p at the beginning of the current plastic loading cycle, respectively. The constant, c , controls the tangent modulus at the onset of plastic yielding and the constant, n , controls the sharpness of the $p-y$ curve. In order to closely approximate the shape of the API (1987) recommended curves for drained sand, Boulanger et al. recommend setting $c = 0.5$ and $n = 2$.

Appropriate values of p_u and y_{50} must be defined as input values at each pile node. The established p_u values can be used directly in OpenSees, however, the necessary values of y_{50} are not inherently defined. Sensible values of this parameter are determined from Equation (6.1) by solving for the displacement at which the force is equal to one-half of p_u , resulting in

$$y_{50} = \frac{p_u}{k_T} \tanh^{-1}(0.5) \quad (9.2)$$

which defines y_{50} in terms of the known values of k_T and p_u at each depth. A similar procedure is utilized to obtain suitable values of the parameter y_{50} for the computed $p-y$ curves. It is important to note that in the *PySimple1* model, the input values of p_u must be in units of force instead of the commonly-used units of force/length. Appropriate values are obtained through multiplication with the tributary lengths discussed in Section 6.2.

9.2.3 Considered $p-y$ Curves

There are two series of BNWF models used to evaluate the $p-y$ curves. In the first, the springs have behavior defined using the $p-y$ curves computed from the 3D simulations. In the second, the springs are defined by $p-y$ curves established using the API (1987) recommendations. Three pile diameters are considered (0.61 m, 1.37 m, 2.5 m), and the analyses are split into two separate cases:

1. *Homogenous Case*: The $p-y$ curves are not reduced to account for the presence of the liquefied layer. Computed $p-y$ curves are obtained from homogenous soil profiles and the API curves are left unmodified.
2. *Reduced Case*: The $p-y$ curves reflect the influence of the liquefied layer. Computed $p-y$ curves are obtained from layered soil profiles with a liquefied middle layer. The p_u distributions of the API curves are reduced through multiplication with the p_u ratios obtained

Table 9.1 Overview of the considered BNWF analysis cases for each pile.

	FE analysis Curves		API Curves	
	Reduced	Homogenous	Reduced	Homogenous
Elastic Pile	X	X	X	X
Elastoplastic Pile	X	X	X	X

through comparison of the $p-y$ curves computed from homogenous and liquefied soil profiles (see Figure 8.2).

Because the API curves have been shown to be too stiff with depth, the lowest recommended subgrade reaction coefficient, $k = 5000 \text{ kN/m}^3$, is used to define the initial stiffness of the API curves. This value does not correspond to the internal friction angle used in the soil constitutive model, however, it increases the applicability of the API curves to the lateral spreading case. The p_u distributions used for these curves are computed using soil properties matching those used as input values in the 3D model. The reductions made to these curves in the reduced analysis case, while not included in the API recommendations, creates a more realistic distribution of $p-y$ with depth and enhances the applicability of the API curves to the lateral spreading case.

All of these cases are analyzed two times, once with elastic beam elements and once with elastoplastic beam elements, creating a total of 24 distinct cases. A brief overview of the considered cases is presented in Table 9.1.

9.2.4 Results

The results of the BNWF analyses are evaluated with respect to the maximum shear force, $\max V$, maximum bending moment, $\max M$, and the maximum curvature, $\max \phi$, in the pile. The maximum pile deflection, $\max U$, and the effective length, L_{eff} , which is the distance between the extreme moment demands in the pile, are also considered. Tables 9.2, 9.3, and 9.4 summarize the results of the BNWF analyses for a 2.5-m, a 1.37-m, and a 0.61-m-diameter pile, respectively.

Table 9.2 Pile bending response summary for BNWF analysis with a 2.5-m-diameter pile.

Elastic Pile Cases					
Curve Type	max V (kN)	max M (kNm)	max ϕ (m^{-1})	max U (m)	L_{eff} (m)
FE analysis, homogenous	50900	285100	0.0015	1.65	16.30
FE analysis, reduced	46700	278900	0.0014	1.64	16.40
API, homogenous	175000	950100	0.0048	1.96	13.10
API, reduced	150000	920600	0.0047	1.94	13.20
Elastoplastic Pile Cases					
Curve Type	max V (kN)	max M (kNm)	max ϕ (m^{-1})	max U (m)	L_{eff} (m)
FE analysis, homogenous	46200	219600	0.0031	1.59	15.70
FE analysis, reduced	42300	217200	0.0030	1.59	15.80
API, homogenous	92800	240000	0.0882	1.35	9.10
API, reduced	78900	240200	0.0665	1.18	10.10

Table 9.3 Pile bending response summary for BNWF analysis with a 1.37-m-diameter pile.

Elastic Pile Cases					
Curve Type	max V (kN)	max M (kNm)	max ϕ (m^{-1})	max U (m)	L_{eff} (m)
FE analysis, homogenous	11900	29400	0.0059	0.87	8.25
FE analysis, reduced	10700	28800	0.0058	0.86	8.30
API, homogenous	25500	60000	0.0120	1.00	6.45
API, reduced	20900	56700	0.0114	1.00	6.60
Elastoplastic Pile Cases					
Curve Type	max V (kN)	max M (kNm)	max ϕ (m^{-1})	max U (m)	L_{eff} (m)
FE analysis, homogenous	4190	6170	0.0378	0.50	5.40
FE analysis, reduced	3980	6210	0.0955	0.67	5.05
API, homogenous	5870	6240	0.1532	0.46	3.25
API, reduced	5410	6180	0.2950	0.69	3.30

Table 9.4 Pile bending response summary for BNWF analysis with a 0.61-m-diameter pile.

Elastic Pile Cases					
Curve Type	max V (kN)	max M (kNm)	max ϕ (m^{-1})	max U (m)	L_{eff} (m)
FE analysis, homogenous	2170	2550	0.0108	0.40	3.70
FE analysis, reduced	1870	2450	0.0104	0.40	3.80
API, homogenous	2700	4040	0.0171	0.49	3.40
API, reduced	2150	3790	0.0161	0.48	3.50
Elastoplastic Pile Cases					
Curve Type	max V (kN)	max M (kNm)	max ϕ (m^{-1})	max U (m)	L_{eff} (m)
FE analysis, homogenous	1290	975	0.0508	0.32	2.80
FE analysis, reduced	1120	950	0.0424	0.33	3.00
API, homogenous	1420	980	0.2640	0.33	2.30
API, reduced	1200	1000	0.0156	0.34	2.65

The maximum shear force, bending moment, and curvature demands returned using the API curves tend to be significantly larger than those returned by the FE analysis. As the pile diameter decreases, the results become more similar, however, the API curves still predict larger demands for the smallest pile. The effective lengths obtained using the API $p-y$ curves tend to be smaller than those returned by the extracted curves, indicative of larger extreme bending demands on the piles.

In the elastoplastic pile cases, the maximum bending moments returned using the two sets of $p-y$ curves are similar due to the fact that the piles are reaching their moment capacity, however, the curvature demands placed upon the piles using the API curves are significantly larger and the effective lengths tend to be shorter. Both of these results indicate that the bending demands on the piles using the API curves are much more severe than those obtained using the FE analysis curves.

The BNWF results are compared to corresponding results obtained from the 3D modeling effort (see Chapter 5) in Tables 9.5, 9.6, and 9.7, which show the relative error between the BNWF and 3D pile bending demands. The elastic pile BNWF cases are compared to the results of the free-head 3D Series 3 cases, which consider elastic piles in elastoplastic soil. The elastoplastic BNWF cases are compared to the free-head 3D Series 4 cases, which model elastoplastic piles in elastoplastic soil. As a reference, the 3D results for both the Series 3 and 4 cases are summarized in Tables 5.2-5.4 (pages 69-69).

When applied to BNWF models, the $p-y$ curves computed from the 3D FE analysis return pile demands that are reasonably similar to 3D lateral spreading simulations. There is a relatively small amount of error which can be attributed to inaccuracies in the curve extraction procedure, the transfer of these extracted curves into the nonlinear spring models, and the inherent error in representing a 3D soil continuum with a series of discrete springs. This similarity in the results validates that the $p-y$ curves computed using the rigid pile kinematic case in 3D, which are free from the influence of pile kinematics, can be used successfully in a simplified BNWF lateral spreading analysis.

Table 9.5 Relative error between BNWF and 3D FE results for 2.5-m-diameter pile.

Elastic Pile Cases		Relative Error			
Curve Type	max V (%)	max M (%)	max ϕ (%)	L_{eff} (%)	
FE analysis, homogenous	5.80	5.10	3.20	1.20	
FE analysis, reduced	13.7	7.20	5.30	1.50	
API, homogenous	223	216	222	18.7	
API, reduced	177	206	212	18.1	
Elastoplastic Pile Cases		Relative Error			
Curve Type	max V (%)	max M (%)	max ϕ (%)	L_{eff} (%)	
FE analysis, homogenous	5.30	3.30	14.0	3.75	
FE analysis, reduced	13.2	4.40	17.9	4.40	
API, homogenous	90.2	5.60	2350	40.0	
API, reduced	61.7	5.70	1750	33.4	

Table 9.6 Relative error between BNWF and 3D FE results for 1.37-m-diameter pile.

Elastic Pile Cases		Relative Error			
Curve Type	max V (%)	max M (%)	max ϕ (%)	L_{eff} (%)	
FE analysis, homogenous	1.00	3.86	3.18	9.20	
FE analysis, reduced	11.1	5.97	5.30	10.3	
API, homogenous	111	95.9	97.3	14.4	
API, reduced	73.3	85.1	86.4	12.8	
Elastoplastic Pile Cases		Relative Error			
Curve Type	max V (%)	max M (%)	max ϕ (%)	L_{eff} (%)	
FE analysis, homogenous	15.7	6.20	63.8	13.3	
FE analysis, reduced	19.9	5.55	8.71	6.78	
API, homogenous	18.1	5.17	46.5	31.7	
API, reduced	8.87	6.02	182	30.4	

Table 9.7 Relative error between BNWF and 3D FE results for 0.61-m-diameter pile.

Elastic Pile Cases		Relative Error			
Curve Type	max V (%)	max M (%)	max ϕ (%)	L_{eff} (%)	
FE analysis, homogenous	7.25	0.83	0.94	2.41	
FE analysis, reduced	7.45	4.59	4.70	5.02	
API, homogenous	33.3	57.3	57.2	6.82	
API, reduced	6.07	47.6	47.4	4.03	
Elastoplastic Pile Cases		Relative Error			
Curve Type	max V (%)	max M (%)	max ϕ (%)	L_{eff} (%)	
FE analysis, homogenous	2.92	0.59	14.7	2.08	
FE analysis, reduced	11.0	2.90	4.36	5.65	
API, homogenous	13.0	0.42	496	20.6	
API, reduced	4.43	1.96	253	7.34	

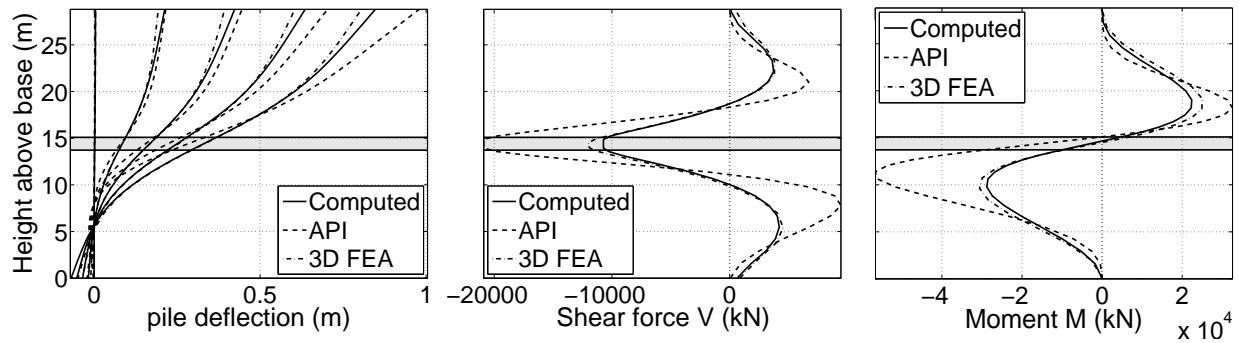


Figure 9.2 Deflected shape, shear force, and moment diagrams for BNWF and 3D FE analyses of lateral spreading for a 1.37-m-diameter pile with linear elastic behavior.

The API $p-y$ curves, which are inherently tied to a top pushover type of pile deformation, tend to be significantly larger than the 3D FE analysis results, even with the modifications made to enhance the applicability of these curves. The deflected pile shapes shown in Figure 9.2 emphasize the effects of the overestimated stiffness in the API curves. As shown, when the computed curves are used, the base of the pile is able to cut backwards into the soil, just as is observed in the 3D model. When this occurs, the pile has a degree of rigid body rotation in its deformation profile, lessening the curvature demands incurred during the lateral spreading event. Using the API curves leads to a condition in which the base of the pile is held firmly in place during the lateral spreading event, increasing the curvature demands on the pile, especially in the lower solid layer.

The shear and moment diagrams of Figure 9.2 further demonstrate the differences in pile response for the two sets of $p-y$ curves. The diagrams corresponding to the computed $p-y$ curves are similar to those corresponding to the 3D FE analysis, while the API curves predict significantly larger shear and moment demands over the full length of the pile.

The results of the elastoplastic pile analyses demonstrate another relative difference between the analysis approaches. As shown in Figure 9.2, there are two extreme moment demands, one in each unliquefied soil layer. Figure 9.3 shows the evolution of these extreme pile moments obtained from the 3D FE analysis and BNWF models with computed and API $p-y$ curves. As a result of the response overpredictions inherent to the API curves, significantly larger curvature demands are placed on the pile and large curvatures develop much earlier in the lateral spreading deformation. The API-based analysis indicates that the pile has reached its moment capacity when the upper layer has displaced approximately 0.24 m (≈ 0.18 diameters) relative to the lower layer. In the computed $p-y$ curve and 3D analyses, the pile moment capacity is reached at about 0.48 m (≈ 0.35 diameters) of upper soil layer displacement. This is a significant difference in perceived pile bending demand between the cases, even with the assumed lateral resistance reductions in the API curves near the liquefied layer.

It is recommended that $p-y$ curves defined using the API (1987) recommendations not be used in a simplified analysis of piles for lateral spreading. The BNWF analyses have shown that the computed $p-y$ curves produce similar results to the 3D model and that there are significant differences between the results obtained using the computed and API $p-y$ curves, even with modifications to the API curves, which serve to increase their applicability to the lateral spreading case. The

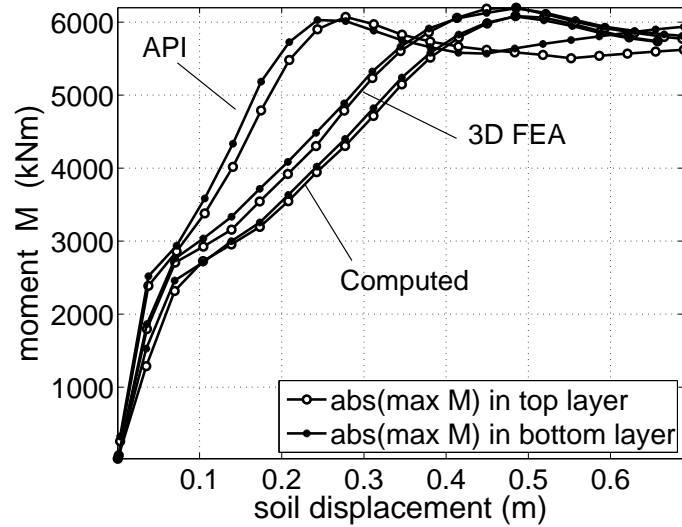


Figure 9.3 Evolution of extreme moment demands in top and bottom layers with increasing displacement of upper soil layer during BNWF and 3D FE lateral spreading analyses for a 1.37-m-diameter pile.

BNWF approach can still be used successfully in a simplified analysis of this problem, however, appropriate considerations must be made with respect to the differences in the pile kinematics used to define the $p-y$ curves and the pile kinematics modeled by the analysis. A careful approach to defining the initial stiffness and ultimate resistance with depth and in the zone of influence of the liquefied layer greatly increases the similarity of the results as compared to 3D FE analysis of lateral spreading.

9.3 VALIDATION AND APPLICATION OF PROPOSED CURVE REDUCTION PROCEDURE

The applicability of the proposed reduction procedure to the lateral spreading problem is validated using a second series of BNWF simulations. Two test profiles are defined that represent arbitrary liquefied layer locations. Both BNWF and 3D FE models are created for these soil profiles. The $p-y$ curves in the BNWF model are defined using several strategies for the purpose of validating the reduction procedure for the lateral spreading case and assessing the applicability of this procedure to existing $p-y$ curve definition methods.

9.3.1 Test Profiles

Two general soil profiles are selected for use as test problems. These profiles have geometries that do not match any of those used in the parameter study to establish the reduction procedure. One profile has a shallow liquefied layer, with a depth to the base of the liquefied layer $H = 10$ m, while the other has a deeper liquefied layer, with $H = 24$ m. Both profiles have a liquefied layer thickness $T = 4$ m, a soil unit weight $\gamma = 17$ kN/m³, and consider a 1.37-m-diameter pile. The

unliquefied soil layers have an internal friction angle $\phi = 38^\circ$. The remaining soil properties are as listed in Table 4.2. 3D models are created for each test profile. These models are used to compute $p-y$ curves using the rigid pile kinematic as well as to simulate lateral spreading in separate analyses.

Separate BNWF models are created for each of the test profiles. These models are similar to that depicted in Figure 9.1, however, in the BNWF analyses used to assess the proposed reduction procedure both the ultimate resistance and initial stiffness of the $p-y$ curves in the liquefied layer are taken to be 10% of their unreduced magnitudes.

9.3.2 Investigated Test Cases

The $p-y$ curves used to describe the soil-pile interaction in the BNWF models are defined using five distinct combinations of p_u and k_T distributions. The five resulting test cases include two validation cases (*VC1* and *VC2*), modeled using parameters directly obtained from the 3D rigid pile simulations, and three practical cases (*PC1*, *PC2*, and *PC3*), modeled using p_u and k_T distributions estimated using methods readily available to practitioners. The investigated cases are summarized below. Figures 9.4 and 9.5 show the distributions of p_u and k_T , respectively, used for each test case.

- Validation cases
 - *VC1*: The $p-y$ curves in this case are defined using distributions of p_u and k_T computed directly from the 3D model, resulting in $p-y$ curves which are reduced for the presence of the liquefied layer specifically for each respective soil profile.
 - *VC2*: This case uses $p-y$ curves with p_u and k_T distributions computed from a homogenous soil 3D model in which the soil has the properties of the unliquefied layers in the test profiles. These curves are reduced for the presence of the liquefied layer using the proposed reduction procedure.
- Practical cases
 - *PC1*: The $p-y$ curves for this case are determined using the API recommendations (1987). The curves representing the unliquefied sand are not reduced for the presence of the liquefied layer.
 - *PC2*: This case uses a distribution of p_u defined using the method of Brinch Hansen (1961) and a k_T distribution defined by correcting the API distribution for overburden pressure after Boulanger et al. (2003). No reduction is made to account for the presence of the liquefied layer.
 - *PC3*: This case uses the p_u and k_T distributions of case *PC2* with the proposed reduction procedure applied to account for the presence of the liquefied layer.

The validation cases are intended to test the applicability of the BNWF model and the proposed reduction procedure to the lateral spreading load case. The $p-y$ curves for *VC1* are obtained

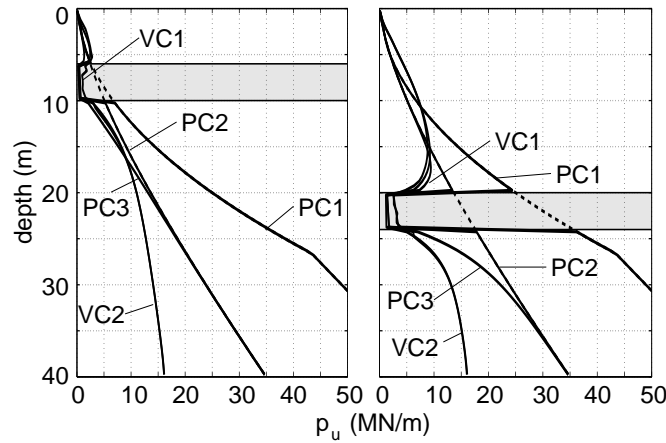


Figure 9.4 Distributions of p_u used in BNWF models.

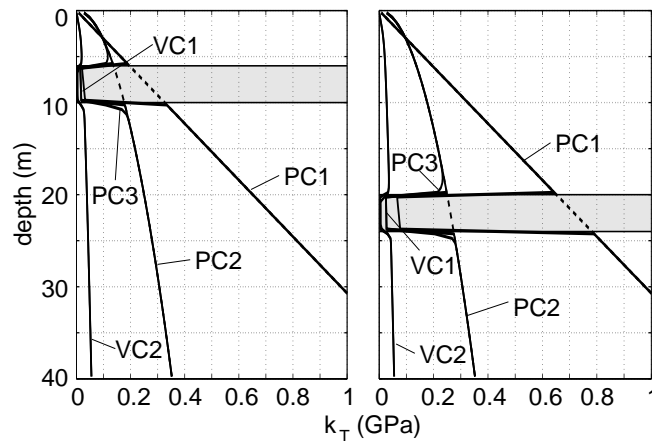


Figure 9.5 Distributions of k_T used in BNWF models.

directly from 3D models of the test profiles. Therefore, any differences in the results of *VC1* and the 3D lateral spreading simulations can be attributed to the error induced by representing the soil continuum as discrete $p-y$ springs. Similarity of the results obtained from *VC2* with the 3D FE analysis verifies the ability of the proposed reduction procedure to appropriately predict the reduction in the unliquefied soil response due to the presence of the liquefied layer.

The practical cases represent the types of predictions that can be made in the absence of 3D FE analysis. These cases are intended to evaluate the applicability of the chosen sets of $p-y$ curves to the BNWF lateral spreading analysis approach and to demonstrate the benefits of the proposed reduction procedure. Case *PC1*, using the API recommendations, represents a common choice of $p-y$ curves for cohesionless soils. Case *PC2* uses alternative methods to define the $p-y$ curves for the purpose of contrasting the results of *PC1*. Differences between the results of *PC3* and *PC2* demonstrate the effects of the reduction procedure for the lateral spreading case.

Table 9.8 Maximum pile bending demands in BNWF lateral spreading simulations.

	Maximum pile shear force (MN)					Maximum pile moment (MNm)				
	<i>VC1</i>	<i>VC2</i>	<i>PC1</i>	<i>PC2</i>	<i>PC3</i>	<i>VC1</i>	<i>VC2</i>	<i>PC1</i>	<i>PC2</i>	<i>PC3</i>
<i>H</i> = 10 m	6.52	6.00	10.75	8.74	7.47	36.7	36.0	45.5	44.0	37.5
<i>H</i> = 24 m	13.2	12.7	42.5	27.8	22.4	41.2	41.0	113.6	78.9	69.3

9.3.3 Results

The results of the BNWF lateral spreading simulations are evaluated through comparison of the maximum shear force and bending moment demands developed in the pile with corresponding demands obtained from the 3D FE analysis, which is believed to be the most accurate representation of the problem. Emphasis has been placed on the relative magnitudes of the shear and moment demands rather than on numerical values. The displaced shapes of the piles are considered in order to gain additional insight on the results.

Figure 9.6 and Table 9.8 present the maximum shear and moment demands obtained from the BNWF and 3D FE lateral spreading simulations for each test profile. Comparison of *VC1* with the 3D FE analysis shows the error induced by using the approach of computing *p*–*y* curves from the 3D model and applying them in a BNWF analysis. The error involved in this process is relatively small. With respect to validation, the maximum shear and moment demands for *VC2* are found to be consistent with both *VC1* and the 3D FE analysis, which verifies that the reduction procedure can be successfully implemented in a lateral loading analysis of a pile in a general soil profile.

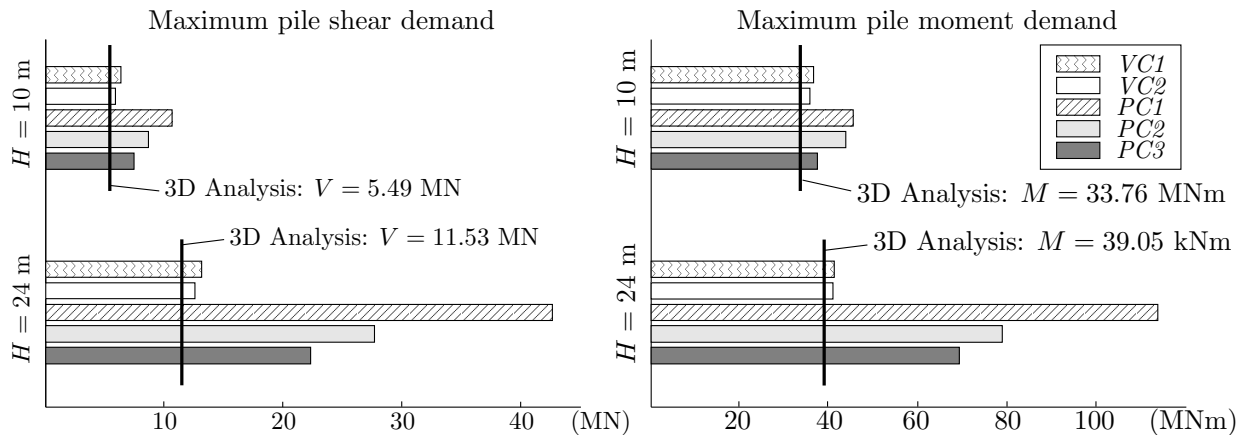


Figure 9.6 Comparison of maximum pile shear and moment demands.

It is interesting to note that the maximum pile demands of *VC2* are somewhat closer to the 3D results than those of *VC1*. This relatively small difference can be attributed to the observation that the reductions in p_u and k_T for *VC2* are greater than those for *VC1* (see Figures 9.4 and 9.5), leading to smaller pile bending demands. This shows that while the reduction procedure does not exactly reproduce the p_u and k_T distributions directly obtained from the 3D model, it is still an effective analysis tool, as the resultant pile response remains similar.

The results of the practical cases highlight several observations. It has been shown that the API recommended distributions of p_u and k_T used in *PC1* are too large at depth, and when applied to a BNWF lateral spreading analysis, produce maximum pile shear and moment demands that far exceed those obtained using 3D FE analysis. This finding is confirmed by the results shown in Figure 9.6, where the pile demands of *PC1* are larger than all other cases, especially for the deeper liquefied layer location.

The methods chosen to define the $p-y$ curves for *PC2* were selected with the knowledge the API $p-y$ curves have excessive capacity and stiffness at depth. The p_u and k_T distributions for this case are more similar to those obtained from the 3D model, and, therefore, the maximum pile bending demands estimated for *PC2* are closer to the 3D FE analysis than those of *PC1*. Application of the proposed reduction procedure to the $p-y$ curves of *PC2* improves the prediction of the pile response even more, as *PC3* estimates lower maximum moment and shear demands in the pile for both test profiles. This result shows that the reduction procedure can be used on independently developed set of $p-y$ curves to appropriately account for the presence of a liquefied layer in a BNWF analysis of lateral spreading, producing pile bending demands that are more consistent with a 3D representation of the problem.

While the results of the validation cases are similar to the 3D FE analysis, for the practical cases there is a significant difference in relative similarity to the 3D results depending upon the depth of the liquefied layer. For the shallower liquefied layer location ($H = 10$ m), the error in the maximum shear and moment demands between the practical cases and the 3D FE analysis is much smaller than for the deeper liquefied layer location ($H = 24$ m). The benefits of informed $p-y$ curve selections are apparent through comparison of the results of *PC1* with *PC2*, and the effectiveness of the proposed reduction procedure is evident in the results of *PC3*; however, the smallest errors between the practical cases and the 3D FE analysis are still larger than the error induced through the BNWF approach.

These observed differences in maximum shear and moment demands can be better understood by considering the deformed shapes of the pile. Figure 9.7 shows the deflected shape of the pile for *VC2* and *PC3*, for both test profiles. For $H = 10$ m, large pile deformations occur near the ground surface and the magnitude of the deformation lessens with increasing depth. Below the liquefied layer, little or no pile deformation occurs. Large pile deformations occur in and around the liquefied layer for $H = 24$ m, while little deformation occurs away from this zone. The significant differences in k_T where pile deformations are small are the main cause for the differences in maximum pile bending demand observed between the practical BNWF cases and the 3D FE analysis.

For the shallower liquefied layer ($H = 10$ m), p_u is low enough in the upper unliquefied layer to control the response of the $p-y$ curves. Changes in initial stiffness make little difference in this region because the pile deformations are large enough to activate the lateral capacity of the $p-y$ curves. Below the liquefied layer, pile deformations are small and k_T controls the behavior of the $p-y$ curves. When k_T is large, the lower portion of the pile is effectively held stationary while the the top is bent over. This concentrates the curvature of the pile over a narrower length, resulting in an increased bending moment, and produces a sharp change in the lateral force carried by the pile, leading to a higher shear force at this point. The lower stiffness observed for the 3D FE analysis allows the curvature to be spread out over a longer section of the pile, leading to lower bending

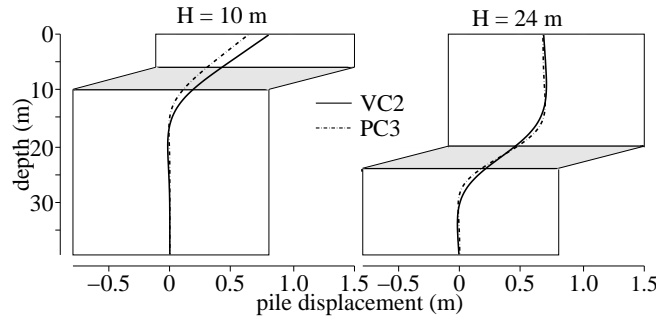


Figure 9.7 Deformed shapes of pile in the VC2 and PC3 BNWF analyses.

demands. These differences in the displaced shape of the pile are highlighted in Figure 9.7 for two analysis cases.

Similar behavior leads to the large bending demands observed with a deeper liquefied layer ($H = 24$ m), however, the depth of the liquefied layer alters the displacement profile of the pile such that two hinges form, whereas only a single hinge developed for the shallow liquefied layer. The combined effect of two hinges and higher values of p_u and k_T at depth for the practical cases leads to the large discrepancies compared to the 3D FE analysis. As shown in Figure 9.7, compared to VC2, the hinge points for PC3 are closer to the liquefied layer and the curvature is concentrated over shorter lengths, both of which are due to the larger values of p_u and k_T for this case. For a deeper liquefied layer location, the selection of $p-y$ curves used in the BNWF analysis significantly affects the simulated pile response. Careful selection of $p-y$ curves is critical to obtaining an accurate estimate of the maximum pile bending demands.

9.4 EFFECTS OF SOIL SHEAR MODULUS ON INITIAL STIFFNESS OF $p-y$ CURVES

The results of the BNWF analyses have shown that the maximum bending demands placed on a pile during a lateral spreading event have a strong dependence on the initial stiffness of the soil response. As shown in Figure 9.5, the k_T distribution computed from the 3D model is significantly lower than either of the estimated distributions. The difference is due to how these distributions are determined. The API initial stiffness distribution is defined as a function of the friction angle, ϕ , of the soil, whereas in the 3D model, the initial stiffness is a function of the shear modulus, G , of the soil constitutive model.

Friction angle is a failure parameter related more to p_u , while k_T is related more fundamentally to G ; however, the friction angle and small strain shear modulus of an actual sand are both directly related to the relative density, and therefore to each other, so defining the initial stiffness of the $p-y$ curves based on ϕ is reasonable. No such intrinsic relation between ϕ and G exists in the Drucker-Prager constitutive model. In an actual sand, the shear modulus decreases with increasing shear strain. Because the constitutive model used in the simulations does not directly consider modulus reduction, the shear modulus of the unliquefied layers must be taken to represent a large strain value. This indicates that comparisons made between values of k_T computed based on a

large strain G and values determined from ϕ , which is related to the small strain shear modulus, may not be entirely appropriate.

For a typical dense sand with a unit weight of 17 kN/m^3 , the small strain shear modulus at one atmosphere ranges between approximately $50,000$ and $100,000 \text{ kPa}$. Additional 3D models are created using these values for G_0 , and used to determine new k_T distributions. These models consider one homogenous soil layer that, with the exception of an increased shear modulus, has the soil parameters defined for the test profiles. The k_T values are computed using the rigid pile kinematic, and all three pile diameters are considered.

The k_T distributions computed from these models are shown in Figure 9.8. Shown for reference are the k_T distributions used for *VC2* ($G = 9260 \text{ kPa}$) and *PC2*. The values of k_T computed from the 3D models increase with increasing shear modulus and show a diameter dependence at shallow depths. The values of k_T computed from the 3D model with larger shear moduli approach, but do not reach, the values estimated from the friction angle.

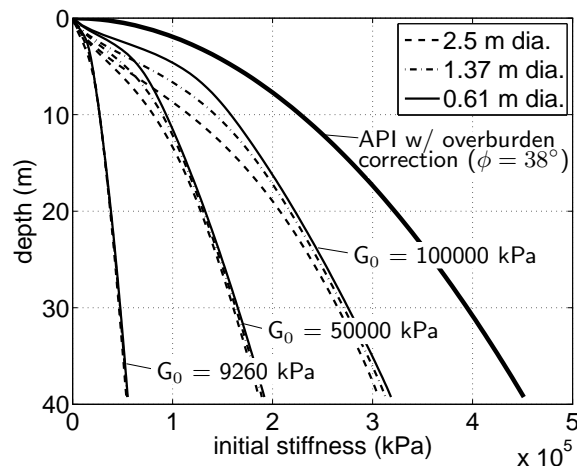


Figure 9.8 Comparison of initial stiffness distributions for various values of soil shear modulus, G .

To determine how these larger k_T distributions affect the pile bending demands, a BNWF lateral spreading analysis is conducted for each test profile and value of G_0 . These analyses consider a reduction in initial stiffness based upon the proposed reduction procedure and the same reduced p_u distribution used for *VC2*. Figure 9.9 compares the results of these analyses to those obtained for *VC2*, and *PC2*, and *PC3*. Table 9.9 presents the values obtained for the two higher shear modulus cases.

For the profile with a shallow liquefied layer ($z = 10 \text{ m}$), the results of the increased shear modulus analyses compare favorably with the other cases. With the exception of *PC2*, in which p_u and k_T are not reduced to account for the presence of the liquefied layer, each case produces approximately the same maximum shear and bending moment demands in the pile. This confirms the previous observation that the initial stiffness of the $p-y$ springs does not control the bending demands in the pile for types of deformations related to the shallow liquefied layer.

The deeper liquefied layer location shows a greater dependence on the initial stiffness of the $p-$

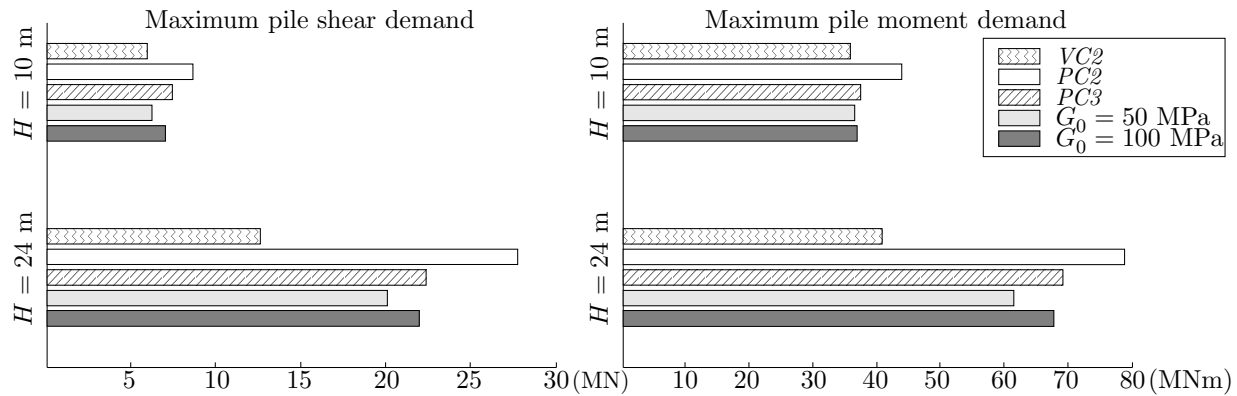


Figure 9.9 Comparison of maximum pile shear and moment demands for higher shear modulus cases.

Table 9.9 Maximum pile bending demands in BNWF lateral spreading simulations for higher shear modulus cases.

	Maximum pile shear force (MN)		Maximum pile moment (MNm)	
	$G_0 = 50$ MPa	$G_0 = 100$ MPa	$G_0 = 50$ MPa	$G_0 = 100$ MPa
$H = 10$ m	6.28	7.12	36.6	37.1
$H = 24$ m	20.1	22.0	61.5	67.9

y springs. The maximum shear and moment demands in the pile increase with increasing G_0 , and the practical cases, which have even larger k_T distributions, produce bending demands that are greater still. For both of the considered soil profiles, the bending demands predicted using $G_0 = 100,000$ kPa, agree well with those estimated in *PC3*. This suggests that when working under the assumption of a small strain shear modulus, the combination of p_u and k_T distribution prediction methods used for *PC3*, when reduced for the presence of the liquefied layer using the proposed reduction procedure, can be used to predict reasonable maximum shear and moment demands in a BNWF lateral spreading analysis.

9.5 SUMMARY

Analysis of pile foundations subject to liquefaction-induced lateral spreads is difficult due to the complexity of the problem. Simplified BNWF analyses using $p-y$ curves are a common design tool for this load case. Careful and informed selection of the $p-y$ curves for a particular analysis, as defined by the characteristic $p-y$ curve parameters of ultimate lateral resistance, p_u , and initial stiffness, k_T , are crucial for the effectiveness of the BNWF approach.

When applied to BNWF models, the $p-y$ curves computed from 3D FE analysis return pile demands that are reasonably similar to 3D lateral spreading simulations, thus validating the approach of computing $p-y$ curves using the rigid pile kinematic. Using $p-y$ curves established using the procedure recommended by the API, the piles in the BNWF models are subject to significantly

larger curvature demands than those returned by the 3D modeling effort. These curves are derived based upon tests of piles loaded at or near the ground surface only, and it has been shown that $p-y$ curves established in this manner are not applicable to the alternative kinematic of the lateral spreading case in which relatively large pile displacements occur with depth.

Lateral spreading analyses were conducted using BNWF and 3D FE approaches to verify and demonstrate the effectiveness of the proposed $p-y$ curve reduction procedure. It was shown that a BNWF analysis using $p-y$ curves obtained from a homogenous soil profile and then reduced using the proposed procedure estimates maximum pile shear and moment demands which compared well with 3D FE analysis. It was also shown that the proposed reduction procedure, when applied to a BNWF lateral spreading analysis in tandem with an informed selection of $p-y$ curves, produced maximum pile bending demands that were more similar to the 3D results than identical unreduced $p-y$ curves. The effect of the magnitude of the soil shear modulus on the initial stiffness of the $p-y$ curves computed from 3D FE analysis is considered, and it is observed that use of a small strain shear modulus estimates pile bending demands which are more similar to the practical methods.

Based upon this work, it is recommended that a BNWF analysis of liquefaction-induced lateral spreading be conducted using $p-y$ curves defined by the p_u distribution of Brinch Hansen (1961) and the API (1987) distribution of k_T , corrected for overburden pressure after Boulanger et al. (2003), in conjunction with the reduction procedure described in this paper. Use of $p-y$ curves defined in this manner seems to estimate maximum pile shear and moment demands that correlate well with a 3D representation of the problem, and will allow a simple BNWF analysis to produce more efficient design solutions.

10 Summary, Conclusions, and Recommendations for Future Work

This report presents a kinematic analysis of a single pile embedded in a laterally spreading layered soil profile. An evaluation of the relevancy of conventional analysis models to this load case is conducted, and a simplified design procedure using a BNWF approach is proposed.

10.1 SUMMARY AND CONCLUSIONS

A summary of the work and associated conclusions of this research is presented in terms of the following items: FE model development, 3D lateral spreading analysis, representative $p-y$ curve computation, evaluation of conventional and computed $p-y$ curves, influence of liquefied layer, and BNWF analysis.

Finite Element Model Development

Chapters 2, 3, and 4 presented the majority of the finite element model development necessary to this research. Additional variations on the main template model that consider increased lateral extents, near-surface effects, a plane strain condition, and variable soil profiles were developed and discussed in Chapters 6, 7, and 8. Each individual component of the models was validated to ensure that verifiably-correct behavior is observed when simple load cases are applied. The main aspects of this work are summarized as follows.

- A 3D soil-pile interaction model was created for the case of a single pile embedded in a soil continuum. This model employs beam-column elements to model the piles, solid brick elements for the soil, and beam-solid contact elements to define the soil-pile interaction.
- Fiber section models were created for three template reinforced concrete pile designs. These models define the constitutive behavior for the beam-column elements used to model the piles. The moment-curvature responses of the composite elastoplastic fiber section models were verified by several means.

- The Drucker-Prager constitutive model used to define the elastoplastic behavior for the cohesionless soils in the lateral spreading model was verified through the applications of stress paths that simulate commonly-used geotechnical tests. It was confirmed that the Drucker-Prager model is able to produce predictable responses to the application of these stress paths.
- Variations in the main soil-pile interaction model were made in order to analyze specific behaviors in greater detail. Models with extended lateral extents were developed and used to evaluate the effects of the fixed boundary in the standard model. Near-surface and plane strain models were developed and analyzed in order to validate observations made using the standard mesh. Models without fixed liquefied layer locations were used to evaluate the influence of the liquefied layer on the soil response.

3D Lateral Spreading Analysis

As discussed in Chapter 5, 24 distinct analysis cases were considered for the lateral spreading kinematic. These cases were divided into four analysis Series depending upon the combination of constitutive models assigned for the pile and soil elements. These four Series were analyzed for two boundary conditions at the head of the pile, fixed and free, resulting in eight analysis cases for each of the three pile designs. Several findings were made based upon this modeling effort.

- For a pile subjected to the kinematic demands of the lateral spreading case, the maximum shear force demand develops at the center of the liquefied layer and there are two extreme moment demands, one in each solid soil layer. The maximum moment demand exists in the lower layer for all but one of the 24 considered cases. The distance between the extreme moments defines the effective length factor for the pile, L_{eff} , a parameter that provides an indication of the severity of the bending demand.
- The liquefied interface acts similarly to a free surface and the adjacent solid soil is able to be pushed into the weaker center layer during the application of lateral loads. This effectively reduces the strength of the solid soil in the regions adjacent to the liquefied layer.
- Plastic hinges form in the pile at the locations of extreme moment in each layer. The plastic deformation/rotation in these locations becomes concentrated over an increasingly smaller length of the pile as the pile-to-soil stiffness ratio decreases.
- The fixity of the pile head is an important consideration. Cases analyzed using a fixed boundary condition at the top of the pile return larger bending moment demands in the piles than corresponding cases analyzed with a free-head condition. Additionally, the maximum moment demand does not generally exist at the point of fixity, but rather, occurs further down in the soil profile. This location depends upon the thickness of the top layer, soil stiffness, and the bending stiffness of the pile.
- The consideration of elastoplastic soil behavior leads to larger estimated maximum moments in the pile than occur with linear elastic soil elements due to the failure of the soil. This observation has been confirmed through the use of two simple beam models, which can be

solved by hand in a relatively simple manner. Elastoplastic soil behavior must be considered in order to obtain appropriate maximum moment and shear demands for piles.

Representative $p-y$ Curve Computation

The soil response obtained from the soil-pile interaction models is evaluated through the computation of representative force density-displacement ($p-y$) curves at each pile node using the procedure described in Chapter 6. Smooth curves are fit to the recorded data using a least square fit. Two functional forms are used: one to establish the initial tangent of the $p-y$ curves and the other to define the complete shape of the curves. In addition to the lateral spreading case, two alternative pile kinematic cases are considered: a top-pushover case and a rigid pile case in which there is a uniform displacement profile with depth. The effects of model-specific phenomena on the extracted results are explored through investigations of variations in the meshing and fixed boundaries. Several conclusions may be drawn from this computational process.

- The force density-displacement ($p-y$) data returned by the 3D models can be fit reasonably well using a hyperbolic tangent function, though the use of this functional form tends to underestimate the initial stiffness displayed by the FE data. Initial stiffness can be established using a polynomial curve fit.
- The kinematics of the pile plays an essential role in defining the obtained soil response and can significantly affect the computed $p-y$ curves. The top-pushover and lateral spreading cases produce pile displacement profiles that vary in magnitude over the length of the piles. At nodes for which the pile displacement is small, not only is the soil response insufficiently activated, the comparably larger displacements which occur at adjacent nodes influence the soil response at these nodes, leading to $p-y$ curves that are not representative of the true soil response. The rigid pile kinematic case must be utilized in order to obtain sensible local $p-y$ curves over the length of the pile.
- Selective mesh refinement results in a condition where the stiffness of the soil continuum varies over the length of the pile. This inconsistent stiffness manifests itself as fluctuations in the recorded soil response. Models with uniformly-sized meshes are analyzed and the inconsistent results obtained from the selectively refined meshes can be smoothed through multiplication with a ratio obtained using the uniform mesh results.
- The fixed boundaries in the model can influence the soil response at large drift. This is confirmed through the use of an additional model created with increased lateral extents in the direction of pile loading. In the default meshes, the proximity of the pile to the boundary causes confining stresses to develop in the deeper portions of the soil that are too large. This effect can be partially alleviated through the use of non-associative plasticity in the soil constitutive model.

Evaluation of Conventional and Computed $p-y$ Curves

The representative $p-y$ curves computed from the 3D FE model using the procedures described in Chapter 6 were used to evaluate several conventional means for describing soil response and establishing $p-y$ curves. The evaluation of the computed $p-y$ curve parameter distributions and comparisons with the conventional methods were discussed in Chapter 7. The considered methods encompass several commonly referenced methods for the definition of distributions of ultimate resistance and initial stiffness with depth. Several observations were made from these comparisons and about the extracted parameter distributions and the following conclusions are drawn.

- Depth appropriate soil failure modes must be considered in the distributions of both the initial stiffness and ultimate lateral resistance of the soil. Near the surface, the lack of overburden pressure leads to the early onset of yield while at depth, the increased overburden pressure leads to the expansion of the elastic regime in the soil. Both of these factors significantly influence both the initial stiffness and ultimate resistance of the computed $p-y$ curves.
- The magnitudes of the computed curves are similar to several of the considered methods at different depths, however, the general form of the results is not reflected in the predicted distributions. It is noted that the current model is not capturing the true ultimate resistance of the soil at depths beyond a few meters. The extracted values beyond this point are extrapolated by the curve-fitting procedure.
- The linear initial stiffness distribution with depth commonly assumed appears to be based upon an extrapolated elastoplastic state. The predicted stiffness at shallow depths correlates fairly well with the 3D FE results, though there is a diameter-dependence that is missing. At increased depths, there is no clear correlation between the computed and estimated results.
- The method most commonly employed when establishing $p-y$ curves for a particular cohesionless soil, that recommended by the API (1987), overestimates both the initial stiffness and ultimate lateral resistance of the soil at depth. This method is based upon field tests in which loads are applied at or above the ground surface. It is likely that the kinematics of the pile in this case contribute to the unrealistically large values that are predicted by this methodology.

Influence of Liquefied Layer

The effects of a liquefied layer on the lateral response of a soil system are evaluated in Chapter 8. This is accomplished through the comparison of $p-y$ curves computed from homogenous soil profiles with corresponding curves computed from layered soil profiles in which a liquefied layer is located between two unliquefied soil layers. Several observations are made and conclusions are drawn.

- The presence of a liquefied layer in the soil profile reduces the initial stiffness and ultimate lateral resistance of the unliquefied soil layers in the areas adjacent to the weaker liquefied middle layer.

- It is observed that the reduction is greatest at the layer interface and decays exponentially with increasing distance from the liquefied layer in both the upper and lower unliquefied layers. The magnitude of the reduction at a particular distance from the liquefied interface depends on the thickness of the liquefied layer, the diameter of the pile, and the vertical effective stress.
- An exponential decay model is proposed to describe the observed parameter reductions.
- A parameter study using the $p-y$ curves computed from 126 combinations of pile diameter, soil profile, and soil properties is used to develop a means to predict reductions for a particular soil profile.
- A simplified procedure is proposed to estimate appropriate reductions in ultimate lateral resistance and initial stiffness for a given soil-pile system that includes a liquefied layer.

Beam on Nonlinear Winkler Foundation Analysis

Beam on nonlinear Winkler foundation analyses of lateral spreading are discussed in Chapter 9. These models are created in order to validate the computed $p-y$ curves, to assess the applicability of conventionally-defined $p-y$ curves to the lateral spreading case, and to validate/demonstrate the proposed procedure to reduce $p-y$ curves to account for the presence of a liquefied soil layer. Several observations and conclusions are made.

- The $p-y$ curves computed from 3D FE analysis produce simulated pile bending responses in BNWF analyses which compare well with corresponding results from 3D lateral spreading simulations. This validates that $p-y$ curves computed using the proposed rigid pile method are representative of the soil response regardless of the analyzed pile kinematics.
- The overestimated values of ultimate lateral resistance and initial stiffness in the API (1987) recommended $p-y$ curves lead to very large pile bending demands that greatly exceed those obtained in 3D analysis. Use of these curves without modification for analysis of lateral spreading, or another load case with deep-seated soil-pile interaction, is not recommended.
- The pile bending responses from BNWF analyses using $p-y$ curves computed from a homogenous soil profile, then reduced using the proposed reduction procedure, compare favorably with corresponding 3D FE analyses that include a liquefied layer. This validates that the reduction procedure is able to estimate appropriate reductions for general combinations of soil profile, soil properties, and pile diameter.
- Further BNWF simulation of lateral spreading identifies that among readily available methods for defining distributions of ultimate lateral resistance and initial stiffness for $p-y$ curves, the method of Brinch Hansen (1961) and the modified API method proposed by Boulanger et al. (2003) seem to most accurately represent the soil response for the lateral spreading load case.

- Application of the proposed reduction process to the parameter distributions estimated by these methods produces pile bending responses that more accurately represent corresponding 3D FE results.

10.2 RECOMMENDATIONS FOR FUTURE WORK

There are several avenues for future work which are suggested by this research. Though many findings have been made, there are nearly as many unanswered questions. These recommendations for future work are subdivided into several categories for clarity.

Finite Element Model Development

- It may be advantageous to explore more combinations of soil and pile properties to further assess how these factors affect the simulations.
- The Drucker-Prager constitutive model used in the simulations is a relatively simple model that does not necessarily capture all aspects of the soil behavior. It may prove useful to explore the findings of this research using a soil model that better captures the true soil behavior.
- A large-deformation model may prove useful in fully capturing the ultimate soil behavior.

Experimental Need

- It may enhance the understanding of this problem to devise a way in which to perform a physical lateral spreading test either at full, or nearly full, scale or at a reduced scale using a shaking table or a centrifuge. This would provide a second set of data with which to evaluate the results of the numerical simulations.
- It has been observed that the soil response obtained from the numerical simulations does not correlate with commonly used empirical methods for predicting this response, especially at depth. Perhaps physical tests, performed using a rigid pile kinematic, along with further numerical simulations can aid in the determination of suitable distributions of initial stiffness and ultimate resistance over the length of the piles.

Soil Response Evaluation

- This research identified shortcomings of several conventional means for representing the lateral response of the soil with depth, however, this work is not conclusive enough to make firm recommendations on revised distributions of ultimate lateral resistance and initial stiffness. Further numerical simulation, perhaps combined with experimental study, would be required for this purpose.

- This research focused on analyses conducted using a single pile embedded in a soil profile in which all surfaces are perpendicular to the pile and there are only three layers. It would be of interest to evaluate the applicability of these findings to any number of additional cases such as pile groups, battered piles, sloping ground conditions, and increased number of soil layers. Any one of these investigations could prove to be a valuable contribution to the general knowledge of laterally loaded piles.

REFERENCES

- ACI Committee 318 (2005). *Building Code Requirements for Structural Concrete (ACI 318-05) and Commentary (ACI 318R-05)*. American Concrete Institute, Farmington Hills, MI.
- American Petroleum Institute (API) (1987). *Recommended Practice for Planning, Designing and Constructing Fixed Offshore Platforms*. API Recommended Practice 2A(RP-2A), Washington, D.C., 17th edition.
- Bazant, Z. P. and Becq-Giraudon, E. (2002). "Statistical prediction of fracture parameters of concrete and implications for choice of testing standard." *Cement and Concrete Research*, 32(4), 529-556.
- Boulanger, R. W., Curras, C. J., Kutter, B. L., Wilson, D. W., and Abghari, A. (1999). "Seismic soil-pile-structure interaction experiments and analyses." *Journal of Geotechnical and Geoenvironmental Engineering, ASCE*, 125(9), 750-759.
- Boulanger, R. W., Kutter, B. L., Brandenburg, S. J., Singh, P., and Chang, D. (2003). *Pile Foundations in liquefied and laterally spreading ground during earthquakes: Centrifuge experiments and analyses*. Center for Geotechnical Modeling, University of California at Davis, Davis, CA. Rep. UCD/CGM-03/01.
- Brandenburg, S. J., Boulanger, R. W., Kutter, B. L., and Chang, D. (2007). "Static pushover analyses of pile groups in liquefied and laterally spreading ground in centrifuge tests." *Journal of Geotechnical and Geoenvironmental Engineering, ASCE*, 133(9), 1055-1066.
- Brinch Hansen, J. (1961). "The ultimate resistance of rigid piles against transversal forces." *Bulletin No. 12*, Geoteknisk Institute, Copenhagen, 5-9.
- Broms, B. B. (1964). "Lateral resistance of piles in cohesionless soils." *Journal of the Soil Mechanics and Foundations Division, ASCE*, 90(SM3), 123-156.
- Brown, D. A. and Shie, C. F. (1990). "Three dimensional finite element model of laterally loaded piles." *Computers and Geotechnics*, 10(1), 59-79.
- Chen, W. F. and Saleeb, A. F. (1994). *Constitutive Equations for Engineering Materials Volume I: Elasticity and Modeling*. Elsevier Science B.V., Amsterdam.
- Drucker, D. C. and Prager, W. (1952). "Soil mechanics and plastic analysis or limit design." *Quarterly of Applied Mathematics*, 10(2), 157-165.
- Finn, W. D. L. and Fujita, N. (2002). "Piles in liquefiable soils: seismic analysis and design issues." *Soil Dynamics and Earthquake Engineering*, 22(9-12), 731-742.
- Fleming, W. G. K., Weltman, A. J., Randolph, M. F., and Elson, W. K. (1985). *Piling Engineering*. Surrey University Press, London.

- Georgiadis, M. (1983). “Development of p - y curves for layered soils.” *Geotechnical Practice in Offshore Engineering*, Reston, VA. ASCE, 536–545.
- Helnwein, P. (2001). “Some remarks on the compressed matrix representation of symmetric second-order and fourth-order tensors.” *Computer Methods in Applied Mechanics and Engineering*, 190(22-23), 2753 – 2770.
- International Center for Numerical Methods in Engineering (CIMNE) (2008). *GiD User Manual*. <http://gid.cimne.upc.es/>.
- Kaplan, M. F. (1961). “Crack propagation and the fracture of concrete.” *Journal of the American Concrete Institute*, 58(5), 591–610.
- Kent, D. C. and Park, R. (1971). “Flexural members with confined concrete.” *Journal of the Structural Mechanics Division, ASCE*, 97(ST7), 1969–1990.
- Kulhawy, F. H. and Mayne, P. W. (1990). *Manual on Estimating Soil Properties for Foundation Design*. Electrical Power Research Institute, EPRI EL–6800, Project 1493–6 Final Report.
- Lam, I. P., Arduino, P., and Mackenzie-Helnwein, P. (2009). “Opensees soil–pile interaction study under lateral spread loading.” *International Foundation Congress & Equipment Expo*, Orlando, FL.
- Matlock, H. and Reese, L. C. (1960). “Generalized solutions for laterally loaded piles.” *Journal of the Soil Mechanics and Foundations Division, ASCE*, 86(SM5), 63–91.
- McClelland, B. and Focht, J. (1958). “Soil modulus for laterally loaded piles.” *Transactions, ASCE*, 123, 1049–1086.
- McGann, C. R., Arduino, P., and Mackenzie-Helnwein, P. (2010). “Lateral resistance reduction for static analysis of lateral spreading.” *Joint Conference Proceedings, 7th International Conference on Urban Earthquake Engineering (7CUEE) & 5th International Conference on Earthquake Engineering (5ICEE)*, Tokyo Institute of Technology, Tokyo, Japan.
- Megson, T. H. G. (2005). *Structural and Stress Analysis*. Elsevier Butterworth Heinemann, Amsterdam.
- OpenSees. *Open System for Earthquake Engineering Simulation*. <http://opensees.berkeley.edu>. Pacific Earthquake Engineering Research Center, University of California, Berkeley.
- Park, R. and Paulay, T. (1975). *Reinforced Concrete Structures*. Wiley & Sons, New York.
- Petek, K. A. (2006). “Development and application of mixed beam–solid models for analysis of soil–pile interaction problems,” Ph.d. thesis, University of Washington.
- Reese, L. C., Cox, W. R., and Koop, F. D. (1974). “Analysis of laterally loaded piles in sand.” *Proceedings of the 5th Offshore Technology Conference*, Vol. 2, Houston. 473–483.

- Reese, L. C. and Van Impe, W. F. (2001). *Single Piles and Pile Groups Under Lateral Loading*. A.A. Balkema, Rotterdam, Netherlands.
- Scott, R. F. (1981). *Foundation Analysis*. Prentice–Hall, Englewood Cliffs, NJ.
- Xu, S. and Zhang, X. (2008). “Determination of fracture parameters for crack propagation in concrete using an energy approach.” *Engineering Fracture Mechanics*, 75(15), 4292–4308.
- Yang, Z. and Jeremic, B. (2005). “Study of soil layering effects on lateral loading behavior of piles.” *Journal of Geotechnical and Geoenvironmental Engineering*, 131(6), 762–770.

PEER REPORTS

PEER reports are available individually or by yearly subscription. PEER reports can be ordered at http://peer.berkeley.edu/publications/peer_reports.html or by contacting the Pacific Earthquake Engineering Research Center, 325 Davis Hall mail code 1792, Berkeley, CA 94720. Tel.: (510) 642-3437; Fax: (510) 665-1655; Email: peer_editor@berkeley.edu

- PEER 2012/05** *Development of Simplified Analysis Procedure for Piles in Laterally Spreading Layered Soils.* Christopher R. McGann, Pedro Arduino, and Peter Mackenzie-Helnwein. December 2012.
- PEER 2012/04** *Unbonded Pre-Tensioned Columns for Bridges in Seismic Regions.* Phillip M. Davis, Todd M. Janes, Marc O. Eberhard, and John F. Stanton. December 2012.
- PEER 2012/03** *Experimental and Analytical Studies on Reinforced Concrete Buildings with Seismically Vulnerable Beam-Column Joints.* Sangjoon Park and Khalid M. Mosalam. October 2012.
- PEER 2012/02** *Seismic Performance of Reinforced Concrete Bridges Allowed to Uplift during Multi-Directional Excitation.* Andres Oscar Espinoza and Stephen A. Mahin. July 2012.
- PEER 2012/01** *Spectral Damping Scaling Factors for Shallow Crustal Earthquakes in Active Tectonic Regions.* Sanaz Rezaeian, Yousef Bozorgnia, I. M. Idriss, Kenneth Campbell, Norman Abrahamson, and Walter Silva. July 2012.
- PEER 2011/10** *Earthquake Engineering for Resilient Communities: 2011 PEER Internship Program Research Report Collection.* Eds. Heidi Faison and Stephen A. Mahin. December 2011.
- PEER 2011/09** *Calibration of Semi-Stochastic Procedure for Simulating High-Frequency Ground Motions.* Jonathan P. Stewart, Emel Seyhan, and Robert W. Graves. December 2011.
- PEER 2011/08** *Water Supply in regard to Fire Following Earthquake.* Charles Scawthorn. November 2011.
- PEER 2011/07** *Seismic Risk Management in Urban Areas. Proceedings of a U.S.-Iran-Turkey Seismic Workshop.* September 2011.
- PEER 2011/06** *The Use of Base Isolation Systems to Achieve Complex Seismic Performance Objectives.* Troy A. Morgan and Stephen A. Mahin. July 2011.
- PEER 2011/05** *Case Studies of the Seismic Performance of Tall Buildings Designed by Alternative Means.* Task 12 Report for the Tall Buildings Initiative. Jack Moehle, Yousef Bozorgnia, Nirmal Jayaram, Pierson Jones, Mohsen Rahnama, Nilesh Shome, Zeynep Tuna, John Wallace, Tony Yang, and Farzin Zareian. July 2011.
- PEER 2011/04** *Recommended Design Practice for Pile Foundations in Laterally Spreading Ground.* Scott A. Ashford, Ross W. Boulanger, and Scott J. Brandenburg. June 2011.
- PEER 2011/03** *New Ground Motion Selection Procedures and Selected Motions for the PEER Transportation Research Program.* Jack W. Baker, Ting Lin, Shrey K. Shahi, and Nirmal Jayaram. March 2011.
- PEER 2011/02** *A Bayesian Network Methodology for Infrastructure Seismic Risk Assessment and Decision Support.* Michelle T. Bensi, Armen Der Kiureghian, and Daniel Straub. March 2011.
- PEER 2011/01** *Demand Fragility Surfaces for Bridges in Liquefied and Laterally Spreading Ground.* Scott J. Brandenburg, Jian Zhang, Pirooz Kashighandi, Yili Huo, and Minxing Zhao. March 2011.
- PEER 2010/05** *Guidelines for Performance-Based Seismic Design of Tall Buildings.* Developed by the Tall Buildings Initiative. November 2010.
- PEER 2010/04** *Application Guide for the Design of Flexible and Rigid Bus Connections between Substation Equipment Subjected to Earthquakes.* Jean-Bernard Dastous and Armen Der Kiureghian. September 2010.
- PEER 2010/03** *Shear Wave Velocity as a Statistical Function of Standard Penetration Test Resistance and Vertical Effective Stress at Caltrans Bridge Sites.* Scott J. Brandenburg, Naresh Bellana, and Thomas Shantz. June 2010.
- PEER 2010/02** *Stochastic Modeling and Simulation of Ground Motions for Performance-Based Earthquake Engineering.* Sanaz Rezaeian and Armen Der Kiureghian. June 2010.
- PEER 2010/01** *Structural Response and Cost Characterization of Bridge Construction Using Seismic Performance Enhancement Strategies.* Ady Aviram, Božidar Stojadinović, Gustavo J. Parra-Montesinos, and Kevin R. Mackie. March 2010.
- PEER 2009/03** *The Integration of Experimental and Simulation Data in the Study of Reinforced Concrete Bridge Systems Including Soil-Foundation-Structure Interaction.* Matthew Dryden and Gregory L. Fenves. November 2009.
- PEER 2009/02** *Improving Earthquake Mitigation through Innovations and Applications in Seismic Science, Engineering, Communication, and Response. Proceedings of a U.S.-Iran Seismic Workshop.* October 2009.

- PEER 2009/01** *Evaluation of Ground Motion Selection and Modification Methods: Predicting Median Interstory Drift Response of Buildings.* Curt B. Haselton, Ed. June 2009.
- PEER 2008/10** *Technical Manual for Strata.* Albert R. Kottke and Ellen M. Rathje. February 2009.
- PEER 2008/09** *NGA Model for Average Horizontal Component of Peak Ground Motion and Response Spectra.* Brian S.-J. Chiou and Robert R. Youngs. November 2008.
- PEER 2008/08** *Toward Earthquake-Resistant Design of Concentrically Braced Steel Structures.* Patxi Uriz and Stephen A. Mahin. November 2008.
- PEER 2008/07** *Using OpenSees for Performance-Based Evaluation of Bridges on Liquefiable Soils.* Stephen L. Kramer, Pedro Arduino, and HyungSuk Shin. November 2008.
- PEER 2008/06** *Shaking Table Tests and Numerical Investigation of Self-Centering Reinforced Concrete Bridge Columns.* Hyung IL Jeong, Junichi Sakai, and Stephen A. Mahin. September 2008.
- PEER 2008/05** *Performance-Based Earthquake Engineering Design Evaluation Procedure for Bridge Foundations Undergoing Liquefaction-Induced Lateral Ground Displacement.* Christian A. Ledezma and Jonathan D. Bray. August 2008.
- PEER 2008/04** *Benchmarking of Nonlinear Geotechnical Ground Response Analysis Procedures.* Jonathan P. Stewart, Annie On-Lei Kwok, Youssef M. A. Hashash, Neven Matasovic, Robert Pyke, Zhiliang Wang, and Zhaohui Yang. August 2008.
- PEER 2008/03** *Guidelines for Nonlinear Analysis of Bridge Structures in California.* Ady Aviram, Kevin R. Mackie, and Božidar Stojadinović. August 2008.
- PEER 2008/02** *Treatment of Uncertainties in Seismic-Risk Analysis of Transportation Systems.* Evangelos Stergiou and Anne S. Kiremidjian. July 2008.
- PEER 2008/01** *Seismic Performance Objectives for Tall Buildings.* William T. Holmes, Charles Kircher, William Petak, and Nabih Youssef. August 2008.
- PEER 2007/12** *An Assessment to Benchmark the Seismic Performance of a Code-Conforming Reinforced Concrete Moment-Frame Building.* Curt Haselton, Christine A. Goulet, Judith Mitrani-Reiser, James L. Beck, Gregory G. Deierlein, Keith A. Porter, Jonathan P. Stewart, and Ertugrul Taciroglu. August 2008.
- PEER 2007/11** *Bar Buckling in Reinforced Concrete Bridge Columns.* Wayne A. Brown, Dawn E. Lehman, and John F. Stanton. February 2008.
- PEER 2007/10** *Computational Modeling of Progressive Collapse in Reinforced Concrete Frame Structures.* Mohamed M. Talaat and Khalid M. Mosalam. May 2008.
- PEER 2007/09** *Integrated Probabilistic Performance-Based Evaluation of Benchmark Reinforced Concrete Bridges.* Kevin R. Mackie, John-Michael Wong, and Božidar Stojadinović. January 2008.
- PEER 2007/08** *Assessing Seismic Collapse Safety of Modern Reinforced Concrete Moment-Frame Buildings.* Curt B. Haselton and Gregory G. Deierlein. February 2008.
- PEER 2007/07** *Performance Modeling Strategies for Modern Reinforced Concrete Bridge Columns.* Michael P. Berry and Marc O. Eberhard. April 2008.
- PEER 2007/06** *Development of Improved Procedures for Seismic Design of Buried and Partially Buried Structures.* Linda Al Atik and Nicholas Sitar. June 2007.
- PEER 2007/05** *Uncertainty and Correlation in Seismic Risk Assessment of Transportation Systems.* Renee G. Lee and Anne S. Kiremidjian. July 2007.
- PEER 2007/04** *Numerical Models for Analysis and Performance-Based Design of Shallow Foundations Subjected to Seismic Loading.* Sivapalan Gajan, Tara C. Hutchinson, Bruce L. Kutter, Prishati Raychowdhury, José A. Ugalde, and Jonathan P. Stewart. May 2008.
- PEER 2007/03** *Beam-Column Element Model Calibrated for Predicting Flexural Response Leading to Global Collapse of RC Frame Buildings.* Curt B. Haselton, Abbie B. Liel, Sarah Taylor Lange, and Gregory G. Deierlein. May 2008.
- PEER 2007/02** *Campbell-Bozorgnia NGA Ground Motion Relations for the Geometric Mean Horizontal Component of Peak and Spectral Ground Motion Parameters.* Kenneth W. Campbell and Yousef Bozorgnia. May 2007.
- PEER 2007/01** *Boore-Atkinson NGA Ground Motion Relations for the Geometric Mean Horizontal Component of Peak and Spectral Ground Motion Parameters.* David M. Boore and Gail M. Atkinson. May 2007.
- PEER 2006/12** *Societal Implications of Performance-Based Earthquake Engineering.* Peter J. May. May 2007.
- PEER 2006/11** *Probabilistic Seismic Demand Analysis Using Advanced Ground Motion Intensity Measures, Attenuation Relationships, and Near-Fault Effects.* Polsak Tothong and C. Allin Cornell. March 2007.

- PEER 2006/10** *Application of the PEER PBEE Methodology to the I-880 Viaduct.* Sashi Kunnath. February 2007.
- PEER 2006/09** *Quantifying Economic Losses from Travel Forgone Following a Large Metropolitan Earthquake.* James Moore, Sungbin Cho, Yue Yue Fan, and Stuart Werner. November 2006.
- PEER 2006/08** *Vector-Valued Ground Motion Intensity Measures for Probabilistic Seismic Demand Analysis.* Jack W. Baker and C. Allin Cornell. October 2006.
- PEER 2006/07** *Analytical Modeling of Reinforced Concrete Walls for Predicting Flexural and Coupled–Shear-Flexural Responses.* Kutay Orakcal, Leonardo M. Massone, and John W. Wallace. October 2006.
- PEER 2006/06** *Nonlinear Analysis of a Soil-Drilled Pier System under Static and Dynamic Axial Loading.* Gang Wang and Nicholas Sitar. November 2006.
- PEER 2006/05** *Advanced Seismic Assessment Guidelines.* Paolo Bazzurro, C. Allin Cornell, Charles Menun, Maziar Motahari, and Nicolas Luco. September 2006.
- PEER 2006/04** *Probabilistic Seismic Evaluation of Reinforced Concrete Structural Components and Systems.* Tae Hyung Lee and Khalid M. Mosalam. August 2006.
- PEER 2006/03** *Performance of Lifelines Subjected to Lateral Spreading.* Scott A. Ashford and Teerawat Juirnarongrit. July 2006.
- PEER 2006/02** *Pacific Earthquake Engineering Research Center Highway Demonstration Project.* Anne Kiremidjian, James Moore, Yue Yue Fan, Nesrin Basoz, Ozgur Yazali, and Meredith Williams. April 2006.
- PEER 2006/01** *Bracing Berkeley. A Guide to Seismic Safety on the UC Berkeley Campus.* Mary C. Comerio, Stephen Tobriner, and Ariane Fehrenkamp. January 2006.
- PEER 2005/16** *Seismic Response and Reliability of Electrical Substation Equipment and Systems.* Junho Song, Armen Der Kiureghian, and Jerome L. Sackman. April 2006.
- PEER 2005/15** *CPT-Based Probabilistic Assessment of Seismic Soil Liquefaction Initiation.* R. E. S. Moss, R. B. Seed, R. E. Kayen, J. P. Stewart, and A. Der Kiureghian. April 2006.
- PEER 2005/14** *Workshop on Modeling of Nonlinear Cyclic Load-Deformation Behavior of Shallow Foundations.* Bruce L. Kutter, Geoffrey Martin, Tara Hutchinson, Chad Harden, Sivapalan Gajan, and Justin Phalen. March 2006.
- PEER 2005/13** *Stochastic Characterization and Decision Bases under Time-Dependent Aftershock Risk in Performance-Based Earthquake Engineering.* Gee Liek Yeo and C. Allin Cornell. July 2005.
- PEER 2005/12** *PEER Testbed Study on a Laboratory Building: Exercising Seismic Performance Assessment.* Mary C. Comerio, editor. November 2005.
- PEER 2005/11** *Van Nuys Hotel Building Testbed Report: Exercising Seismic Performance Assessment.* Helmut Krawinkler, editor. October 2005.
- PEER 2005/10** *First NEES/E-Defense Workshop on Collapse Simulation of Reinforced Concrete Building Structures.* September 2005.
- PEER 2005/09** *Test Applications of Advanced Seismic Assessment Guidelines.* Joe Maffei, Karl Telleen, Danya Mohr, William Holmes, and Yuki Nakayama. August 2006.
- PEER 2005/08** *Damage Accumulation in Lightly Confined Reinforced Concrete Bridge Columns.* R. Tyler Ranf, Jared M. Nelson, Zach Price, Marc O. Eberhard, and John F. Stanton. April 2006.
- PEER 2005/07** *Experimental and Analytical Studies on the Seismic Response of Freestanding and Anchored Laboratory Equipment.* Dimitrios Konstantinidis and Nicos Makris. January 2005.
- PEER 2005/06** *Global Collapse of Frame Structures under Seismic Excitations.* Luis F. Ibarra and Helmut Krawinkler. September 2005.
- PEER 2005/05** *Performance Characterization of Bench- and Shelf-Mounted Equipment.* Samit Ray Chaudhuri and Tara C. Hutchinson. May 2006.
- PEER 2005/04** *Numerical Modeling of the Nonlinear Cyclic Response of Shallow Foundations.* Chad Harden, Tara Hutchinson, Geoffrey R. Martin, and Bruce L. Kutter. August 2005.
- PEER 2005/03** *A Taxonomy of Building Components for Performance-Based Earthquake Engineering.* Keith A. Porter. September 2005.
- PEER 2005/02** *Fragility Basis for California Highway Overpass Bridge Seismic Decision Making.* Kevin R. Mackie and Božidar Stojadinović. June 2005.
- PEER 2005/01** *Empirical Characterization of Site Conditions on Strong Ground Motion.* Jonathan P. Stewart, Yoojoong Choi, and Robert W. Graves. June 2005.

- PEER 2004/09** *Electrical Substation Equipment Interaction: Experimental Rigid Conductor Studies.* Christopher Stearns and André Filiatrault. February 2005.
- PEER 2004/08** *Seismic Qualification and Fragility Testing of Line Break 550-kV Disconnect Switches.* Shakhzod M. Takhirov, Gregory L. Fenves, and Eric Fujisaki. January 2005.
- PEER 2004/07** *Ground Motions for Earthquake Simulator Qualification of Electrical Substation Equipment.* Shakhzod M. Takhirov, Gregory L. Fenves, Eric Fujisaki, and Don Clyde. January 2005.
- PEER 2004/06** *Performance-Based Regulation and Regulatory Regimes.* Peter J. May and Chris Koski. September 2004.
- PEER 2004/05** *Performance-Based Seismic Design Concepts and Implementation: Proceedings of an International Workshop.* Peter Fajfar and Helmut Krawinkler, editors. September 2004.
- PEER 2004/04** *Seismic Performance of an Instrumented Tilt-up Wall Building.* James C. Anderson and Vitelmo V. Bertero. July 2004.
- PEER 2004/03** *Evaluation and Application of Concrete Tilt-up Assessment Methodologies.* Timothy Graf and James O. Malley. October 2004.
- PEER 2004/02** *Analytical Investigations of New Methods for Reducing Residual Displacements of Reinforced Concrete Bridge Columns.* Junichi Sakai and Stephen A. Mahin. August 2004.
- PEER 2004/01** *Seismic Performance of Masonry Buildings and Design Implications.* Kerri Anne Taeko Tokoro, James C. Anderson, and Vitelmo V. Bertero. February 2004.
- PEER 2003/18** *Performance Models for Flexural Damage in Reinforced Concrete Columns.* Michael Berry and Marc Eberhard. August 2003.
- PEER 2003/17** *Predicting Earthquake Damage in Older Reinforced Concrete Beam-Column Joints.* Catherine Pagni and Laura Lowes. October 2004.
- PEER 2003/16** *Seismic Demands for Performance-Based Design of Bridges.* Kevin Mackie and Božidar Stojadinović. August 2003.
- PEER 2003/15** *Seismic Demands for Nondeteriorating Frame Structures and Their Dependence on Ground Motions.* Ricardo Antonio Medina and Helmut Krawinkler. May 2004.
- PEER 2003/14** *Finite Element Reliability and Sensitivity Methods for Performance-Based Earthquake Engineering.* Terje Haukaas and Armen Der Kiureghian. April 2004.
- PEER 2003/13** *Effects of Connection Hysteretic Degradation on the Seismic Behavior of Steel Moment-Resisting Frames.* Janise E. Rodgers and Stephen A. Mahin. March 2004.
- PEER 2003/12** *Implementation Manual for the Seismic Protection of Laboratory Contents: Format and Case Studies.* William T. Holmes and Mary C. Comerio. October 2003.
- PEER 2003/11** *Fifth U.S.-Japan Workshop on Performance-Based Earthquake Engineering Methodology for Reinforced Concrete Building Structures.* February 2004.
- PEER 2003/10** *A Beam-Column Joint Model for Simulating the Earthquake Response of Reinforced Concrete Frames.* Laura N. Lowes, Nilanjan Mitra, and Arash Altoontash. February 2004.
- PEER 2003/09** *Sequencing Repairs after an Earthquake: An Economic Approach.* Marco Casari and Simon J. Wilkie. April 2004.
- PEER 2003/08** *A Technical Framework for Probability-Based Demand and Capacity Factor Design (DCFD) Seismic Formats.* Fatemeh Jalayer and C. Allin Cornell. November 2003.
- PEER 2003/07** *Uncertainty Specification and Propagation for Loss Estimation Using FOSM Methods.* Jack W. Baker and C. Allin Cornell. September 2003.
- PEER 2003/06** *Performance of Circular Reinforced Concrete Bridge Columns under Bidirectional Earthquake Loading.* Mahmoud M. Hachem, Stephen A. Mahin, and Jack P. Moehle. February 2003.
- PEER 2003/05** *Response Assessment for Building-Specific Loss Estimation.* Eduardo Miranda and Shahram Taghavi. September 2003.
- PEER 2003/04** *Experimental Assessment of Columns with Short Lap Splices Subjected to Cyclic Loads.* Murat Melek, John W. Wallace, and Joel Conte. April 2003.
- PEER 2003/03** *Probabilistic Response Assessment for Building-Specific Loss Estimation.* Eduardo Miranda and Hesameddin Aslani. September 2003.
- PEER 2003/02** *Software Framework for Collaborative Development of Nonlinear Dynamic Analysis Program.* Jun Peng and Kincho H. Law. September 2003.

- PEER 2003/01** *Shake Table Tests and Analytical Studies on the Gravity Load Collapse of Reinforced Concrete Frames.* Kenneth John Elwood and Jack P. Moehle. November 2003.
- PEER 2002/24** *Performance of Beam to Column Bridge Joints Subjected to a Large Velocity Pulse.* Natalie Gibson, André Filiatrault, and Scott A. Ashford. April 2002.
- PEER 2002/23** *Effects of Large Velocity Pulses on Reinforced Concrete Bridge Columns.* Greg L. Orozco and Scott A. Ashford. April 2002.
- PEER 2002/22** *Characterization of Large Velocity Pulses for Laboratory Testing.* Kenneth E. Cox and Scott A. Ashford. April 2002.
- PEER 2002/21** *Fourth U.S.-Japan Workshop on Performance-Based Earthquake Engineering Methodology for Reinforced Concrete Building Structures.* December 2002.
- PEER 2002/20** *Barriers to Adoption and Implementation of PBEE Innovations.* Peter J. May. August 2002.
- PEER 2002/19** *Economic-Engineered Integrated Models for Earthquakes: Socioeconomic Impacts.* Peter Gordon, James E. Moore II, and Harry W. Richardson. July 2002.
- PEER 2002/18** *Assessment of Reinforced Concrete Building Exterior Joints with Substandard Details.* Chris P. Pantelides, Jon Hansen, Justin Nadauld, and Lawrence D. Reaveley. May 2002.
- PEER 2002/17** *Structural Characterization and Seismic Response Analysis of a Highway Overcrossing Equipped with Elastomeric Bearings and Fluid Dampers: A Case Study.* Nicos Makris and Jian Zhang. November 2002.
- PEER 2002/16** *Estimation of Uncertainty in Geotechnical Properties for Performance-Based Earthquake Engineering.* Allen L. Jones, Steven L. Kramer, and Pedro Arduino. December 2002.
- PEER 2002/15** *Seismic Behavior of Bridge Columns Subjected to Various Loading Patterns.* Asadollah Esmaeily-Gh. and Yan Xiao. December 2002.
- PEER 2002/14** *Inelastic Seismic Response of Extended Pile Shaft Supported Bridge Structures.* T.C. Hutchinson, R.W. Boulanger, Y.H. Chai, and I.M. Idriss. December 2002.
- PEER 2002/13** *Probabilistic Models and Fragility Estimates for Bridge Components and Systems.* Paolo Gardoni, Armen Der Kiureghian, and Khalid M. Mosalam. June 2002.
- PEER 2002/12** *Effects of Fault Dip and Slip Rake on Near-Source Ground Motions: Why Chi-Chi Was a Relatively Mild M7.6 Earthquake.* Brad T. Aagaard, John F. Hall, and Thomas H. Heaton. December 2002.
- PEER 2002/11** *Analytical and Experimental Study of Fiber-Reinforced Strip Isolators.* James M. Kelly and Shakhzod M. Takhirov. September 2002.
- PEER 2002/10** *Centrifuge Modeling of Settlement and Lateral Spreading with Comparisons to Numerical Analyses.* Sivapalan Gajan and Bruce L. Kutter. January 2003.
- PEER 2002/09** *Documentation and Analysis of Field Case Histories of Seismic Compression during the 1994 Northridge, California, Earthquake.* Jonathan P. Stewart, Patrick M. Smith, Daniel H. Whang, and Jonathan D. Bray. October 2002.
- PEER 2002/08** *Component Testing, Stability Analysis and Characterization of Buckling-Restrained Unbonded Braces™.* Cameron Black, Nicos Makris, and Ian Aiken. September 2002.
- PEER 2002/07** *Seismic Performance of Pile-Wharf Connections.* Charles W. Roeder, Robert Graff, Jennifer Soderstrom, and Jun Han Yoo. December 2001.
- PEER 2002/06** *The Use of Benefit-Cost Analysis for Evaluation of Performance-Based Earthquake Engineering Decisions.* Richard O. Zerbe and Anthony Falit-Baiamonte. September 2001.
- PEER 2002/05** *Guidelines, Specifications, and Seismic Performance Characterization of Nonstructural Building Components and Equipment.* André Filiatrault, Constantin Christopoulos, and Christopher Stearns. September 2001.
- PEER 2002/04** *Consortium of Organizations for Strong-Motion Observation Systems and the Pacific Earthquake Engineering Research Center Lifelines Program: Invited Workshop on Archiving and Web Dissemination of Geotechnical Data, 4–5 October 2001.* September 2002.
- PEER 2002/03** *Investigation of Sensitivity of Building Loss Estimates to Major Uncertain Variables for the Van Nuys Testbed.* Keith A. Porter, James L. Beck, and Rustem V. Shaikhutdinov. August 2002.
- PEER 2002/02** *The Third U.S.-Japan Workshop on Performance-Based Earthquake Engineering Methodology for Reinforced Concrete Building Structures.* July 2002.
- PEER 2002/01** *Nonstructural Loss Estimation: The UC Berkeley Case Study.* Mary C. Comerio and John C. Stallmeyer. December 2001.

- PEER 2001/16** *Statistics of SDF-System Estimate of Roof Displacement for Pushover Analysis of Buildings.* Anil K. Chopra, Rakesh K. Goel, and Chatpan Chintanapakdee. December 2001.
- PEER 2001/15** *Damage to Bridges during the 2001 Nisqually Earthquake.* R. Tyler Ranf, Marc O. Eberhard, and Michael P. Berry. November 2001.
- PEER 2001/14** *Rocking Response of Equipment Anchored to a Base Foundation.* Nicos Makris and Cameron J. Black. September 2001.
- PEER 2001/13** *Modeling Soil Liquefaction Hazards for Performance-Based Earthquake Engineering.* Steven L. Kramer and Ahmed-W. Elgamal. February 2001.
- PEER 2001/12** *Development of Geotechnical Capabilities in OpenSees.* Boris Jeremić. September 2001.
- PEER 2001/11** *Analytical and Experimental Study of Fiber-Reinforced Elastomeric Isolators.* James M. Kelly and Shakhzod M. Takhirov. September 2001.
- PEER 2001/10** *Amplification Factors for Spectral Acceleration in Active Regions.* Jonathan P. Stewart, Andrew H. Liu, Yoojoong Choi, and Mehmet B. Baturay. December 2001.
- PEER 2001/09** *Ground Motion Evaluation Procedures for Performance-Based Design.* Jonathan P. Stewart, Shyh-Jeng Chiou, Jonathan D. Bray, Robert W. Graves, Paul G. Somerville, and Norman A. Abrahamson. September 2001.
- PEER 2001/08** *Experimental and Computational Evaluation of Reinforced Concrete Bridge Beam-Column Connections for Seismic Performance.* Clay J. Naito, Jack P. Moehle, and Khalid M. Mosalam. November 2001.
- PEER 2001/07** *The Rocking Spectrum and the Shortcomings of Design Guidelines.* Nicos Makris and Dimitrios Konstantinidis. August 2001.
- PEER 2001/06** *Development of an Electrical Substation Equipment Performance Database for Evaluation of Equipment Fragilities.* Thalia Agnanos. April 1999.
- PEER 2001/05** *Stiffness Analysis of Fiber-Reinforced Elastomeric Isolators.* Hsiang-Chuan Tsai and James M. Kelly. May 2001.
- PEER 2001/04** *Organizational and Societal Considerations for Performance-Based Earthquake Engineering.* Peter J. May. April 2001.
- PEER 2001/03** *A Modal Pushover Analysis Procedure to Estimate Seismic Demands for Buildings: Theory and Preliminary Evaluation.* Anil K. Chopra and Rakesh K. Goel. January 2001.
- PEER 2001/02** *Seismic Response Analysis of Highway Overcrossings Including Soil-Structure Interaction.* Jian Zhang and Nicos Makris. March 2001.
- PEER 2001/01** *Experimental Study of Large Seismic Steel Beam-to-Column Connections.* Egor P. Popov and Shakhzod M. Takhirov. November 2000.
- PEER 2000/10** *The Second U.S.-Japan Workshop on Performance-Based Earthquake Engineering Methodology for Reinforced Concrete Building Structures.* March 2000.
- PEER 2000/09** *Structural Engineering Reconnaissance of the August 17, 1999 Earthquake: Kocaeli (Izmit), Turkey.* Halil Sezen, Kenneth J. Elwood, Andrew S. Whittaker, Khalid Mosalam, John J. Wallace, and John F. Stanton. December 2000.
- PEER 2000/08** *Behavior of Reinforced Concrete Bridge Columns Having Varying Aspect Ratios and Varying Lengths of Confinement.* Anthony J. Calderone, Dawn E. Lehman, and Jack P. Moehle. January 2001.
- PEER 2000/07** *Cover-Plate and Flange-Plate Reinforced Steel Moment-Resisting Connections.* Taejin Kim, Andrew S. Whittaker, Amir S. Gilani, Vitelmo V. Bertero, and Shakhzod M. Takhirov. September 2000.
- PEER 2000/06** *Seismic Evaluation and Analysis of 230-kV Disconnect Switches.* Amir S. J. Gilani, Andrew S. Whittaker, Gregory L. Fenves, Chun-Hao Chen, Henry Ho, and Eric Fujisaki. July 2000.
- PEER 2000/05** *Performance-Based Evaluation of Exterior Reinforced Concrete Building Joints for Seismic Excitation.* Chandra Clyde, Chris P. Pantelides, and Lawrence D. Reaveley. July 2000.
- PEER 2000/04** *An Evaluation of Seismic Energy Demand: An Attenuation Approach.* Chung-Che Chou and Chia-Ming Uang. July 1999.
- PEER 2000/03** *Framing Earthquake Retrofitting Decisions: The Case of Hillside Homes in Los Angeles.* Detlof von Winterfeldt, Nels Roselund, and Alicia Kitsuse. March 2000.
- PEER 2000/02** *U.S.-Japan Workshop on the Effects of Near-Field Earthquake Shaking.* Andrew Whittaker, ed. July 2000.
- PEER 2000/01** *Further Studies on Seismic Interaction in Interconnected Electrical Substation Equipment.* Armen Der Kiureghian, Kee-Jeung Hong, and Jerome L. Sackman. November 1999.

- PEER 1999/14** *Seismic Evaluation and Retrofit of 230-kV Porcelain Transformer Bushings.* Amir S. Gilani, Andrew S. Whittaker, Gregory L. Fenves, and Eric Fujisaki. December 1999.
- PEER 1999/13** *Building Vulnerability Studies: Modeling and Evaluation of Tilt-up and Steel Reinforced Concrete Buildings.* John W. Wallace, Jonathan P. Stewart, and Andrew S. Whittaker, editors. December 1999.
- PEER 1999/12** *Rehabilitation of Nonductile RC Frame Building Using Encasement Plates and Energy-Dissipating Devices.* Mehrdad Sasani, Vitelmo V. Bertero, James C. Anderson. December 1999.
- PEER 1999/11** *Performance Evaluation Database for Concrete Bridge Components and Systems under Simulated Seismic Loads.* Yael D. Hose and Frieder Seible. November 1999.
- PEER 1999/10** *U.S.-Japan Workshop on Performance-Based Earthquake Engineering Methodology for Reinforced Concrete Building Structures.* December 1999.
- PEER 1999/09** *Performance Improvement of Long Period Building Structures Subjected to Severe Pulse-Type Ground Motions.* James C. Anderson, Vitelmo V. Bertero, and Raul Bertero. October 1999.
- PEER 1999/08** *Envelopes for Seismic Response Vectors.* Charles Menun and Armen Der Kiureghian. July 1999.
- PEER 1999/07** *Documentation of Strengths and Weaknesses of Current Computer Analysis Methods for Seismic Performance of Reinforced Concrete Members.* William F. Cofer. November 1999.
- PEER 1999/06** *Rocking Response and Overturning of Anchored Equipment under Seismic Excitations.* Nicos Makris and Jian Zhang. November 1999.
- PEER 1999/05** *Seismic Evaluation of 550 kV Porcelain Transformer Bushings.* Amir S. Gilani, Andrew S. Whittaker, Gregory L. Fenves, and Eric Fujisaki. October 1999.
- PEER 1999/04** *Adoption and Enforcement of Earthquake Risk-Reduction Measures.* Peter J. May, Raymond J. Burby, T. Jens Feeley, and Robert Wood.
- PEER 1999/03** *Task 3 Characterization of Site Response General Site Categories.* Adrian Rodriguez-Marek, Jonathan D. Bray, and Norman Abrahamson. February 1999.
- PEER 1999/02** *Capacity-Demand-Diagram Methods for Estimating Seismic Deformation of Inelastic Structures: SDF Systems.* Anil K. Chopra and Rakesh Goel. April 1999.
- PEER 1999/01** *Interaction in Interconnected Electrical Substation Equipment Subjected to Earthquake Ground Motions.* Armen Der Kiureghian, Jerome L. Sackman, and Kee-Jeung Hong. February 1999.
- PEER 1998/08** *Behavior and Failure Analysis of a Multiple-Frame Highway Bridge in the 1994 Northridge Earthquake.* Gregory L. Fenves and Michael Ellery. December 1998.
- PEER 1998/07** *Empirical Evaluation of Inertial Soil-Structure Interaction Effects.* Jonathan P. Stewart, Raymond B. Seed, and Gregory L. Fenves. November 1998.
- PEER 1998/06** *Effect of Damping Mechanisms on the Response of Seismic Isolated Structures.* Nicos Makris and Shih-Po Chang. November 1998.
- PEER 1998/05** *Rocking Response and Overturning of Equipment under Horizontal Pulse-Type Motions.* Nicos Makris and Yiannis Roussos. October 1998.
- PEER 1998/04** *Pacific Earthquake Engineering Research Invitational Workshop Proceedings, May 14–15, 1998: Defining the Links between Planning, Policy Analysis, Economics and Earthquake Engineering.* Mary Comerio and Peter Gordon. September 1998.
- PEER 1998/03** *Repair/Upgrade Procedures for Welded Beam to Column Connections.* James C. Anderson and Xiaojing Duan. May 1998.
- PEER 1998/02** *Seismic Evaluation of 196 kV Porcelain Transformer Bushings.* Amir S. Gilani, Juan W. Chavez, Gregory L. Fenves, and Andrew S. Whittaker. May 1998.
- PEER 1998/01** *Seismic Performance of Well-Confined Concrete Bridge Columns.* Dawn E. Lehman and Jack P. Moehle. December 2000.

ONLINE REPORTS

The following PEER reports are available by Internet only at http://peer.berkeley.edu/publications/peer_reports.html

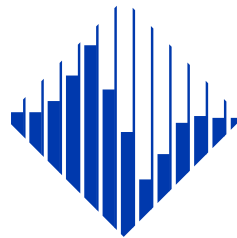
- PEER 2012/102** *Procedure to Restart an Interrupted Hybrid Simulation: Addendum to PEER Report 2010/103.* Vesna Terzic and Božidar Stojadinovic. October 2012.
- PEER 2012/101** *Mechanics of Fiber Reinforced Bearings.* James M. Kelly and Andrea Calabrese. February 2012.
- PEER 2011/107** *Nonlinear Site Response and Seismic Compression at Vertical Array Strongly Shaken by 2007 Niigata-ken Chuetsu-oki Earthquake.* Eric Yee, Jonathan P. Stewart, and Kohji Tokimatsu. December 2011.
- PEER 2011/106** *Self Compacting Hybrid Fiber Reinforced Concrete Composites for Bridge Columns.* Pardeep Kumar, Gabriel Jen, William Trono, Marios Panagiotou, and Claudia Ostertag. September 2011.
- PEER 2011/105** *Stochastic Dynamic Analysis of Bridges Subjected to Spatially Varying Ground Motions.* Katerina Konakli and Armen Der Kiureghian. August 2011.
- PEER 2011/104** *Design and Instrumentation of the 2010 E-Defense Four-Story Reinforced Concrete and Post-Tensioned Concrete Buildings.* Takuya Nagae, Kenichi Tahara, Taizo Matsumori, Hitoshi Shiohara, Toshimi Kabeyasawa, Susumu Kono, Minehiro Nishiyama (Japanese Research Team) and John Wallace, Wassim Ghannoum, Jack Moehle, Richard Sause, Wesley Keller, Zeynep Tuna (U.S. Research Team). June 2011.
- PEER 2011/103** *In-Situ Monitoring of the Force Output of Fluid Dampers: Experimental Investigation.* Dimitrios Konstantinidis, James M. Kelly, and Nicos Makris. April 2011.
- PEER 2011/102** *Ground-motion prediction equations 1964 - 2010.* John Douglas. April 2011.
- PEER 2011/101** *Report of the Eighth Planning Meeting of NEES/E-Defense Collaborative Research on Earthquake Engineering.* Convened by the Hyogo Earthquake Engineering Research Center (NIED), NEES Consortium, Inc. February 2011.
- PEER 2010/111** *Modeling and Acceptance Criteria for Seismic Design and Analysis of Tall Buildings.* Task 7 Report for the Tall Buildings Initiative - Published jointly by the Applied Technology Council. October 2010.
- PEER 2010/110** *Seismic Performance Assessment and Probabilistic Repair Cost Analysis of Precast Concrete Cladding Systems for Multistory Buildings.* Jeffrey P. Hunt and Božidar Stojadinovic. November 2010.
- PEER 2010/109** *Report of the Seventh Joint Planning Meeting of NEES/E-Defense Collaboration on Earthquake Engineering. Held at the E-Defense, Miki, and Shin-Kobe, Japan, September 18–19, 2009.* August 2010.
- PEER 2010/108** *Probabilistic Tsunami Hazard in California.* Hong Kie Thio, Paul Somerville, and Jascha Polet, preparers. October 2010.
- PEER 2010/107** *Performance and Reliability of Exposed Column Base Plate Connections for Steel Moment-Resisting Frames.* Ady Aviram, Božidar Stojadinovic, and Armen Der Kiureghian. August 2010.
- PEER 2010/106** *Verification of Probabilistic Seismic Hazard Analysis Computer Programs.* Patricia Thomas, Ivan Wong, and Norman Abrahamson. May 2010.
- PEER 2010/105** *Structural Engineering Reconnaissance of the April 6, 2009, Abruzzo, Italy, Earthquake, and Lessons Learned.* M. Selim Günay and Khalid M. Mosalam. April 2010.
- PEER 2010/104** *Simulating the Inelastic Seismic Behavior of Steel Braced Frames, Including the Effects of Low-Cycle Fatigue.* Yuli Huang and Stephen A. Mahin. April 2010.
- PEER 2010/103** *Post-Earthquake Traffic Capacity of Modern Bridges in California.* Vesna Terzic and Božidar Stojadinović. March 2010.
- PEER 2010/102** *Analysis of Cumulative Absolute Velocity (CAV) and JMA Instrumental Seismic Intensity (I_{JMA}) Using the PEER–NGA Strong Motion Database.* Kenneth W. Campbell and Yousef Bozorgnia. February 2010.
- PEER 2010/101** *Rocking Response of Bridges on Shallow Foundations.* Jose A. Ugalde, Bruce L. Kutter, and Boris Jeremic. April 2010.
- PEER 2009/109** *Simulation and Performance-Based Earthquake Engineering Assessment of Self-Centering Post-Tensioned Concrete Bridge Systems.* Won K. Lee and Sarah L. Billington. December 2009.
- PEER 2009/108** *PEER Lifelines Geotechnical Virtual Data Center.* J. Carl Stepp, Daniel J. Ponti, Loren L. Turner, Jennifer N. Swift, Sean Devlin, Yang Zhu, Jean Benoit, and John Bobbitt. September 2009.

- PEER 2009/107** *Experimental and Computational Evaluation of Current and Innovative In-Span Hinge Details in Reinforced Concrete Box-Girder Bridges: Part 2: Post-Test Analysis and Design Recommendations.* Matias A. Hube and Khalid M. Mosalam. December 2009.
- PEER 2009/106** *Shear Strength Models of Exterior Beam-Column Joints without Transverse Reinforcement.* Sangjoon Park and Khalid M. Mosalam. November 2009.
- PEER 2009/105** *Reduced Uncertainty of Ground Motion Prediction Equations through Bayesian Variance Analysis.* Robb Eric S. Moss. November 2009.
- PEER 2009/104** *Advanced Implementation of Hybrid Simulation.* Andreas H. Schellenberg, Stephen A. Mahin, Gregory L. Fenves. November 2009.
- PEER 2009/103** *Performance Evaluation of Innovative Steel Braced Frames.* T. Y. Yang, Jack P. Moehle, and Božidar Stojadinovic. August 2009.
- PEER 2009/102** *Reinvestigation of Liquefaction and Nonliquefaction Case Histories from the 1976 Tangshan Earthquake.* Robb Eric Moss, Robert E. Kayen, Liyuan Tong, Songyu Liu, Guojun Cai, and Jiaer Wu. August 2009.
- PEER 2009/101** *Report of the First Joint Planning Meeting for the Second Phase of NEES/E-Defense Collaborative Research on Earthquake Engineering.* Stephen A. Mahin et al. July 2009.
- PEER 2008/104** *Experimental and Analytical Study of the Seismic Performance of Retaining Structures.* Linda Al Atik and Nicholas Sitar. January 2009.
- PEER 2008/103** *Experimental and Computational Evaluation of Current and Innovative In-Span Hinge Details in Reinforced Concrete Box-Girder Bridges. Part 1: Experimental Findings and Pre-Test Analysis.* Matias A. Hube and Khalid M. Mosalam. January 2009.
- PEER 2008/102** *Modeling of Unreinforced Masonry Infill Walls Considering In-Plane and Out-of-Plane Interaction.* Stephen Kadysiewski and Khalid M. Mosalam. January 2009.
- PEER 2008/101** *Seismic Performance Objectives for Tall Buildings.* William T. Holmes, Charles Kircher, William Petak, and Nabih Youssef. August 2008.
- PEER 2007/101** *Generalized Hybrid Simulation Framework for Structural Systems Subjected to Seismic Loading.* Tarek Elkhoraibi and Khalid M. Mosalam. July 2007.
- PEER 2007/100** *Seismic Evaluation of Reinforced Concrete Buildings Including Effects of Masonry Infill Walls.* Alidad Hashemi and Khalid M. Mosalam. July 2007.

The Pacific Earthquake Engineering Research Center (PEER) is a multi-institutional research and education center with headquarters at the University of California, Berkeley. Investigators from over 20 universities, several consulting companies, and researchers at various state and federal government agencies contribute to research programs focused on performance-based earthquake engineering.

These research programs aim to identify and reduce the risks from major earthquakes to life safety and to the economy by including research in a wide variety of disciplines including structural and geotechnical engineering, geology/seismology, lifelines, transportation, architecture, economics, risk management, and public policy.

PEER is supported by federal, state, local, and regional agencies, together with industry partners.



PEER Core Institutions:
University of California, Berkeley (Lead Institution)
California Institute of Technology
Oregon State University
Stanford University
University of California, Davis
University of California, Irvine
University of California, Los Angeles
University of California, San Diego
University of Southern California
University of Washington

PEER reports can be ordered at http://peer.berkeley.edu/publications/peer_reports.html or by contacting

Pacific Earthquake Engineering Research Center
University of California, Berkeley
325 Davis Hall, mail code 1792
Berkeley, CA 94720-1792
Tel: 510-642-3437
Fax: 510-642-1655
Email: peer_editor@berkeley.edu

ISSN 1547-0587X